Moveout and Geometry

Dissertation
zur Erlangung des Doktorgrades
an der Fakultät für
Mathematik, Informatik und Naturwissenschaften
im Fachbereich Geowissenschaften
der Universität Hamburg

vorgelegt von

Benjamin Schwarz

Hamburg, 2015

Tag der Disputation: 23.06.2015
Folgende Gutachter empfehlen die Annahme der Dissertation:
Prof. Dr. Dirk Gajewski
PD Dr. Claudia Vanelle

Abstract

The knowledge of systematic traveltime differences in seismic recordings is essential for many important applications in exploration. Based on the assumption of locally coherent wavefields, I discuss the important concept of traveltime moveout and revisit the notion of virtual seismic sources, which, being central ingredients of the famous normal incidence point (NIP) and normal wave experiments, make use of reciprocity and raypath symmetries to replace the generally complex two-way ray geometry of a reflection by analogous simplified one-way propagating wavefronts. Using this concept of virtual seismic sources, I re-derive the well-known traveltime moveout expressions of the hyperbolic common reflection surface (CRS), multifocusing and the recently introduced implicit CRS operator, solely based on the simple geometry of straight rays and circular wavefronts. In the cause of these derivations I find, that the double-square-root moveouts of multifocusing and the implicit CRS reduce to the same expressions Höcht et al. found for the zero-offset section and the common-reflection-point (CRP) gather. In these domains, the traveltime moveout is fully governed either by the normal or by the NIP wavefront, which indicates a high potential for unification of these approaches.

Continuing this path of unification, I catch up ideas of de Bazelaire formulated in the late eighties and suggest two conceptually different mechanisms to justify the assumption of straight rays and circular wavefronts for generally heterogeneous media. While one of these mechanisms constitutes in a shift in velocity to account for overburden heterogeneity, in the second approach a constant shift of the reference time leads to the same adaption of the moveout, indicating a fundamental duality of higher-order expressions in heterogeneous media. Based on this dual formulation, I suggest generalized expressions for the classical common midpoint (CMP) hyperbola, the hyperbolic CRS moveout, multifocusing and the implicit CRS operator, for which the joint application of both mechanisms suggests exciting applications, like diffraction separation, multiple discrimination or the inversion of the excitation time of a passive seismic source, whose applicability is confirmed in synthetic and field data examples. Utilizing the formal coincidence of the fictitious NIP and the physically real passive seismic one-way experiment, subsequent inversion of the passive seismic wavefront measurements via NIP tomography resulted in a reasonable estimate of the true velocity gradient. In this framework, the often misinterpreted role of multifocusing gets a unique explanation.

Complementing the moveout duality for heterogeneous media, I study the higher orders of these operators under controlled conditions and conclude that the fundamental notion of coupling is essential to explain the observed systematic differences. In that frame I find that the decreased performance of hyperbolic CRS for diffractions can be quantitatively explained by a lack of the necessary influence of the normal wave radius on the higher offset orders and consequently, a coupling strength, which is decreased by up to a factor of three, compared to the accurate diffraction reference. For diffractions, the study of the higher orders reveals that, while the midpoint half-offset coordinates obey the strongest possible coupling, the respective source receiver moveout contributions are completely decoupled for any reference offset. Following from this higher-order analysis, I, again, propose versatile applications, like finite-offset extrapolation, diffraction operator decomposition and partial CRS migration and demigration and proof their applicability for synthetic and field data examples.

Zusammenfassung

Die Kenntnis von Laufzeitunterschieden registrierter seimischer Wellen bildet die Grundlage für viele wichtige Anwendungen in der Exploration. Unter der Annahme lokaler Kohärenz können Abweichungen im aufgezeichneten Wellenfeld primär auf Laufzeitunterschiede zurückgeführt werden. Zur kollektiven Beschreibung dieser Laufzeitunterschiede hat es sich in der Vergangenheit als nützlich herausgestellt, ein einfacher zu beschreibendes Ersatzproblem anstelle der komplizierten tatsächlichen Zwei-Weg-Strahlgeometrie heranzuziehen. Dieser Idee zugrundeliegend stellt das Konzept virtueller Quellen im Untergrund den zentralen Bestandteil meiner Arbeit dar. Aufbauend auf dieser Formulierung von einfacher zu beschreibenden Ersatzproblemen, stelle ich detaillierte Herleitungen bekannter Laufzeitapproximationen zur Verfügung, ohne dabei wie konventionell auf Prinipien der paraxialen Strahlentheorie zurückzugreifen, sondern einzig basierend auf der Annahme der einfachen Geometrie lokal kreisförmiger Wellenfronten. Im Zuge dieser Herleitungen ergeben sich anschauliche Symmetrien und Korrespondenzen in den Subdomainen der *zero-offset* (ZO) und der *common reflection point* (CRP) Konfiguration, die auf eine Vereinheitlichung dieser Beschreibungen hindeuten.

Diesen Hinweisen folgend stelle ich zwei Mechanismen vor, um das Bild kreisförmiger Wellenfronten mit allgemein heterogenen Medien zu verbinden, die zu einer weiteren Vereinheitlichung der etablierten Methoden führen. Basierend auf diesen Mechanismen und den einfachen geometrischen Herleitungen stelle ich generalisierte Laufzeitoperatoren vor, welche, je nach Wahl des Ersatzproblems, die konventionell in der Litaratur motivierte oder, basierend auf dem zweiten Mechanismus, eine neue Erscheinungsform annehmen. Ein Vergleich dieser dualen Operatoren untermauert die zuvor beobachtete Vereinheitlichung der verschiedenen Approximationen und motiviert interessante Anwendungen in verschiedenen Bereichen der Seismik, wie z.B. die Zeitlokalisierung einer passiven seismischen Quelle. Die *normal incidence point* (NIP) Tomographie basiert auf lokalen Neigungs- und Krümmungsmessungen einer konzeptionellen Einwegs-Welle, die ihren Ursprung in einer fiktiven Quelle im Untergrund zu haben scheint. Während ihre Anwendbarkeit für Reflektionen bereits bestätigt wurde, zeige ich, dass eine Anwendung auf Diffraktionen und passive seismische Daten nicht nur prinzipiell möglich ist, sondern aufgrund des Ein-Weg-Charakters der entsprechenden Laufzeitunterschiede auch deutlich natürlicher erscheint.

Ergänzend zu der besprochenen Dualität für heterogene Medien studiere ich die höheren Ordnungen der hergeleiteten Operatoren und schlussfolgere, dass das grundlegende Konzept der Kopplung von zentraler Bedeutung ist, um die beobachteten systematischen Abweichungen verschiedener Approximationen zu erklären. In diesem Rahmen schliesse ich, dass die schlechte Anpassung der hyperbolischen *common reflection surface* (CRS) Näherung mit der geringen Koordinaten-Kopplung des entsprechenden Operators, qualitativ und quantitativ, erklärt werden kann. Für Diffraktionen hingegen ergibt sich im Rahmen dieser Studien eine maximale Kopplung für die *midpoint* und *half-offset* Koordinaten und eine entsprechende vollständige Entkopplung in den akquisitionsnahen Quell- und Empfängerkoordinaten, woraus sich neue Anwendungen, wie etwa ein fundamentales Dekompositionsprinzip oder eine hochauflösende Diffraktions-Tomographie ergeben. Wie zuvor untermauere ich die Realisierbarkeit der vorgestellten Konzepte mit synthetischen und industriellen Felddatenbeispielen.

Contents

List of Figures

List of Tables

1. Introduction

With the strong advent of full-waveform inversion (FWI, Tarantola, 1984) in both, exploration and earthquake or passive seismology (e.g., Fichtner et al., 2009), there seems to exist a tool that naturally unifies the two fields, since it has (in principle) the potential to handle arbitrary bandwidths and the full wavefield (Tarantola, 1984; Virieux and Operto, 2009). Being a major topic of current research in exploration, despite first promising attempts (e.g., Biondi and Almomin, 2013; Warner and Guasch, 2014), the practical (stable and efficient) implementation of FWI is truly challenging and the quality of the results crucially depends on the condition of the input data and the starting model. In addition, current successful implementations in exploration almost exclusively target diving waves or are in the need of low frequencies to guarantee conversion, which results in the need of large-offset data acquisition and an undesirable neglection of high frequencies in the reflected or backscattered portion of the wavefield (e.g., Virieux and Operto, 2009). Traveltime inversion schemes, like stereotomography (Billette and Lambaré, 1998), were shown to also provide reasonably high accuracy and resolution for deep reflection targets, indicating the complementary nature of full-waveform methods and traveltime-based tomography, which suggests a high potential of combined use of both methodologies (e.g., Prieux et al., 2013).

In contrast to FWI and depth imaging, approximations in time allow for efficient and robust workflows, which in areas of moderate lateral complexity can lead to a reasonable degree of accuracy. The main benefit of imaging in time is the principal independence of a user-provided velocity model, which forms the crucial ingredient for processing in depth (Landa, 2007). Being based on the assumption of local coherence of the recorded wavefield, stacking techniques can be employed in a purely data-driven fashion. While in complex settings the requirement of local coherence is not always fulfilled, data acquired in regions with moderate lateral velocity changes can, even on large scales, be described reasonably well with analytic traveltime operators. Exploiting the main benefit of the locally coherent summation of traces, stacking can lead to a significant increase of the signal-to-noise ratio (Mayne, 1962; Jäger et al., 2001), which can be considered also beneficial for more sophisticated depth imaging techniques (Baykulov et al., 2011). As a generalization of the classical CMP stack by Mayne, the common-reflection-surface (CRS) stack (Jäger et al., 2001; Mann, 2002) makes optimal use of the redundancy of information in the acquired data. In addition, the estimated attributes of the conceptual normal (N) and normal incidence point (NIP) wave experiments (Hubral, 1983), can be used for many important applications like diffraction separation and imaging (Dell and Gajewski, 2011), multiple supression (Dümmong and Gajewski, 2008), the estimation of Fresnel zones (Mann, 2002), migration weights (Spinner, 2006), geometrical spreading (Hubral, 1983), time migration velocities (Mann, 2002; Bobsin, 2014) or tomographic velocity inversion for depth imaging (Duveneck, 2004), just to name a few.

Although a parabolic traveltime formula, which can be seen as a truncated Taylor series expansion of the traveltime, seems to be the most intuitive choice, applications to synthetic and field data have suggested that a hyperbolic operator usually results in a better fit (Schleicher et al., 1993; Vanelle, 2002; Jäger, 1999). Because more com-

plex subsurface settings are nowadays encountered in hydrocarbon exploration, diffractions and other highly curved subsurface features become increasingly important. In addition, due to the respective high angle coverage, diffractions are thought to contain super-resolved information about the subsurface (Khaidukov et al., 2004) and are strong indicators of fault structures. Fomel and Grechka (2001) concluded that even for a homogeneous background, the description of diffracted traveltimes is a higher-order problem and, in non-local vicinities, cannot be accurately described by hyperbolic or parabolic operators. Due to this nonhyperbolicity of diffractions and traveltimes from highly curved reflectors, efforts have been made to derive higher-order traveltime approximations (e.g., Landa et al., 2010; Fomel and Kazinnik, 2013; Vanelle et al., 2010; Schwarz et al., 2014c).

While on the one hand, the most commonly used hyperbolic CRS moveout expression is conventionally gained via squaring the parabolic approximation resulting from paraxial ray theory and omitting higher orders than two (Bortfeld, 1989; Schleicher et al., 1993; Vanelle, 2002), many authors also pointed out, that this expression provides the exact solution for the reflection at a planar dipping interface in a homogeneous medium (e.g., Ursin, 1982; Schleicher et al., 1993), which suggests that the underlying derivations could very well be also based on the simple geometry of straight rays (Levin, 1971). Although the hyperbolic expression is based on a second-order expansion of the actual traveltime, even the neglection of higher orders (after squaring) does not prevent the actual traveltime, consisting of a sqare-root-expression, from being of higher order (e.g., Thore et al., 1994). The multifocusing moveout on the other hand (Gelchinsky et al., 1999; Landa et al., 1999; Tygel et al., 1999), is conventionally derived partially from straight-ray geometry and partially based on concepts of zero-order ray theory (Gelchinsky et al., 1999), thereby naturally implying higher orders than two. However, due to the mixing of ray-theoretical and geometrical arguments, the conventional derivations seem not so easily accessible. For highly curved features like diffractions, Schwarz (2011) and Schwarz et al. (2014c) found that the double-square-root operators of multifocusing and the implicit CRS approach behave quite differently, when heterogeneity is present in the overburden, although both are of similar order and based on the same attributes of the NIP and the normal wave (Hubral, 1983). So, the landscape of existing moveout approximations, due to varying mathematical complexity and different incorporation of attributes, appears very versatile and systematic differences reveal to be not sufficiently covered and explained in literature (see, e.g., Jäger, 1999).

The finite-offset CRS stack (Zhang et al., 2001), due to the lower symmetry of the underlying raypaths, is of higher dimensionality than the zero-offset formulation and, therefore, is suited for the local description of the full acquired prestack data, resulting in improved illumination in complex subsurface settings related to, e.g., salt structures and complicated fault systems (Spinner et al., 2012). In addition, since it generally accounts for the asymmetry of the source and the receiver ray segments, it was shown to be also applicable to PS converted wave data (Bergler et al., 2002). In less complex subsurface settings and for pure mode reflections, however, the local application of globally defined zero-offset operators to finite-offset targets was proven to be reasonably justified and led to impressive results (Baykulov and Gajewski, 2009; Eisenberg-Klein et al., 2008), indicating that finite-offset processing applied to the full prestack data volume is not always required and zero-offset operators can be used instead for such environments.

The main aim of this thesis is to provide a generalized view on existing moveout approximations. Inspired by Shah (1973), Höcht et al. (1999) and Vanelle (2012), I seek to unify existing approaches and reveal their underlying symmetries with the only help of simple geometry. In addition, geometry gives the exciting opportunity, to leave the second-order limitations of paraxial ray theory behind and to study the important concepts of globality and coupling in a controlled and simple framework, which, due to their higher-order nature, cannot be fully understood by confinement to first and second orders. In fact, as will become clear, all systematic differences observed for the different considered moveouts can, without exception, all be attributed to orders higher than two.

Chapter 2 gives a brief and simple introduction to the concept of traveltime moveout and its connection to the assumption of local coherence in the recorded wavefield. By discussing the differences of the complementary but equivalent pictures of rays and wavefronts I provide a general formulation of moveout, which formally reduces the measurement of traveltime differences to the measurement of a one-way wavefront. Concluding this chapter, I briefly review the underlying symmetries of the fundamental NIP and normal wave experiments. Based on the intrinsic ambiguities arising from pure traveltime measurements, I discuss the important notion of a virtual seismic source.

Based on the wavefront interpretation of traveltime moveout, which was suggested in Chapter 2, in part following previous investigations of other authors, **Chapter 3** is concerned with the re-derivation of important, well-known traveltime expressions, like the classical CMP hyperbola, the hyperbolic CRS moveout, multifocusing and the recently introduced implicit CRS approach from pure and simple straight-ray geometry and the connected implication of circular wavefront measurements. In this circular wavefront picture, I find that the double-square-root operators of multifocusing and implicit CRS reduce to exactly the same expressions for the normal wave experiment in the zero-offset section and in the CRP configuration, thereby revealing the exact correspondence with the geometrically derived parametric CRS expression by Höcht et al. (1999).

In **Chapter 4** I review and generalize two different mechanisms to ensure the applicability of the geometrically derived operators in the presence of heterogeneity. Following the paths of de Bazelaire (1988) and Höcht et al. (1999), I introduce generalized transformation formulae which directly connect the two complementary mechanisms and therefore lead to a dual description of higher-order moveouts. In the context of the presented general duality, the unique and often misinterpreted role of multifocusing gets a reasonable and sound explanation. Parts of this chapter have been published as conference abstracts (Schwarz et al., 2014a, 2015b).

Chapter 5 is dedicated to a detailed and rigour study of the important concept of coupling, which, in general, can be approached from two angles, where either the two virtual wavefront measurements are coupled, i.e. influence each other, or, following from the selectivity according to Snell's law in the CRP domain, a coupling between the midpoint and half-offset or source and receiver coordinates can be observed. Based on the notion of globality, which follows from higher-order accuracy and following ideas of Lavaud et al. (2004) and Vanelle et al. (2014), I suggest extrapolation equations,

which allow for the prediction of finite-offset traveltimes and attributes from zero-offset measurements. Concluding this chapter I discuss the special role of the diffraction case, for which, following from higher-order analysis and the virtual source interpretation, a complete decoupling of source and receiver measurements can be observed. Consequently, I find that zero-offset and finite-offset information is highly redundant for diffractions, which suggests a powerful decomposition scheme, in which exact finite-offset measurements can be composed of two pure zero-offset measurements. Parts of this chapter have been published as conference abstracts and have, in addition, inspired a masters thesis (Schwarz et al., 2014b; Bauer, 2014; Bauer et al., 2015).

Concluding this thesis, in **Chapter 6**, I suggest a variety of potential applications, which are direct implications of the symmetries and dualities studied in the previous chapters. Based on the higher-order moveout duality for heterogeneous media (Chapter 4) and the notions of globality and coupling (Chapter 5), I propose the concept of multi-operator analysis, in which different operators are applied to the same targets and conclusions are drawn from the systematic differences that can be observed. Following from this multi-operator analysis, I present new diffraction filters, which for the presented complex synthetic examples, reveal a better separation of diffracted and reflected energy. In addition, I confirm the applicability of the finite-offset extrapolation equations introduced in Chapter 5 for a complex field data example, for which an efficient subsequent local refinement scheme leads to accurate operator fit and attribute quality in the full considered prestack volume. Furthermore, I discuss the potential and the limitations of CRS-based partial time migration, whose applicability is closely connected to the notion of globality discussed in Chapter 5. Following the virtual source interpretation, suggested at the end of Chapter 2, I present the results of NIP tomography for a diffraction, where the required NIP wave attributes were either measured with the hyperbolic CRS or the double-square-root implicit CRS operator. Concluding this chapter, I propose a time-based passive seismic workflow, in which the application of the dual description of a simple one-way diffraction operator allows for a robust inversion of the generally unknown true source excitation time. Following from the virtual source interpretation, I demonstrate that the NIP wave tomographic inversion can directly be used for subsequent passive seismic velocity model building. Parts of this chapter have been published in the form of conference abstracts (Schwarz et al., 2014a, 2015a,b).

2. Traveltime measurements

In this first chapter of the thesis I will give a brief introduction to the seismic method and discuss the potential benefits and pitfalls of neglecting phase and amplitude information of the recorded signal. As will become clear, based on local coherence in the wavefield, in certain vicinities the amplitude and phase of the signal do not vary significantly and the differences can in good approximation be fully attributed to the traveltimes. Based on this assumption of local coherence, I introduce traveltime moveout as the central concept of my thesis. I continue with a brief discussion of the ray wavefront duality and conclude with the important notion of circular wavefronts and virtual sources.

2.1. The seismic experiment

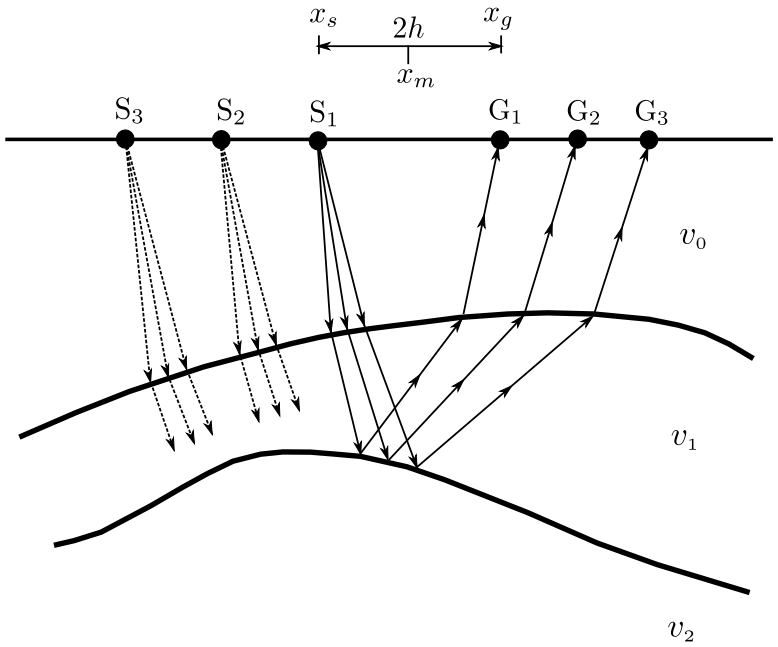

Figure 2.1.: The typical active seismic experiment traditionally performed in subsurface exploration consists of an active source S and an array of receivers that records the reflected, critically refracted and backscattered seismic energy from the subsurface. Each trace is either denoted by the corresponding source and receiver positions, x_s and x_g or their midpoint coordinate x_m and half the offset between source and receiver (h).

In contrast to earthquake seismology, the active seismic method deals with controlled sources commonly placed at or near the earth's surface. Depending on the type of source chosen, the starting conditions, like i.e. the excitation times are generally well-determined. Figure 2.1 shows a typical setup of an active seismic experiment. While a sufficiently large count of receivers, denoted by G, can lead to a better illumination of the subsurface, the repeated controlled excitation of artificial seismic sources, besides

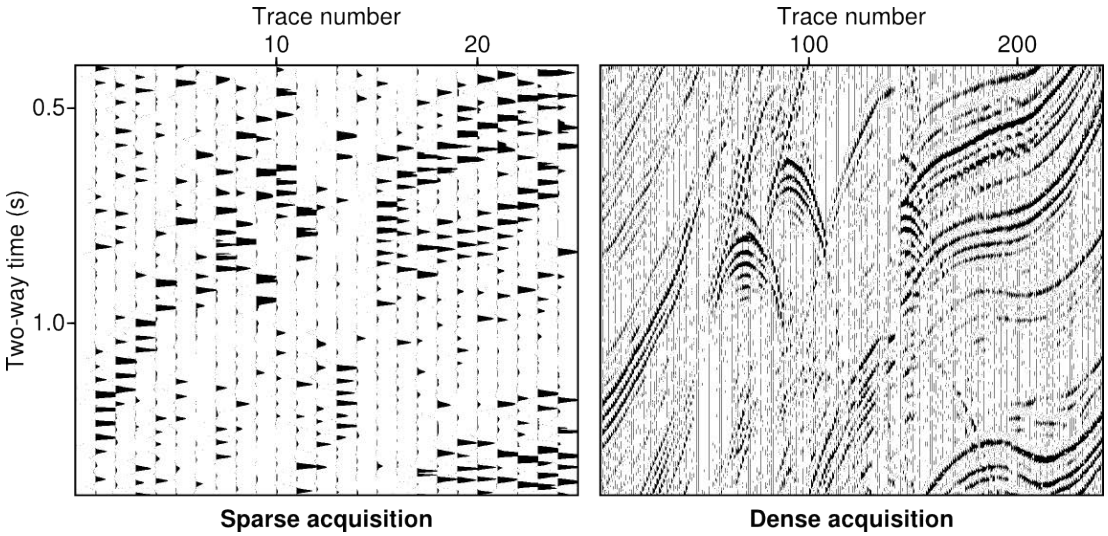

Figure 2.2.: Illustration of the importance of source receiver coverage for the concept of local coherence. Shown is a thinned out version (left, only every 10th trace is displayed) and the original zero-offset section (right) of the well-known Marmousi synthetic dataset (Versteeg, 1994). The concept of local coherence of the recorded wavefield is only applicable, if the acquisition is sufficiently dense.

additional illumination also yields a high redundancy in the data. The recorded seismic traces, each corresponding to a specific source receiver pair, are commonly characterized either by the lateral locations of the source (x_s) or the receiver (x_g), respectively, or by the quantities

$$x_m = \frac{x_g + x_s}{2} \quad , \quad h = \frac{x_g - x_s}{2} \quad , \tag{2.1}$$

where x_m represents the lateral position of the midpoint and h denotes the half-offset between source and receiver. While the source and receiver positions are closer related to the actual acquisition geometry, the freshly introduced midpoint and half-offset coordinates turn out to be particularly useful for the subsequent processing of the recorded data. As illustrated in Figure 2.1, the energy of a source excited at the acquisition surface radiates into the subsurface (e.g., Sheriff and Geldart, 1995). While most of this energy, for near-vertical incidence, usually gets transmitted and subsequently attenuated, the active seismic method aims at imaging the subsurface via the reflected, critically refracted or backscattered, i.e. diffracted portion of the wavefield. While these surface recordings contain amplitude, phase and traveltime information, the concepts and assumptions presented and utilized in this thesis are all based on the high-frequency approximation, in which the seismic energy, in accordance with geometrical optics, is commonly described by rays or wavefronts (e.g., Červený, 2001), neglecting phase and amplitude information. As a consequence, in the following, a *measurement* will only consider traveltimes.

2.2. Local coherence

As argued in Section 2.1, an active seismic experiment usually invokes a multitude of sources and receivers. Therefore, features in the subsurface are commonly expected to be covered multiple times. While on global scales, i.e. for earthquake seismology, receiver networks, due to the large area to be covered, can be considered generally sparse, active seismic networks are sufficiently denser. Although recently, attempts have been made to install large and dense arrays also on the global scale (e.g., Burdick et al., 2008), one can argue that the characteristics of the recorded signal, i.e. traveltime, amplitude and phase, are generally expected to change noticeably inbetween two neighbouring stations when considering a global passive seismic acquisition.

Figure 2.2 illustrates the general importance of coverage density for the identification of structural patterns in the seismic data. While for a sparse acquisition, these patterns, corresponding to the time response of geological features, are not or only partially recognizable, a sufficiently dense acqusition[1] reveals continuously varying traveltimes and only small amplitude and phase variation for neighbouring traces. As will be argued in Chapters 5 and 6, the concept of local coherence, i.e. the local similarity between neighbouring traces, is central to many important processing steps, which aim at making use of the redundancy of information in the data. The process of stacking, in this context, can only be considered a successful operation, if the summed data is similar in the respective vicinity, i.e. *locally coherent*.

2.3. Traveltime moveout

In the previous section, I discussed the idea that a sufficiently dense acquisition, i.e. a dense source receiver coverage, allows for the recognition of locally coherent events and patterns in the data. As has been argued, in the corresponding local vicinities differences in phase and amplitude are mostly negligible and the traveltime moveout Δt, generally defined via

$$t = t_0 + \Delta t \tag{2.2}$$

is the central discrimination criterion. In (2.2) t_0 and t denote the traveltime of a reference ray, recorded at the central trace and the corresponding event traveltime of a neighbouring trace. Please note that if the reference traveltime is known, the traveltime moveout Δt is the only quantity needed to determine the corresponding traveltimes in the vicinity (compare Figure 2.3). As can be deduced from Figure 2.2, traveltimes of a particular coherent event mostly vary smoothly from trace to trace and, thus, can commonly be described by a continuous function $\Delta t(\Delta x)$, where Δx is the lateral separation of a trace in the local vicinity of the reference trace, whose position is denoted by x_0. The moveout can be estimated in the vicinity of any reference ray, which might either correspond to a zero-offset (ZO) or a finite-offset (FO) configuration. As will be discussed in Chapter 5, zero-offset-based moveout approximations are commonly used in comparably large vicinities, whereas finite-offset approaches are applied more locally. All moveouts have in common that in order to describe the traveltimes of neighbouring rays, only one reference traveltime, i.e. the traveltime of a central ray and the function Δt is needed. However, for a sparse source receiver coverage, the concept of moveout can be of limited use, if the typical trace separation violates the coherence assumption.

[1] Ten times more traces are available in this example.

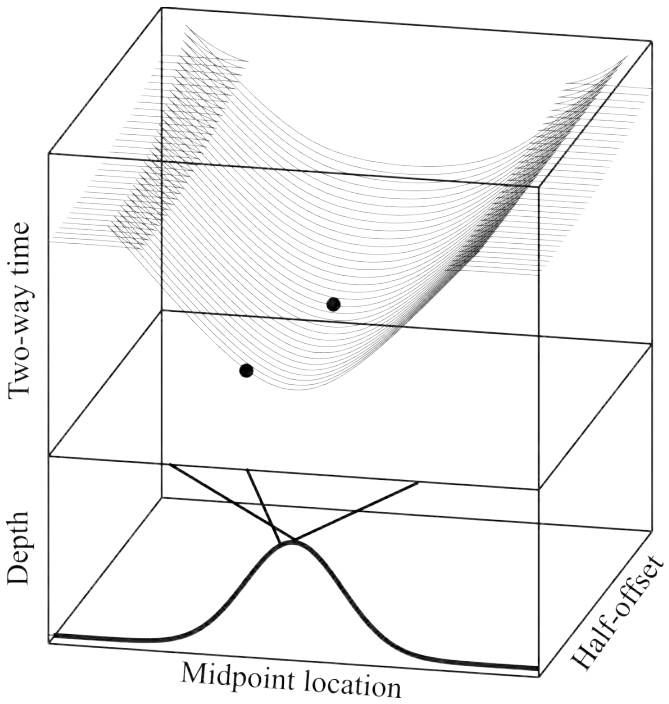

Figure 2.3.: Provided the acquisition is sufficiently dense, the traveltime response of the subsurface appears as a locally smoothly varying entity. Shown is a simple synthetic example (Müller, 1999), in which the corresponding 2D subsurface model consisting of a dome-like reflecting structure in a constant velocity background has a distinct and characteristic traveltime response. The two dots indicate the traveltimes corresponding to the two ray paths visualized in the model.

While until now I confined myself to the intuitive ray picture, in the next section I will introduce the competing concept of wavefronts, which will turn out to be particularly suited to describe differences in traveltime.

2.4. Rays and wavefronts

In the high-frequency approximation, the concepts of rays and wavefronts are equally important (Červený, 2001). The basic characteristics of both approaches can be explained in Figure 2.4, which shows a family of rays and a set of wavefronts, both describing exactly the same wave propagation. While the rays can be considered integral quantities, containing all their past, a wavefront can be interpreted as a snapshot showing the end positions of infinitely many neighbouring rays corresponding to the same propagation time. Consequently, the ray concept is well-suited to describe total traveltimes, which are integral quantities, whereas a set of wavefronts, as shown in Figure 2.4, helps to compare the traveltimes at two spatially separated positions.

Due to their integral character, rays appear most suited to formulate Snell's law for reflection or refraction at an interface (compare Figure 2.4). Nevertheless, the same physical phenomenon can also be expressed in terms of wavefront relations, coupling the curvature before and after encountering the discontinuity. So, although presented as competing concepts, rays and wavefronts are generally coupled to each other. In

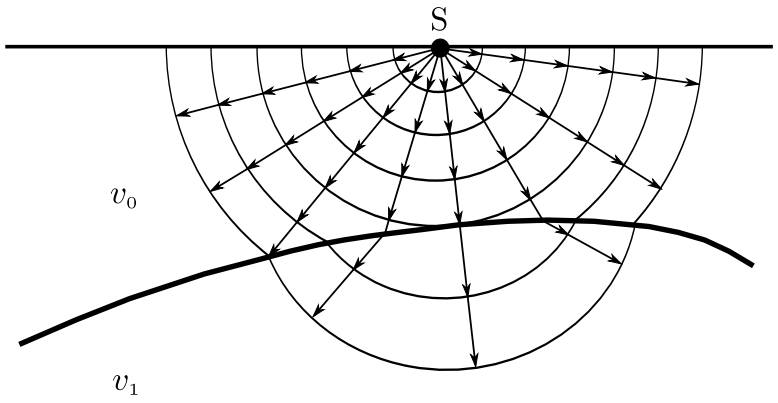

Figure 2.4.: Rays and wavefronts provide a conjugate view on the propagation of wavefields (e.g., Červený, 2001). Both approaches are closely related and are based on the same high-frequency assumption but have unique advantages in certain fields of application. For a constant velocity medium and at planar or circular interfaces, rays and wavefront curvatures can be related via simple concepts of geometry.

isotropic media, rays are always normal on the wavefront (e.g., Červený, 2001) and for the homogeneous case, the length of a ray R_0 is proportional to its traveltime $t_0 = R/v$ and exactly equal to the curvature radius of the respective wavefront. At a later time $t = t_0 + \Delta t$, the corresponding wavefront radius reads

$$R = R_0 + v\Delta t \quad , \tag{2.3}$$

which lets us arrive at the following simple expression for the traveltime moveout

$$\Delta t = \frac{R - R_0}{v} \quad . \tag{2.4}$$

As I will demonstrate in Chapter 3 and Chapter 4, formula (2.4), despite its formal simplicity, can be used to derive all well-established closed-form moveout expressions. Although the underlying assumption of homogeneity is, of course, generally not fulfilled, I will show in Chapter 4 how the notion of circular wavefronts and, consequently, straight rays can also be maintained for the heterogeneous case.

2.5. Virtual sources

In the previous section I introduced a simple yet general expression for the traveltime moveout in a homogeneous medium, for which the travel distance, i.e. the ray path, the respective traveltime and the curvature radius of the corresponding wavefront are directly proportional to each other. In this section I would like to emphasize that, as immediately follows from equation (2.4), the traveltime moveout observed on several neighbouring traces is fully governed by the knowledge of the wavefront curvature. As a consequence, the measurement of traveltimes of a locally coherent event can be reduced to the measurement of one reference traveltime t_0 and a wavefront measurement R_0, which governs the traveltime differences observed on the neighbouring traces.

In physical reality, the true wavefront propagation is generally complicated and, due to the confinement of the acquisition instrumentation to the earth's surface, usually

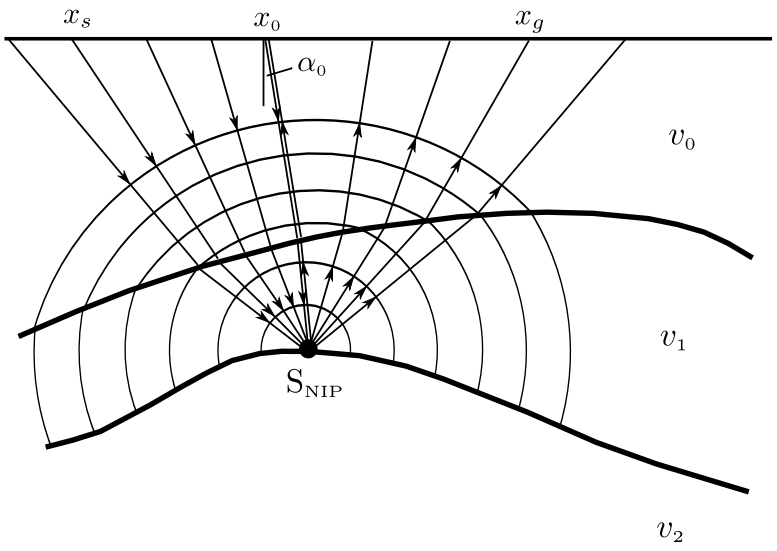

Figure 2.5.: Based on the reciprocity of ray paths, the normal incidence point (NIP), or more generally, the common reflection point (CRP), can be viewed as a virtual seismic source (Hubral, 1983). For Snell's law to be fulfilled only certain emission angles are realized and thus, for a general reflection, the source and receiver angles are coupled in the NIP or the CRP gather.

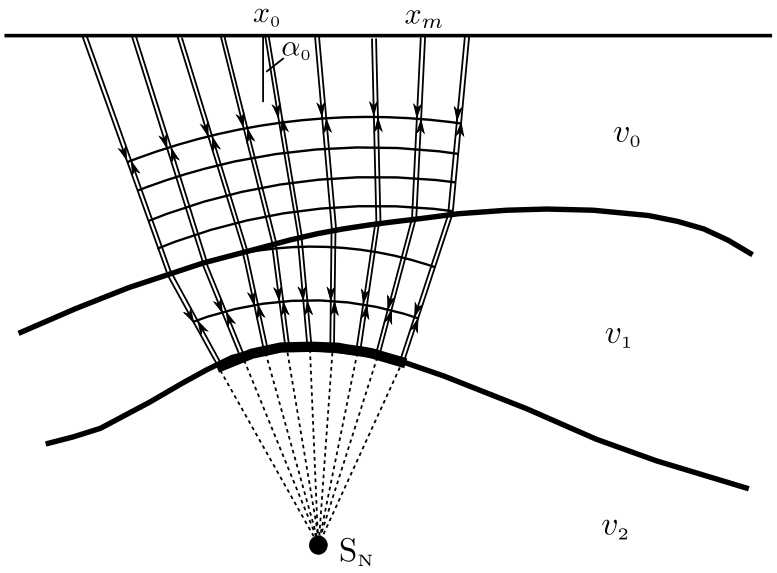

Figure 2.6.: In the zero-offset case the up- and down-going ray paths coinside and based again, like for the NIP wave (see Figure 2.5) on the reciprocity principle, the traveltime response from a locally circular reflector segment can be described by a one-way wavefront emitted in S_N and traveling at half the actual medium velocity (Hubral, 1983). Since all considered rays in the zero-offset configuration are normal rays, there are no restricted emission angles from the virtual source as in the general NIP case.

undergoes rapid directional changes, like reflection or diffraction, on its way from the source to the receiver. Thus, we generally have to deal with a two-way process, whereas equation (2.4) is defined for simple one-way wave propagation, which at first sight is a strong limitation. However, based on the famous and physically important NIP and normal wave experiments introduced by Hubral (1983), I argue that due to reciprocity and connected ray path symmetries the picture of a one-way propagating wavefront is still fully capable of describing the observed moveout in the data. Figure 2.5 and Figure 2.6 illustrate the underlying symmetries of the NIP and the normal wave experiment, respectively. While the NIP wavefront describes the true traveltime moveout for the presented configuration of a common reflection point (CRP), the normal wave accurately simulates the true observed moveout in the zero-offset section, for which source and receiver positions coincide.

For a planar horizontal reflector and vertical heterogeneity only, the CRP coincides with the CMP and the NIP and the normal wave experiment do not influence each other, i.e. their domains, the zero-offset section and the CRP gather, are decoupled from each other. Please note however, that even a simple tilt of the target reflector already implies that the CRP coordinates depend on both, the midpoint and the half-offsets, resulting in a coupling of the NIP and the normal wave contributions to the traveltime moveout. It is interesting to observe that the second-order parabolic zero-offset approximation (e.g., Bortfeld, 1989; Schleicher et al., 1993; Jäger et al., 2001) does not account for this CRP coupling, in support of the NIP wave theorem, which states that the traveltime moveout in the CMP gather up to second order is fully characterized by properties of the NIP wave (Hubral, 1983). However, as will become clear in Chapter 3 and Chapter 5 of this thesis, this CRP coupling is not negligible and important in order to accurately describe curved subsurface structures like diffractors.

It is important to note that in the context of traveltime moveout, the notion of a CRP is more general than the one of the NIP, since the latter is only defined, if a normal ray, i.e. zero-offset ray, is part of the considered ray ensemble. For the general finite-offset case, i.e. if only finite-offset rays are considered, I suggest to describe the respective symmetry in the CRP gather by a so-called CRP wave experiment, corresponding to a conceptual one-way wavefront originating at the CRP, rather than the zero-offset-related NIP. As I will stress in the context of globality in Chapter 5, this CRP experiment is also well-defined, if a finite-offset moveout approximation and consequently, a finite-offset reference ray is considered. In turn, the suggested generalized CRP wave becomes equivalent to the NIP wave, if the zero-offset ray is part of the considered ray ensemble.

Further generalizing the idea behind the NIP and the normal wave concept, one can argue that, due to the general ambiguities of surface-based traveltime measurements, complicated two-way wave propagation can, in certain subsets of the multicoverage response, be simulated by an equivalent one-way process, which generally is much simpler to describe. Emphasizing this statement, Figure 2.7 shows four different subsurface settings with a true wave propagation of varying complexity, which, due to the ambiguous nature of traveltime moveout, can all be explained by the suggested simple expression (2.4), which was derived for the straight-ray one-way propagation of a circular wavefront. Concluding this rather general exposition, as briefly mentioned before, I argue that even moveouts which correspond to complicated ray geometries, can, often in good

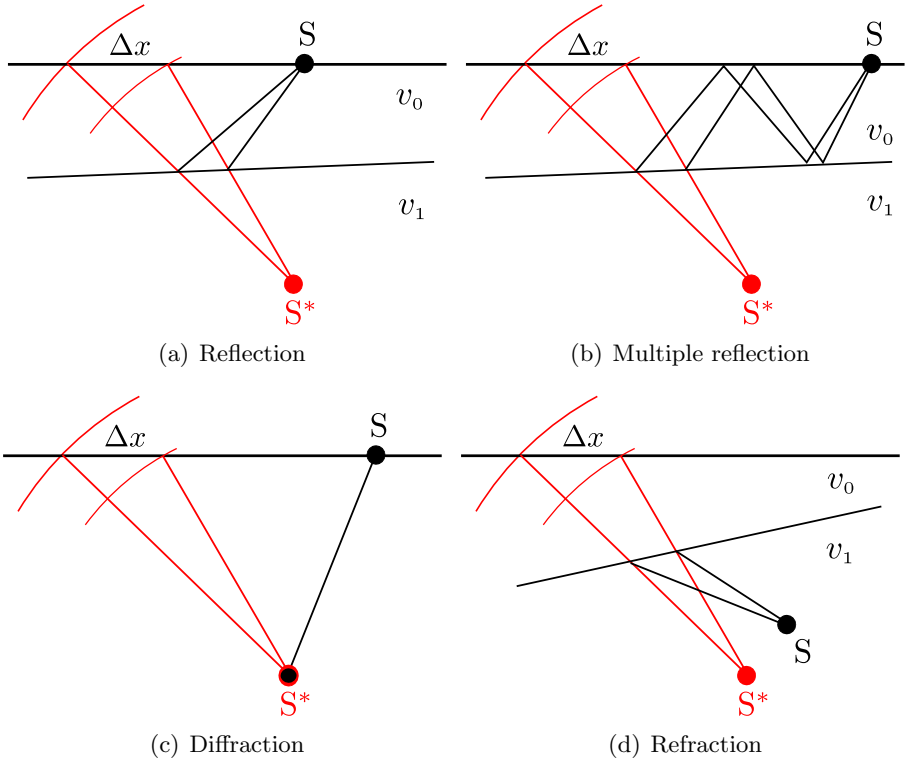

Figure 2.7.: When confined to the earth's surface, as in traditional seismic acquisition, one and the same traveltime moveout (geometrically illustrated in red color) can be explained by many different scenarios, like (a) reflection, (b) multiple reflection, (c) diffraction, or refraction at a local discontinuity. Due to the neglection of amplitude and phase information, traveltime measurements, thus, can be highly ambiguous, posing problems for inversion. In the frame of this work I argue that in turn all of the presented propagation types can be described by one and the same vitual source and a very simple connected geometry.

approximation, be described by a much simpler geometry of straight rays (see Chapter 3). As I will show in the following chapters, the concept of virtual seismic sources[2] is particularly useful in the context of tomography and, due to the formal reduction of two-way to one-way processes, establishes a strong connection to the natural one-way moveouts arising from diffraction and the excitation of a passive seismic source.

[2]The term *virtual source* is commonly used in the context of seismic interferometry (e.g., Wapenaar and Fokkema, 2006). In the frame of this thesis, it only denotes the apparent focus of a seismic wavefront.

3. Straight-ray traveltimes

In the previous chapter, I concluded that the traveltime moveout, i.e. the traveltime difference observed between different points at the acquisition surface, is in general not uniquely defined and can, in a sufficiently small vicinity Δx around a certain reference, be described by the geometry of a locally circular emerging wavefront (see Figure 3.1(b)). While for a planar wavefront, which is illustrated in Figure 3.1(a), the traveltime moveout can conveniently be described by employing simple trigonometry at a rectangular triangle,

$$\sin\alpha = \frac{v\Delta t}{\Delta x} \quad \Leftrightarrow \quad \Delta t = \frac{\sin\alpha}{v}\Delta x \quad , \tag{3.1}$$

the geometry for traveltime moveout resulting from a circular emerging wavefront obeys the law of cosines and we have

$$\begin{aligned} (v\Delta t + R)^2 &= \Delta x^2 + R^2 - 2R\Delta x\cos(90^\circ + \alpha) \\ \Leftrightarrow \quad \Delta t &= \frac{\sqrt{R^2 + 2R\Delta x\sin\alpha + \Delta x^2} - R}{v} \quad , \end{aligned} \tag{3.2}$$

where R is the finite local curvature of the wavefront measured at the reference location and Δt denotes the traveltime difference occurring due to the inclination and the curvature of the wavefront, respectively (please compare expression (2.4)). Without loss of generality, in both presented expressions for the planar and the circular wavefront moveout, the velocity v represents a locally constant velocity near the acquisition surface. Both these expressions have already been derived by other authors (e.g., Shah, 1973; Vanelle, 2012; Höcht et al., 1999; Gelchinsky et al., 1999) and formed the central building blocks of Shah's unique approach to relate traveltime differences to properties in the depth domain, which resulted in a simple geometrical derivation of the parabolic CRS moveout[1].

Since up to the first order, both presented moveout expressions (3.1) and (3.2) coincide, the circular wavefront approximation is of higher order and therefore accurate for larger displacements Δx from the reference location. As will become clear in the cause of this chapter, in principle, equation (3.2) together with Snell's law and reciprocity, is sufficient to derive the hyperbolic CRS moveout, the double-square-root multifocusing expression and the implict CRS operator, purely from geometry. As motivated in the previous chapter, the general non-uniqueness of surface-based wavefront measurements can compromise the inversion of subsurface properties. But, as concluded before, it also allows for the replacement of a rather complicated ray geometry by a simple one-way problem, which is much easier and more convenient to describe (compare Figure 2.7). Connected to this idea of replacing a complex problem with a simple auxiliary setting that leads to the same outcome is very closely related to the concept of a virtual kinematic seismic source (see Chapter 2). Consequently, I argue that for every straight-ray geometry and circular wavefronts there exists an accompanying picture of a virtual source located at the respective wavefront focus in depth.

[1] For a clear re-derivation of Shah's approach, I refer to Vanelle (2012).

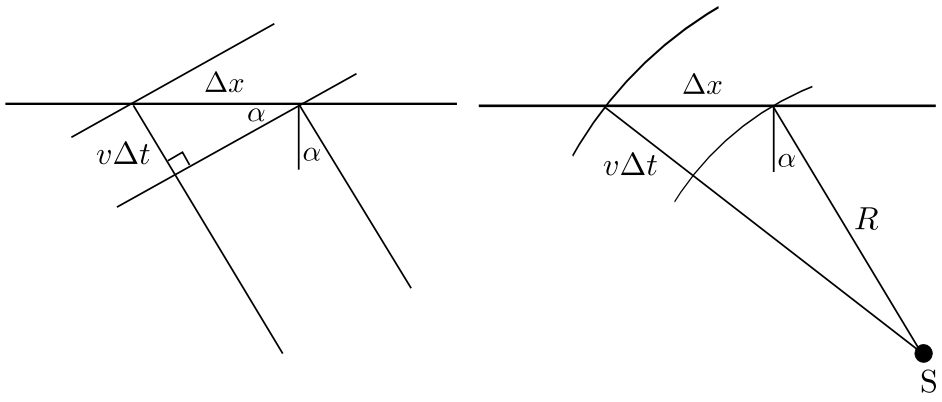

(a) (b)

Figure 3.1.: Geometrical derivation of moveout arising from (a) a planar and (b) a circular wavefront in a constant velocity medium. As motivated in Chapter 2, the circular wavefront seems to stem from its focusing point, which acts as a virtual source to the surface-bound observer (compare Figure 2.7).

3.1. The planar reflector

The special case of a planar reflector, since it closely resembles the very important setting of planar layering in a typical sedimentary environment, has a long history in exploration seismology (e.g., Sheriff and Geldart, 1995; Yilmaz, 2001). Although the corresponding ray path geometry can still appear complicated, the concept of a virtual seismic source (mirrored at the reflector) reduces the essential two-way reflection geometry to a simple auxiliary one-way problem. Figure 3.2 shows a sketch of a zero-offset and a finite-offset reflection at an inclined planar interface. Following the original derivation by Levin (1971), the difference between the zero-offset and the finite-offset traveltime, resulting from the separation of $2h$ between the source S and the receiver G, can be derived, again, by applying the law of cosines,

$$v^2t^2 = 4h^2 + 4(R_{\text{NIP}} - \delta)^2 - 8h(R_{\text{NIP}} - \delta)\cos(90^\circ + \alpha) \quad , \tag{3.3}$$

where the NIP wave radius R_{NIP} coincides with the distance of the reference midpoint to the reflector and the emergence angle α coincides with the dip of the interface. The right sketch of Figure 3.2 reveals that the quantity δ is determined via

$$\delta = h\sin\alpha \quad . \tag{3.4}$$

Insertion of substitution (3.4) into the the preceding triangle relation (3.3) and subtraction of the zero-offset traveltime $2R_{\text{NIP}}/v$ leads to the exact CMP reflection moveout for an inclined planar reflector and a constant velocity overburden (Levin, 1971)

$$\Delta t = \sqrt{\left(\frac{2R_{\text{NIP}}}{v}\right)^2 + \frac{4h^2\cos^2\alpha}{v^2}} - \frac{2R_{\text{NIP}}}{v} \quad . \tag{3.5}$$

While for the derivation of (3.5) a central midpoint and symmetrically separated source and receiver combination were chosen, it is also possible to derive the moveout of two neighbouring zero-offset rays. Since in this case, for a planar reflector, the according

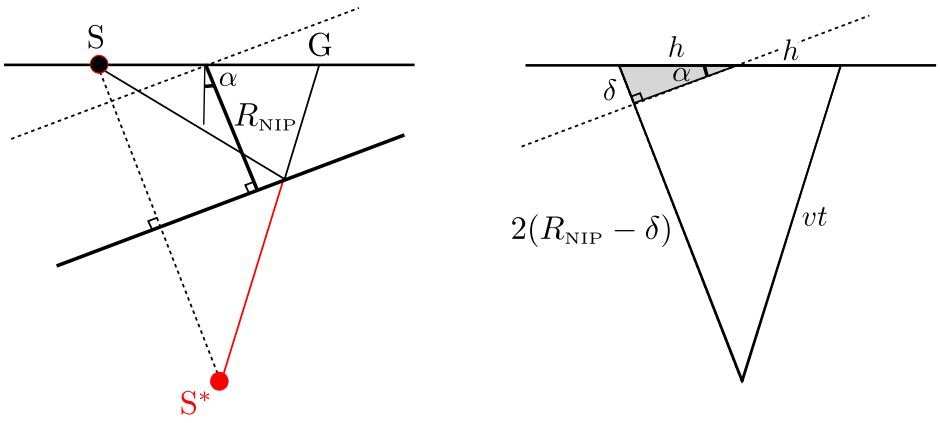

Figure 3.2.: In the geometrical derivation of the moveout arising from reflection at an inclined planar interface, the law of cosines can be employed (Levin, 1971). Since no simplifications or approximations need to be applied, the resulting expression is exact for this specific case of a planar inclinded reflector with a homogeneous overburden (e.g., Schleicher et al., 1993).

zero-offset rays are parallel to each other, the simple first order expression (3.1), valid for a planar emerging wavefront, applies and the zero-offset moveout reads

$$\Delta t = \frac{2 \sin \alpha}{v} \Delta x_m \quad , \tag{3.6}$$

where $\Delta x_m = x_m - x_0$ denotes the surface separation of the two considered zero-offset rays. Please note, that this is in full agreement with the more general exploding reflector experiment (Hubral, 1983) underlying the fictitious normal wavefront concept (Chapter 2.5). Since two-way traveltimes are concerned, the infinitely curved normal wavefront is assumed to travel at half the actual overburden speed, resulting in an additional factor of 2 in equation (3.6).

3.2. From CMP to CRS

In the previous section we derived the traveltime moveout resulting from the reflection at an inclined planar interface for two different subsets of the acquired multicoverage data, the CMP gather, where traces with coinciding source receiver offset are considered and a family of neighbouring rays in the zero-offset section. While it can be argued, as can be seen for vanishing inclination, that most redundancy in the data can be found in the CMP gather, i.e. in half-offset direction (see Figure 2.3), the effect of the reflection point dispersal (Deregowski, 1986), which generally happens for non-vanishing reflector inclinations, together with the process of diffraction lead to a distribution of redundant information over several midpoints. For the latter case, energy stemming from one point in depth can in fact essentially be scattered over the full range of midpoints in the acquisition. To overcome these limitations and in order to make full use of the multicoverage response, the common reflection surface (CRS) moveout has been formulated, which has an extension in both, half-offset and midpoint direction. Due to the incorporation of several neighbouring CMP gathers, the otherwise necessary process of dip-moveout correction (DMO) is naturally incorporated in the according expressions.

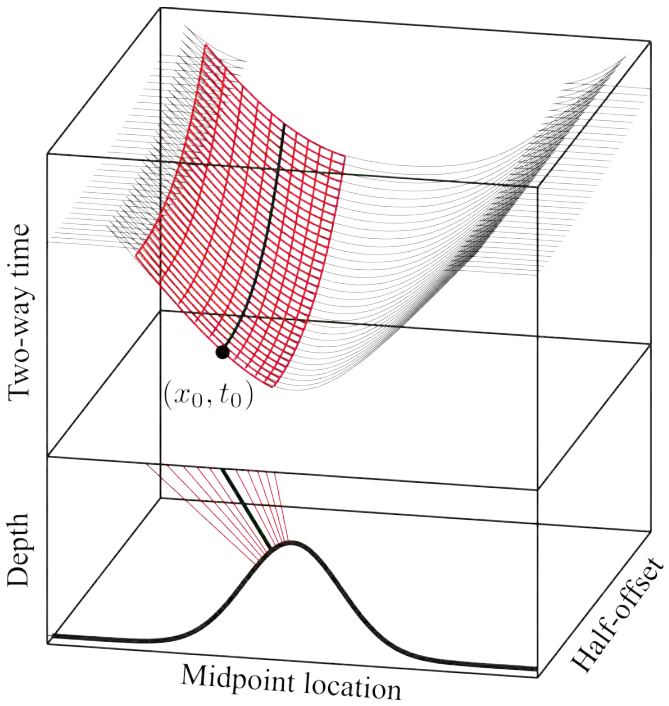

Figure 3.3.: In contrast to the classical CMP moveout, represented by the bold black curve, the CRS moveout spans the recorded multicoverage response not only in offset, but also in midpoint direction (red surface). Consequently, it incorporates the classical CMP moveout as a subset (after Müller, 1999).

For the considered case of a planar inclined reflector, it is actually straight-forward to arrive at the corresponding CRS expression, since the respective moveout expressions have already been derived in the previous section. Equations (3.5) and (3.6) can be coupled via the common zero-offset reference traveltime at the central midpoint. Accordingly, the parametric expressions

$$t_{\mathrm{CMP}} = \sqrt{t_{ZO}^2 + \frac{4h^2 \cos^2 \alpha}{v^2}} \quad , \tag{3.7a}$$

$$t_{\mathrm{ZO}} = \frac{2R_{\mathrm{NIP}}}{v} + \frac{2 \sin \alpha}{v} \Delta x_m \quad , \tag{3.7b}$$

define the exact CRS traveltime for a planar reflector in a homogeneous medium (e.g., Schleicher et al., 1993). Combined to one equation, the CRS formula reads

$$t(\Delta x_m, h) = \sqrt{\left(\frac{2R_{\mathrm{NIP}}}{v} + \frac{2 \sin \alpha}{v} \Delta x_m \right)^2 + \frac{4h^2 \cos^2 \alpha}{v^2}} \quad . \tag{3.8}$$

It is interesting to note that for a planar reflector with a homogeneous overburden, the full midpoint half-offset response can be described by equation (3.8), making it a truly global description for this particular case[2].

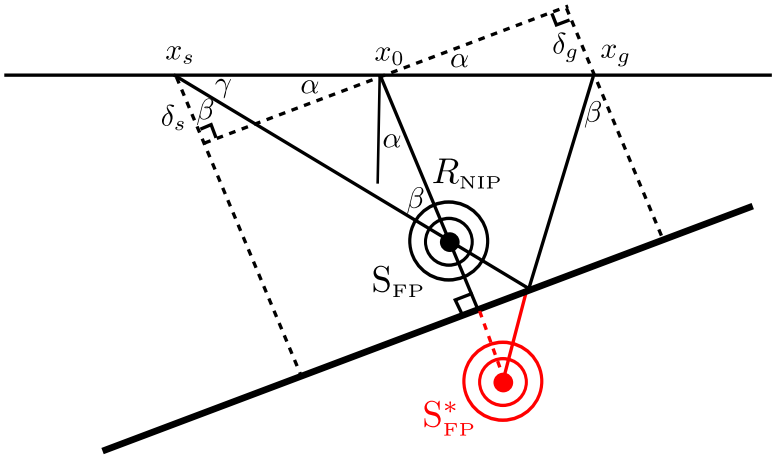

Figure 3.4.: As previously shown (compare Figure 3.2), the CMP moveout resulting from the reflection at a planar inclinded interface can generally be described by assuming a virtual image of the true source below the reflector. The alternative point of view taken by the multifocusing approach is based on a lower degree of symmetry of the ray paths by assuming two different wavefronts originating from the intersection point of the normal ray and the finite-offset ray, which as well can be thought of as a virtual seismic source.

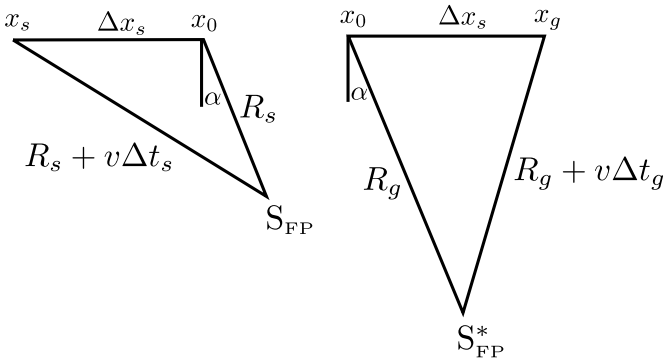

Figure 3.5.: The focusing wavefronts R_s and R_g determining the moveout at source and receiver are related to the ray geometry of the planar reflector problem via simple trigonometric relations. Due to the general asymmetry between those two wavefronts in case of an inclined reflector, the multifocusing moveout is described by two rather than one square-root (as opposed to the equivalent derivation by Levin (1971) illustrated in 3.2).

3.3. A different view

In this section, I discuss a second equivalent solution to the planar reflector problem, which makes use of a different virtual source. Aside from considering the image of the actual source position, mirrored at the inclined reflector, as in Section 3.1 (see Figure 3.2), the intersection point of the zero-offset and the finite-offset ray and its corresponding mirror image can also serve as virtual seismic sources, which explain the straight ray geometry. Observe in Figure 3.4 that in this case, two wavefronts, one initiated at the true intersection point, the other at the mirror image, are measured at the central ray location x_0. Again, application of the law of cosines leads to the respective moveouts at the source and at the receiver, separated by the source displacement $\Delta x_s = x_s - x_0$ and $\Delta x_g = x_g - x_0$ (compare Figure 3.5)

$$\Delta t_s = \frac{\sqrt{R_s^2 + 2R_s\Delta x_s \sin\alpha + \Delta x_s^2} - R_s}{v} \quad , \tag{3.9a}$$

$$\Delta t_g = \frac{\sqrt{R_g^2 + 2R_g\Delta x_g \sin\alpha + \Delta x_g^2} - R_g}{v} \quad . \tag{3.9b}$$

Again, like for the CMP moveout, this result is in accordance with the moveout expression arising from a general circular emerging wavefront (compare equation (3.2)). Since the ray intersection point and its mirror image acting as a virtual seismic source (see, e.g., Landa et al., 1999), are the foci of the circular wavefronts related to the source and the receiver moveouts, respectively and due to the fact that these change for varying source receiver combinations, Gelchinsky et al. (1999) termed this moveout approach *multifocusing*.

According to the geometry in Figure 3.4, the zero-offset measurements of the source-related wavefront R_s and the respective receiver-related wavefront R_g can be expressed in terms of the NIP wave radius via

$$R_s = R_{\text{NIP}} - \frac{R_{\text{NIP}}}{\phi} = \frac{1-\phi}{-\phi K_{\text{NIP}}} \quad , \tag{3.10a}$$

$$R_g = R_{\text{NIP}} + \frac{R_{\text{NIP}}}{\phi} = \frac{1+\phi}{\phi K_{\text{NIP}}} \quad , \tag{3.10b}$$

where ϕ is equal to the ratio of the distance between the ray intersection point, i.e. the position of the virtual source of the focusing wavefronts and the NIP wave radius. According to equations (3.10), the focusing parameter uniquely defines the position of the wavefront foci and therefore is commonly called the focusing parameter. Following the approach of Landa et al. (1999), the focusing parameter for the planar reflector can be derived from the geometry shown in Figure 3.4. According to the law of sines, we have

$$\frac{R_s}{\sin\gamma} = \frac{\Delta x_s}{\sin\beta} \quad . \tag{3.11}$$

With the trigonometric correspondence $\gamma = 90° - \beta - \alpha$ and R_s isolated, we get

$$R_s = \Delta x_s \frac{\cos\alpha + \beta}{\sin\beta} = \Delta x_s \left(\frac{\cos\alpha}{\cos\beta} - \sin\alpha \right) \quad . \tag{3.12}$$

[2]For more details on aspects of globality and its connection to geometry, I refer to Chapter 5 of this thesis.

In the following, I seek to express the angle β in terms of the source and receiver deviations Δx_s and Δx_g. According to Figure 3.4, the following correspondence applies[3]

$$(R_{\mathrm{NIP}} + \delta_s)\tan\beta + (R_{\mathrm{NIP}} - \delta_g)\tan\beta = (\Delta x_s - \Delta x_g)\cos\alpha \quad . \tag{3.13}$$

With $\delta_s = \Delta x_s \sin\alpha$ and $\delta_g = -\Delta x_g \sin\alpha$ we get the desired expression for the angle β,

$$\tan\beta = \frac{(\Delta x_s - \Delta x_g)\cos\alpha}{2R_{\mathrm{NIP}} + (\Delta x_s + \Delta x_g)\sin\alpha} \quad , \tag{3.14}$$

whose combination with equations (3.12) and (3.10a) yields the planar focusing parameter

$$\phi = \frac{\Delta x_g - \Delta x_s}{\Delta x_s + \Delta x_g + 2K_{\mathrm{NIP}}\Delta x_s \Delta x_g \sin\alpha} \quad , \tag{3.15}$$

where $K_{\mathrm{NIP}} = R_{\mathrm{NIP}}^{-1}$. Please note, that this expression differs from Landa et al.'s result by a minus sign and that the definitions for the source and the receiver wavefronts are as well exchanged compared to Landa et al. (1999). As becomes immediately obvious, this is no contradiction, since a change of the sign in the focusing parameter (3.15) in turn leads to an exchange of the wavefront curvature definitions (3.10). So to conclude, the combination of equations (3.10) and (3.15) is fully consistent with the literature.

Please note, that although the presented multifocusing expressions are similarly accurate as the previous solution (3.8) but reveal a higher mathematical complexity, they, in principle, are more flexible, since the source and receiver distances can be chosen arbitrarily, whereas the derivation of equation (3.8) is based on a higher degree of symmetry in the CMP gather. In addition, (3.9) is formulated in terms of two fictitious wavefront measurements, which can also be carried out at two separated source and receiver locations. As a consequence, the concept of the focusing wave proves to be also useful when the intersection point of two finite-offset rays is considered as a virtual seismic source (Landa et al., 2014).

3.4. Curved reflectors

In the previous sections, both, the CRS moveout and the multifocusing moveout were derived for the planar reflector geometry by making use of simple principles of geometry and the powerful concept of a virtual seismic source. In the following, again based solely on geometrical reasoning, I extend the multifocusing and the CRS approach to the problem of a reflector with non-vanishing, i.e. finite, curvature. As mentioned in Chapter 2, the NIP wave theorem (Hubral, 1983) states that, up to second order, the moveout in the CMP gather is fully governed by the common-reflection-point-related concept of the NIP wave. This means that the influence of reflector curvature, represented by the normal wave parameter R_{N} (see again Chapter 2) is a higher-order phenomenon in offset direction. In the zero-offset section however, as has been argued in the first chapter of this thesis, the normal wave is fully sufficient to describe the traveltime moveout. Based on the general moveout definitions (3.1) and (3.2), it can be concluded that the influence of the normal wave enters at second order in Δx_m.

[3]Since the source and the receiver distance are defined in opposite directions, they have opposite sign in these derivations (see also Landa et al., 1999).

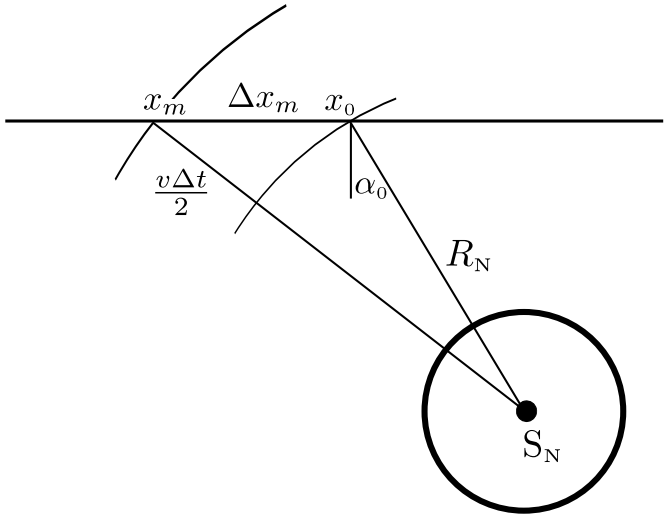

Figure 3.6.: In the zero-offset case, every ray is a normal ray and a corresponding circular wavefront focuses in the centre of the circle locally approximating the reflector. As long as the reflector has circular shape, the geometrically derived expression, like for the planar case, is exact for a constant overburden velocity. Both, multifocusing and the implicit CRS, reduce to this moveout in the zero-offset section.

Following from the familiar circular wavefront geometry and with the help of the law of sines, the zero-offset moveout for a finitely curved interface can be written as

$$\Delta t = 2\frac{\sqrt{R_{\mathrm{N}}^2 + 2R_{\mathrm{N}}\Delta x_m \sin\alpha + \Delta x_m^2} - R_{\mathrm{N}}}{v} \quad . \tag{3.16}$$

Please note again that the factor of 2 results from the fact that the fictitious normal wave, in order to describe the moveout of recorded two-way times, is thought to travel at half the actual medium velocity (compare Figure 2.6 in Chapter 2). Expanding the total zero-offset traveltime $2R_{\mathrm{NIP}}/v + \Delta t$, with Δt as defined in (3.16), we get a new set of parametric equations for the hyperbolic CRS moveout

$$t_{\mathrm{CMP}} = \sqrt{t_{ZO}^2 + \frac{4h^2\cos^2\alpha}{v^2}} \quad , \tag{3.17}$$

$$t_{\mathrm{ZO}} = \frac{2R_{\mathrm{NIP}}}{v} + \frac{2\sin\alpha}{v}\Delta x_m + \frac{\cos^2\alpha}{vR_{\mathrm{N}}}\Delta x_m^2 \quad . \tag{3.18}$$

The corresponding combined hyperbolic CRS equation, with higher discriminant orders than two neglected, reads

$$t = \sqrt{\left(\frac{2R_{\mathrm{NIP}}}{v} + \frac{2\sin\alpha}{v}\Delta x_m\right)^2 + \frac{4\cos^2\alpha}{v^2}\left(\frac{R_{\mathrm{NIP}}}{R_{\mathrm{N}}}\Delta x_m^2 + h^2\right)} \quad , \tag{3.19}$$

which is the same result Vanelle (2012) and Höcht et al. (1999) found. For constant velocity, i.e. straight-ray geometry, this equation is equivalent to the solutions found by Schleicher et al. (1993) and Jäger et al. (2001). At the moment, like for all other derivations in this chapter, we are confined to the assumption of a homogeneous overburden to ensure the applicability of the circular wavefront geometry (following equation (2.4)

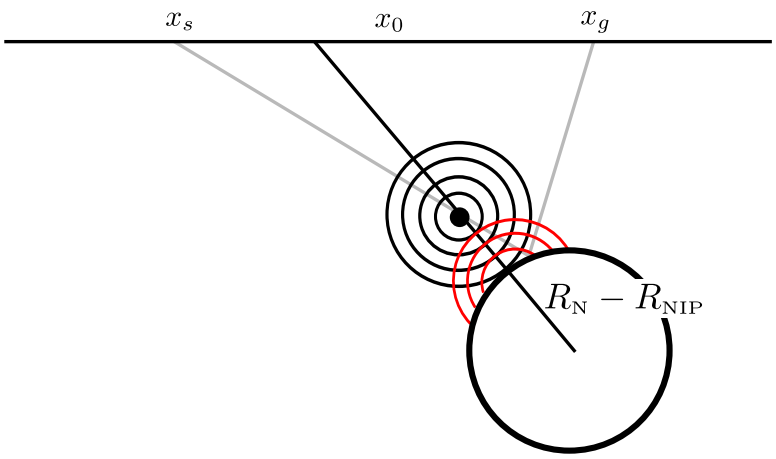

Figure 3.7.: As argued before, the multifocusing moveout provides a different approach to the description of the planar reflector problem resulting in double-square-root expression. Based on the reflection law for wavefronts at curved interfaces and on reciprocity (e.g., Hubral et al., 1980), a relationship between the focusing wavefront curvatures and the NIP and normal wave curvatures can be derived geometrically.

in Chapter 2). However, in the following chapter, the generalization of these concepts to heterogeneous media is considered. In that context I will suggest universal substitutions, which, when applied to formula (3.19) yield the well known CRS expression by Jäger et al. (2001), which was derived via paraxial ray theory and, therefore, is valid in heterogeneous media.

As motivated before, the multifocusing moveout reveals additional complexity, when compared to the corresponding hyperbolic CRS formula, which provides the same high accuracy. In the following, it will become clear that the flexible asymmetric approach of two coupled wavefront measurements related to the source and the receiver is quite favourable to incorporate reflector curvature in the operator. Revisiting the multifocusing equations (3.9), (3.10) and (3.15), we find that in order to incorporate curvature, the moveout expressions at the source and the receiver do not need to be changed. Instead, the focusing wavefront definitions (3.10), dealing with the reflection at a planar interface, can simply be re-written for the more general case of normal reflection at a circular interface of curvature $(R_N - R_{NIP})^{-1}$ (compare Figure 3.7). Since, according to the preceding derivations (e.g., Landa et al., 2010), R_{NIP}/ϕ is the distance between the location of the virtual focusing wave source S_{FP} at the ray intersection and the normal incidence point (NIP), it resembles the incoming wavefront before the reflection at the interface. According to Hubral et al. (1980), the curvatures of the incoming wavefront and the interface simply add up for the normal case and we get for the receiver-related wavefront

$$\begin{aligned} R_g &= R_{NIP} + \frac{1}{\phi K_{NIP} + (R_N - R_{NIP})^{-1}} \\ \Leftrightarrow \quad K_g &= \frac{K_N + \phi(K_{NIP} - K_N)}{K_{NIP} + \phi(K_{NIP} - K_N)} K_{NIP} \quad , \end{aligned} \tag{3.20}$$

where $K_g = R_g^{-1}$. To ensure reciprocity, the positive sign of the ϕ term corresponds to the case of interchanged source and receiver deviations. Consequently, the correspond-

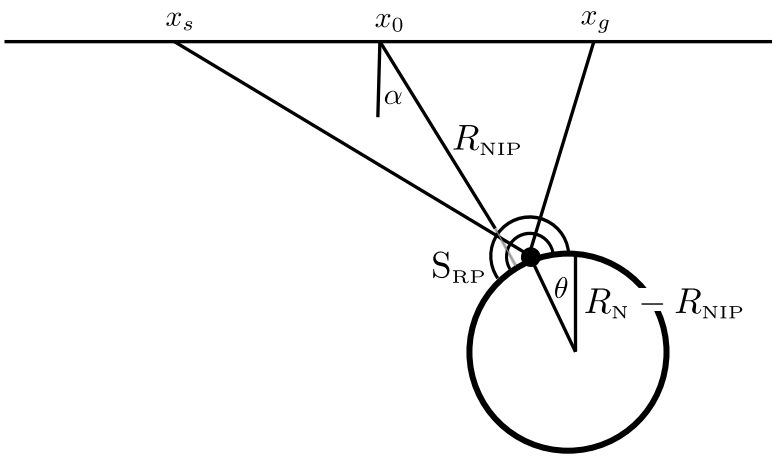

Figure 3.8.: The implicit CRS moveout, like a number of other attempts before (Höcht et al., 1999; Landa et al., 2010) solves the problem of finding the reflection point on a locally circular interface (Vanelle et al., 2010; Schwarz, 2011). The reflection point, in this context can again be interpreted as a virtual source from which the measured wavefronts R_s and R_g at source and receiver originate. The coordinates $(x_{\mathrm{RP}}, z_{\mathrm{RP}})$ of the reflection point S_{RP} can be parameterized by the polar angle θ, which can be computed in an efficient iterative scheme (Vanelle et al., 2010). Again, the resulting implicit CRS moveout is exact for the specific case of a circular reflector in a homogeneous medium.

ing source curvature can be written

$$K_s = \frac{K_{\mathrm{N}} - \phi(K_{\mathrm{NIP}} - K_{\mathrm{N}})}{K_{\mathrm{NIP}} - \phi(K_{\mathrm{NIP}} - K_{\mathrm{N}})} K_{\mathrm{NIP}} \quad . \tag{3.21}$$

Please note again, that in our geometrical derivation the focusing parameter has the opposite sign of the reference in literature (compare, e.g., Landa et al., 1999), which gets compensated by the reversed sign in our focusing wavefront definitions (3.20) and (3.21). Please note that these expressions differ slightly from the literature (for the sake of comparison with a flipped sign),

$$K_s = \frac{K_{\mathrm{N}} - \phi K_{\mathrm{NIP}}}{K_{\mathrm{NIP}} - \phi K_{\mathrm{NIP}}} K_{\mathrm{NIP}} \quad , \tag{3.22a}$$

$$K_g = \frac{K_{\mathrm{N}} + \phi K_{\mathrm{NIP}}}{K_{\mathrm{NIP}} + \phi K_{\mathrm{NIP}}} K_{\mathrm{NIP}} \quad , \tag{3.22b}$$

where the derivations for finite reflector curvature, in contrast to the presented ones, were not derived from geometry but from zero-order ray theory (Gelchinsky et al., 1999; Landa et al., 2010). Note however, that the new definitions converge to the same important subsets for certain special configurations, like, e.g., $K_{s,g} \to K_{\mathrm{N}}$ for the zero-offset case, where $\phi \to 0$ and $K_{s,g} \to K_{\mathrm{NIP}}$ for diffractions, where $K_{\mathrm{N}} \to K_{\mathrm{NIP}}$. Since it is generally expected that the focusing parameter, for finite-reflector curvatures, should incorporate the normal wave curvature K_{N}, and due to the fact, that the suggested geometrical expressions (3.20) and (3.21), in contrast to the literature versions (3.22), have an additional term connecting ϕ and K_{N}, I argue that they might even be used for a more general circular focusing parameter (see, e.g., Landa et al., 2010).

The implicit CRS (Vanelle et al., 2010; Schwarz et al., 2014c), similar to the preceding investigations, was derived from the straight-ray reflection geometry at a circular interface of curvature $(R_{\mathrm{N}} - R_{\mathrm{NIP}})^{-1}$. While it has not been the first approach to consider the problem of reflection at a circular interface (Höcht et al., 1999; Landa et al., 2010), it provides a solution that is straight-forward to implement and can be applied efficiently. Since the original derivation, invoking the evaluation of Snell's law on the circular interface, was already solely based on geometry, I will only sketch the geometrical reasoning and instead focus on the circular wavefront interpretation of the implicit CRS moveout[4].

The implicit CRS, as already mentioned, is derived by finding the finite-offset reflection point on a circular interface. Accordingly, it turned out to be reasonable, to express the traveltime of the source ray segment t_s and its corresponding counterpart at the receiver t_g in terms of the cartesian reflection point coordinates x_{RP} and z_{RP}. According to Figure 3.9, simple application of the Pythagorean theorem leads to

$$t = t_s + t_g = \frac{\sqrt{(x_s - x_{\mathrm{RP}})^2 + z_{\mathrm{RP}}^2}}{v} + \frac{\sqrt{(x_g - x_{\mathrm{RP}})^2 + z_{\mathrm{RP}}^2}}{v} \quad . \tag{3.23}$$

Since the reflection point needs to be located on the circular interface, the choice of polar coordinates turns out to be reasonable (compare Figure 3.8) and the reflection point location reads

$$x_{\mathrm{RP}} = x_0 + R_{\mathrm{N}} \sin\alpha - (R_{\mathrm{N}} - R_{\mathrm{NIP}}) \sin\theta \quad , \tag{3.24a}$$

$$z_{\mathrm{RP}} = R_{\mathrm{N}} \cos\alpha - (R_{\mathrm{N}} - R_{\mathrm{NIP}}) \cos\theta \quad , \tag{3.24b}$$

with θ denoting the polar angle parametrizing the reflection point (see Figure 3.8). The problem of finding the reflection point can, for fixed α, R_{NIP} and R_{N}, which define the model geometry, consequently be reduced to finding the value of θ corresponding to a physical reflection obeying Snell's law. While the original derivation (Vanelle et al., 2010; Schwarz, 2011) was based on Fermat's principle of least time, I argue that the corresponding angle solution can also be gained via straight-forward application of the law of sines. Both approaches lead to the following implicit expression for the reflection point angle

$$\tan\theta = \tan\alpha + \frac{\Delta x_m}{R_{\mathrm{N}} \cos\alpha} + \frac{h}{R_{\mathrm{N}} \cos\alpha} \frac{R_s - R_g}{R_s + R_g} \quad , \tag{3.25}$$

where the $R_s = vt_s$ and $R_g = vt_g$. Due to the fact that R_s and R_g, according to equations (3.23) and (3.24), themselves depends on θ, (3.25) is an implicit expression. Based on the zero-offset starting guess however, Vanelle et al. (2010) showed that iterative application of (3.25) leads to very accurate estimates of the finite-offset reflection points.

The implicit CRS moveout, like all other geometrically derived operators, has an appealing circular wavefront interpretation. As can be seen in Figure 3.8, the straight ray segments R_s and R_g, following the virtual source approach, correspond to a source and a receiver-related measurement of the finite-offset reflection point wave curvature radius. In that frame, the implicit CRS, similar to multifocusing, links the source and the receiver measurement via a focusing parameter. As a conclusion, the implicit CRS

[4]For more details on the derivation of the implicit CRS moveout, I refer to Vanelle et al. (2010), Schwarz (2011) and Schwarz et al. (2014c).

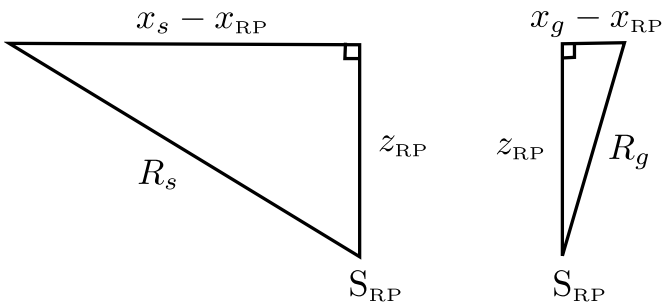

Figure 3.9.: Like in the other cases, the derivation of the implicit CRS reflection point wavefronts emerging at source and receiver can be based on simple geometrical relations like the Pythagorean theorem.

operator is similarly flexible with respect to extendibility to finite-offset (see Chapter 5) and the multifocusing parameter ϕ serves the same purpose as θ for linking the source and the receiver contributions of the traveltime.

3.5. CRP correspondence

Although derived from the same geometric principles and based on the same assumptions of circular wavefronts and virtual sources, the hyperbolic CRS operator (3.19), multifocusing (3.9) and the implicit CRS traveltime (3.23) have a different mathematical structure and incorporate the zero-offset-based conventional CRS attributes α, R_{NIP} and R_{N} in a different way. Consequently, they contain different degrees of approximation. The hyperbolic operator, in contrast to the other two approximations, incorporates the NIP and the normal wavefront measurements, related to the normal ray, under one square-root. As has been argued before, the two circular wavefront measurements, however, can only be accurately described (in a straight-ray sense), if two square-roots are part of the operator.

In Chapter 2, I reintroduced the fictitious NIP and normal wave concepts (Hubral, 1983) based on useful symmetry principles, which apply in certain sub-configurations of the acquired multicoverage response. As argued, the normal wave experiment inherits the strong normal ray symmetry, which states, that the down and up-going ray segments coincide. In the straight-ray picture, corresponding to circular wavefronts, expression (3.16) defines the exact zero-offset moveout, provided the considered reflector segment is locally circular. It is interesting to see that both, multifocusing and the implict CRS, reduce to this formula for the zero-offset case, while the hyperbolic operator only for $R_{\mathrm{NIP}} = R_{\mathrm{N}}$ coincides with this expression.

In the following I would like to shed some light on how the presented, geometrically derived operators describe the moveout in the common reflection point (CRP) gather, which, according to the NIP wave theorem (Hubral, 1983), coincides with the CMP gather up to second order in h. Perroud et al. (1999) and Höcht et al. (1999) found that the moveout in this CRP gather is solely characterized by the NIP wave, therefore, in the zero-offset section and in CRP coordinates, the moveout, according to (3.2), is fully and accurately described by a total of two square-roots (Höcht et al., 1999).

Taking a different route, Höcht et al. (1999), instead of invoking conventional paraxial

ray arguments, argued that the CRS moveout can be defined as a set of neighbouring CRP trajectories, coupled to each other via the normal wave moveout in the zero-offset section. For the CRP gather, he found the following set of expressions for the definition of the traveltime

$$\Delta t(h) = \sqrt{\frac{4R_{\text{NIP}}^2}{v^2}\frac{1}{2}\left(\sqrt{\frac{h^2}{r_{\text{T}}^2}+1}+1\right)+\frac{4h^2}{v^2}} \quad , \tag{3.26a}$$

$$\Delta x_m(h) = r_{\text{T}}\left(\sqrt{\frac{h^2}{r_{\text{T}}^2}+1}-1\right) \quad , \tag{3.26b}$$

where $2r_{\text{T}} = R_{\text{NIP}}/\sin\alpha$. Please note that, consequently, the CRP moveout, as motivated in Chapter 2, is defined for coupled midpoint half-offset coordinates. In the case of a planar horizontal interface, i.e. vanishing reflector inclination, the common midpoint resembles the common reflection point and equations (3.26) reduce to the conventional uncoupled CMP hyperbola. In the following, I will study the CRP response for multifocusing , the implicit CRS moveout and the hyperbolic CRS moveout.

For the transitions $R_{\text{N}} \to \infty$ and $\phi^{-1} \to 0$, as illustrated in Figure 3.10(a), the foci of the different focusing wave experiments all coincide with the normal incidence point and, therefore, formally describe the CRP configuration (e.g., Perroud et al., 1999). The corresponding traveltime expression is of double-square-root-type and, as desired, fully characterized by the NIP wave,

$$t = \frac{\sqrt{R_{\text{NIP}}^2 + 2R_{\text{NIP}}\Delta x_s \sin\alpha + \Delta x_s^2}}{v} + \frac{\sqrt{R_{\text{NIP}}^2 + 2R_{\text{NIP}}\Delta x_g \sin\alpha + \Delta x_g^2}}{v} \quad . \tag{3.27}$$

For the considered constant velocity case, equation (3.27) likewise accurately describes the response of a point diffractor and a CRP (or NIP) experiment[5], which both can be interpreted as virtual seismic sources. In contrast to the uniform radiation at a diffractor, the CRP experiment only invokes pairs of rays which are coupled via Snell's reflection law. Consequently, the emergence locations of these pairs, denoted by Δx_s and Δx_g are coupled and therefore depend on each other. In fact, the condition $\phi^{-1} = 0$ implies this source receiver coupling, which reads[6]

$$\Delta x_s(\Delta x_g) = \frac{-\Delta x_g}{1 + 2K_{\text{NIP}}\sin\alpha\Delta x_g} \quad . \tag{3.28}$$

Please note that the above relation between the acquisition coordinates corresponds to the same expression Gelchinsky et al. (1999) found for the common reflection element (CRE) method. For the implicit CRS operator, the transitions $R_N \to \infty$ and $\theta \to \alpha$, fully equivalent to multifocusing, lead to the same CRE traveltime (3.27)[7]. In full accordance with the preceding findings for the multifocusing operator, the transition $\theta \to \alpha$ transforms the implicit angle formula (3.25) to[8]

$$0 = \Delta x_s + \Delta x_g + (\Delta x_g - \Delta x_s)\frac{R_s - R_g}{R_s + R_g} \quad , \tag{3.29}$$

[5] According to the findings in Section 2.5, the NIP experiment is a special case of the CRP experiment, which, per definition, contains a zero-offset (normal) ray.

[6] ϕ is the focusing parameter defined as (3.15).

[7] The implicit CRS reflection point angle θ is defined according to (3.25).

[8] For the sake of comparability, source and receiver coordinates are chosen.

where R_s and R_g coincide with the enumerators of the corresponding shot and receiver contributions in the CRE moveout (3.27). After some algebra, we arrive at the following relation

$$\Delta x_s \left(\frac{\Delta x_s}{1 + 2K_{\mathrm{NIP}} \sin\alpha \Delta x_s} \right) = \Delta x_g \left(\frac{\Delta x_g}{1 + 2K_{\mathrm{NIP}} \sin\alpha \Delta x_g} \right) \quad , \tag{3.30}$$

which either has $\Delta x_s = \Delta x_g$ or the CRE coupling (3.28) as its solution. Consequently both, mutifocusing and implicit CRS reduce to the same expression (see Figure 3.10), which corresponds to the CRE moveout (Gelchinsky et al., 1999; Cruz et al., 2000). In addition, the CRE coordinate coupling (3.28) is fully contained in both operators. Both approaches reduce to the same moveout in the zero-offset section (Schwarz, 2011). Consequently, multifocusing and the implicit CRS are perfectly equivalent in the zero-offset and CRP coordinates, in which the normal and the NIP wave are fully decoupled (compare Chapter 2).

It is interesting to note that, in fact, this strong correspondence of the two double-square-root operators can even be extended to the parametric CRS by Höcht et al. (1999). While the substitution of midpoint and half-offset coordinates in (3.28) proves its equivalence to (3.26b), the correspondence of Höcht et al.'s CRP traveltime (3.26a) and the CRE formula can be shown by inserting the expression for the midpoint coupling (3.26b) into (3.27). Since, however, this proof of equivalence of the traveltimes invokes lengthy algebra, I provide the necessary derivations in Appendix A. Consequently, the parametric CRS by Höcht et al. (1999), the multifocusing approach by Gelchinsky et al. (1999) and the implicit CRS moveout by Vanelle et al. (2010) and Schwarz et al. (2014c) are expressed by exactly the same simple set of expressions

$$\Delta t(\Delta x_m) = 2\frac{\sqrt{R_{\mathrm{N}}^2 + 2R_{\mathrm{N}}\Delta x_m \sin\alpha + \Delta x_m^2} - R_{\mathrm{N}}}{v} \quad , \tag{3.31a}$$

$$\Delta t(h) = \sqrt{\frac{4R_{\mathrm{NIP}}^2}{v^2}\frac{1}{2}\left(\sqrt{\frac{h^2}{r_{\mathrm{T}}^2}+1}+1\right) + \frac{4h^2}{v^2}} - \frac{2R_{\mathrm{NIP}}}{v} \quad , \tag{3.31b}$$

$$\Delta x_m(h) = r_{\mathrm{T}}\left(\sqrt{\frac{h^2}{r_{\mathrm{T}}^2}+1}-1\right) \quad , \tag{3.31c}$$

again, with $2r_{\mathrm{T}} = R_{\mathrm{NIP}}/\sin\alpha$. One can thus conclude that the only differences in these three approaches constitute in the way those three equations are coupled to each other. It can be shown (see Appendix B), that the link of the zero-offset and the CRP response suggested by Höcht et al. fully corresponds to the one chosen for the implicit CRS. Throughout this chapter, all derivations were based on straight-ray geometry, which may seem as a strong limitation of the applicability of the presented concepts to realistic heterogeneous media. However, in the next chapter, I will show that the assumption of straight rays or circular wavefronts, due to two different mechanisms, can successfully be maintained even for heterogeneous media.

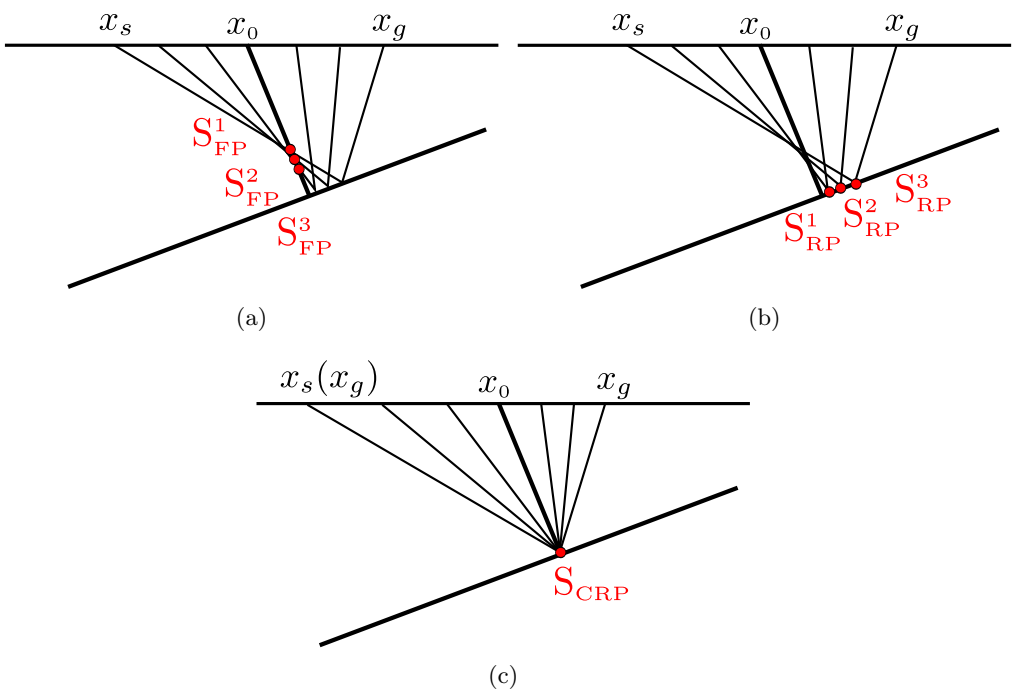

Figure 3.10.: As has been found by many previous authors (e.g., Höcht et al., 1999; Landa et al., 2010), the CMP moveout for reflection at a curved interface must be described by both, the NIP and the normal wave, to achieve high accuracy for a broad range of offsets. So as a result, the need for two wavefronts (see Chapter 2) implies the need for two square-roots in the moveout expression. For coinciding reflection points, i.e. a common reflection point (CRP) however, the moveout is fully determined by the NIP wave alone, leading to a single-square-root formula in the CRS gather. Hyperbolic CRS, multifocusing and iCRS, as a consequence, reduce to exactly the same expression for this case.

4. Accounting for heterogeneity

I showed in the previous chapter that the well-known and established formulae of CRS (Jäger et al., 2001; Mann, 2002) and multifocusing (Gelchinsky et al., 1999; Landa et al., 1999; Tygel et al., 1999), as well as new formulations like the implicit CRS by Vanelle et al. (2010) and Schwarz (2011) can all be derived from straight-ray geometry. Based on the work of Hubral (1983) and Gelchinsky et al. (1999), I argued that the concept of virtual sources, in this context, proved to be very useful and provides physical insight into the coupling of the acquisition-related coordinates at the surface. Being based on the measurements of circular wavefronts at different positions on the acquisition surface, the straight-ray derivations revealed some intuitive insight into the similarities and characteristic differences of the different moveout expressions. One major conclusion was that in general, provided the overburden can be assumed to be homogeneous, the assumption of circular wavefronts and, therefore, straight rays leads to globally exact expressions for certain analytical reflector shapes. While the paraxial approximations are generally confined, due to their second-order nature, to certain limited vicinities around a reference ray, the geometrically derived circular wavefront solutions provide an exact moveout description for the specific reflector shape they are designed for.

De Bazelaire (1988) showed for the simple but very important heterogeneous case of a layered system, that the straight-ray geometry interpretation of the hyperbolic CMP moveout can, besides traditionally assuming an effective velocity, also be maintained, if the optical projection of the problem, implying a shift in time, is considered instead. Höcht et al. (1999) made use of this optical approach in a more general sense, which allowed them to also account for moderate lateral variations. Although this duality, i.e. the assumption of an optical projection or an auxiliary medium of effective velocity to account for heterogeneity is, in principle, known in parts by the community, I hereby seek to review this concept in the most general sense for the CRS-type moveouts. In fact, as will be shown in the following sections, the existence of this duality is closely related to the central concept of circular wavefronts and straight ray geometry and vanishes for the classical expansion-type traveltime operators, like i.e. the parabolic formula (Schleicher et al., 1993), which were derived from paraxial ray theory. In fact, I argue that without increasing the number of parameters, all higher-order approximations, which have a circular wavefront interpretation, are based on the concept of straight rays, and consequently describe moveout in an auxiliary medium of constant velocity. Depending on the incorporation of parameters, the actual subsurface model is either replaced by a medium with effective properties or the method describes traveltime differences for the optical analogue in a medium of constant near-surface velocity.

In the following, I continue the path of unification of CRS and, especially, multifocusing and the implicit CRS, by providing both a forward and an inverse transformation from the optical domain to the effective medium and vice versa. In this context, I introduce generalized moveout expressions, where the auxiliary medium can be chosen by the user, by supplying the according substitutions. Supported by simple and complex synthetic data examples I will find that the double-square-root operators, when

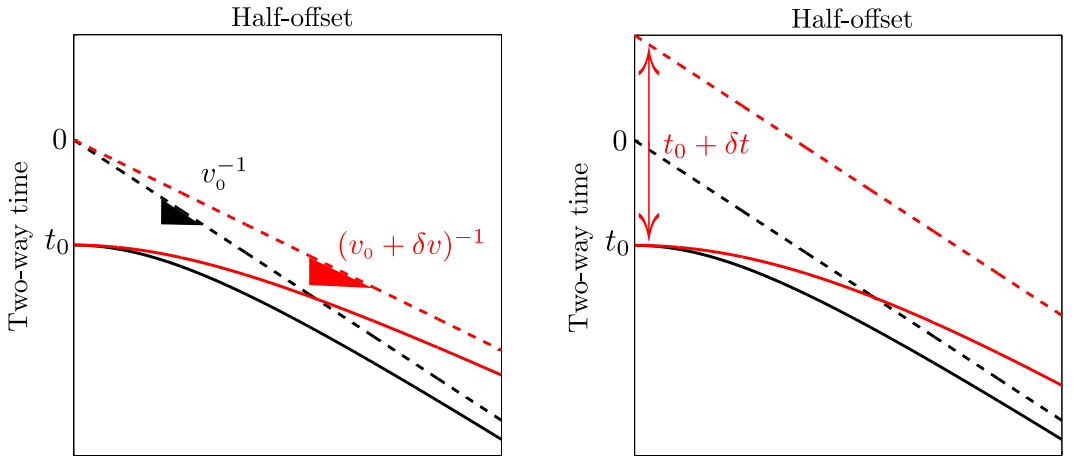

(a) Shift in velocity (b) Shift in time

Figure 4.1.: Two different ways to change the CMP moveout to account for heterogeneity: (a) Classical approach, where the velocity is perturbed. (b) Application of a shift δt to the reference time t_0. Actual traveltime curves are in bold lines, their respective asymptotes are dotted. Both shifts leads to a comparable perturbation of moveout (indicated in red color).

expressed in the same auxiliary medium, can be considered equivalent descriptions. Furthermore, I find that all differences in performance between the considered moveouts can either be attributed to the order of approximation (i.e., double-square-root or single-square-root), which is connected to the handling of reflector curvature, or to the choice of the auxiliary medium, accounting for overburden heterogeneity. In addition, the joint use of both parametrizations turns out to lead to systematic deviations, which can contribute to interesting applications, like diffraction and multiple characterization and separation (see Chapter 6). Concluding this thesis, in the end of the application part (Chapter 6), I find that the application of an effective medium diffraction operator, in contrast to its optical counterpart, delivers an estimate of the excitation time of a passive seismic source.

4.1. Shift in time or in velocity?

Without loss of generality but for the sake of mathematical simplicity, I will first rederive the classical NMO hyperbola, which had a significant impact in the development of stacking methods in seismic processing (Mayne, 1962; Hertweck et al., 2007). For the simple case of one planar horizontal reflector below an overburden of constant velocity v, the exact traveltime moveout expression can, as was demonstrated in the previous chapter, be gained from geometry. According to the Pythagorean theorem, it may be expressed as

$$\Delta t = \sqrt{\left(\frac{2R_{\mathrm{NIP}}}{v}\right)^2 + \left(\frac{2h}{v}\right)^2} - \frac{2R_{\mathrm{NIP}}}{v} \quad , \tag{4.1}$$

where R_{NIP} is defined according to the geometric relations found in Chapter 3 (see Figure 4.3). For constant velocity, the quantity $2R_{\mathrm{NIP}}/v$ is equal to the true zero-offset traveltime recorded at x_0. As can be inferred from Figure 4.1(a) the medium velocity

v is responsible for the slope of the hyperbola's asymptote, resembling the direct wave traveltime. While, especially in the context of exploration in sedimentary settings, the assumption of a planar target reflector is often reasonable, the absence of velocity changes in the overburden seems physically not well motivated and generally unrealistic.

In order to be able to stick to the simple mathematical construct (4.1) and the geometrical appealing picture of straight rays, the allowance for a constant shift in velocity δv seems the most intuitive approach to deal with heterogeneity in the medium. Following from this velocity shift (as indicated in Figure 4.1(a)), the traveltime moveout is perturbed and the connected asymptote changes its slope. Accordingly, the traveltime moveout is now described in a medium with the effective velocity $v_{\text{shift}} = v + \delta v$:

$$\Delta t_v = \Delta t(t_0, v_{\text{shift}}) = \sqrt{t_0^2 + \frac{4h^2}{v_{\text{shift}}^2}} - t_0 \quad , \tag{4.2}$$

where t_0 is the zero-offset two-way traveltime[1]. In practice, the approach of shifting the velocity to optimally fit the data is commonly known as velocity analysis (Taner and Koehler, 1969) and has been applied successfully for half a century. In the late eighties, de Bazelaire (1988), motivated by the concept of projections in geometrical optics, introduced an alternate way to maintain the picture of straight rays in a complex medium. In contrast to classical velocity analysis, he proposed that the reference time rather than the velocity should be shifted when heterogeneity occurs in the overburden, i.e.

$$\Delta t_t = \Delta t(t_{\text{shift}}, v_0) = \sqrt{t_{\text{shift}}^2 + \frac{4h^2}{v_0^2}} - t_{\text{shift}} \quad , \tag{4.3}$$

with $t_{\text{shift}} = t_0 + \delta t$. As Figure 4.1(b) illustrates, the hyperbola's asymptote changes its overall position in time, but its slope is maintained during this perturbation. Both operations, a constant shift in time and in velocity, results in a similar adaptation of the hyperbolic moveout and for short offsets, these approaches lead to similar results. Nevertheless, I will show in the cause of this work that noticeable systematic deviations between these approximations occur for higher offsets and a higher degree of heterogeneity in the overburden. Following this brief reintroduction of the two different mechanisms to account for heterogeneity for the classical CMP hyperbola, I argue that the preceding findings also apply to the more general CRS concept. In addition, I suggest a simple and, in the context of auxiliary media, more intuitive parametrization, that allows for a generalized definition of higher-order moveouts.

4.2. The two faces of normal moveout

As introduced in Chapter 3, the common-reflection-surface (CRS) moveout by Jäger et al. (2001) can be viewed as a generalization of the classical CMP moveout to neighbouring CMPs. As a consequence, as can also be inferred from equation (3.19), the number of degrees of freedom increases from two to four. Having been introduced in the context of migration (Hubral, 1983), the CRS attributes α, R_{NIP}, and R_{N} contain both, geometrical properties of the imaged reflector and propagation effects due to the overburden (see also Section 2.5). According to the NIP-wave theorem (Hubral, 1983),

[1]Please note that for the heterogeneous case, t_0 and the reflector depth R are not connected via geometry any-more (compare Figure 4.3).

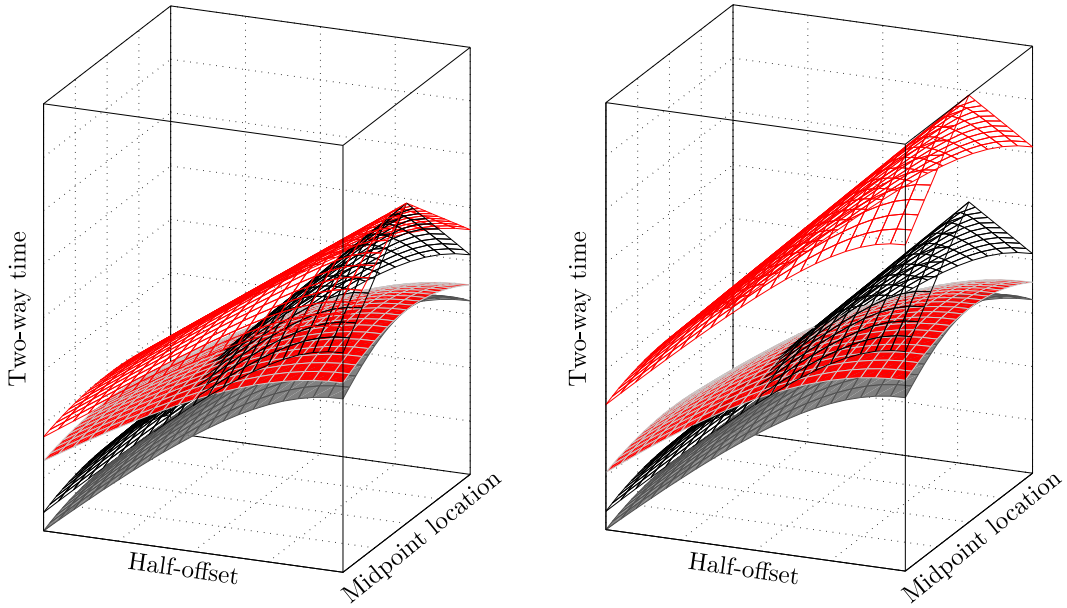

(a) Shift in velocity (b) Shift in time

Figure 4.2.: Velocity-shifted CRS moveout (a) and time-shifted CRS moveout (b). Like for the CMP stack, the perturbed moveout surfaces (solid grid) and their asymptotes (hollow grid) are shown in red color.

hyperbolic moveout with half-offset h, i.e. in the CMP gather, does not depend on the curvature of the reflector, which is why curvature is not accounted for in formulae (4.2) and (4.3). In midpoint direction, however, reflector curvature is a lower, i.e., second-order effect and generally has a strong impact on the traveltime differences of neighbouring rays.

In the following, I propose an alternative to the conventional CRS parametrization by making use of the fact that certain combinations of the CRS parameters remain unaffected by the choice of the auxiliary medium. While in conventional CRS the reflector curvature is related to the parameter R_{N}, I now suggest to instead use the combination

$$\rho = \frac{R_{\mathrm{NIP}}}{R_{\mathrm{N}}} \quad , \tag{4.4}$$

since it remains unchanged, when we go from the constant near-surface velocity medium of the time shift to the effective constant velocity medium underlying the approach of shifting the velocity and vice versa. In addition, the horizontal slowness or ray parameter

$$p_{0x} = \frac{\sin\alpha}{v_0} \quad , \tag{4.5}$$

following from intuition, should be independent of the choice of the auxiliary medium, since it describes the midpoint (i.e. zero-offset) slope of the actual reflection event in the vicinity of measurement location x_0. In addition, it is known that the horizontal slowness, according to Snell's law, is a general propagation invariant. The shifted zero-offset traveltime represents the reference time of the projected problem and therefore is

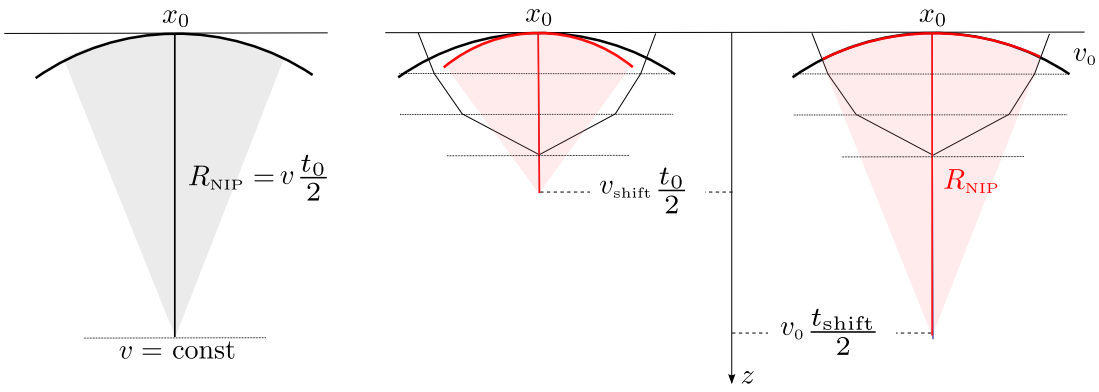

Figure 4.3.: Illustration of the relationship between wavefront curvature and reference traveltime. In case of a single planar target reflector with constant velocity overburden (a), the wavefront curvature R and the distance to the reflector coincide and the hyperbolic approximation is exact, while they differ for the heterogeneous case (b). The solid black lines represent the actual raypath, whereas red color indicates the velocity shift and time shift mechanism, respectively.

defined in the auxiliary medium of constant near-surface velocity. As can be concluded from geometry (see Figure 4.3), it bears a close connection to the NIP wave radius,

$$t_{\mathrm{shift}} = \frac{2R_{\mathrm{NIP}}}{v_0} \quad , \tag{4.6}$$

and, as a consequence, following from this geometrical reasoning, links the zero-order and the second-order terms of t (see also Chapter 5). The relationship of the shifted velocity to the CRS attributes was already established, e.g., by Mann (2002) by identifying it in the reduced hyperbolic CRS formula for diffractions, or independently by Schwarz (2011) by matching the expansion coefficients of the suggested geometrical implicit CRS approach to the parabolic CRS traveltime. Following the choice of the horizontal slowness as an independent parameter, this velocity can be defined in slowness notation, which seems more consistent and turns out to simplify expressions

$$p_{\mathrm{shift}}^2 = \left(\frac{1}{v_{\mathrm{shift}}}\right)^2 = p_{0x}^2 + \frac{t_0}{t_{\mathrm{shift}}}\left(p_0^2 - p_{0x}^2\right) \quad , \tag{4.7}$$

where $p_0 = 1/v_0$. Since in this formula, the shifted velocity is linked to the time shift of the projection approach and, in accordance with the early work by de Bazelaire (1988), who motivated the use of concepts from geometrical optics, I consider it a *generalized osculating equation*, which is also valid in the CRS framework (compare Figure 4.2(a) and Figure 4.2(b)). In the next section, we parametrize the hyperbolic CRS formula (Jäger et al., 2001), the nonhyperbolic implicit CRS (Vanelle et al., 2010; Schwarz et al., 2014c), and multifocusing (Gelchinsky et al., 1999) by means of the above suggested substitutions (4.4) to (4.7).

4.3. Generalized expressions

For the two different representations of the CMP hyperbola (4.2) and (4.3), it becomes apparent that a simple exchange $(t_0, v_{\mathrm{shift}}) \leftrightarrow (t_{\mathrm{shift}}, v_0)$ transforms the initial operator

to the other representation. I conclude from this fact that each moveout expression can be written in a generalized form, i.e., for a general auxiliary medium of constant velocity $\hat{v}$ with its respective reference time $\hat{t}_0$. Depending on the choice of $(\hat{t}_0, \hat{v})$, this generalized moveout $\Delta\hat{t}$ has *two faces*, one accounting for heterogeneity by means of a time shift, the other making use of an effective overburden velocity:

$$(\hat{t}_0, \hat{v}) = \begin{cases} (t_0, v_{\text{shift}}) & , \\ (t_{\text{shift}}, v_0) & . \end{cases} \tag{4.8}$$

I would like to emphasize in this context that the choice of either the effective or the near-surface velocity for the auxiliary medium directly implies the corresponding reference traveltime. This connection is expressed by the generalized osculating equation (4.7), which can be rewritten as

$$\hat{p}^2 = p^2(\hat{t}_0) = p_{0x}^2 + \frac{\hat{t}_0}{t_{\text{shift}}}\left(p_0^2 - p_{0x}^2\right) = \begin{cases} p_{\text{shift}}^2 & \text{for } \hat{t}_0 = t_0 \quad , \\ p_0^2 & \text{for } \hat{t}_0 = t_{\text{shift}} \quad . \end{cases} \tag{4.9}$$

As will be supported by data examples at the end of this section and in the application part of this thesis, the dependence of moveout on the actual imaging traveltime t_0 has striking implications, like, in particular, the effect of moveout stretch after NMO correction or the potential for source time inversion in passive seismic monitoring. In the following, I introduce generalized versions of the CRS, implicit CRS, and multifocusing operators and reveal in which auxiliary medium they were originally formulated.

Hyperbolic moveout

The CRS moveout is a natural generalization of the CMP moveout, in which redundant information from neighbouring CMP gathers is exploited. Due to this incorporation of adjacent CMPs, the according description is a surface rather than a curve, like in the classical CMP approach. Although the parabolic formula (Schleicher et al., 1993), being equivalent to the truncated second-order Taylor series expansion of the traveltime (see Chapter 5), seems the most natural choice for applications like stacking, most implementations appearing in literature are based on a hyperbolic expression (Schleicher et al., 1993; Jäger et al., 2001), which in our notation reads

$$\Delta\hat{t} = \Delta t(\hat{t}_0, \hat{p}) = \sqrt{(\hat{t}_0 + 2p_{0x}\Delta x_m)^2 + 4(\hat{p}^2 - p_{0x}^2)(\rho\Delta x_m^2 + h^2)} - \hat{t}_0 \quad . \tag{4.10}$$

Similar to the classical CMP stack, numerical investigations as well as application in actual sedimentary environments (e.g., Jäger, 1999) support the notion that the hyperbolic CRS moveout is more suited than the parabolic formula when the subsurface consists of a mostly horizontally layered system. Although it has been introduced via squaring the parabolic expression (Schleicher et al., 1993), which was gained from paraxial ray theory (with subsequent neglection of terms of higher order than two), we showed in Chapter 3 that expression (4.10) can also be derived from geometry. For confinement to the CMP gather and vanishing reflector inclination, i.e. $p_{0x} = 0$, the generalized hyperbolic CRS expression reduces to the generalized CMP moveout,

$$\Delta\hat{t} = \Delta t(\hat{t}_0, \hat{p}) = \sqrt{\hat{t}_0^2 + 4\hat{p}^2h^2} - \hat{t}_0 \quad , \tag{4.11}$$

which, depending on the choice of reference time $\hat{t}_0$ and, in consequence, the auxiliary medium, reduces either to formula (4.2) or (4.3). It is interesting to note that, similar to

the nonhyperbolic higher-dimensional moveouts discussed in the following subsection, the hyperbolic CRS formula (4.10) is exact for a certain subsurface model, which in this case constitutes of a planar dipping target reflector beneath a constant velocity overburden (e.g., Schleicher et al., 1993). Both formulae, the hyperbolic CRS (4.10) and the classical CMP hyperbola were first formulated in the effective constant velocity auxiliary medium, which is why their moveout correction depends on the reference time t_0 and therefore also may result in wavelet stretch after correction (Hertweck et al., 2005). While the second face of the CMP hyperbola was already suggested by de Bazelaire in the late eighties (de Bazelaire, 1988), the time-shifted version of hyperbolic CRS was briefly mentioned only in the work of Höcht et al. (1999) and now finds its solid theoretical foundation in the frame of the auxiliary media interpretation of higher-order moveouts.

Nonhyperbolic moveout

Coexisting with the hyperbolic CRS method for fifteen years, the multifocusing approach (Gelchinsky et al., 1999) is based on a double-square-root expression for the reflection traveltime moveout. Similar to the hyperbolic CRS formula (4.10), this moveout can be derived from geometry and therefore intrinsically relies on the assumption of straight rays (Landa et al., 2010). Due to the higher mathematical complexity, the multifocusing moveout has not gained sufficient attention for a long time, but became increasingly important to the community with the rise of interest in imaging diffracted seismic events (e.g., Landa et al., 2010). Although it is based on the same kinematic attributes as the CRS method, namely α, R_{NIP}, and R_{N}, it turns out to noticeably deviate from the hyperbolic approximation when reflectors are curved and when the overburden is heterogeneous (Schwarz et al., 2014c). In this work, I seek to demystify the role of the multifocusing moveout by reformulating it in a general constant velocity auxiliary medium. By making use of substitutions (4.4) to (4.7), we end up with the following generalized form of the multifocusing moveout,

$$\Delta\hat{t} = \Delta t(\hat{t}_0, \hat{p}) = t_s + t_g - \left(\frac{\rho - \phi^2}{\rho^2 - \phi^2}\right)\hat{t}_0, \tag{4.12}$$

where the traveltime contributions t_s and t_g are connected to the down-going and upgoing segments of the reflected ray,

$$t_s = \sqrt{\left[\left(\frac{1+\phi}{\rho+\phi}\right)\frac{\hat{t}_0}{2} + p_{0x}\Delta x_s\right]^2 + (\hat{p}^2 - p_{0x}^2)\Delta x_s^2} \quad , \tag{4.13}$$

$$t_g = \sqrt{\left[\left(\frac{1-\phi}{\rho-\phi}\right)\frac{\hat{t}_0}{2} + p_{0x}\Delta x_g\right]^2 + (\hat{p}^2 - p_{0x}^2)\Delta x_g^2} \quad . \tag{4.14}$$

The focusing parameter ϕ is a function of the source and receiver offsets $\Delta x_s = x_s - x_0$ and $\Delta x_g = x_g - x_0$ and therefore changes for each individual ray considered in the vicinity of the central ray observed at midpoint x_0. Expressed in the previously introduced notation, it reads[2]

$$\phi = \frac{\Delta x_s - \Delta x_g}{\Delta x_s + \Delta x_g + 4\Delta x_s \Delta x_g \, p_{0x} \, \hat{t}_0^{-1}} \quad . \tag{4.15}$$

[2]For the geometrical derivation of the multifocusing moveout, I refer to Chapter 3.

Please observe that, in contrast to the hyperbolic CRS approach and its classical CMP hyperbola subset, which almost exclusively appear as effective medium representations in literature (Schwarz et al., 2014a), multifocusing originally describes the projected problem observed in the constant near-surface velocity medium. Therefore, it appears in literature in time shift parametrization.

Starting from geometrical considerations, similar to the multifocusing approach, Schwarz (2011) observed that the nonhyperbolic double-square-root type implicit CRS operator can be represented not only in one but two auxiliary domains. While the velocity-shifted effective medium representation turns out to behave similarly to CRS for moderate reflector curvatures and mostly vertical velocity changes in the overburden, the time-shifted version showed a strikingly strong resemblance to multifocusing, theoretically, and backed up by data examples, for the case of high reflector curvatures and in the diffraction limit. Similar to the multifocusing approach, implicit CRS treats the down- and up-going contributions of the approximated raypaths separately. In its generalized form it reads

$$\Delta\hat{t} = \Delta t(\hat{t_0}, \hat{p}) = t_s + t_g - \hat{t}_0 \quad . \tag{4.16}$$

The traveltime contributions t_s and t_g, similar to the multifocusing approach (4.12) are mathematically complex hyperbolic approximations of the source and receiver traveltimes in the generalized auxiliary medium of constant slowness $\hat{p}$,

$$t_s = \sqrt{\left[\frac{1}{\rho}\frac{\hat{t}_0}{2} + p_{0x}\Delta x_s\right]^2 + \left(\hat{p}^2 - p_{0x}^2\right)\Delta x_s^2 - \left(\frac{1}{\rho} - 1\right)\hat{t}_0\,\hat{p}\,\sin\theta\Delta x_s + d} \quad , \tag{4.17}$$

$$t_g = \sqrt{\left[\frac{1}{\rho}\frac{\hat{t}_0}{2} + p_{0x}\Delta x_g\right]^2 + \left(\hat{p}^2 - p_{0x}^2\right)\Delta x_g^2 - \left(\frac{1}{\rho} - 1\right)\hat{t}_0\,\hat{p}\,\sin\theta\Delta x_g + d} \quad , \tag{4.18}$$

where d is a correction term for the finite reflector curvatures,

$$d = \left(\frac{1}{\rho} - 1\right)\left(\frac{\hat{t}_0}{2}\right)^2\left[\frac{1}{\rho}\left(1 - \frac{2}{\hat{p}}\left(p_{0x}\sin\theta + \sqrt{\hat{p}^2 - p_{0x}^2}\cos\theta\right)\right) - 1\right] \quad . \tag{4.19}$$

Please note that this contribution vanishes for the diffraction case, where $\rho = R_{\mathrm{NIP}}/R_{\mathrm{N}} = 1$. Solving the problem of reflection from a circular reflector in a constant velocity medium, the implicit CRS iterates for the angle θ, which geometrically represents the angle defining the finite-offset reflection point (see Chapter 3). It therefore plays a similar role as the focusing parameter (4.15) in connecting traveltime contributions of the up- and down-going ray segments,

$$\tan\theta = \frac{1}{\sqrt{\hat{p}^2 - p_{0x}^2}}\left[p_{0x} + \rho\hat{p}^2\hat{t}_0^{-1}\left(\Delta x_s + \Delta x_g + [\Delta x_g - \Delta x_s]\frac{t_s - t_g}{t_s + t_g}\right)\right] \quad . \tag{4.20}$$

At this point, I would like to emphasize the special role of the multifocusing moveout, which, in contrast to all other presented methods, like CRS and the implicit CRS, was originally formulated in the constant near-surface velocity medium and therefore, like the shifted hyperbola by de Bazelaire (1988), relies on a time shift to account for heterogeneity. Without commenting on the auxiliary medium itself, Landa (2007) already stated that the multifocusing moveout correction does not encounter moveout stretch (since it does not depend on the reference traveltime t_0) and reduces to the time-shifted

hyperbola by de Bazelaire in the CMP gather, when the overburden consists of a horizontally layered system. With this work, I seek to properly define the unique role of the multifocusing approach and argue that it behaves completely equivalent to other double-sqare-root expressions, like the considered implicit CRS operator, when viewed in the same auxiliary medium.

Since both, generalized multifocusing and the generalized implicit CRS, reduce to exactly the same expressions for planar horizontal layering in the CMP gather or the increasingly important diffraction case, I consider them being of comparable accuracy. Both operators reduce to the exact solution for one single planar reflector (in the CMP gather) and for a point diffractor with a constant velocity background. This supports the finding that all higher-order expressions with the same number of degrees of freedom as the parabolic formula, i.e. hyperbolic CRS, the implicit CRS or multifocusing, are exact for a certain subsurface model and can also be derived from geometry. Please note that these approaches, in consequence, are confined by an asymptotic curve or surface (illustrated in figures 4.1(a) to 4.2(b)). The parabolic formula neither has two faces, like the higher-order expressions, nor does an asymptote exist and it happens to be never exact, no matter how simple the model is chosen.

Since all presented generalized moveouts, for small vicinities, i.e. up to second-order, are equivalent to the parabolic formula, and due to the fact that the two double-square-root expressions are capable of handling low and high reflector curvatures equally well provided that lateral velocity changes are moderate, we consider either the generalized implicit CRS or multifocusing as the most general moveout expression in this context. As I will show in Chapter 6, these theoretical notions can also be supported in actual data applications. In addition, we will show that the existence of two faces for the higher-order moveouts, besides unification, also bears strong potential for wavefield characterization and applications in data-driven passive seismic investigations.

4.4. Auxiliary media

In this section I will briefly review the circular wavefront picture introduced and utilized in the previous chapter. By closer investigating the formal structure of the generalized CRS parametrization introduced in Section 4.3, it becomes obvious that the two mechanisms suggested to account for heterogeneity are both connected to properties of the NIP wave only. Based on the concept of a virtual seismic source, in the context of true-amplitude migration, Hubral (1983) introduced the NIP concept, in which a fictitious wave is thought to be initiated at the normal incidence point (see Section 2.5). Based on the fundamental assumptions of ray path symmetry and reciprocity, this NIP wave is initiated at zero time, travels at half the actual medium velocity, and finally is measured at the central zero-offset location x_0 (compare Figure 2.5) at time t_0, which is equal to the true zero-offset reference ray traveltime. So in conclusion, the NIP wave recording (in the circular wavefront picture) can be characterized via the full set of properties

$$(t_0, \alpha, R_{\text{NIP}}) \tag{4.21}$$

measured at the surface. Due to the fact that this wavefront, according to its definition, is known to have infinite curvature and is multi-directional, when initiated at the NIP, and since the traveltime is equal to the actual zero-offset reference traveltime, the

NIP wave, in principle, contains all heterogeneity effects felt in the overburden during the expiration of time t_0. Bearing in mind, that, consequently, only the full set (4.21) fully characterizes the NIP wave measurement, the two different suggested mechanisms, consisting either in a shift in time or a shift in velocity, can be pictured very intuitively. In essence, both approaches try to approximate the actual NIP experiment from two different angles (see Figure 4.4). Being confined by the straight-ray assumption, they can only accurately describe certain aspects of the NIP wave, i.e. a subset of (4.21).

Following the work of de Bazelaire (1988) and Höcht et al. (1999), the time shift mechanism maintains the straight-ray (or circular wavefront) assumption by shifting the actual reference time t_0, which, as argued above, also corresponds to the actual traveltime of the NIP wave, to the value

$$t_{\text{shift}} = \frac{2R_{\text{NIP}}}{v_0} \quad , \tag{4.22}$$

which is the optical straight-ray projection of the actual wavefront measurement. Thus, the time-shift mechanism accurately describes the geometry of the surface recording of the actual NIP wavefront and the corresponding emergence angle, but fails at physically describing the actual traveltime of the NIP wave, denoted by t_0, due to the imposed straight-ray limitation. In consequence, the time-shift approaches do not incorporate the actual reference time t_0, but only use the actual measured wavefront curvature and angles to approximate traveltime differences, i.e. moveout. If a velocity-shift is considered to account for heterogeneity, the constant velocity is adapted to the actual NIP wave traveltime, which corresponds to the true recorded zero-offset reference traveltime t_0. As a consequence, the other surface-based NIP wave attributes, i.e. the actual curvature radius R_{NIP} and the emergence angle α get perturbed by this velocity change and, again, due to the straight-ray limitations, do not represent the actual surface measurements any-more. They rather are represented by effective properties, which, due to the generalized osculating equation, can be related to their actual values via (Schwarz, 2011):

$$\hat{v}_0 = v_{\text{shift}} = v_{\text{NMO}} \left[1 + \left(\frac{v_{\text{NMO}}}{v_0} \sin\alpha \right)^2 \right]^{-\frac{1}{2}} \quad , \tag{4.23a}$$

$$\sin\hat{\alpha} = \sin\alpha(v_{\text{shift}}) = \frac{v_{\text{shift}}}{v_0} \sin\alpha \quad , \tag{4.23b}$$

$$\hat{R}_{\text{NIP}} = R_{\text{NIP}}(v_{\text{shift}}) = \frac{v_{\text{shift}} t_0}{2} \quad , \tag{4.23c}$$

$$\hat{R}_{\text{N}} = R_{\text{N}}(v_{\text{shift}}) = \frac{\hat{R}_{\text{NIP}}}{R_{\text{NIP}}} R_{\text{N}} \quad , \tag{4.23d}$$

$$\tag{4.23e}$$

where the hat indicates the effective character of the respective attribute and

$$v_{\text{NMO}} = \sqrt{\frac{2v_0 R_{\text{NIP}}}{t_0 \cos^2\alpha}} \tag{4.24}$$

is the dip dependent NMO velocity known from the classical CMP moveout (e.g., Mann, 2002). Please note that the system (4.23) can be inserted into any CRS-type operator (like, e.g., conventional multifocusing) to arrive at its effective medium representation. If the considered operator is already formulated in the effective medium, it should not change under the above substitutions.

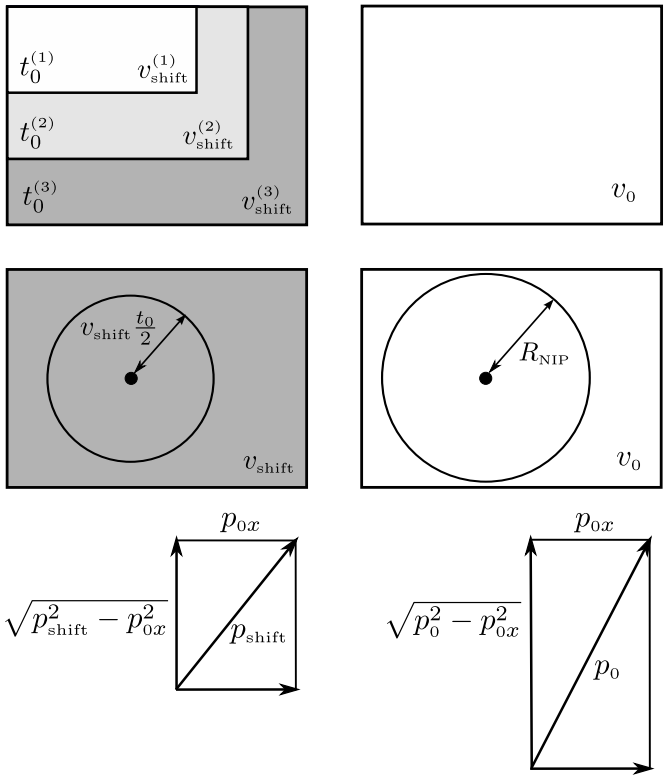

Figure 4.4.: Illustration of the auxiliary medium underlying the velocity (left) and the time shift (right) approach. The constant effective medium velocity v_{shift} according to equation (4.23a) depends on the actual reference time t_0 and therefore changes for every time step, whereas the time shift approach describes the optical projection in a medium with the constant near-surface velocity v_0. While the velocity shift mechanism couples the true reference time t_0 to R_{NIP}, the shifted reference time is generally different from the actual reference time and adapts to the true NIP wave curvature radius.

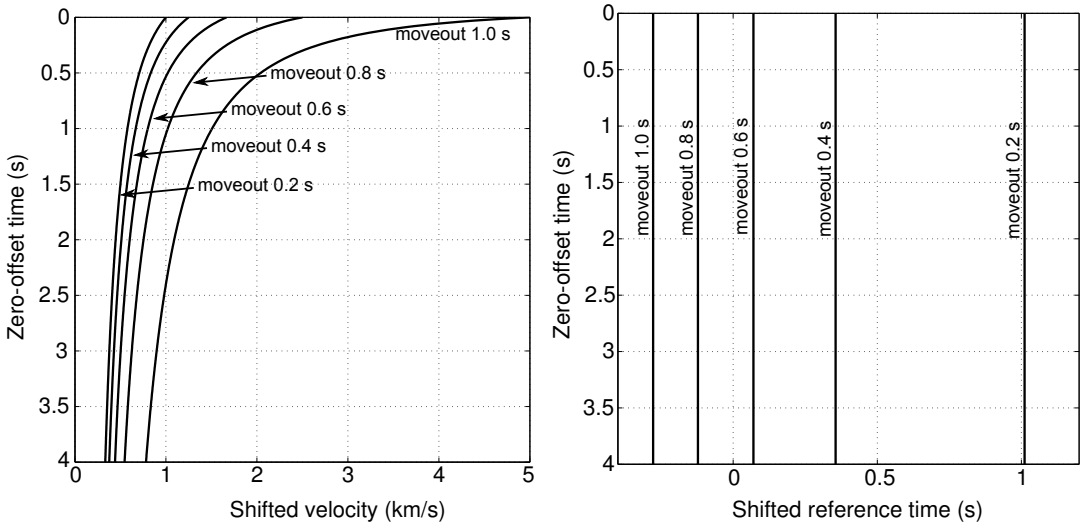

(a) (b)

Figure 4.5.: Iso-moveout curves for the velocity-shifted classical NMO hyperbola (a) and the time-shifted hyperbola by de Bazelaire (b) for a fixed finite-offset. Although of higher dimensionality, similar dependencies also apply for the surface-based CRS, implicit CRS and multifocusing.

4.5. Moveout stretch

As already indicated in the previous sections, the choice of the auxiliary medium directly implies the choice of a specific conceptually different mechanism to account for heterogeneity. Due to the fact that the effective medium moveouts all have in common that they directly depend on the zero-offset reference traveltime t_0, moveout stretch may be observed for all these approaches. It is interesting to note that this effect, however, may also show for data modelled in a hypothetical medium of perfectly constant velocity (Perroud and Tygel, 2004). For the sake of simplicity, I demonstrate this behavior for the hyperbolic CMP moveout (4.11) only, but I would like to stress that the presented findings also apply to the more general multi-dimensional CRS-type methods. Figures 4.5(a) and 4.5(b) show *iso-moveout* curves, i.e. curves of constant moveout, for the velocity-shifted CMP hyperbola and its time-shifted counterpart for a fixed finite-offset. Presented are five different constant moveouts with the shifts in velocity and in time as functions of the reference traveltime t_0. By comparing 4.5(a) and 4.5(b) one can observe that in order to describe one particular moveout for different reference traveltimes t_0, the shift in velocity needs to be changed, whereas time shift moveouts remain constant for the whole range of reference traveltimes, and, therefore do not depend on t_0 (see also Hertweck et al., 2005). This implies that in order to describe the moveout as a constant along the recorded seismic wavelet, the velocity shift needs to be changed according to the operator's iso-moveout curve.

In consequence, the intuitive choice of a constant velocity shift for one event results in neglection of the slope of the velocity shift iso-moveout curve along the wavelet, which leads to over-corrections for some parts and under-corrections for others, meaning an undesired increase of the signal period at higher offsets. As can be concluded from Figure 4.5(a), this effect is generally most pronounced at shallow times t_0, whereas it

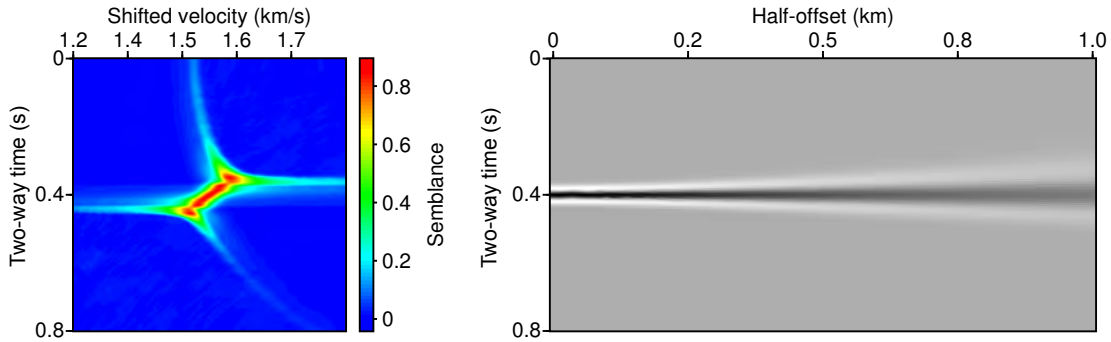

(a) Shift in velocity

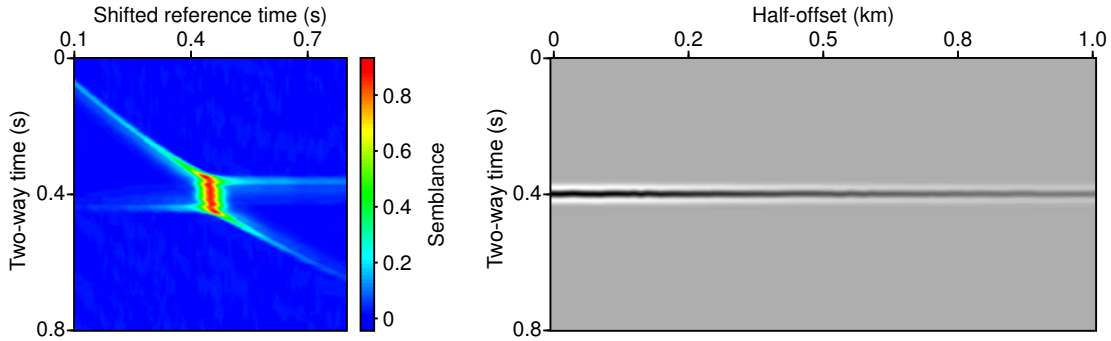

(b) Shift in time

Figure 4.6.: Illustration of the moveout stretch resulting from the dependency of the velocity-shifted moveout on the reference time along the wavelet (a). The time-shifted moveout correction (b), even for higher offsets, does not result in stretching of the signal. The left panels show closeups of the corresponding semblance panels (see Chapter 6), where the inclination of the high values indicating strong coherence reveals the dependency of the velocity-shifted moveout on the true reference time t_0 along the wavelet (Hertweck et al., 2005).

becomes almost negligible for higher values of t_0. As can be inferred from Figure 4.5(b), the time-shifted moveouts do not show this dependency and the intuitive choice of a constant time-shift for a single event leaves the frequency content unchanged. Figure 4.6(a) and Figure 4.6(b) demonstrate this with a simple data example, where the measured event of a single shallow planar horizontal layer is corrected either via the correct medium velocity as shifted velocity (Figure 4.6(a)) or the corresponding correct reference traveltime as the shifted traveltime. One can clearly observe the effect of moveout stretch for the velocity shift approach, whereas this phenomenon does not show for the time shift mechanism.

As mentioned before, the higher order moveout approximations are exact for a certain subsurface configuration, in which the rays are straight and wavefronts are strictly circular. Following from the presented mechanisms that allow for an extension of the geometrically derived formulae to heterogeneous media, I will discuss the operators' potential of higher order accuracy in a rigorous framework, in which the coupling of coordinates will prove to play a central role.

5. On globality

Traveltime moveout formulae are generally known to be reasonably accurate provided the propagation velocities in the overburden change mostly in the vertical. If this assumption of vanishing or mild lateral heterogeneity is not fulfilled, moveout operators usually loose accuracy even for small or moderate separation from the reference ray. Moveout expressions gained via paraxial ray theory face second order limitations (Bortfeld, 1989; Schleicher et al., 1993). Thus, they only provide a reasonably accurate description in the paraxial vicinity of the central ray, even if the overburden velocity does not vary at all. Therefore, one can state, that even when confined to the paraxial vicinity they never provide the numerically exact traveltime no matter how small the neighbourhood is chosen.

If the moveout on the other hand is described by circular wavefronts, i.e. by geometry, it provides a higher-order description and leads to more accurate traveltimes provided the true subsurface velocity distribution and the true kinematics of the wave propagation can be sufficiently well described in an auxiliary constant velocity medium. I hereby would like to emphasize that in contrast to the paraxial approximations, the circular wavefront approximations, which can all be related to straight ray geometry, all provide the numerically exact solution to a specific problem. It can, e.g., be shown, that the hyperbolic CRS formula provides the exact solution to reflection off a planar interface beneath a homogeneous overburden. Multifocusing and the implicit CRS operator in addition even provide exact traveltimes for a point diffractor and are highly accurate as long as the reflector can be approximated reasonably well by the geometry of a circle.

I argue that although the assumption of straight rays or circular wavefronts might be rather unrealistic and generally not fulfilled, there are known to exist many settings important in, e.g., hydrocarbon or geothermal exploration, in which a small degree of overburden heterogeneity is not implausible and reflects physical reality[1]. So in contrast to the paraxial ray theory approximations, the geometrically derived higher-order operators are valid on a global scale, i.e. provide higher-order accuracy, for specific subsurface configurations but reduce to the same second-order zero-offset expressions for more complex media. Geometrical operators based on the assumption of circular wavefront observations in this frame can be considered truly global approximations, thereby extending the range of applicability of paraxial approximations for relatively small magnitudes of heterogeneity. In addition, important concepts like CRP coordinate coupling (Perroud et al., 1999; Höcht et al., 1999), dip moveout (Deregowski, 1986) or the offset response to reflector curvature can be illuminated and studied in a controlled simple framework, where all important relations are explained via simple geometric relations.

In this chapter of the thesis, I review the aspect of globality, in a theoretical but also in a practical sense. The first three sections are devoted to the question of how

[1] These example include sea-floor imaging with a constant velocity water column, sedimentary environments with weak velocity gradients or data acquired in hardrock environments, where velocities are generally large but mostly don't vary very much (e.g., Eaton et al., 2003).

the chosen coordinates are coupled, e.g. due to reflector dip, reflector curvature or lateral overburden heterogeneity. The common reflection point (CRP) concept, already introduced in the second chapter of the thesis, is very useful to explain the effect of overburden heterogeneity on this mutual dependency of coordinates. Following the first three chapters, I discuss different strategies to make use of the global character of the circular wavefront approximations, like hyperbolic CRS, multifocusing and the implicit CRS[2]. In the frame of this chapter, for convenience, I introduce a matrix notation for the Taylor series expansion, which helps to picture the coupling of coordinates in an intuitive way. The elements of these matrices correspond to the derivatives of different order for the considered moveouts, which can directly be used as extrapolation operators to finite-offset, thereby spanning the bridge to locally accurate prestack traveltimes.

Concluding this chapter, I review the diffraction response in this context, which, due to the high redundancy of raypaths and the break-down of Snell's law, inhibits a striking connection between zero-offset and finite-offset traveltimes. This can be conveniently explained by the full decoupling of source and receiver coordinates for highly curved target structures. I suggest a scheme, which allows for a locally accurate description even for, in principle, arbitrarily large source receiver offsets solely based on the measurement of the zero-offset diffraction response.

5.1. Higher orders

As mentioned above, the geometrically derived operators are based on the assumption of locally circular wavefronts propagating in an auxiliary medium of constant velocity[3]. So, in consequence, these descriptions generally do not suffer the fundamental second-order limitations of paraxial ray theory as long as the overburden heterogeneity is moderate. For constant velocity overburden, these expressions might even deliver exact traveltimes also for very large source receiver distances, which makes them truly global approximations for those cases.

In order to understand the known to be decreased performance of the hyperbolic CRS operator with respect to the two considered double-square-root operators of multifocusing and the implicit CRS, in this chapter I look into the structure of the higher-order terms, which determine the accuracy for large offsets, i.e. on a global scale. In general, the Taylor series expansion of the true traveltime can be written as

$$t = t_0 + \sum_{i=1}^{\infty}\sum_{j=1}^{\infty} \frac{1}{(i+j)!}\, \frac{\partial^{i+j} t}{\partial \eta^i \partial \zeta^j}\bigg|_{\eta_0,\zeta_0} (\eta-\eta_0)^i (\zeta-\zeta_0)^j \quad , \tag{5.1}$$

where the coordinate set (η, ζ) can either be identified with the source and receiver locations (x_s, x_g) or the midpoint and half-offset distances (x_m, h). For the most general case of an arbitrarily complex medium, in principle, the full Taylor series (5.1) is needed to provide an exact description of the traveltimes in the vicinity of the chosen reference coordinates (η_0, ζ_0). For simpler subsurface configurations, not all terms in the series are needed and many of the coefficients are inter-related, i.e. coupled, so the number of degrees of freedom is automatically reduced.

[2]For the respective moveout definitions, I refer to Chapter 3 and Chapter 4.

[3]Either this velocity is an effective velocity coupling the true zero-offset traveltime to the radius of the NIP wavefront or it coincides with the actual near-surface velocity (cee Chapter 4).

In order to get an intuitive idea of the coupling of coefficients, I suggest to rewrite expression (5.1) in a simple matrix notation,

$$t = \Delta\vec{\eta}^T \, \underline{\mathbf{T}}_{\eta\zeta}\big|_{\eta_0,\zeta_0} \, \Delta\vec{\zeta} \quad . \tag{5.2}$$

The matrix $\underline{\mathbf{T}}_{\eta\zeta}$ contains the respective partial derivatives with respect to η and ζ at the corresponding line and column positions. An increasing line number in the matrix indicates increasing η derivative orders, the column number corresponds to the order of the partial ζ derivative,

$$\underline{\mathbf{T}}_{\eta\zeta} = \begin{pmatrix} t_{00} & t_{01} & \dots \\ t_{10} & t_{11} & \\ \vdots & & \ddots \end{pmatrix} \quad , \tag{5.3}$$

with

$$t_{ij} = \frac{1}{(i+j)!} \frac{\partial^{i+j} t}{\partial \eta^i \zeta^j} \quad . \tag{5.4}$$

The vectors $\Delta\vec{\eta}$ and $\Delta\vec{\zeta}$ are defined as

$$\Delta\vec{\eta} = \begin{bmatrix} (\eta-\eta_0)^0 & (\eta-\eta_0)^1 & (\eta-\eta_0)^2 & \dots \end{bmatrix}^T \quad , \tag{5.5a}$$

$$\Delta\vec{\zeta} = \begin{bmatrix} (\zeta-\zeta_0)^0 & (\zeta-\zeta_0)^1 & (\zeta-\zeta_0)^2 & \dots \end{bmatrix}^T \quad . \tag{5.5b}$$

Again, like for the derivative matrix, the position in these vectors indicates the order of the deviation from the reference position. As will be shown in the following section, this matrix formulation is particularly useful for an intuitive understanding of the coupling of the midpoint half-offset or source receiver domain coordinates.

5.2. Coupling

As motivated in Chapter 3, the simple reflection off a curved interface can in general be described via two circular wavefront measurements. In case of finite reflector curvature, these two wavefronts generally only decouple from each other, when the coordinates are chosen appropriately. Considering the well-known NIP and normal wavefront measurements, the zero-offset and CRP coordinates need to be chosen in order to achieve a complete separation of the NIP and normal wave influence[4]. In this particular coordinate system, the corresponding derivative matrix would take the following form

$$\underline{\mathbf{T}}_{m,h(m)} = \begin{pmatrix} t_{00} & t_{01} & t_{02} & \dots \\ t_{10} & 0 & 0 & \dots \\ t_{20} & 0 & 0 & \dots \\ \vdots & \vdots & \vdots & \ddots \end{pmatrix} \quad , \tag{5.6}$$

where the subscript m denotes the midpoint coordinate, i.e. x_m, corresponding to the description in the zero-offset section and $h(m)$ indicates the coordinate in the CRP gather, where generally the half-offset, due to Snell's law, depends on the chosen midpoint location and vice versa. In the CMP gather, the moveout can only be accurately

[4] In zero-offset and CRP coordinates, the normal wave exclusively describes the zero-offset response, while the NIP wavefront fully governs the moveout in the CRP gather. For more details, see Section 3.5.

described using the measurements of both, the normal and the NIP wavefront, when considering higher orders than two[5]. As indicated in expression (5.6), the decoupling of the moveouts in the CRP gather and the zero-offset section clearly shows in the vanishing mixed terms. In this particular coordinate system, only the pure derivatives, i.e. the first row and the first column of the derivative matrix take finite values not equal to zero. In general though, the exact CRP coordinates are not known, thus, one may state that in a realistic scenario, either the coordinates or the circular wavefronts determining the moveout are coupled to each other, when the target reflector has finite curvature (e.g., Höcht et al., 1999).

In order to better appreciate the importance of this coupling for the accurate description of traveltimes, I compare the fourth-order truncations of the hyperbolic CRS and the diffraction traveltime derivative matrices and briefly elaborate on their structure. For both, the hyperbolic CRS and the diffraction operator, I present the derivative matrices for the commonly used midpoint half-offset coordinate frame. In addition, I provide the source receiver derivative matrix for the diffraction traveltime moveout, since the respective mixed coefficients take a drastically different form in this particular domain. To illustrate the role of coupling for target reflectors with finite curvature and to support the special findings for the diffraction case, a controlled analytical example with constant velocity overburden is presented and discussed at the end of this section.

The role of reflector curvature

The hyperbolic CRS operator can be viewed as a hybrid expression, which happens to be only exact for a planar inclined reflector in a homogeneous medium (compare Chapter 3). In fact, it can also account for finite reflector curvatures, indicated by the incorporation of the normal wave parameters, but by setting $\Delta x_m = 0$ in formula (3.19) one immediately finds that the influence of the normal wave, which is necessary for an accurate description also at large offsets is limited to the zero-offset section in the hyperbolic operator. Thus, the naturally expected coupling between the NIP and the normal wave in the CMP gather cannot be observed for the hyperbolic approximation. This finding is in accordance with the NIP wave theorem formulated by Hubral (1983), which states that up to second order, the zero-offset moveout in the CMP gather is fully characterized by the NIP wave. In turn this means that the necessary coupling can be addressed to orders higher than two.

In order to not obscure the main message of this investigation and to maintain readability, I confine myself to only present the corresponding derivative matrix elements for the special zero-offset case. Please note however, that the more general finite-offset derivatives of the hyperbolic operator (up to fourth order) can be found in Appendix C.2. While the zero-offset coefficients explain the behaviour of the zero-offset formulation of the operator, the finite-offset coefficients can be used i.e. for extrapolation of traveltimes and moveout attributes to finite-offset[6]. The fourth-order zero-offset derivative matrix $\underline{\mathbf{T}}_{mh}$, formulated for midpoint and half-offset coordinates (indicated

[5] According to the NIP wave theorem (Hubral, 1983), the moveout in the CMP gather is fully described by the propagation of the conceptual NIP wave, when orders up to two, i.e. the paraxial vicinity, are considered.

[6] For more details on the extrapolation, I refer to Section 5.4

by the subscripts m and h) reads

$$\underline{\mathbf{T}}_{mh} = \begin{pmatrix} t_{00} & 0 & t_{02} & 0 & t_{04} \\ t_{10} & 0 & t_{12} & 0 & \dots \\ t_{20} & 0 & t_{22} & \dots & \dots \\ t_{30} & 0 & \dots & \dots & \dots \\ t_{40} & \dots & \dots & \dots & \dots \end{pmatrix} \quad . \tag{5.7}$$

Please note that the matrix is not complete, since only orders ≤ 4 are considered. The vanishing coefficients are a result of reciprocity and can be found for all CRS-like operators, including multifocusing and the implicit CRS. In the following, I would like to investigate in three very particular geometric examples of a planar horizontal reflector, a circular reflector, i.e. a reflector with finite curvature and a point diffractor in a constant velocity background. The respective models of the three considered cases are displayed in the left of Figure 5.1. For the most general case of a finitely curved reflector, as mentioned before, both, the NIP and the normal wave, are needed to accurately describe the traveltime response in the CMP gather. Höcht et al. (1999) introduced a fourth-order truncated Taylor series expansion of the parametric CRS (see Chapter 3.5 and Appendix B), which provides the exact solution for reflection at a circular interface. Up to second order, the zero-offset coefficients, like for the implicit CRS and multifocusing (e.g., Schwarz, 2011; Fomel and Kazinnik, 2013) correspond exactly to the coefficients gained via geometrical reasoning by Shah (1973) or with paraxial ray theory (Schleicher et al., 1993; Jäger et al., 2001). For constant velocity they can be written

$$t_{00} = \frac{2R_{\mathrm{NIP}}}{v} \quad , \tag{5.8a}$$

$$t_{10} = \frac{2\sin\alpha}{v} \quad , \tag{5.8b}$$

$$t_{20} = \frac{\cos^2\alpha}{vR_{\mathrm{N}}} \quad , \tag{5.8c}$$

$$t_{02} = \frac{\cos^2\alpha}{vR_{\mathrm{NIP}}} \quad . \tag{5.8d}$$

Thus, as expected and as stated by the NIP wave theorem, the midpoint and the normal wave influence and correspondingly the zero-offset and CMP moveout are decoupled up to second order for all operators. Consequently, the important coupling and therefore the differences between the different approaches are contained in the higher-order terms. For the finitely curved reflector, Höcht et al. (1999) found the following expressions for the higher-order terms

$$t_{30} = -\frac{\sin\alpha\cos^2\alpha}{vR_{\mathrm{N}}^2} \quad , \tag{5.9a}$$

$$t_{12} = -\frac{\sin\alpha\cos^2\alpha(2R_{\mathrm{NIP}} + R_{\mathrm{N}})}{vR_{\mathrm{NIP}}^2 R_{\mathrm{N}}} \quad , \tag{5.9b}$$

$$t_{40} = -\frac{\cos^2\alpha(5\cos^2\alpha - 4)}{4vR_{\mathrm{N}}^3} \quad , \tag{5.9c}$$

$$t_{04} = -\frac{\cos^2\alpha(R_{\mathrm{N}}\cos^2\alpha - 4R_{\mathrm{NIP}}\sin^2\alpha)}{4vR_{\mathrm{NIP}}^3 R_{\mathrm{N}}} \quad , \tag{5.9d}$$

$$t_{22} = -\frac{\cos^2\alpha}{2vR_{\mathrm{NIP}}^3 R_{\mathrm{N}}^2}\left[R_{\mathrm{NIP}}^2(8\cos^2\alpha - 6) + R_{\mathrm{NIP}}R_{\mathrm{N}}(5\cos^2\alpha - 4) - 2R_{\mathrm{N}}^2\sin^2\alpha\right] \quad . \tag{5.9e}$$

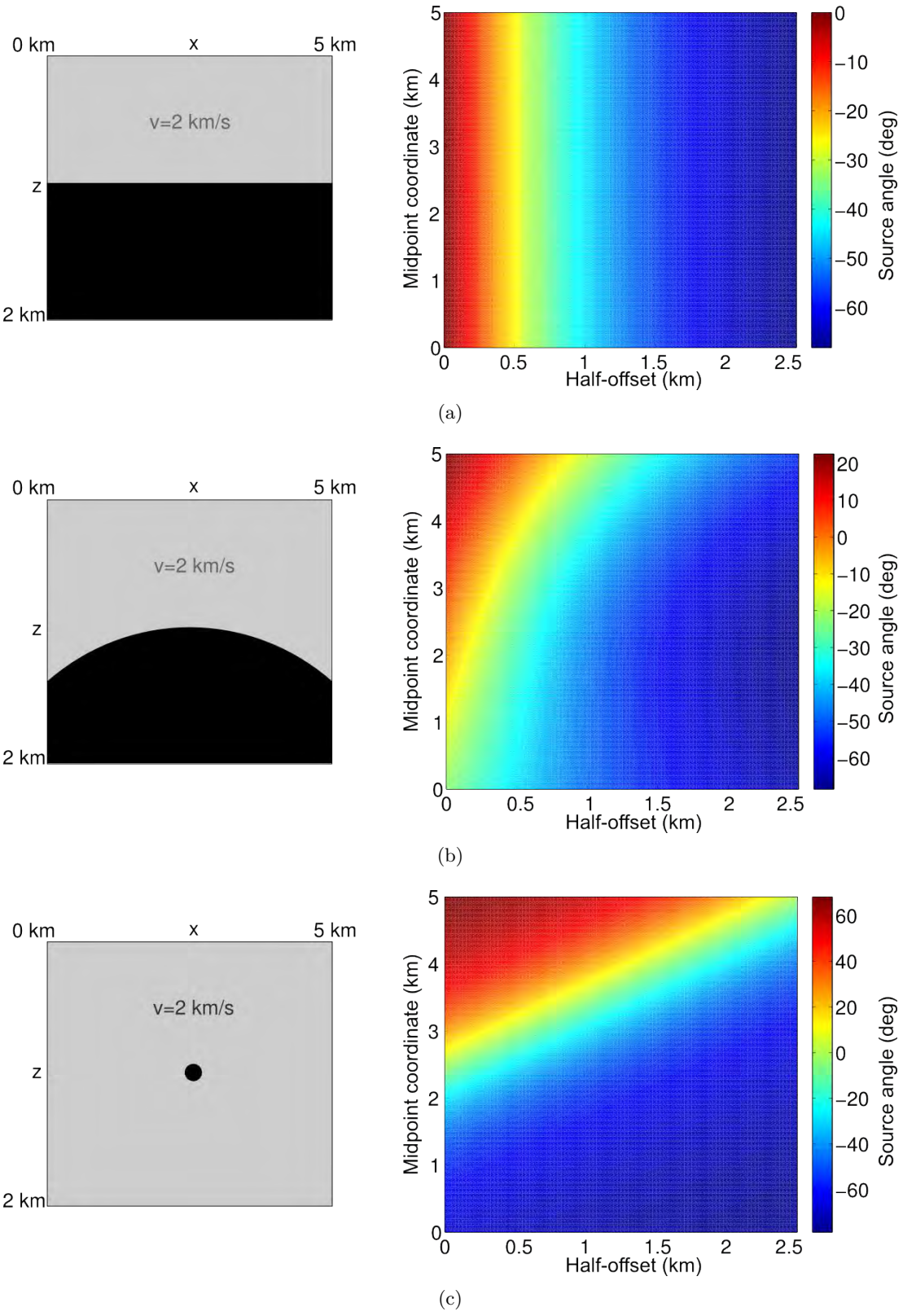

Figure 5.1.: Illustration of the midpoint half-offset coupling for (a) a planar horizontal reflector, (b) a reflector with finte curvature, and (c) an infinitely curved point diffractor in a constant velocity medium. Shown are the respective model plots (left) and the corresponding source ray angle distributions (right) as a function of midpoint location x_m and half-offset h. For the diffraction, the strongest midpoint half-offset coupling can be observed.

If we consider a planar but tilted reflector, we have $R_{\mathrm{N}} \to \infty$ and expressions 5.9 are fully determined by the NIP wave. While, however, the pure midpoint derivatives from second to fourth order vanish for this case, the mixed terms t_{12} and t_{22} still take finite values as long as the reflector is tilted. These contributions are proportional to the sine of the emergence angle α and consequently vanish for a horizontal target reflector. Thus, these mixed order terms carry the effect of the reflection point dispersal due to the inclination of the interface. For CRP coordinates, as mentioned above, the reflection point dispersal and, accordingly, the mixed terms vanish and the moveouts in the zero-offset section and the CRP gather are decoupled (compare matrix (5.6)). For the case of a planar horizontal reflector (and vanishing lateral heterogeneity), the CRP gather and the CMP gather are equivalent and the derivative matrix takes the form

$$\underline{\mathbf{T}}_{mh} = \begin{pmatrix} t_{00} & 0 & t_{02} & 0 & t_{04} \\ 0 & 0 & 0 & 0 & \dots \\ 0 & 0 & 0 & \dots & \dots \\ 0 & 0 & \dots & \dots & \dots \\ 0 & \dots & \dots & \dots & \dots \end{pmatrix} \quad . \tag{5.10}$$

To illustrate this decoupling of midpoint and half-offset coordinates for the planar reflector, Figure 5.1(a) shows the finite-offset source emergence angle as a function of midpoint and half-offset location for the respective model shown on the left. Interestingly the source angle distribution can be considered a visual equivalent of the derivative matrix $\underline{\mathbf{T}}_{mh}$. Consequently, the finite-offset source angle only changes in offset direction, thus the corresponding traveltime moveout in offset direction is fully decoupled from changes in the midpoint coordinate. Figure 5.1(b) shows the source angle distribution, again as a function of midpoint coordinate and half-offset, for a simple homogeneous model with finite reflector curvature. One can clearly see that the distribution is affected by both changes in midpoint and offset direction. The corresponding zero-offset (fourth-order) derivative matrix (5.7) contains the two non-vanishing mixed derivative elements t_{12} and t_{22} indicating the coupling of coordinates.

Hyperbolic CRS and diffractions

The hyperbolic CRS operator (3.19) is known to be not well-suited for imaging diffraction at larger offsets (e.g., Landa et al., 2010; Schwarz, 2011). Investigating the structure of the higher-order coefficients can contribute to better appreciate this finding. As mentioned before, the coupling of the midpoint and half-offset coordinates, which implies a coupling of the NIP and the normal wave moveouts, can generally be observed for finite reflector curvatures. In fact, as can be seen in Figure 5.1(c), the diffraction reveals the strongest possible coupling of the finite-offset source angles, when observed in midpoint half-offset coordinates. If we, for example, compare the mixed term t_{12}^{diff} of the zero-offset diffraction moveout derivative matrix with the corresponding hyperbolic counterpart t_{12}^{hyp},

$$t_{12}^{\mathrm{diff}} = -\frac{\sin\alpha\cos^2\alpha}{vR_{\mathrm{NIP}}^2} \quad , \tag{5.11a}$$

$$t_{12}^{\mathrm{hyp}} = -\frac{1}{3}\frac{\sin\alpha\cos^2\alpha}{vR_{\mathrm{NIP}}^2} \quad , \tag{5.11b}$$

we find that the hyperbolic moveout's coupling strength is smaller by a factor of 3. In addition, in contrast to the more general solution shown in (5.9), the hyperbolic

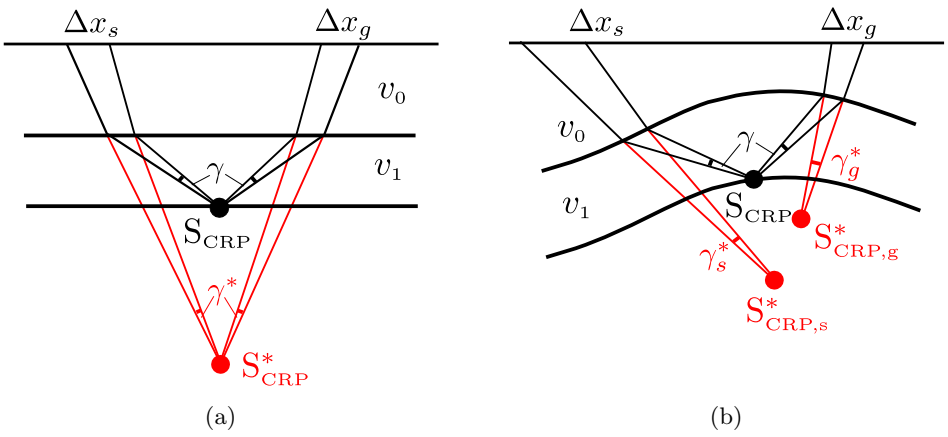

Figure 5.2.: Illustration of the finite-offset CRP geometry, where, as motivated in Chapter 2 and Chapter 3, the common reflection point can be viewed as a vitual seismic point source. While for moderate vertical heterogeneity or a constant velocity overburden, the image of the CRP as observed in the vicinity of the source $S^*_{CRP,s}$ and the correponding image $S^*_{CRP,g}$ seen from the receiver do coincide (a), they generally appear at different positions, when lateral velocity changes are present in the medium (b).

term, like its diffraction counterpart, does not depend on the normal wave radius R_N handling the reflector curvature. This absence of the normal wave radius becomes most drastically visible, if we compare the fourth-order half-offset derivative of the general finite-curvature solution of Höcht et al. (1999), denoted by t_{04}^{curv} with the corresponding term in the hyperbolic CRS derivative matrix,

$$t_{04}^{curv} = -\frac{\cos^2\alpha(R_N\cos^2\alpha - 4R_{NIP}\sin^2\alpha)}{4vR_{NIP}^3R_N} \quad , \tag{5.12a}$$

$$t_{04}^{hyp} = -\frac{1}{4}\frac{\cos^4\alpha}{vR_{NIP}^3} \quad . \tag{5.12b}$$

In the planar reflector limit, i.e. for $R_N \to \infty$, both of these expression coincide, implying that the higher-order offset terms are only accurate for planar reflectors and increasingly inaccurate for strong interface curvatures or diffractors. Since the hyperbolic operator (3.19) coincides with the diffraction operator for $R_N = R_{NIP}$ and $h = 0$, i.e. in the zero-offset section, the corresponding pure midpoint derivatives are equal to the diffraction response for this particular case[7].

5.3. Heterogeneity and finite offsets

As mentioned before, the circular wavefront description and the connected straight-ray geometry only lead to higher-order accuracy, as long as the heterogeneity in the overburden is generally moderate and the major velocity variations happen in the vertical direction. Only under these conditions, the coupling between the source and the receiver experiment can be described by geometric relations in the auxiliary medium of constant velocity. I will show in the following section that in the case of moderate

[7]For more details on the higher orders of the diffraction moveout and the hyperbolic operator, I refer to Appendix C.1 and Appendix C.2.

heterogeneity, the reference ray of a geometrically derived operator like multifocusing or the implicit CRS, can, in principle, be chosen freely and doesn't necessarily have to be a zero-offset ray.

At this point, I would like to take a different view on the subject of globality. As argued in the beginning, a sufficiently large derivative matrix $\underline{T}_{\eta\zeta}$ leads to a globally accurate traveltime moveout description in η and ζ[8]. From a mathematical point of view, this globality can always be achieved, when the individual components of the derivative matrix are treated as independent, decoupled entities. As a consequence however, this would mean that we have to face a problem of much higher dimensionality since many more degrees of freedom are allowed. For the second-order finite-offset derivative matrix

$$\underline{\mathbf{T}}_{\eta\zeta} = \begin{pmatrix} t_{00} & t_{01} & t_{02} \\ t_{10} & t_{11} & \dots \\ t_{20} & \dots & \dots \end{pmatrix} \tag{5.13}$$

we would end up with a total number of six independent parameters, one determining the reference traveltime and the remaining five to describe the moveout in the second order vicinity (Bortfeld, 1989; Schleicher et al., 1993; Zhang et al., 2001). We know however, that for a constant velocity medium, where the assumption of straight rays and circular wavefronts is strictly valid, generally three independent attributes are sufficient to fully and accurately describe the reflection at an interface of finite curvature and the reference ray, in principle can be chosen freely (see the argument above). So as long as geometry can be applied to the problem, the dimensionality can be reduced without any harm to the accuracy. In other words, as long as the auxiliary medium allows for a reasonably good description of the true kinematic wavefield propagation, principles of basic geometry establish a coupling of the derivative matrix coefficients, which leads to a reduction of the degrees of freedoms in the system.

I would like to emphasize at this point that the concept of coupling, which, due to its importance is extensively discussed in the cause of this chapter, is not established via geometry. On the contrary, for constant velocity media the fundamental physical coupling, generally resulting from Snell's law and the complexity of the target interface and the traversed medium can be governed by simple geometry. For strong heterogeneity, especially in lateral direction, the physical coupling cannot be described via geometric relations any more and all derivative matrix elements must be treated independently.

As motivated in Chapter 2, in the zero-offset vicinity, the finite-offset traveltime response appears to stem from a virtual source located at the normal incidence point (NIP) on the reflector. Due to coincident source and receiver at the reference point, we found that the measurement of only one wavefront, the NIP wavefront, is sufficient to describe the moveout in that vicinity. In the more general finite-offset experiment, the reference ray is not necessarily a normal ray and instead two measurements of the common reflection point (CRP) wave, one at the reference source, the other at the receiver, need to be taken into account (see Figure 5.2). So in the context of geometry

[8] As emphasized before, these general coordinates can be identified either with midpoint and half-offset (x_m, h) or source and receiver coordinates (x_s, x_g).

and circular wavefronts, the finite offset CRP moveout can be written as

$$t_{00} = t_0 + \frac{\sqrt{R_s^2 + 2R_s\Delta x_s \sin\alpha_s + \Delta x_s^2} - R_s}{v_s} + \frac{\sqrt{R_g^2 + 2R_g\Delta x_g \sin\alpha_g + \Delta x_g^2} - R_g}{v_g}, \tag{5.14}$$

where the subscripts s and g denote the quantities at the source and the receiver, respectively. Please note, that for moderate heterogeneity, predominantly in the vertical direction, the velocities in the vicinity of the source and near the receiver should coincide and we can set $v_s = v_g = v$. In addition, as was discussed in Chapter 3, the coupling of the source and receiver coordinates $\Delta x_s(\Delta x_g)$ or the wavefront emergence angles and curvature radii can in such cases be described via geometry. In the general case, where the reference offset between source and receiver is chosen very large and where the medium is vertically and laterally complex, $\Delta x_s(\Delta x_g)$ is generally not known and the source and receiver moveouts in the CRP gather need to be described in two separate auxiliary media. The coefficients of the second-order finite-offset source receiver derivative matrix $\underline{\mathbf{T}}_{sg}$ can be derived from (5.14). For a fixed finite offset, the pure derivative matrix elements read

$$t_{00} = t_0 \quad , \tag{5.15a}$$

$$t_{10} = \frac{\sin\alpha_s}{v_s} \quad , \tag{5.15b}$$

$$t_{01} = \frac{\sin\alpha_g}{v_g} \quad , \tag{5.15c}$$

$$t_{20} = \frac{1}{2}\frac{\cos^2\alpha_s}{v_s R_s} \quad , \tag{5.15d}$$

$$t_{02} = \frac{1}{2}\frac{\cos^2\alpha_g}{v_g R_g} \quad . \tag{5.15e}$$

Please note that our sign convention for the angles α_s and α_g differs from the one of Zhang et al. (2001), resulting in a different sign for the first-order terms. Aside from that, the geometrically derived first- and second-order terms agree with the parabolic finite-offset CRS formula by Zhang et al. (2001). In the frame of paraxial ray theory (Bortfeld, 1989; Schleicher et al., 1993; Zhang et al., 2001) the second-order mixed term t_{11}, containing information on the coupling of the source and the receiver wavefront measurements, is described via the surface-to-surface propagator matrix element B (Bortfeld, 1989; Červený, 2001).

5.4. Diffraction symmetries

It turned out that the derivative matrix formalism is particularly suited to explain the process of coordinate coupling for reflections. In the previous chapter, I argued that, in principle, the NIP wave concept can intuitively be extended, even if no normal rays, i.e. finite-offset rays, are considered. In this section I emphasize the special role of the diffraction as the response of a scattering object, for which Snell's reflection law does not have to be accounted for. In order to fully comprehend the special role of the diffraction, I would like, for convenience, to return to the simple case of a diffractor in a constant velocity medium, for which, according to the investigations in Section 5.2,

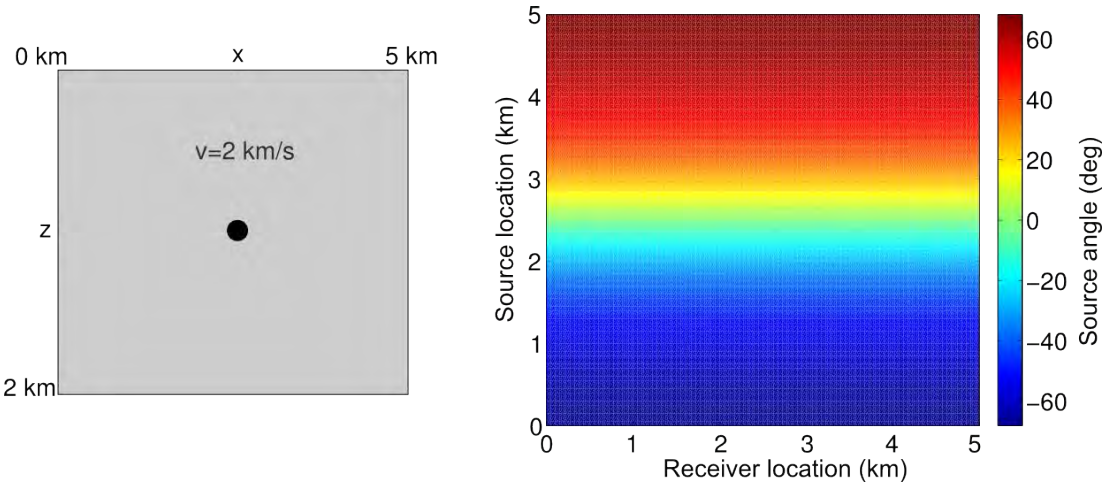

(a)

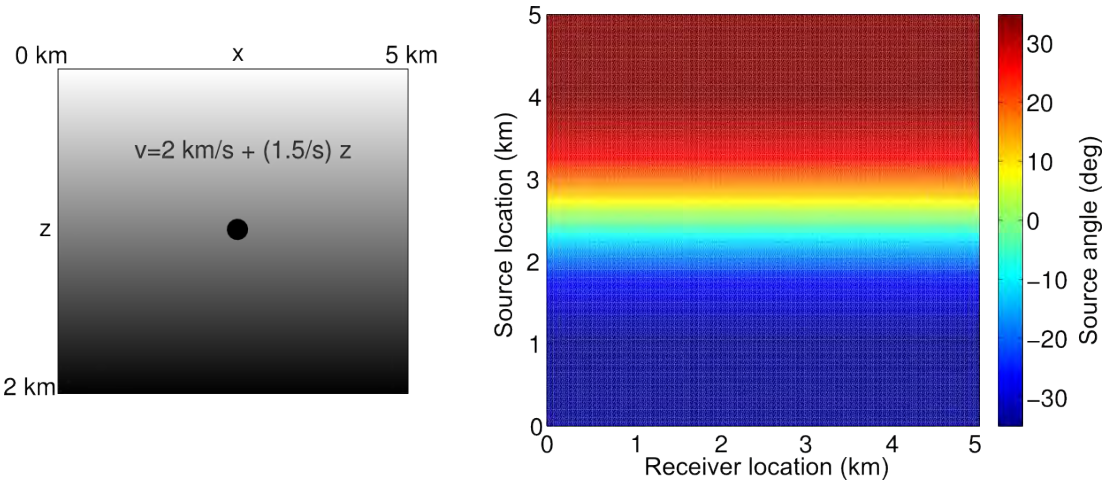

(b)

Figure 5.3.: Illustration of the decoupling of source and receiver coordinates for a diffractor in a homogeneous medium (a) and a strong vertical gradient background (b). In correspondence with Figure 5.1 the model plot (left) and the corresponding source angle distribution (right), this time as a function of source and receiver location x_s and x_g, are displayed. Although not presented here, please note that this decoupling of diffraction information in the source-receiver domain is fundamental and can be observed in arbitrarily heterogeneous media.

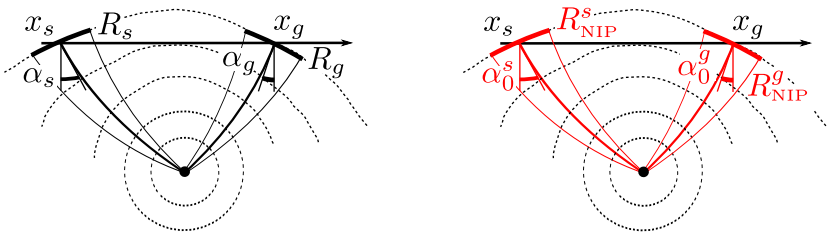

Figure 5.4.: As motivated in Chapter 2 a diffractor can be interpreted as a virtual seismic source. Due to the infinte local curvature of a diffracting structure, every ray emitted from this virtual source is a NIP ray and the finite-offset CRP attributes can be exchanged by their according zero-offset NIP counterparts at the respective locations (Schwarz et al., 2014b; Bauer, 2014).

the strongest midpoint half-offset coupling could be observed (compare Figure 5.1). As shown in the previous section, the zero-offset version of the general fourth-order midpoint half-offset derivative matrix reads

$$\underline{\mathbf{T}}_{mh} = \begin{pmatrix} t_{00} & 0 & t_{02} & 0 & t_{04} \\ t_{10} & 0 & t_{12} & 0 & \dots \\ t_{20} & 0 & t_{13} & \dots & \dots \\ t_{30} & 0 & \dots & \dots & \dots \\ t_{40} & \dots & \dots & \dots & \dots \end{pmatrix} \quad . \tag{5.16}$$

While for finitely curved reflectors, the corresponding elements t_{ij} are generally different from each other, comparison for the diffraction case reveals that the non-vanishing coefficients of the same order, i.e. constant $i + j$, coincide with each other. While for the first order, a comparison is not possible, since the offset term vanishes for the zero-offset case, the coefficients of order two, three and four read (compare equations (5.8) and (5.9) and Appendix C)

$$t_{20} = t_{02} = \frac{\cos^2 \alpha}{v R_{\mathrm{NIP}}} \quad , \tag{5.17}$$

$$t_{30} = t_{12} = -\frac{\sin \alpha \cos^2 \alpha}{v R^2_{\mathrm{NIP}}} \quad , \tag{5.18}$$

$$t_{40} = t_{22} = -\frac{\cos^2 \alpha (5 \cos^2 \alpha - 4)}{4 v R^3_{\mathrm{NIP}}} . \tag{5.19}$$

So in fact, up to fourth order, we have a high degree of symmetry in the midpoint half-offset derivative matrix, which is directed in the cross-diagonal direction, i.e. following the positions of the same order. Figure 5.1 reveals visually this particular diffraction symmetry in the presented midpoint half-offset distribution of the finite offset source angles. One can conclude from this quantitative comparison of the coefficients in the derivative matrix, that midpoint and offset traveltime information is not only coupled, which is generally the case for reflectors with finite-curvature, but in fact exactly equivalent for diffractions.

As it turns out, the presented symmetry is even more pronounced in the source receiver domain. The corresponding finite-offset source receiver derivative matrix $\underline{\mathbf{T}}_{sg}$ for the diffraction moveout can, in analogy with multifocusing and the implicit CRS,

be written as the sum of a source and a receiver contribution[9]

$$\underline{\mathbf{T}}_{sg} = \frac{1}{v}\begin{pmatrix} \mathcal{S}_{00} & 0 & 0 & 0 & 0 \\ \mathcal{S}_{10} & 0 & 0 & 0 & \dots \\ \mathcal{S}_{20} & 0 & 0 & \dots & \dots \\ \mathcal{S}_{30} & 0 & \dots & \dots & \dots \\ \mathcal{S}_{40} & \dots & \dots & \dots & \dots \end{pmatrix} + \frac{1}{v}\begin{pmatrix} \mathcal{G}_{00} & \mathcal{G}_{01} & \mathcal{G}_{02} & \mathcal{G}_{03} & \mathcal{G}_{04} \\ 0 & 0 & 0 & 0 & \dots \\ 0 & 0 & 0 & \dots & \dots \\ 0 & 0 & \dots & \dots & \dots \\ 0 & \dots & \dots & \dots & \dots \end{pmatrix} \quad . \tag{5.20}$$

The matrix picture shows a clear separation of the source and receiver contributions. So, while in the midpoint half-offset domain the respective source and receiver contributions generally have the same magnitude for the same order, but opposite signs (leading to cancellation of the total traveltime derivative) for uneven orders of the half-offset derivatives, the source and receiver matrices are fully decoupled from each other. Figure 5.3 again, like for the other examples, shows the finite-offset source angle distribution in the source receiver domain for a constant velocity medium and a unrealistically strong vertical velocity gradient. The decoupling of source and receiver can be observed for both cases, indicating that the revealed symmetry is a fundamental and characteristic property of a diffraction, no matter how strong the heterogeneity in the overburden.

As argued in Appendix C, the clearly revealed decoupling of the source and the receiver contribution can also be found for the more general finite-offset operator. In fact, the finite-offset CRP coupling, which is implied by Snell's law for the reflection case is obsolete for diffractions and the finite-offset CRP operator (5.14) can be used for arbitrary source receiver combinations (see Figure 5.4). In the following section, I will discuss different strategies of predicting finite-offset traveltimes and attributes from zero-offset measurements.

5.5. From zero-offset to finite-offset

While the previous section of this chapter on globality mainly dealed with the simple but important phenomenon of moveout or coordinate coupling and general aspects of globality, this section is devoted to provide tools for extrapolation from zero-offset to a finite-offset reference ray. As discussed in the previous section, the circular wavefront concept is particularly useful, when heterogeneity is moderate in the overburden. If this condition is fulfilled, I argued that the choice of the reference ray is basically free and the considered approximation, depending on the generality of the reflector shape it was derived for, can achieve higher-order accuracy. Following the paths of Lavaud et al. (2004) and Vanelle et al. (2014) and based on the assumption that the description of straight-ray analogues in an auxiliary medium of constant velocity is valid, I propose to use the general second-order finite-offset derivative matrices $\underline{\mathbf{T}}_{mh}$ of hyperbolic CRS, multifocusing and the implicit CRS operator for the extrapolation from zero-offset to finite-offset (see Figure 5.5(a)). In this context, the respective geometrically derived operators, formulated in terms of zero-offset NIP and normal-wave attributes are assumed to be globally accurate.

Based on this assumption of globality, the partial CRS approach introduced by Baykulov and Gajewski (2009) utilizes finite-offset subsets of zero-offset CRS moveouts

[9]Please note that, for convenience, the order-dependent Taylor normalization $1/(i+j)!$ is omitted. For more details, like i.e. the actual derived coefficients, I refer to Appendix C.

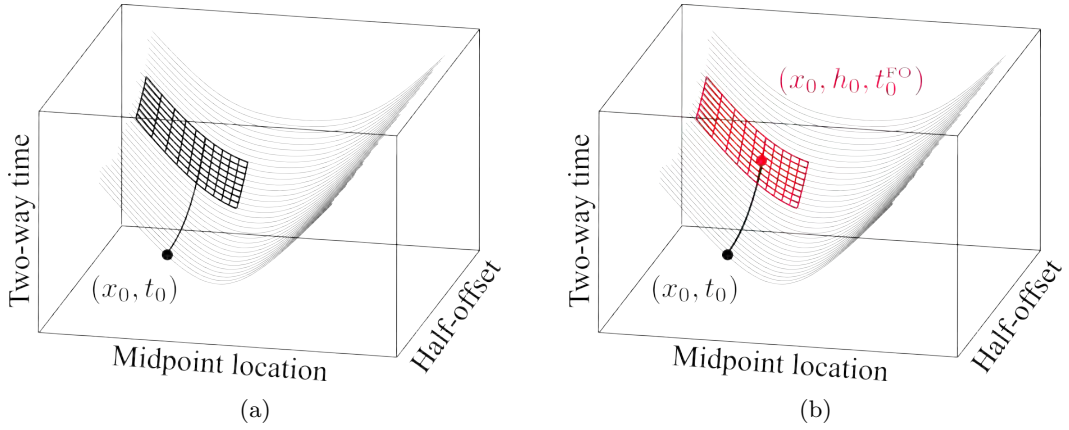

Figure 5.5.: Illustration of the local finite-offset refinement (b) of traveltimes and attributes extrapolated from stable zero-offset measurements (a). As will be demonstrated in Chapter 6, the extrapolation and refinement of traveltimes and attributes can lead to efficient full prestack data-analysis, resulting in suitable input for i.e. prestack stereotomography (Billette and Lambaré, 1998).

for efficient prestack data enhancement, interpolation and regularization (Eisenberg-Klein et al., 2008). In this work, I seek to extend the approach of partial CRS by not only extracting local traveltimes but also higher-order information from the zero-offset operators. As will be demonstrated in Chapter 6, even under unfavourable conditions, like, e.g., non-negligible lateral heterogeneity in the overburden, the extrapolated finite-offset traveltimes and attributes can form a very useful starting point for local true finite-offset measurements (Figure 5.5(b)). Following from this powerful application, which can be useful for finite-offset migration, interpolation, diffraction separation (Bauer et al., 2015) and locally sensitive full prestack attribute analysis for e.g. prestack stereotomography (Billette and Lambaré, 1998), the heading of this section might be loosely rephrased as *from global to local*.

In order to maintain readability and clarity and due to the fact that local refinement of the source and receiver slopes will be considered in the application part in Chapter 6, I will only present the respective zeroth and first-order extrapolators of the different operators. Please note however that finite-offset extrapolation equations up to second order – for multifocusing and the implicit CRS – and even up to fourth order – for hyperbolic CRS and the diffraction moveout – are available in Appendix C.

CRS extrapolation

The derivative matrix notation proved to be a useful approach to investigate in the higher-order structure of the geometrically derived traveltime moveout operators. The corresponding Taylor series coeffiecients can be accessed in an orderly manner and it can be formulated for different sets of coordinates and for an arbitrary reference, i.e. the reference does not necessarily have to be the zero-offset. By utilizing this fact, in the following, I introduce the first-order midpoint half-offset components of $\underline{\mathbf{T}}_{mh}$ for the hyperbolic CRS traveltime operator, which can be used for the extrapolation of slope information. The resulting coefficients can, via simple relations between the midpoint

half-offset and source receiver domain (see Appendix C), be related to the slopes p_s and p_g at the source and the receiver, which play a central role in the highly resolving prestack stereotomography[10] (Billette and Lambaré, 1998). In matrix notation, the hyperbolic CRS operator can be written

$$t_{00} = t_0 + \sqrt{\left(\hat{t}_0 + a\Delta x_m\right)^2 + b\Delta x_m^2 + ch^2} - \hat{t}_0 \quad , \tag{5.21}$$

where

$$\hat{t}_0 = \frac{2R_{\mathrm{NIP}}}{v} \quad , \tag{5.22a}$$

$$a = \frac{2\sin\alpha}{v} \quad , \tag{5.22b}$$

$$b = \frac{4\cos^2\alpha}{v^2}\frac{R_{\mathrm{NIP}}}{R_{\mathrm{N}}} \quad , \tag{5.22c}$$

$$c = \frac{4\cos^2\alpha}{v^2} \quad . \tag{5.22d}$$

Depending on the choice of the auxiliary medium, i.e. whether the time-shifted or the velocity-shifted version of the CRS operator is considered, the velocity v is either the effective velocity or the velocity near the surface (see Chapter 4). Consequently, again depending on the choice of the mechanism that accounts for heterogeneity, the wavefront attributes α, R_{NIP} and R_{N} represent either the actual surface measurements or effective quantities measured in the auxiliary medium of effective velocity. As mentioned before, the midpoint and half-offset slopes can be identified with the first-order finite-offset derivative matrix elements of the hyperbolic zero-offset CRS operator (5.21). They read

$$t_{10} = \frac{a\hat{t}_0 + (a^2 + b)\Delta x_m}{t_{00}} \quad , \tag{5.23a}$$

$$t_{01} = \frac{ch}{t_{00}} \quad . \tag{5.23b}$$

Since for the extrapolation from zero-offset to finite-offset, a successful zero-offset measurement is provided, the midpoint displacement Δx_m is not needed and can be set to zero. This is equivalent to choosing (x_0, h_0), where x_0 is the reference midpoint and h_0 represents a constant finite reference half-offset, which defines the extrapolation distance (compare Figure 5.5(a)). Consequently, the extrapolated reference time t_0^{FO} and midpoint and half-offset slopes p_m and p_h read

$$t_0^{\mathrm{FO}} = t_{00}(x_0, h_0) = t_0 + \sqrt{\hat{t}_0 + ch_0^2} - \hat{t}_0 \quad , \tag{5.24a}$$

$$p_m = t_{10}(x_0, h_0) = a\frac{\hat{t}_0}{t_0^{\mathrm{FO}}} \quad , \tag{5.24b}$$

$$p_h = t_{01}(x_0, h_0) = \frac{ch_0}{t_0^{\mathrm{FO}}} \quad . \tag{5.24c}$$

It is of course obvious, that for complex media, where as argued above straight ray geometry in the auxiliary medium is not fully capable of describing the true wave propagation with high accuracy, the extrapolation distance h_0 should not be chosen too large. It should in general lie within a vicinity of the zero-offset location, in which

[10] Often, stereotomography is also referred to as *slope tomography*.

the respective zero-offset operator used for extrapolation is known to be sufficiently accurate[11]. The physically meaningful source and receiver slopes p_s and p_g can be easily derived from (see, e.g., Lavaud et al., 2004)

$$p_s = \frac{1}{2}\left(p_h - p_m\right) \quad , \tag{5.25a}$$

$$p_g = \frac{1}{2}\left(p_h + p_m\right) \quad , \tag{5.25b}$$

which, together with expressions (5.24) result in the same extrapolation equations Vanelle et al. (2014) found for the hyperbolic CRS operator. The second-order finite-offset derivative matrix elements, which can be used to arrive at second-order finite-offset extrapolation expressions can be found in Appendix C. In Chapter 6 I demonstrate that the slope extrapolation, even for complex subsurface configurations, can serve as a reasonable starting point for efficient local finite-offset refinement (see Figure 5.5(b)).

Multifocusing extrapolation

Similarly, the nonhyperbolic multifocusing moveout (Gelchinsky et al., 1999) can be used to predict finite-offset traveltimes and attributes from zero-offset measurements. Due to its high accuracy for diffractions, in contrast to hyperbolic CRS, the multifocusing-based extrapolation should yield higher quality for highly curved subsurface structures. The multifocusing approximation can, in accordance with the convenient matrix notation introduced in Section 5.1, be expressed as a sum of a source and a receiver contribution,

$$t_{00} = t_0 + \frac{S_{00} - s_{00}}{v} + \frac{G_{00} - g_{00}}{v} \quad , \tag{5.26}$$

where

$$S_{00} = \sqrt{(\Delta x_s + s_{00}\sin\alpha)^2 + s_{00}^2\cos^2\alpha} \quad , \tag{5.27a}$$

$$G_{00} = \sqrt{(\Delta x_g + g_{00}\sin\alpha)^2 + g_{00}^2\cos^2\alpha} \tag{5.27b}$$

are the focusing wavefronts observed at the source and the receiver position, respectively. The corresponding source and receiver focusing wavefronts, observed at the reference midpoint location x_0 generally depend on the acquisition coordinates and thus are also expressed in the form of derivative matrices,

$$s_{00} = \frac{1 - \phi_{00}}{K_{\mathrm{N}} - \phi_{00}K_{\mathrm{NIP}}} \quad , \tag{5.28a}$$

$$g_{00} = \frac{1 + \phi_{00}}{K_{\mathrm{N}} + \phi_{00}K_{\mathrm{NIP}}} \quad , \tag{5.28b}$$

with $K_{\mathrm{NIP}} = 1/R_{\mathrm{NIP}}$ and $K_{\mathrm{N}} = 1/R_{\mathrm{N}}$. Since the focusing parameter, similar to the focusing wavefronts is a function of the midpoint and half-offset coordinates, taking the derivative of the focusing wavefront curvatures also implies taking the derivative of the focusing parameter, which was shown to be expressed as

$$\phi_{00} = \frac{\Delta x_s - \Delta x_g}{\Delta x_s + \Delta x_g + 2K_{\mathrm{NIP}}\sin\alpha\Delta x_s\Delta x_g} \quad . \tag{5.29}$$

[11] More details on the validity and accuracy of the CRS slope extrapolation scheme and results of actual data application can be found in Chapter 6.

So in comparison with the diffraction case and the hyperbolic CRS operator, the multifocusing moveout, due to the underlying formalism of a wavefront focusing at the intersection point of a zero-offset and a finite-offset ray, reveals a generally strong coupling of the acquisition coordinates. As a consequence, the formulation of the derivative matrix $\underline{\mathbf{T}}_{mh}$ also invokes the construction of the derivative matrices $\underline{\mathbf{s}}_{mh}$, $\underline{\mathbf{g}}_{mh}$ and $\underline{\phi}_{mh}$.

The main goal of this part of the thesis, as mentioned before, is the formulation of extrapolation operators, which predict finite-offset attributes from zero-offset information. Since the finite-offset coefficient extrapolators are generally cumbersome to derive, I hereby again confine myself to zeroth and first orders, i.e. slope information. Due to the fact that expressions become quite lengthy, I present the derivatives of the different constituting matrices, like i.e. the focusing wavefront or the focusing parameter matrix, separately. For traveltime extrapolation, like it is used in the partial CRS stack (Baykulov and Gajewski, 2009), expression (5.26) is already sufficient. In order to extract first-order attributes from the zero-offset multifocusing moveout, the respective derivative matrix elements have to be considered,

$$t_{10} = \frac{1}{v}\left(S_{10} - s_{10} + G_{10} - g_{10}\right) \quad , \tag{5.30}$$

$$t_{01} = \frac{1}{v}\left(S_{01} - s_{01} + G_{01} - g_{01}\right) \quad . \tag{5.31}$$

As pointed out in Section 3.3, the multifocusing formula describes the traveltime response resulting from a wavefront which appears to originate from a virtual seismic source located at the intersection point of the zero-offset reference and the respective finite-offset ray. So, in consequence, the traveltime derivative matrix elements of first order can only be established, if the respective derivatives of the focusing wavefronts, observed at the central midpoint x_0 are known. The focusing wavefront determining the traveltime moveout at the source, i.e. its observation at the source position has the following derivatives (see also Appendix C)

$$S_{10} = \frac{(\Delta x_s + s_{00}\sin\alpha)(1 + s_{10}\sin\alpha) + s_{00}s_{10}\cos^2\alpha}{S_{00}} \quad , \tag{5.32}$$

$$S_{01} = \frac{(\Delta x_s + s_{00}\sin\alpha)(s_{01}\sin\alpha - 1) + s_{00}s_{01}\cos^2\alpha}{S_{00}} \quad . \tag{5.33}$$

The observation of the focusing wave emerging at the receiver position, in turn complements the source observation. Thus, the derivatives of the wavefront observed at the receiver take the very similar form

$$G_{10} = \frac{(\Delta x_g + g_{00}\sin\alpha)(1 + g_{10}\sin\alpha) + g_{00}g_{10}\cos^2\alpha}{G_{00}} \quad , \tag{5.34}$$

$$G_{01} = \frac{(\Delta x_g + g_{00}\sin\alpha)(1 + g_{01}\sin\alpha) + g_{00}g_{01}\cos^2\alpha}{G_{00}} \quad . \tag{5.35}$$

Both, the source and the receiver observation are linked via the respective focusing wave observations at the common central midpoint x_0. Due to the coinciding measurement location, these two wavefronts can be related to the wavefronts of the NIP and the normal wave[12]. The derivatives for the source-related wavefront at the central midpoint

[12]Following from zero-order ray theory or just from simple geometry, see Chapter 3.

location read

$$s_{10} = \frac{\phi_{10}(K_{\text{NIP}} - K_{\text{N}})}{(K_{\text{N}} - \phi_{00}K_{\text{NIP}})^2} \quad , \tag{5.36}$$

$$s_{01} = \frac{\phi_{01}(K_{\text{NIP}} - K_{\text{N}})}{(K_{\text{N}} - \phi_{00}K_{\text{NIP}})^2} \quad . \tag{5.37}$$

The corresponding receiver-related measurement at the central midpoint location, again, due to reciprocity and in order to complement the source related wavefront, has a very similar form

$$g_{10} = \frac{\phi_{10}(K_{\text{N}} - K_{\text{NIP}})}{(K_{\text{N}} + \phi_{00}K_{\text{NIP}})^2} \quad , \tag{5.38}$$

$$g_{01} = \frac{\phi_{01}(K_{\text{N}} - K_{\text{NIP}})}{(K_{\text{N}} + \phi_{00}K_{\text{NIP}})^2} \quad . \tag{5.39}$$

The focusing parameter connecting these two zero-offset measurements of the focusing wave can also be expanded up to first order and the respective derivatives read

$$\phi_{10} = -\frac{2\phi_{00}^2[1 + K_{\text{NIP}} \sin\alpha(\Delta x_s + \Delta x_g)]}{\Delta x_s - \Delta x_g} \quad , \tag{5.40}$$

$$\phi_{01} = -\frac{2\phi_{00}[1 + K_{\text{NIP}} \sin\alpha\phi_{00}(\Delta x_s - \Delta x_g)]}{\Delta x_s - \Delta x_g} \quad . \tag{5.41}$$

In conclusion, the multifocusing-based expressions for extrapolation from zero-offset to a finite offset h_0 can, like for the hyperbolic CRS operator, be gained by inserting $x_s^0 = x_0 - h_0$ and $x_g^0 = x_0 + h_0$ into the equations presented above. In full accordance with the CRS extrapolation scheme, $t_{00}(x_0, h_0)$ represents the finite-offset reference traveltime and $t_{10}(x_0, h_0)$ and $t_{01}(x_0, h_0)$ are the finite-offset midpoint and half-offset slopes, respectively. Again, the physically meaningful source and receiver slopes can be gained applying transformations (5.25). Please note that, like for CRS, also the second-order mutifocusing extrapolation equations are available and can be found in Appendix C.

Implicit CRS extrapolation

Extrapolation based on the implicit CRS moveout, like for the case of multifocusing, usually invokes more complicated derivations, which is a result of the generally more subtle and nested coupling of the source and receiver contributions in the operator. Similar to multifocusing, the implicit CRS expression can be described by two wavefront measurements, which, for the general case of a finitely curved target reflector, are related to each other by geometry. In both cases, the traveltime response is described by the observation of two wavefronts, one emerging at the source, the other at the receiver position

$$t_{00} = t_0 + \frac{S_{00} + G_{00}}{v} - \frac{2R_{\text{NIP}}}{v} \quad . \tag{5.42}$$

While the focus of the multifocusing wavefronts lies at the intersection point of the zero-offset and the finite-offset ray, the implicit CRS wavefronts are thought to be initiated at the finite-offset reflection point. Depending on the choice of the auxiliary medium, like stated before, the v either represents an effective velocity or the velocity near the surface, which in turn means that the attributes of the NIP and the normal wave

correspond to effective measurements, compensating the reference traveltime or they represent the actual true measurements, when a time-shift is applied. The finite-offset reflection point wavefront radii S_{00} and G_{00} can be parametrized by the corresponding reflection point coordinates x_{00} and z_{00}, which generally depend on the source receiver or midpoint half-offset coordinates. In terms of the reflection point coordinates they read

$$S_{00} = \sqrt{(\Delta x_s - x_{00})^2 + z_{00}^2} \quad , \tag{5.43a}$$

$$G_{00} = \sqrt{(\Delta x_g - x_{00})^2 + z_{00}^2} \quad . \tag{5.43b}$$

The first-order derivatives of the traveltime can thus be expressed via $t_{ij} = (S_{ij}+G_{ij})/v$. Like for the multifocusing moveout, the source and receiver wavefront measurements of the finite-offset reflection point wave are generally coupled via the reflection point coordinates, which consequently should be also expressed in the derivative matrix notation

$$x_{00} = x_0 - R_{\mathrm{N}} \sin\alpha + (R_{\mathrm{N}} - R_{\mathrm{NIP}})\sigma_{00} \quad , \tag{5.44a}$$

$$z_{00} = R_{\mathrm{N}} \cos\alpha - (R_{\mathrm{N}} - R_{\mathrm{NIP}})\gamma_{00} \quad . \tag{5.44b}$$

To maintain clarity in the exposition and to prevent unnecessary confusion following from the repeated application of trigonometric identities, the sine (denoted by σ_{00}), the cosine (abbreviated with γ_{00}) and the tangent (λ_{00}) of the reflection point angle θ (compare Figure 3.8) are also defined in derivative matrix notation,

$$\sigma_{00} = [\sin\theta]_{00} = \lambda_{00}\gamma_{00} \quad , \tag{5.45a}$$

$$\gamma_{00} = [\cos\theta]_{00} = (1 + \lambda_{00}^2)^{-\frac{1}{2}} \quad , \tag{5.45b}$$

$$\lambda_{00} = [\tan\theta]_{00} = \frac{\Delta x_m + R_{\mathrm{N}} \sin\alpha}{R_{\mathrm{N}} \cos\alpha} + \frac{h}{R_{\mathrm{N}} \cos\alpha} \frac{S_{00} - G_{00}}{S_{00} + G_{00}}. \tag{5.45c}$$

With $\Delta x_{00} = x_{00} - x_0$, the source wavefront derivative matrix components can be expressed as follows

$$S_{10} = \frac{(\Delta x_s - \Delta x_{00})(1 - x_{10}) + z_{00} z_{10}}{S_{00}} \quad , \tag{5.46a}$$

$$S_{01} = \frac{(\Delta x_s - \Delta x_{00})(-1 - x_{01}) + z_{00} z_{01}}{S_{00}} \quad . \tag{5.46b}$$

The corresponding reflection point wave curvature, as it is observed at the receiver position, has the following first-order derivatives

$$G_{10} = \frac{(\Delta x_g - \Delta x_{00})(1 - x_{10}) + z_{00} z_{10}}{G_{00}} \quad , \tag{5.47a}$$

$$G_{01} = \frac{(\Delta x_g - \Delta x_{00})(1 - x_{01}) + z_{00} z_{01}}{G_{00}} \quad . \tag{5.47b}$$

As can be observed in equations (5.44), the finite-offset reflection point derivatives are directly proportional to the derivatives of the sine and the cosine of the reflection point angle, i.e. σ_{ij} and γ_{ij}. The corresponding relationships read

$$x_{ij} = (R_{\mathrm{N}} - R_{\mathrm{NIP}})\sigma_{ij} \quad , \tag{5.48a}$$

$$z_{ij} = -(R_{\mathrm{N}} - R_{\mathrm{NIP}})\gamma_{ij} \quad . \tag{5.48b}$$

The respective elements of the matrix $\underline{\sigma}_{mh}$ containing the finite-offset midpoint and half-offset derivatives of the sine of the reflection point angle are

$$\sigma_{10} = \lambda_{10}\gamma_{00} + \lambda_{00}\gamma_{10} \quad , \tag{5.49a}$$

$$\sigma_{01} = \lambda_{01}\gamma_{00} + \lambda_{00}\gamma_{01} \quad . \tag{5.49b}$$

The respective derivatives of the cosine of the reflection point angle, in accordance, also need to be known up to first order. They read

$$\gamma_{10} = -\lambda_{00}\lambda_{10}\gamma_{00}^3 \quad , \tag{5.50a}$$

$$\gamma_{01} = -\lambda_{00}\lambda_{01}\gamma_{00}^3 \quad . \tag{5.50b}$$

Vanelle et al. (2010) chose a geometrically intuitive tangent relation (see also Chapter 3) to implicitly evaluate the angle parametrizing the reflection point on a circular interface with a local curvature radius of $R_{\mathrm{N}} - R_{\mathrm{NIP}}$. Although a similar expression could also be derived for the sine or the cosine, the tangent expression proved to be useful in application (Schwarz et al., 2014c). The corresponding first order derivatives read

$$\lambda_{10} = \frac{1}{R_{\mathrm{N}}\cos\alpha}\left[1 + 2h\frac{S_{10}G_{00} - S_{00}G_{10}}{(S_{00}+G_{00})^2}\right] \quad , \tag{5.51a}$$

$$\lambda_{01} = \frac{1}{R_{\mathrm{N}}\cos\alpha}\left[\frac{S_{00}-G_{00}}{S_{00}+G_{00}} + 2h\frac{S_{01}G_{00} - S_{00}G_{01}}{(S_{00}+G_{00})^2}\right] \quad . \tag{5.51b}$$

Like before, $t_{00}(x_0, h_0)$ corresponds to the extrapolated finite-offset reference time t_0^{FO} and the midpoint and half-offset slopes p_m and p_h are equal to $t_{10}(x_0, h_0)$ and $t_{01}(x_0, h_0)$, respectively. Also, like for CRS and multifocusing, the extrapolated source and receiver slopes can be gained via the relations (5.25). The corresponding second-order derivative matrix elements, which can be used for the prediction of finite-offset second-order attributes, can likewise be found in Appendix C.

Geometry and multiple rays

In the previous subsection I derived extrapolation relations, which can be used to predict finite-offset traveltime slopes from zero-offset measurements. While for the hyperbolic CRS operator, the extrapolators (5.24) are relatively simple expressions, which are straight-forward to comprehend, the corresponding first-order extrapolation relations of multifocusing and the implict CRS are significantly more complex and, due to the nested nature of the coupling of the source and receiver contributions, not straight forward to derive[13]. In a way it can be argued that the presented strategy of extrapolation via the finite-offset derivative matrices is closer related to the ray approach of paraxial ray theory, where traveltimes and their derivatives, rather than the geometry of circular wavefronts, which is generally favoured in the frame of this thesis, are considered.

Consequently, I intend to show in this subsection that the desired physically meaningful finite-offset slopes at source and receiver can also be derived directly from geometry. In the circular wavefront picture, which is connected to the validity of the straight-ray description in the auxiliary medium, traveltimes are replaced by the curvature radii of conceptual waves. Thus, in an auxiliary medium of constant velocity, the traveltimes

[13]This holds in particular for the higher-order derivatives, presented in Appendix C.

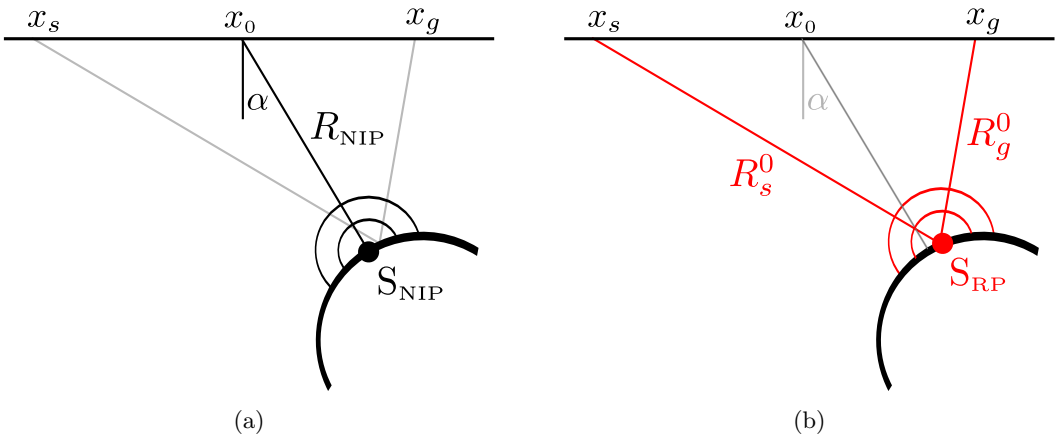

Figure 5.6.: The implicit CRS moveout aims at finding the reflection point on a circular interface (Vanelle et al., 2010; Schwarz, 2011). Utilizing the virtual source interpretation introduced in Chapter 2 and Chapter 3, the finite-offset reflection point traveltime can be approximated by the zero-offset reflection point location, expressed by the NIP wave parameters α and R_{NIP} and the finite-offset reflection point characterized by the RP wave curvatures R_s and R_g. The quantity $R_{\text{N}} - R_{\text{NIP}}$ defines the local reflector curvature in the auxiliary medium and connects the zero-offset and the finite-offset measurements.

can be expressed with the travel distances corresponding to the wavefront radii, divided by the constant auxiliary medium velocity. Following from the simple triangle geometry of the implicit CRS moveout (see Figure 3.9), the emergence angle at source and receiver can generally be determined, if the reflection point in the auxiliary medium is known. For the implicit CRS, according to Figure 3.9, we have[14]

$$p_s = \frac{\cos(90^\circ - \alpha_s)}{v} = \frac{\sin\alpha_s}{v} = \frac{x_0 - h_0 - x_{\text{RP}}(x_0, h_0)}{vR_s(x_0, h_0)} \quad , \tag{5.52a}$$

$$p_g = \frac{\cos(90^\circ - \alpha_g)}{v} = \frac{\sin\alpha_g}{v} = \frac{x_0 + h_0 - x_{\text{RP}}(x_0, h_0)}{vR_g(x_0, h_0)} \quad . \tag{5.52b}$$

In case the actual medium is homogeneous the geometrically derived operators, depending on the generality of the reflector shape, for which they were derived, the corresponding expressions lead to highly accurate source and receiver angles even for very large offsets, emphasizing the true global character of these approaches for that case. As mentioned before, even for moderate heterogeneity, which is supposed to be most pronounced in the vertical direction, the wave propagation can often still be successfully described in an auxiliary medium of constant velocity. Expressions (5.52) are quite universal and can also be formulated for e.g. multifocusing, where the lateral reflection point coordinate x_{RP} in (5.52) is replaced by the respective lateral coordinates of the focusing point x_{FP} and its virtual image x^*_{FP}. In the final part of this thesis, I will show that even for field data application, the much simpler geometrical slope extrapolators (5.52) have the same accuracy as their considerably more complicated derivative-based counterparts formulated in the previous subsection.

[14]Since no derivatives but pure geometry is considered in this frame, I returned from the matrix notation to the conventional notation, which was used in Chapter 3.

Inspired by the generalized moveout approximation of Fomel and Stovas (2010) and following this geometrical path for the extrapolation of traveltimes and attributes, I suggest a hybrid approach to characterize traveltimes globally, by combining zero-offset and finite-offset measurements. The implicit CRS operator appears very suited for this purpose, because it is based on determining the respective reflection point for every offset in the considered range. As motivated earlier, it can be argued that geometrically derived moveout expressions, which are formulated in terms of a source and a receiver-related wavefront measurement (i.e. of double-square-root type), can, in principle, be formulated for an arbitrary finite-offset reference ray. In fact, Landa et al. (2014) showed that the multifocusing operator, being based on a source and a receiver-related measurement of the focusing wave, has exactly the same shape for the zero-offset and the finite-offset case.

The implict CRS moveout (Vanelle et al., 2010; Schwarz, 2011) is based on a circular reflector geometry, which can be expressed very conveniently by normal-ray-related wavefront measurements, i.e. of the normal and the NIP wave. The finite-offset reflection point is parametrized by the circle's radius $R_{\mathrm{N}} - R_{\mathrm{NIP}}$ and the reflection point angle θ, which in general is an implicit expression (see Chapter 3). For a fixed finite-offset but variable midpoint displacement, the tangent of θ reads

$$\tan\theta(\Delta x_m, h_0) = \tan\alpha + \frac{\Delta x_m}{R_{\mathrm{N}}\cos\alpha} + \frac{h_0}{R_{\mathrm{N}}\cos\alpha}\frac{R_s^0 - R_g^0}{R_s^0 + R_g^0} \quad , \tag{5.53}$$

where $R_s^0 = R_s(x_0, h_0)$ and $R_g^0 = R_g(x_0, h_0)$ correspond to the fixed source and receiver contributions calculated with the zero-offset implicit CRS operator. In the wavefront picture (see Figure 5.6), as mentioned before, these source and receiver contributions of the implicit CRS moveout can be interpreted as source and receiver measurements of fictitious wavefronts which seem to originate at a virtual source located at the finite-offset reflection point defined by θ. Vanelle et al. (2010) suggested to set $h_0 = 0$ in equation (5.53) to arrive at a starting guess for the finite-offset reflection point angle and to refine iteratively by using the same expression with $h_0 \neq 0$. Following this procedure we can calculate the finite-offset reflection point wave curvatures from zero-offset measurements. Here, I propose to use these extrapolated finite-offset wavefront curvatures to express the angle update formula in terms of the finite-offset deviation $\Delta h = h - h_0$ by incorporating the finite-offset solution (5.53). As a result we get the following hybrid expression

$$\begin{aligned}\tan\theta(\Delta x_m, \Delta h) = \tan\theta(\Delta x_m, h_0) &+ \frac{\Delta h}{R_{\mathrm{N}}\cos\alpha}\frac{R_s - R_g}{R_s + R_g} \\ &+ \frac{2h_0}{R_{\mathrm{N}}\cos\alpha}\frac{R_s R_g^0 - R_s^0 R_g}{(R_s + R_g)(R_s^0 + R_g^0)} \quad ,\end{aligned} \tag{5.54}$$

which contains the three zero-offset attributes α, R_{NIP} and R_{N} and the constant finite-offset curvatures R_s^0 and R_g^0. Since $\tan\theta(\Delta x_m)$ for given R_s^0 and R_g^0 is an explicit expression, it can serve as the finite-offset starting guess. Although formula (5.54) appears more complicated than the zero-offset version, it is provided with a better starting guess that incorporates attributes of a zero-offset and a finite-offset ray. The implicit CRS operator itself, in accordance, can be written as a hybrid expression

$$t(\alpha, R_{\mathrm{NIP}}, R_{\mathrm{N}}, R_s^0, R_g^0) = t_0 + \frac{R_s + R_g}{v} - \frac{R_s^0 + R_g^0}{v} \quad . \tag{5.55}$$

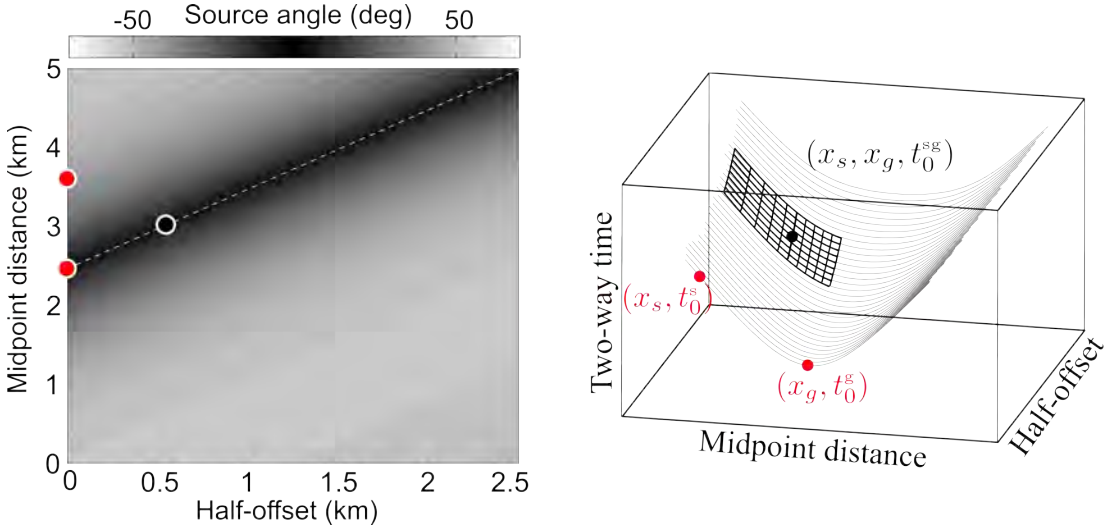

Figure 5.7.: Due to the decoupling of source and receiver traveltime information for diffractions, the true finite-offset response (indicated by a black dot) can be decomposed into two zero-offset responses at the corresponding source and receiver locations (shown in red). Bauer (2014) showed that this decomposition scheme in turn allows for powerful applications, like i.e. the prediction of true prestack traveltimes entirely based on zero-offset measurements.

The finite-offset reference attributes R_s^0 and R_g^0 can be forward-calculated using the zero-offset operator but have a physical meaning for the finite-offset case. Therefore I argue, that the hybrid finite-offset implicit CRS formulation (5.55) can be used as a multi-ray approximation, in which R_s^0 and R_g^0 can be treated as additional degrees of freedom, which can be refined to achieve a better finite-offset fit. Interestingly, like for the finite offset CRS approach by Zhang et al. (2001), this operator, as a consequence, has also a total of six degrees of freedom, which is formally consistent with the findings made in Section 5.3.

Diffraction decomposition

With the help of the derivative matrix formalism I formally revealed in Section 5.4 that for diffractions, zero-offset and finite-offset source and receiver wavefront measurements are equivalent. I found that, since on the one hand all uneven-ordered terms in the fourth-order zero-offset midpoint half-offset derivative matrix $\underline{\mathbf{T}}_{mh}$ vanish and on the other hand all non-vanishing matrix elements of the same order coincide with each other, one can conclude that the source and the receiver contributions are of the same magnitude but have alternating sign for uneven orders in h. This means that all the necessary information is contained in the pure midpoint derivatives, representing the moveout in the zero-offset section. By comparing the zero-offset equation (3.27), for which, like in the finite-offset case, the coordinates are not coupled by Snell's law, with

the finite-offset CRP formula (5.14), we arrive at the following important identity

$$t_{sg} = \frac{1}{2}\left(t_0^s + 2\frac{\sqrt{(R_{\text{NIP}}^s)^2 + 2R_{\text{NIP}}^s \Delta x_s \sin\alpha_0^s + \Delta x_s^2} - R_{\text{NIP}}^s}{v_0^s}\right) + \frac{1}{2}\left(t_0^g + 2\frac{\sqrt{(R_{\text{NIP}}^g)^2 + 2R_{\text{NIP}}^g \Delta x_g \sin\alpha_0^g + \Delta x_g^2} - R_{\text{NIP}}^g}{v_0^g}\right), \tag{5.56}$$

where t_{sg} is the finite-offset traveltime and the superscripts s and g denote the results of the preceding zero-offset measurement carried out at the current receiver position. According to equation (5.56) and the sketch in Figure 5.7, we have, in the circular wavefront picture, the following set of identities

$$t_0^{sg} = \frac{t_0^s + t_0^g}{2} \quad , \tag{5.57a}$$

$$\alpha_s = \alpha_0^s \quad , \tag{5.57b}$$

$$\alpha_g = \alpha_0^g \quad , \tag{5.57c}$$

$$R_s = R_{\text{NIP}}^s \quad , \tag{5.57d}$$

$$R_g = R_{\text{NIP}}^g \quad , \tag{5.57e}$$

which uniquely and globally defines the traveltime response of a diffraction. Thus, (5.56) governs a striking connection of zero-offset and finite-offset information for diffractions, which, as a result of the full decoupling of the source and the receiver moveout and symmetries in the common source (CS) and common receiver (CR) gathers, respectively, opens up exciting possibilities for potential applications. In conclusion, zero-offset and finite-offset information is highly redundant for diffractions and zero-offset traveltime operators at a source and a receiver may be decomposed to accurate finite-offset operators (see Figure 5.7). Please note at this point that this decomposition of traveltimes is formally exact for diffractions, whereas for reflections, extrapolation based on a single operator and subsequent optimization is required.

6. Applications

In the cause of the derivations, which were carried out in the first five chapters of this thesis, interesting symmetries, correspondences and dualities were revealed, which provide a unified view on presently used traveltime moveout approximations. Being based on simple aspects of geometry only, the derivations did not rely on conventional ray theory, which to the inexperienced observer can appear less comprehensible. This chapter in turn is fully dedicated to potential applications following from the revealed symmetries and dualities. Traveltime moveout, in principle, can be of interest in many fields of processing, however, its central role for the coherent summation of traces is obvious. Therefore, in the first section of this chapter, I will briefly review the general concept of stacking and comment on different fields of its applications. Details on the respective datasets and used codes and processing parameters can be found in Appendix E and Appendix F.

6.1. Stacking as a tool

Stacking still plays a fundamental role in seismic data processing. While the summation itself helps to decrease data redundancy and leads to a first interpretable time image with a high signal-to-noise ratio, the estimated parameters form the foundation of many important subsequent processing steps, including depth imaging. In contrast to the classical NMO/DMO approach (Mayne, 1962; Deregowski, 1986), recent works have indicated that even for complex settings, a macro-velocity model is not needed to perform all important time imaging tasks (e.g., Mann, 2002).

In integral notation (e.g., Fomel and Kazinnik, 2013), the classical CMP stack, first formulated by Mayne (1962), can be written as

$$A(x_0, t_0) = \int a(x_0, h, t_0 + \Delta t)\mathrm{d}h \quad , \tag{6.1}$$

where a is the respective amplitude at the offset h and $\Delta t(h)$ is the moveout of the CMP hyperbola (3.5). The stacked amplitude, resulting from the coherent summation along h, is denoted by A. Although a vertical stack, i.e. in a time window δt around $t_0 + \Delta t$ is also involved in current implementations, the respective integral is omitted here to keep things brief and concise[1]. For the CMP case, as expressed in (6.1), the summation is carried out over a trajectory in a subset of the full prestack volume.

In the CRS stack (Jäger et al., 2001; Mann, 2002) this concept is extended to a range of several CMPs around the central midpoint location x_0, parametrized by the midpoint displacement Δx_m (compare Figure 3.3). The corresponding summation operator, according to the previous notation, reads

$$A(x_0, t_0) = \int\int a(x_0 + \Delta x_m, h, t_0 + \Delta t)\mathrm{d}x_m\,\mathrm{d}h \quad , \tag{6.2}$$

[1] The width of this window δt is usually comparable to the expected mean period of the signal (e.g., Yilmaz, 2001).

i.e. in this case the stack of amplitudes is performed along a moveout surface, commonly defined by the hyperbolic CRS expression (3.19) (Jäger et al., 2001). The construct (6.2) turns out to be very flexible, since, logistically, it governs the midpoint half-offset coupling of the CRP trajectories (Höcht et al., 1999), the classical CMP stack (6.1), and, in addition also the surface-wise summation of Kirchhoff-type prestack time migration (e.g., Yilmaz, 2001; Spinner, 2006). Since, however, the higher-order analysis presented in Chapter 5 revealed a lack of higher-order coupling, which was found to be needed for an accurate description of diffraction traveltimes, I argue that the diffraction subset of the implicit CRS or multifocusing[2] are a more appropriate choice to perform the task of prestack time migration. In fact, Bobsin (2014) presented a fully data-driven scheme for prestack time migration based on the double-square-root implicit CRS operator. In order to perform the task of time migration using (6.2), the respective operator needs to be parametrized in terms of the coordinates of the diffraction's apex,

$$x_a = x_0 - R_{\mathrm{NIP}} \sin\alpha \quad , \tag{6.3a}$$

$$t_a = t_0 + \frac{2R_{\mathrm{NIP}}}{v} \cos\alpha \quad , \tag{6.3b}$$

which, for the choice of an effective medium, i.e $v = v_{\mathrm{shift}}$ correspond to expressions found by Mann (2002) and Schwarz (2011). For the respective optical projection, i.e. the choice of the near-surface velocity $v = v_0$, the apex coordinates are equivalent to the apex definition by Keydar et al. (1990), Höcht et al. (1999) and Schwarz (2011). Accordingly, the Kirchhoff-type time migration can be written as

$$A(x_a, t_a) = \int\int a(x_a + \Delta x_m, h, t_a + \Delta t)\mathrm{d}x_m\,\mathrm{d}h, \tag{6.4}$$

where $\Delta x_m = x_m - x_a$ and Δt is the diffraction operator, expressed in terms of (x_a, t_a). The most general summation, however, is the one in the vicinity of a finite-offset ray defined by the triplet (x_0, h_0, t_0). The respective finite-offset CRS stack, consequently, reads

$$A(x_0, h_0, t_0) = \int\int a(x_0 + \Delta x_m, h_0 + \Delta h, t_0 + \Delta t)\mathrm{d}x_m\,\mathrm{d}h. \tag{6.5}$$

Please note that, logistically, this definition is exactly the same for the partial CRS stack suggested by Baykulov and Gajewski (2009), with the only difference that Δt in this case is a globally defined zero-offset operator, whereas for the generic finite-offset CRS stack, it is defined in terms of the true finite-offset attributes, which were actually measured at (x_0, h_0, t_0). At this point, I would like to stress the logistical importance of the work of Baykulov and Gajewski (2009), since it allows, under the assumption of globality (see Chapter 5), to perform coherent summation and summation-based migration in the full prestack volume or any subset of it, while only zero-offset measurements have to be performed.

The main benefit of coherent summation was already stressed by Mayne (1962) and can be identified with the increase of the signal-to-noise ratio. Traditionally, this meant that the process of stacking leads to a simulated zero-offset section, which exhibits a significantly decreased noise level, allowing for a better interpretation and depth-converted images of the subsurface. In the framework of the finite-offset CRS stack (Zhang et al.,

[2]For the diffraction case, we have $R_{\mathrm{N}} = R_{\mathrm{NIP}}$ and the multifocusing operator and the implicit CRS moveout reduce to exactly the same expression.

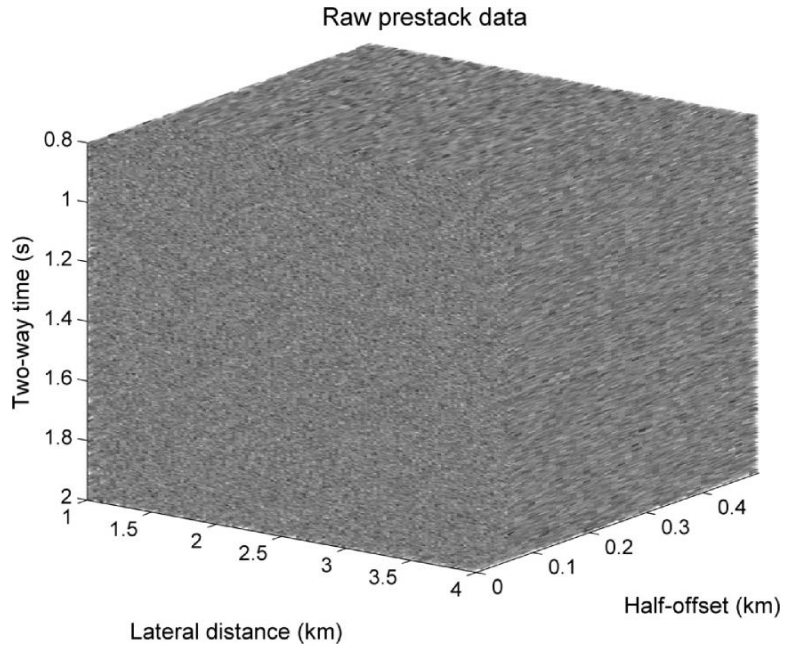

(a)

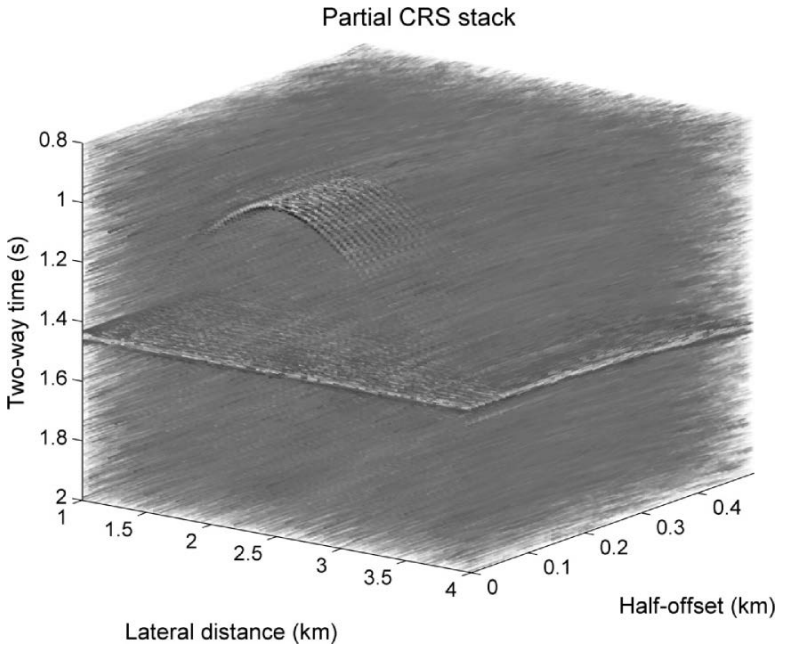

(b)

Figure 6.1.: Raw prestack data (a) and the corresponding partial CRS stack of the simple synthetic gradient dataset. The events are barely visible in the raw volume, whereas the CRS stack successfully improved the signal-to-noise ratio in the prestack data.

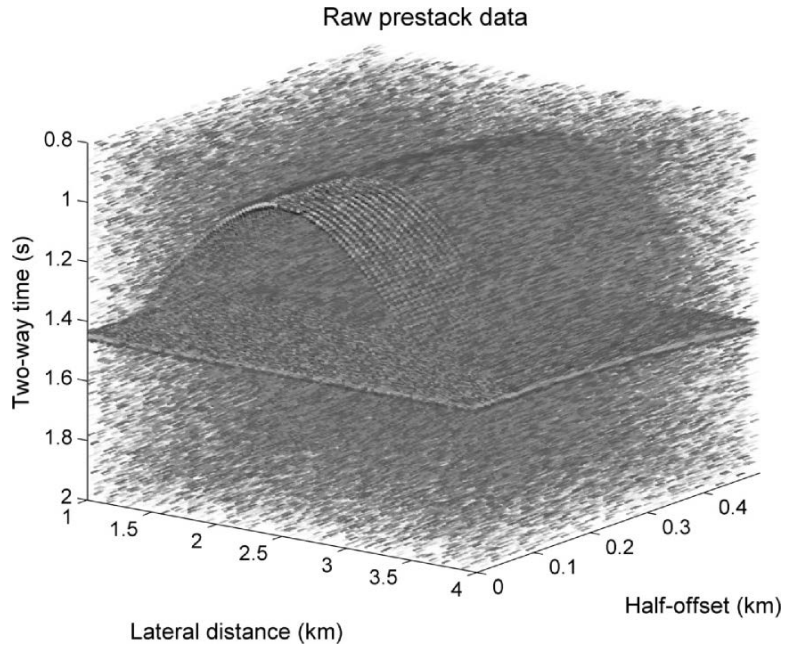

(a)

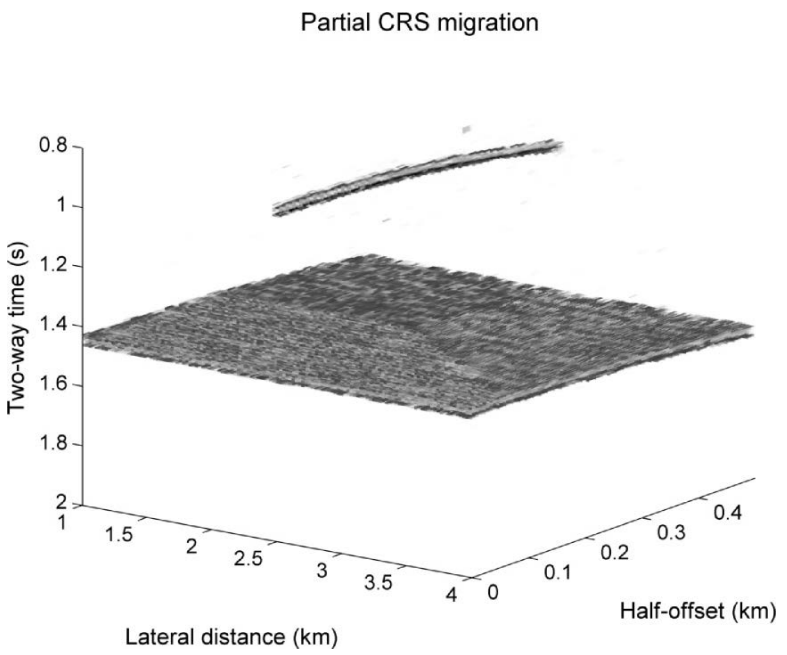

(b)

Figure 6.2.: Similar to the conventional stack, the CRS-based migration can also be performed partially in the prestack data. Due its inherent relation to the surface-based CRS stack, the Kirchhoff-type time migration also, as a by-product, leads to an increase in the signal-to-noise ratio.

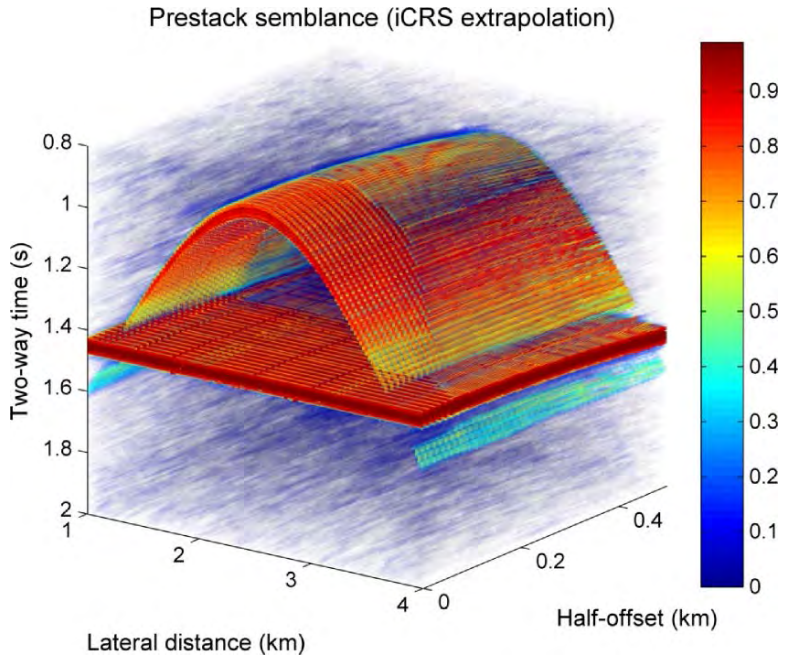

(a)

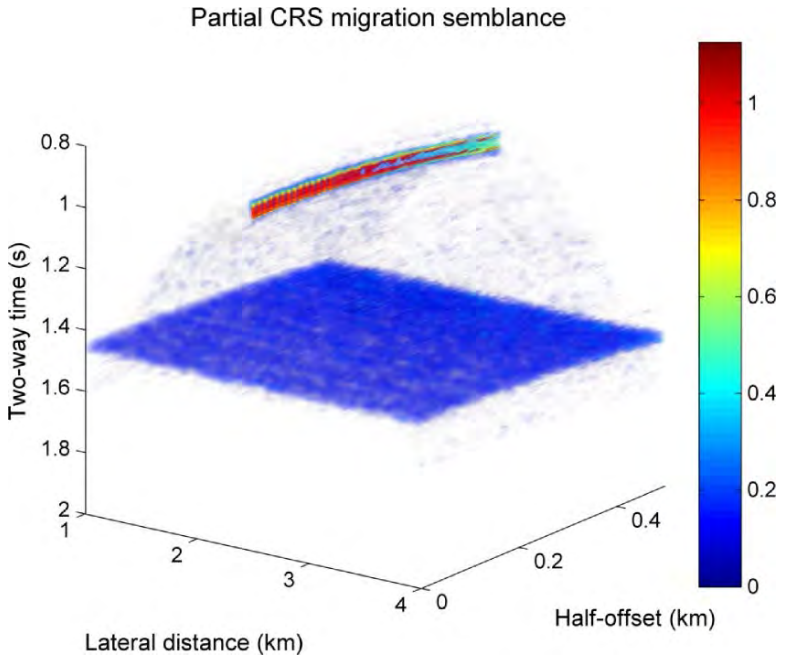

(b)

Figure 6.3.: Similar to conventional stack and migration, the partial CRS framework allows to compute the local semblance coefficient in the prestack data, which forms the basis for the powerful combination of zero-offset and finite-offset CRS processing.

2001) or the zero-offset-based partial CRS stack (Baykulov and Gajewski, 2009), this benefit can be extended to the prestack domain, because every trace in the full original prestack data can be enhanced (Baykulov and Gajewski, 2009). Figure 6.1(a) shows the prestack data volume generated for a simple vertical gradient model[3]. The signal-to-noise ratio is extremely low and no locally coherent event can be observed. Figure 6.1(b) on the other hand shows the respective data cube locally enhanced via the partial CRS approach by Baykulov and Gajewski (2009). The signal-to-noise ratio is noticeably increased and the coherent events corresponding to a planar reflector and a shallow point diffractor, became clearly visible (compare Figure E.1). Baykulov and Gajewski (2009) and Höcht et al. (2009) showed, that the summation operator (6.5) can also serve for trace interpolation and regularization.

Extending the CRS-based time migration approach of Spinner (2006) and Bobsin (2014), I suggest to also perform the task of partial time migration (Yilmaz, 2001; Dell and Gajewski, 2011) in the framework of the partial CRS stack. The resulting partial CRS time migration is, like the prestack analogue, applicable in a fully data-driven fashion, with all the benefits discussed by, e.g., Dell and Gajewski (2011). Figure 6.2(a) shows the simple data example used before the illustration of the noise suppression capabilities of the partial CRS method, in this case, for illustration purposes, with a slightly lower noise level applied. Figure 6.2(b) reveals that the suggested summation-based partial CRS migration not only leads to the desired focusing of the diffracted energy in the finite-offset sections, but that also, due to the summation approach, the noise level gets sufficiently reduced (Dell and Gajewski, 2011). In Section 6.4 I will demonstrate the applicability of the suggested partial CRS migration for a complex field dataset.

As argued, the partial CRS stack can be considered the most general approach to stacking. Due to the globality assumption and the surface-wise summation, which can be applied, in principle, to any reference trace in the prestack volume, it was shown to be even capable of performing partial time migration. Taner and Koehler (1969) found that the process of summation can also be used to formulate an objective function, which takes high values for locally coherent summation and low values if the summation is not coherent. The according semblance coefficient

$$S(x_0, h_0, t_0) = \frac{1}{n} \frac{A^2(x_0, h_0, t_0)}{\int\int a^2(x_0 + \Delta x_m, h_0 + \Delta h, t_0 + \Delta t) \mathrm{d}x_m \, \mathrm{d}h} \tag{6.6}$$

can be interpreted as the ratio of stacked energy, which is proportional to the square of the stacked amplitude A, defined according to (6.5), to the total energy in the considered portion of the wavefield[4]. As an objective measure of trust, the semblance coefficient (6.6), being formulated in terms of summation operations, can be used as a moveout measurement tool, thereby providing the important link to the theoretical arguments made in the chapters 2 - 5. Due to the globality assumption underlying the partial CRS logistics, the coherence of a zero-offset operator can be studied in detail for all offesets, by computing the partial CRS semblance coefficients for all offsets (see Figure 6.3(a)). Since it normalizes the coherent energy by the overall energy in the summation operator, the corresponding partial CRS time migration coherence reaches the highest values for diffractions, since time migration, in a sense, can likewise be

[3]Information on the model and the respective dataset can be found in the Appendix.
[4]The number of traces contributing to the coefficient is denoted by n.

interpreted as a virtual seismic source experiment (e.g., Yilmaz, 2001). Figure 6.3(b) shows the partial migration semblance for the simple synthetic gradient example. While the partial CRS migration coherence has reasonably high values for the diffraction, for all considered offsets, the values corresponding to the planar reflector are generally very small. Utilizing this separability of diffractions and reflections, I suggest an iterative partial demigration scheme for the partial migration coherence, whose output can be used as a prestack diffraction filter. In addition, the partial CRS coherence (6.6), as I will show in Section 6.3, can be utilized as an objective measure of globality, where high values indicate the validity of the zero-offset operator and, consequently, low values imply the requirement of local finite-offset refinement.

6.2. Multiple-operator analysis

In this section, I seek to systematically investigate the performance of the time shift and the velocity shift mechanism to account for overburden heterogeneity. To clearly emphasize the differences of the two faces of the suggested generalized operators and to motivate some potential applications of their simultaneous use, I confine myself to the comparison of the achieved semblance and the NIP wave attributes α and R_{NIP}, which will turn out to either efficiently characterize diffractions or velocity changes in the model. On the left side of Figure 6.4 the difference of the achieved semblance between the nonhyperbolic implicit CRS operator and the weakly coupled hyperbolic CRS moveout is displayed for the simple gradient example consisting of a planar reflector and a shallow diffractor[5]. One can see that the implicit CRS operator achieves considerably higher semblance values for the diffraction, whereas both operators, as expected from the higher-order analysis in Chapter 5, provide similar accuracy for the planar reflector. On the right side of Figure 6.4 the semblance difference between the velocity-shifted and the time-shifted implicit CRS operator is displayed. Similar to the previous comparison, both provide an equivalent fit for the planar reflector, while the flanks of the diffraction are very differently described. Similar observations can be made for the NIP wave's emergence angle α, whose difference sections can be found on the left and right side of Figure 6.5, respectively. Again, due to the insufficient coupling of the midpoint and half-offset contributions, the hyperbolic CRS estimates of α are noticeably different from the one obtained by application of the double-square-root implicit CRS operator, when the diffraction is considered. The same behaviour can be observed for the operator comparison displayed on the right side of Figure 6.5, where, except for the apex position, the angle estimates of the velocity shift mechanism differ noticeably from the time-shift-based values. Again, all operators coincide for the planar reflector.

The NIP wave radius estimate differences, presented in Figure 6.6, in turn, reveal a somewhat different tendency for the dual descriptions shown on the right side. In contrast to the findings for the coherence and the angle α, the NIP wave radius estimates of the velocity-shifted implicit CRS and the time-shifted implicit CRS are different for both, the diffraction and the reflection event, revealing the different nature of both approaches in heterogeneous media. In contrast to this, the comparison of the hyperbolic CRS operator and implicit CRS shown on the left reveals the same trend as for the other attributes, i.e. pronounced differences for the diffraction and vanishing deviations for the reflection. One can conclude from this simple synthetic study that the opera-

[5]For more information on the model I refer to Appendix E.1.

tor duality, introduced in Chapter 4, similar to the coordinate coupling characteristics revealed in Chapter 5 can be utilized to detect curvature and discriminate between diffractions and reflections.

On the other hand, the application of both faces of the implicit CRS operator in addition revealed that, in the presence of heterogeneity, even reflection events are differently described by both mechanisms. Figure 6.8, showing the respective attribute differences for the gradient and for constant velocity, suggests that the NIP wave radius difference section might be used to detect heterogeneity in the overburden. In Figure 6.7, the coherence difference between multifocusing, as it appears in the literature, and both versions of the implicit CRS moveout are displayed for the very same diffraction but different velocity gradients in the overburden. While for constant velocity, all three expressions perform equally well, the fundamental moveout duality for heterogeneity becomes increasingly obvious for non-vanishing and stronger gradients. Although this can be considered a simple example, it nevertheless can be viewed as convincing evidence of the unification of CRS and multifocusing, when the time shift mechanism is used to account for heterogeneity.

To ensure realistic circumstances and sufficient applicability of the preceding conclusions, I choose the complex BP 2004 velocity benchmark (Billette and Brandsberg-Dahl, 2005), since it contains all relevant geological features that can lead to higher-order effects in the traveltime moveout. Figure E.2 shows the BP model with its wide range of velocity gradients and complex features like a salt-body system on the left and shallow strong vertical velocity changes on its right. Resulting from the model, as can be observed in the top of Figure 6.9, the velocity-shifted stacked zero-offset section of the BP multi-coverage data shows very pronounced and complex diffraction patterns in the left part and strong surface-related multiple reflections in the right part. The bottom of Figure 6.9 shows the angle estimate difference of the two versions of the implicit CRS operator on the left and the corresponding deviations in R_{NIP} on the right. As can be inferred from these deviation patterns, the angle differences are only non-negligible for events stemming from highly curved structures like the complex rugged top-of-salt being present in the left side of the model, whereas differences in R_{NIP} seem to indicate the general presence and the strength of velocity variations in the overburden. Please note that the surface-related multiple reflections are not affected by velocity changes in the subsurface and can therefore be clearly distinguished from the primary reflections whose rays were exposed to the heterogeneity of the shallow layers in the model. Although not stressed here, simple quantitative studies on synthetic data indicated that velocity-shifted operators tend to estimate the CRS attributes more accurately than their time-shifted counterparts when the heterogeneity of the overburden increases (Schwarz, 2011).

Please observe in Figure 6.14, that the general findings for the simple gradient example can also be confirmed for the much more complex and realistic BP velocity benchmark dataset. Figures 6.10 - 6.13 show two closeups of Figure 6.9 (indicated by frames) for all three multi-parameter operators considered in this section. One can observe the strong systematics in the attribute deviations, which, for the case of the nonhyperbolic double-square-root operators of the implicit CRS and multifocusing, only show, when a time-shifted version is compared with an expression shifted in velocity and vice versa. The time-shifted face of the implicit CRS turns out to estimate the

attributes absolutely equivalently to the multifocusing formulation, which only appears in time-shifted notation in existing literature (Gelchinsky et al., 1999). In accordance, the estimate differences vanish, when we compare the effective medium version of the implicit CRS, which was suggested by Schwarz et al. (2014c), with the new effective medium (velocity-shifted) formulation of multifocusing. The same systematics also show for the hyperbolic CRS operator, indicating that the generalized operators have the potential to provide additional insight into the character and physical origin of a recorded event.

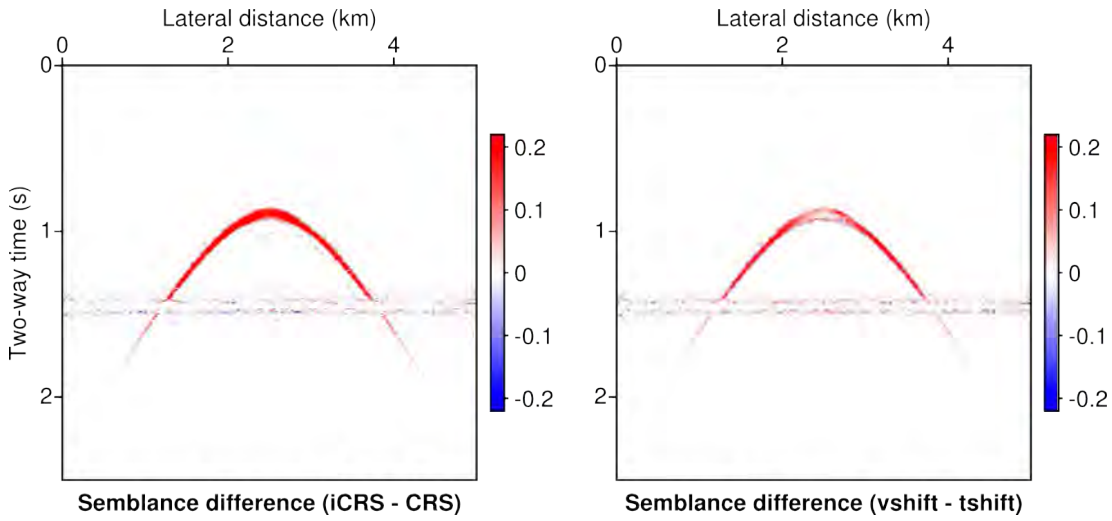

Figure 6.4.: Semblance difference for the simple synthetic test dataset consisting of a point diffractor and a planar horizontal reflector in a constant vertical velocity gradient medium. Due to the double-square-root character of the implicit CRS (iCRS) and the missing dependency of the CRS moveout on the normal wave radius R_{N} in the CMP gather, the differences are strongly visible for the diffraction, whereas they vanish for the low curvature event (left). As demonstrated in Chapter 4, each operator can account for heterogeneity in two different ways, by a shift in time or a shift in velocity (right), here shown for the implicit CRS.

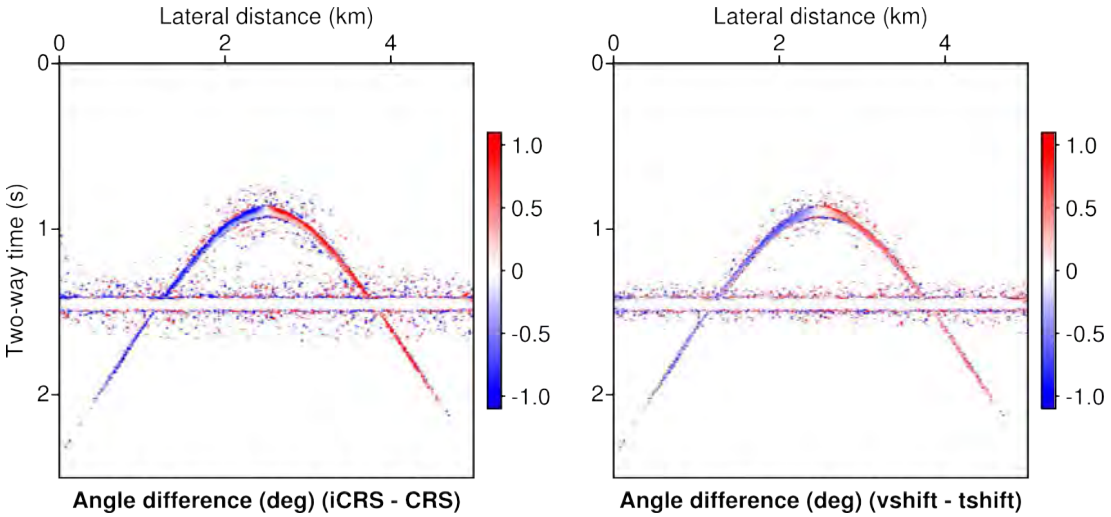

Figure 6.5.: Difference of the emergence angle estimate between double-square-root implicit CRS (iCRS) and hyperbolic CRS (left) and the corresponding difference for the two faces of the implicit CRS operator (right). In both cases, like for the semblance coefficient in Figure 6.4, the differences are only noticeable for the diffraction.

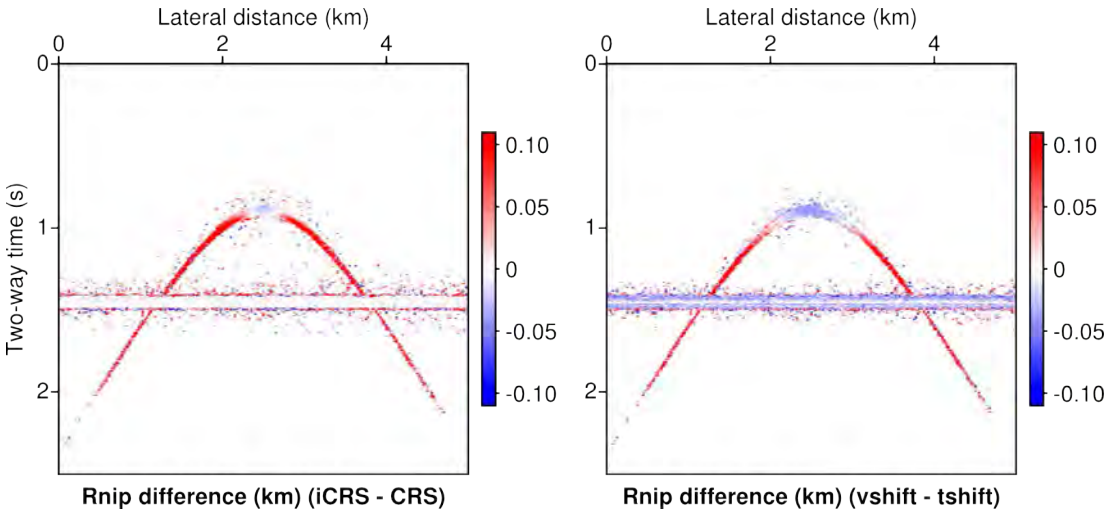

Figure 6.6.: Difference of the NIP wave radius measured with the implicit CRS (iCRS) and the CRS operator (left) and the corresponding deviations for the two representations of the implicit CRS operator (right). It is interesting to note that, while curvature is nicely distinguishable by the comparison of CRS and implicit CRS, the difference of R_{NIP} for the two faces of the implicit CRS operator for the reflection seems to indicate that heterogeneity is present in the overburden.

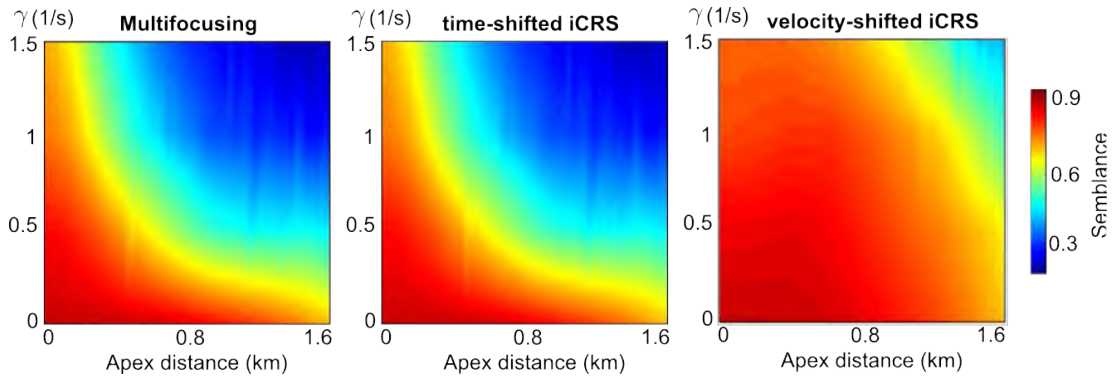

Figure 6.7.: Comparison of conventional (time-shifted) multifocusing (left) with the two faces of the implicit CRS (iCRS) operator for a diffraction in 1 km depth (compare model E.1) and varying strength of the background velocity gradient γ. Displayed is the best fit semblance coefficient for each operator as a function of lateral distance to the apex and γ.

Improved diffraction filters

As a result of the preceding examples, I will briefly discuss the potential to design diffraction filters from the observed and theoretically formulated error systematics. In all considered examples the deviations of angle and coherence between CRS and implicit CRS and between the dual descriptions of the implicit CRS were most pronounced for events stemming from highly curved subsurface features like diffracting structures, whereas the corresponding differences vanished for reflection events connected to moderately curved or nearly planar features in the respective models. Dell and Gajewski (2011) suggested to use an exponential weight of the difference between the normal and the NIP wave radius to efficiently discriminate reflection and diffraction events in the data

$$w_{\mathrm{Dell}} = e^{-\frac{|R_{\mathrm{N}} - R_{\mathrm{NIP}}|}{|R_{\mathrm{N}} + R_{\mathrm{NIP}}|}} \quad . \tag{6.7}$$

Due to the fact that w_{Dell} takes values between 0 and 1, a threshold can be chosen to separate diffracted from reflected energy (Dell and Gajewski, 2011). Since the difference in the emergence angle estimation of the two versions of the implicit CRS operator appeared to be a very consistent and reliable diffraction indicator throughout the presented investigations, I choose the following angle-based diffraction weight for further study

$$w_{\mathrm{angle}} = 1 - e^{-(\alpha_v^2 - \alpha_t^2)} \quad , \tag{6.8}$$

where α_v and α_t denote the emergence angle estimated with the velocity-shifted and the time-shifted version of the implicit CRS moveout, respectively. Figure 6.15(a) and Figure 6.15(b) show the corresponding diffraction weights, defined according to expressions (6.7) and (6.8), for the BP dataset. While the conventional weight by Dell and Gajewski (2011), estimated only with the velocity-shifted implicit CRS operator, generally provides a good discrimination between reflection and diffraction events especially in the shallow regions of the model, the separation potential decreases noticeably in the deeper parts of the section. In addition, reflections are still addressed with comparably large weights, which may lead to insufficient separation for a poorly user-chosen

threshold. Observe in Figure 6.16(a), that in fact, if the threshold is chosen to low, the separation can be considered not successful.

Figure 6.15(b) on the other hand reveals, that the discrimination is generally much stronger than for the conventional weight, when deeper parts of the section are concerned. This can be explained by the fact that the conventional weight (6.7) is generally more accurate, the more accurate the single operator describes events of different curvature. The new weight does not necessarily rely on an accurate description of neither of the considered operators, the only requirement for a good discrimination is a consistent systematic difference between both operators. In that sense, one might loosely phrase the new approach as *error-based*, whereas the conventional weight, as mentioned before, relies on accuracy, which might be a more limiting criterion. While the new weight, as can be observed in Figure 6.16(b), leads to a sharper discrimination, it generally fails for the apex position, suggesting to combine the two weights to make use of the benefits of both approaches. In Figure 6.15(c) and 6.16(c), the sum of the conventional and the angle-based weight and the respective separation result are displayed, revealing consistently high weight values for the full length of the diffraction tails and values for reflections, which are very comparable to the ones of the conventional weight. This means, that the combined use of two operators leads to the design of an improved diffraction separation criterion.

6.3. Extrapolation and refinement

While the preceding section was concerned with the detection of curvature and heterogeneity by utilizing the different error systematics of the hyperbolic operator and the double-square-root operators and their dual descriptions for higher-order phenomena like diffraction, this section investigates the applicability of the extrapolation equations suggested in Chapter 5. As stated at the beginning of this chapter, stacking can be considered a very versatile tool, which not only delivers stack and attributes, but also provides a measure of the operator fit via the partial semblance coefficient (Taner and Koehler, 1969), which is defined according to (6.6). Figure 6.17(a) shows a semi-transparent plot of the partial semblance distribution for the simple example with a diffractor in a vertical velocity gradient medium, gained through extrapolation of the finite-offset slopes according to the zero-offset-based hyperbolic CRS extrapolation (5.25). While for small offsets the extrapolation is reasonably accurate, the quality of fit, following from the weak higher-order coupling revealed in Chapter 5, degrades for values of h above 500 m, which strongly reflects in the corresponding low partial semblance values. If this extrapolation semblance is below a user-defined threshold, I suggest to perform a local finite-offset (FO) refinement by testing controlled small perturbations of the extrapolated slopes,

$$p_s^{\text{refined}} = p_s^{\text{extrap}} + \delta p_s \quad , \tag{6.9a}$$

$$p_g^{\text{refined}} = p_g^{\text{extrap}} + \delta p_g \quad . \tag{6.9b}$$

In Figure 6.17(b) the corresponding semblance distribution resulting from the slope extrapolation based on the implicit CRS, according to the geometrical formulae (5.52), is displayed. While the hyperbolic description, as mentioned above, deteriorates for higher offsets, the double-square-root implicit CRS provides consistently high partial semblance values indicating its higher-order accuracy for this particular gradient example. Figure 6.18(b) on the other hand shows the according distribution after coherence-

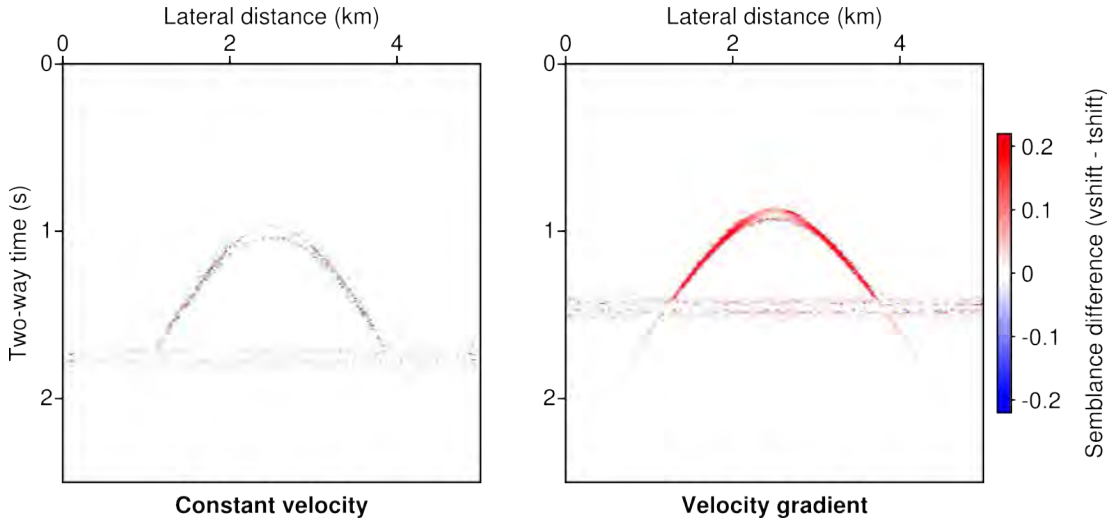

(a)

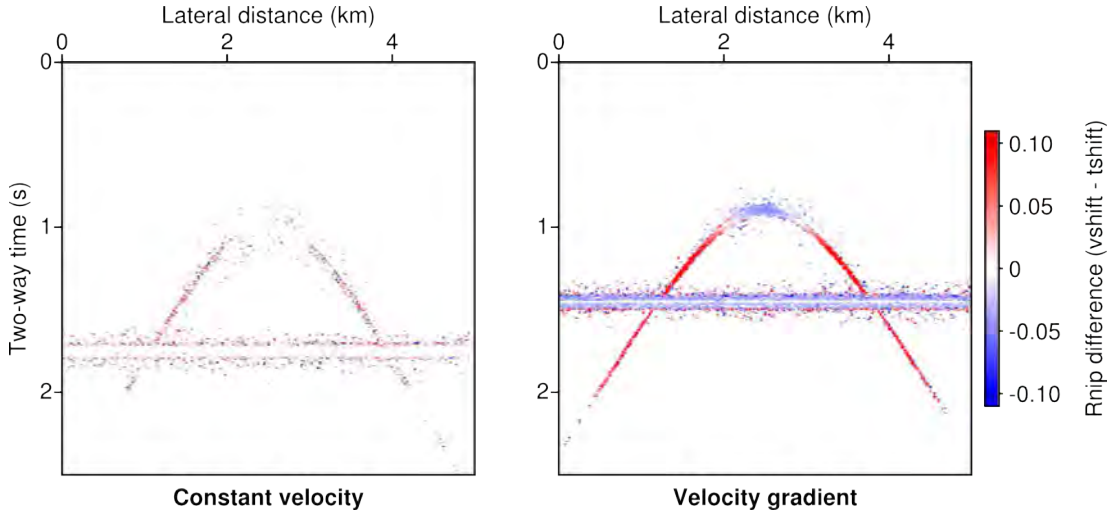

(b)

Figure 6.8.: Semblance and NIP wave radius difference between the two faces of the implicit CRS operator for two versions of the simple synthetic example introduced in the beginning of Chapter 6. Shown are the corresponding constant velocity case (left) and the results for the vertical velocity gradient of γ =0.5 s^{-1}. It becomes apparent, as can also be concluded from theory (see Chapters 3 and 4), that the duality of each operator vanishes, when the propagation medium is homogeneous.

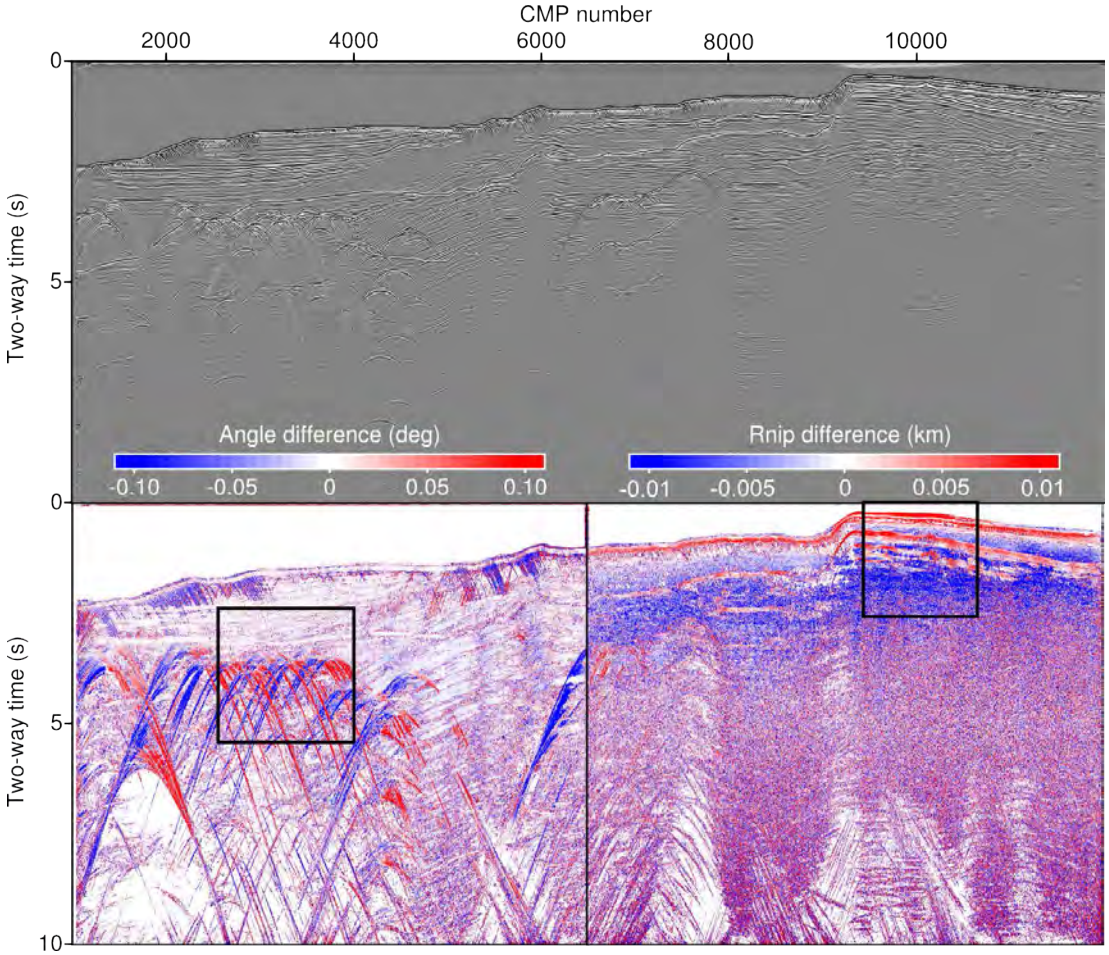

Figure 6.9.: Implicit CRS stack (top) and attribute difference (bottom) for the BP velocity benchmark dataset, arising from the comparison of the time-shifted and velocity-shifted versions of the implicit CRS operator. In the left part, the angle difference, in accordance with the simple gradient example (compare Figure 6.5) indicates the response from highly-curved structures, whereas in the right part, the difference of the NIP wave radius provides a measure of overburden heterogeneity, where multiple reflections, whose rays only traveled through the constant velocity water column, can clearly be distinguished from primaries.

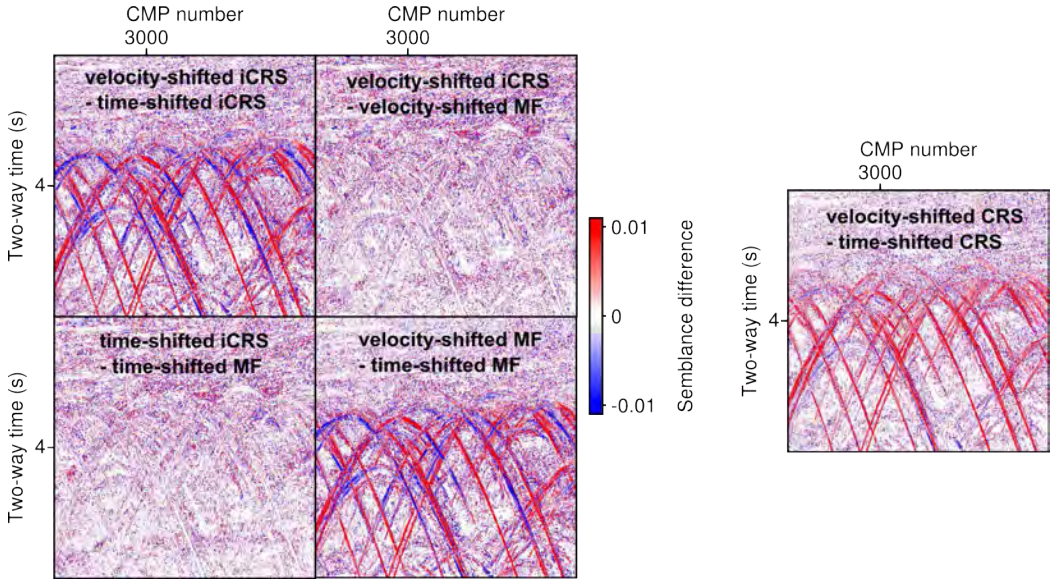

Figure 6.10.: Closeup of the semblance deviations for the complex BP dataset (indicated by the left box in Figure 6.9). Displayed are comparisons of the dual representations (see Chapter 4) of double-square-root-based implicit CRS (iCRS) and multifocusing (left) and hyperbolic CRS (right). One can observe that differences between the implicit CRS and multifocusing can be fully explained by the mechanism that accounts for heterogeneity.

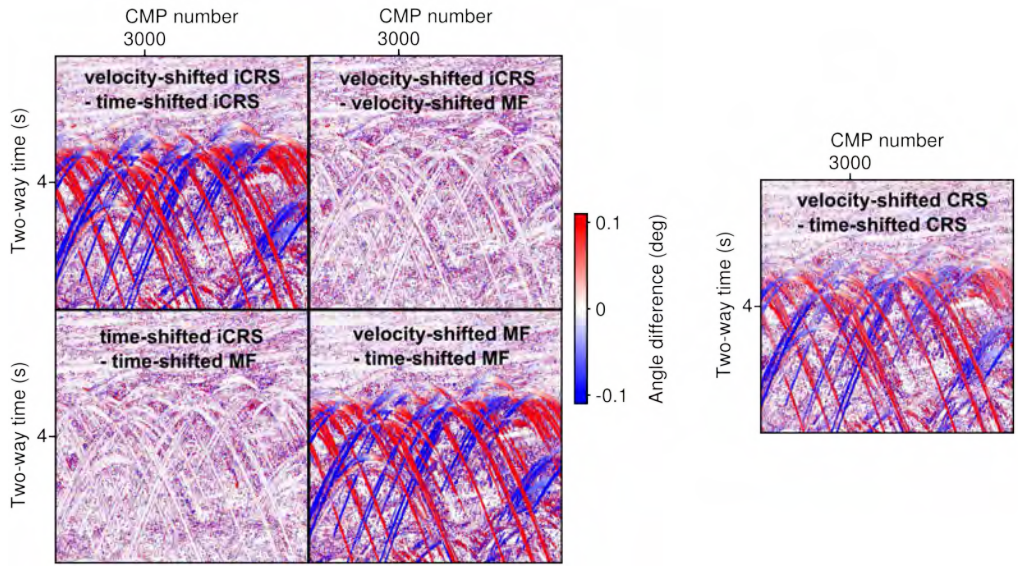

Figure 6.11.: Closeup of the angle deviations for the complex BP dataset (corresponding to the semblance comparison in Figure 6.10). Displayed are comparisons of the dual representations (see Chapter 4) of the implict CRS (iCRS) and multifocusing (left) and hyperbolic CRS (right). Again, the implicit CRS and multifocusing can be viewed as equivalent moveout descriptions, when both are based either on a time or a velocity shift.

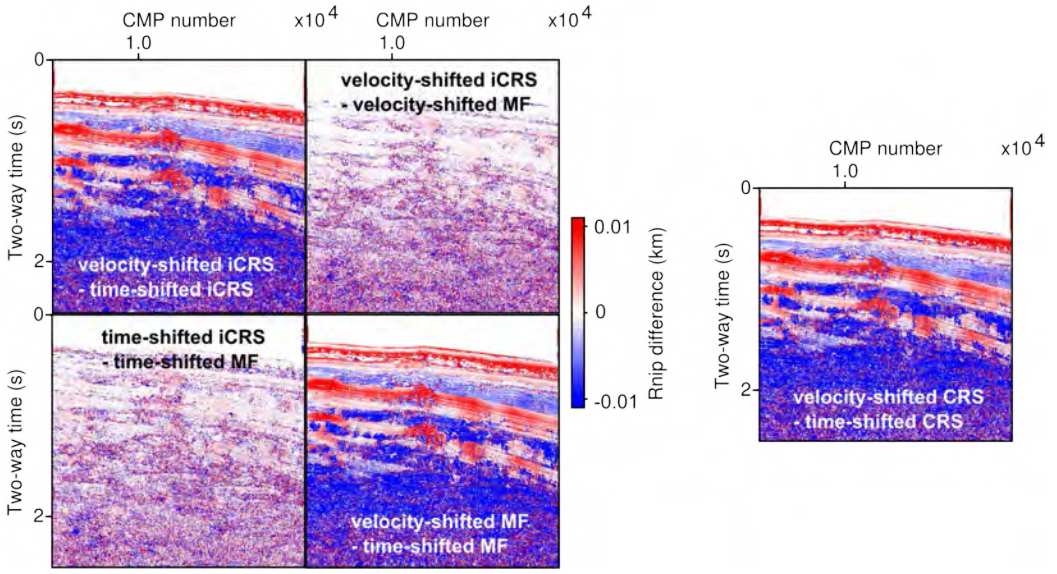

Figure 6.12.: NIP wave radius deviations for a closeup of the BP velocity benchmark dataset (indicated by the right box in Figure 6.9). Again, like for the semblance (Figure 6.10) and the emergence angle (Figure 6.11), the implicit CRS (iCRS) and multifocusing are equivalent descriptions. Please note, that blue colors correspond to the background velocity changes affecting the primaries and red colors correspond to multipe reflections at the water bottom (compare Figure E.2).

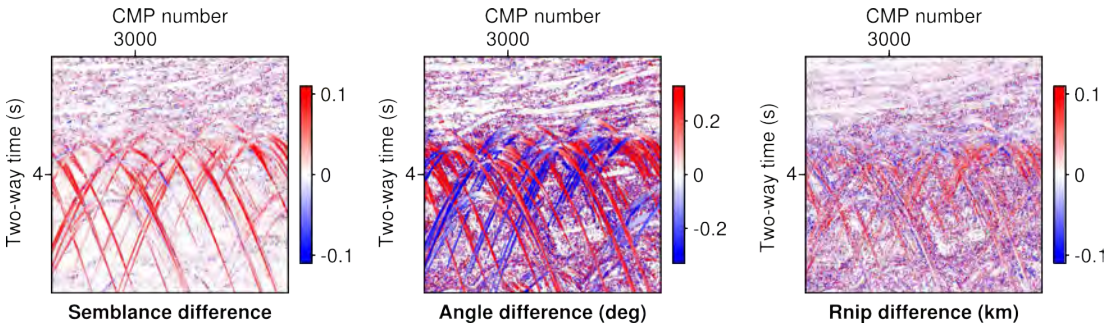

Figure 6.13.: Attribute differences between hyperbolic CRS and the double-square-root implicit CRS for the same closeup as in Figures 6.10 and 6.11 (indicated by the left frame in Figure 6.9). In correspondence with the simple gradient model results, all deviations can be attributed to the better fit of the implicit CRS for events stemming from highly curved subsurface structures (in this case, the complicated diffraction patterns related to the rugged top-of-salt).

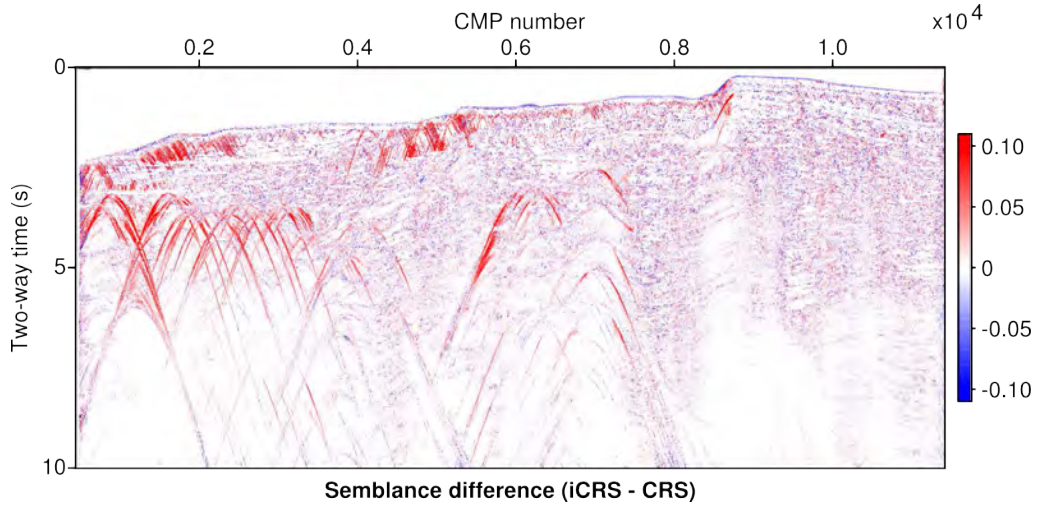

(a)

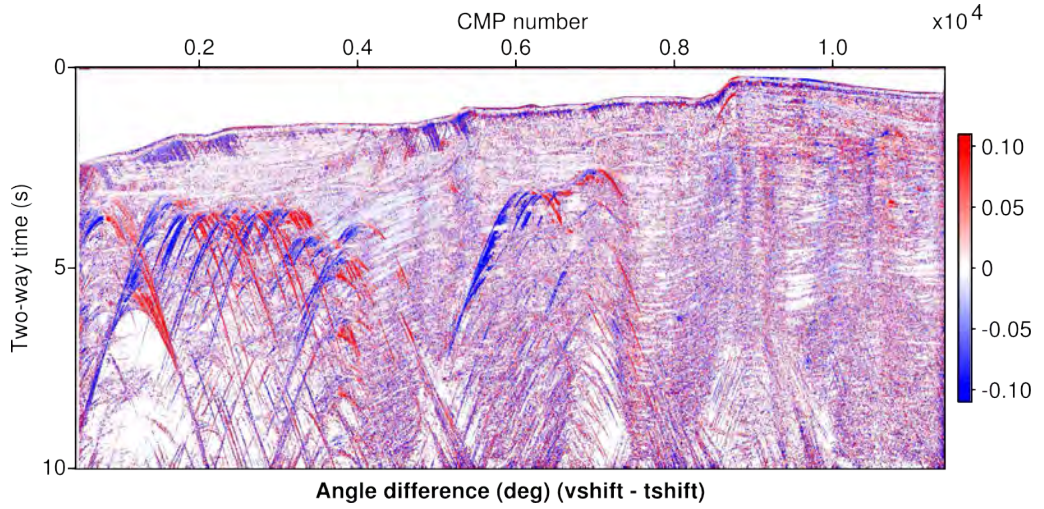

(b)

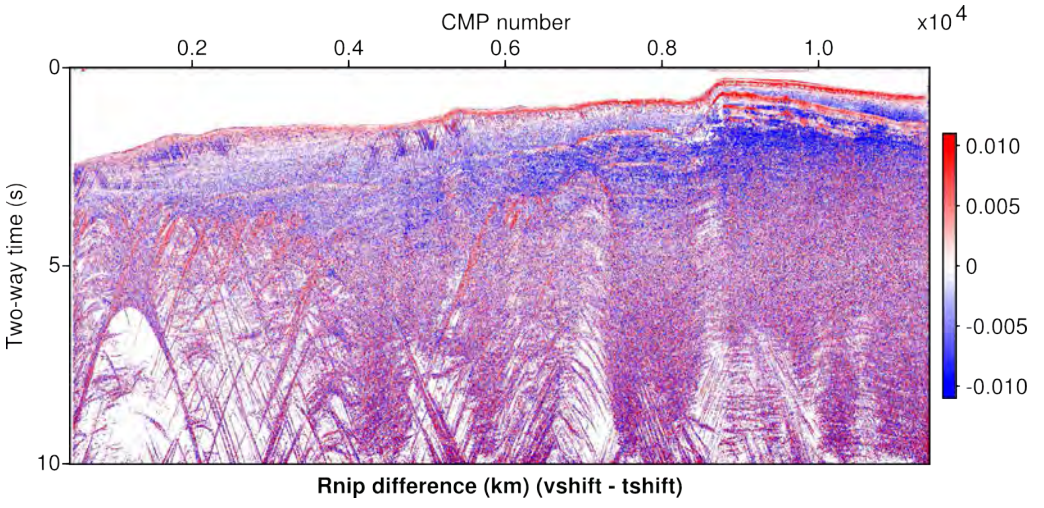

(c)

Figure 6.14.: The coherence deviation between the implicit CRS (iCRS) and conventional CRS (a) and the angle differences between the two faces of the implicit CRS operator (b) are most pronounced for the diffraction events. As mentioned before, the corresponding deviations for the NIP wave radius turn out to be a robust indicator of heterogeneity (c).

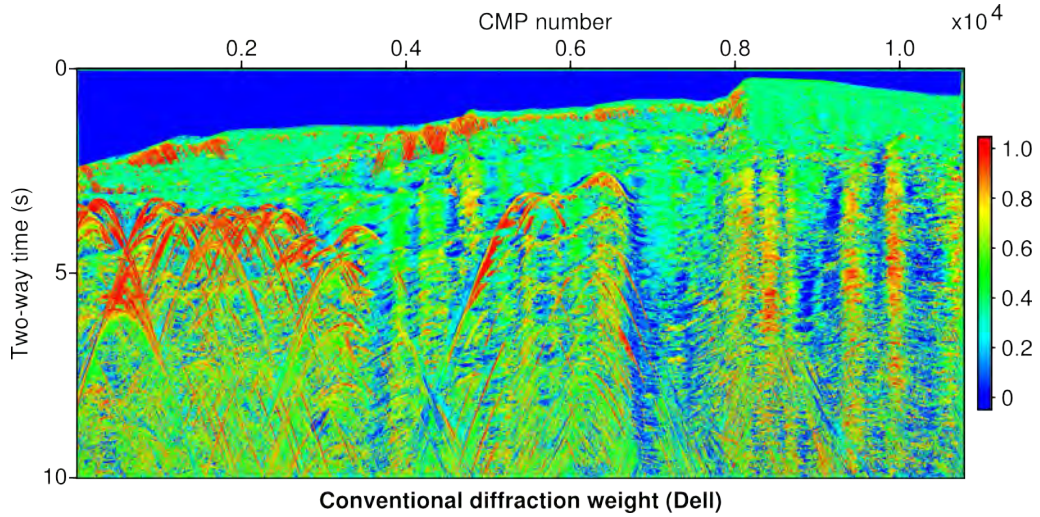

(a)

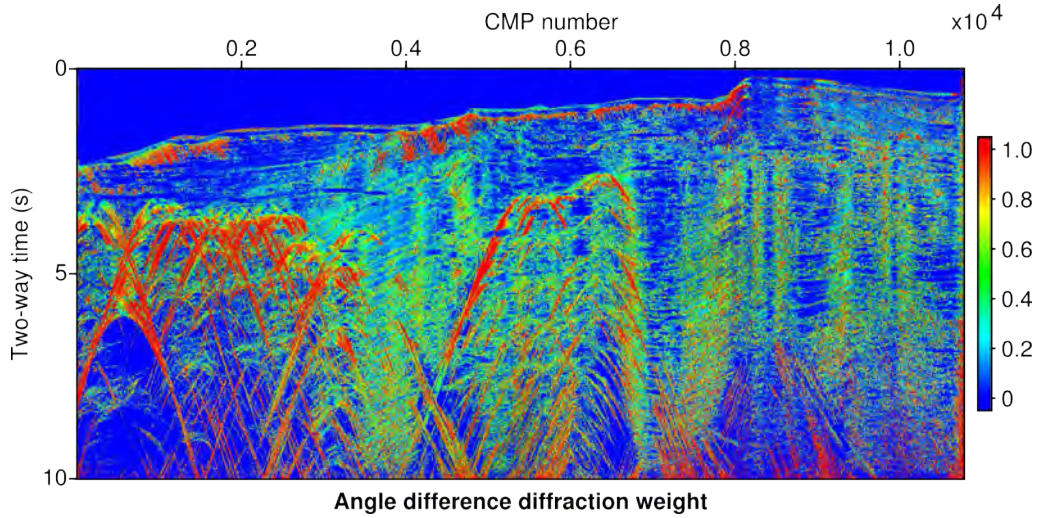

(b)

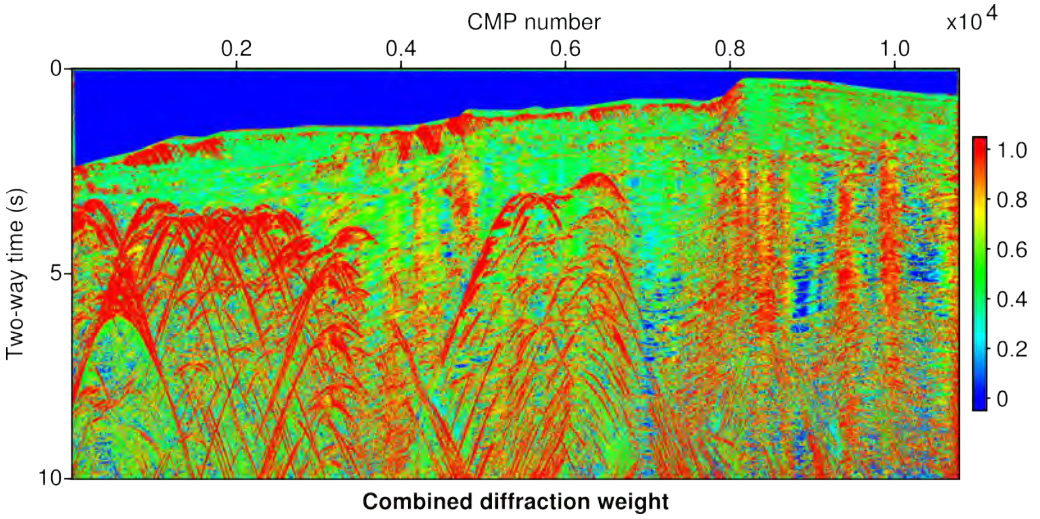

(c)

Figure 6.15.: Comparison of the conventional CRS-based diffraction weight (Dell and Gajewski, 2011) shown in (a) with a new multi-operator-based diffraction weight utilizing the angle difference (b) and their sum (c).

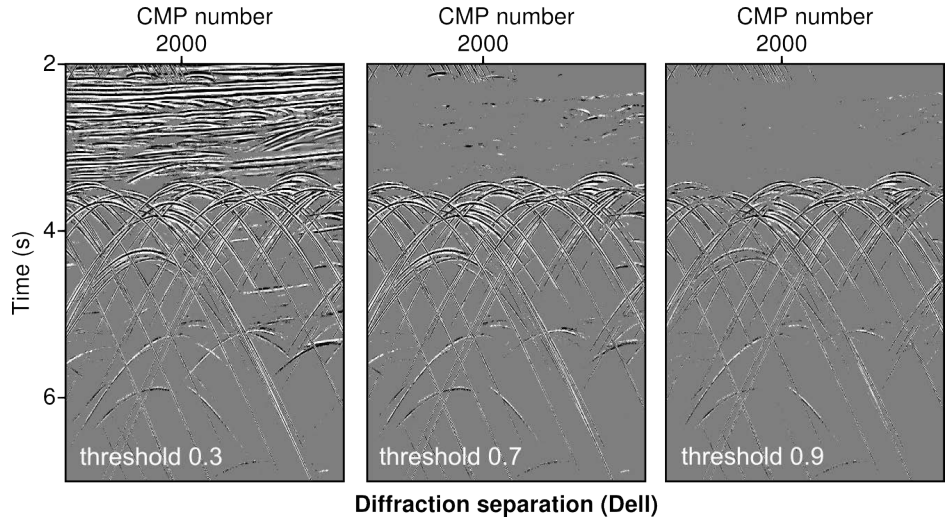

(a)

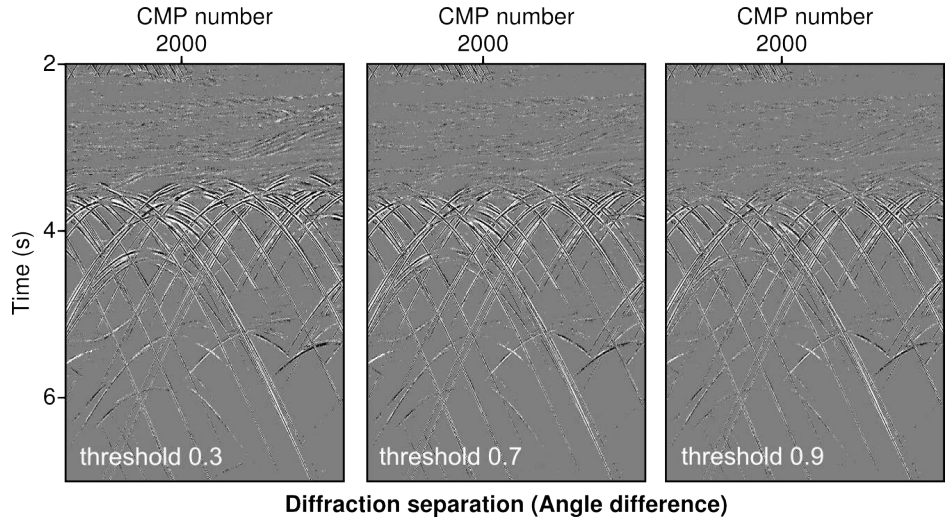

(b)

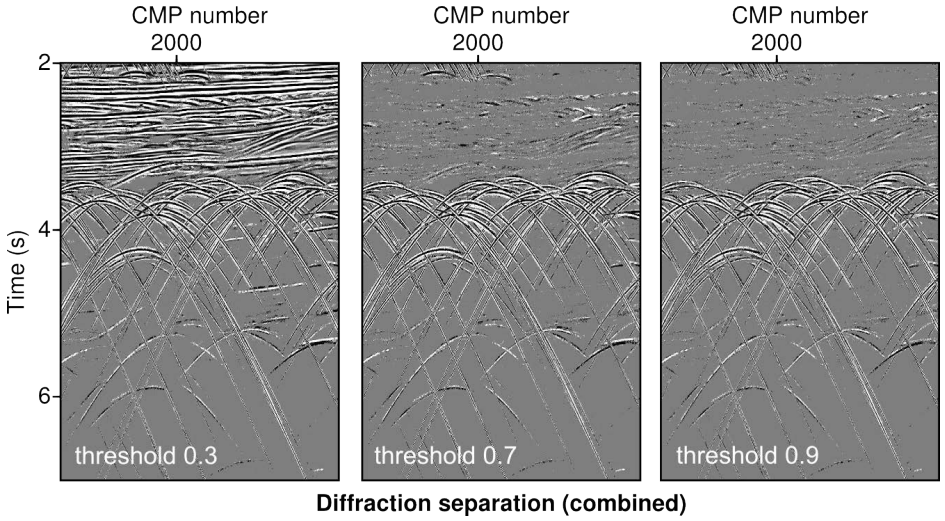

(c)

Figure 6.16.: Comparison of diffraction separation based on the conventional weight (a), the multi-operator weight (b) and the combined weight (c) shown in Figure 6.15.

steered local refinement, while the prestack semblance values are equally high for small and large offsets and only very mild distortions occur.

While in the presented simple synthetic example we had fully controlled conditions that allow to prove the general feasibility of our proposed extrapolation and refinement scheme, we chose to test the method on a complex field dataset to ensure the applicability in a more realistic setting. Figure 6.19 shows a near-offset stack section, in which strong amplitude variations, complicated diffraction patterns and steeply dipping events as well as multiple reflections can be observed. The data were recorded offshore Israel in the eastern Mediterranean by TGS Nopec[6]. The area is known to be dominated by salt-tectonics and there is reasonable evidence for according features on the presented line (Gradmann et al., 2005). In Figure 6.21(a), the local finite-offset coherence resulting from the CRS-based slope extrapolation of the left part of the considered line (the first 500 midpoints) is displayed for the near-offset, $h_0 = 500$ m, and $h_0 = 1000$ m, respectively. Figure 6.22(a) shows the corresponding zero-offset-based extrapolation coherence for three neighbouring CMPs from the same part of the field dataset. Although reasonably high semblance values are achieved for most of the significant contributions, the events do not seem to be imaged with consistently high accuracy. In contrast, Figure 6.21(b) and Figure 6.22(b) reveal that the inexpensive subsequent local slope refinement (6.9) leads to an increase of operator fit for most parts of the section for all displayed offsets.

In Figure 6.20 the respective receiver angle estimates, corresponding to the receiver slope p_g, are displayed for the Taylor-coefficient-based hyperbolic slope extrapolation following expressions (5.25) (Figure 6.20(a)) and the intuitive and simple geometrical implicit CRS extrapolation according to equations (5.52) (Figure 6.20(b)). Both are in good agreement with each other for all considered offsets. Figure 6.21(c) shows a comparison of the receiver emergence angle resulting from slope extrapolation, local refinement and application of the FO CRS stack by Zhang et al. (2001). While the overall trend of the angle values is consistent for all methods, the framed portions of the sections mark some of the regions, where the straight-forward extrapolation is less resolved and fine-structured than the refined result, which in turn is in good agreement with the FO reference. This general observation can also be made in Figure 6.23, where especially in the deeper parts stronger fluctuations are revealed after efficient subsequent finite-offset refinement.

6.4. Partial time migration and demigration

As indicated in the first section of this chapter, stacking and Kirchhoff-type migration are logistically and conceptually closely connected. In this section I will demonstrate the general applicability of partial CRS migration for the complex TGS field data example, which was introduced in the previous section. In order to better appreciate the presented results I refer once again to the simple gradient example (see Appendix E.1). While in the previous section, in the context of extrapolation, the partial semblance coefficient (6.6) served as an objective criterion for local finite-offset refinement, following the ideas discussed at the beginning of this chapter, I will show in this section that the partial CRS migration coherence not only provides insight into the general fit to diffractions, but that it can also serve as an imaging tool indicating the position of

[6]For more information on this field dataset, I refer to Appendix E.3.

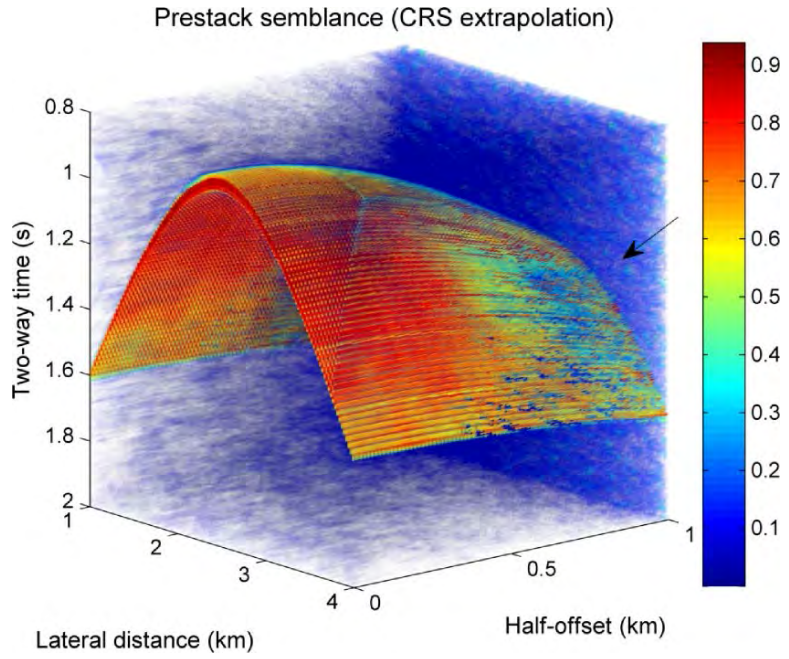

(a)

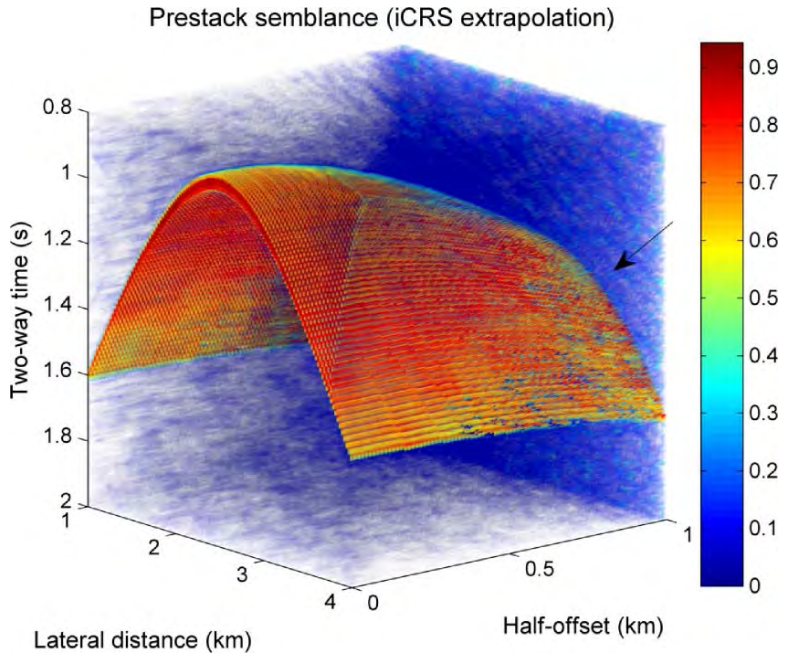

(b)

Figure 6.17.: Prestack coherence volumes for the point diffractor in the simple gradient model introduced in Section 6.1, resulting from the extrapolation of traveltimes using (a) hyperbolic CRS and (b) double-square-root-based implicit CRS (iCRS). For large offsets the implicit CRS operator provides a better fit to the diffraction event.

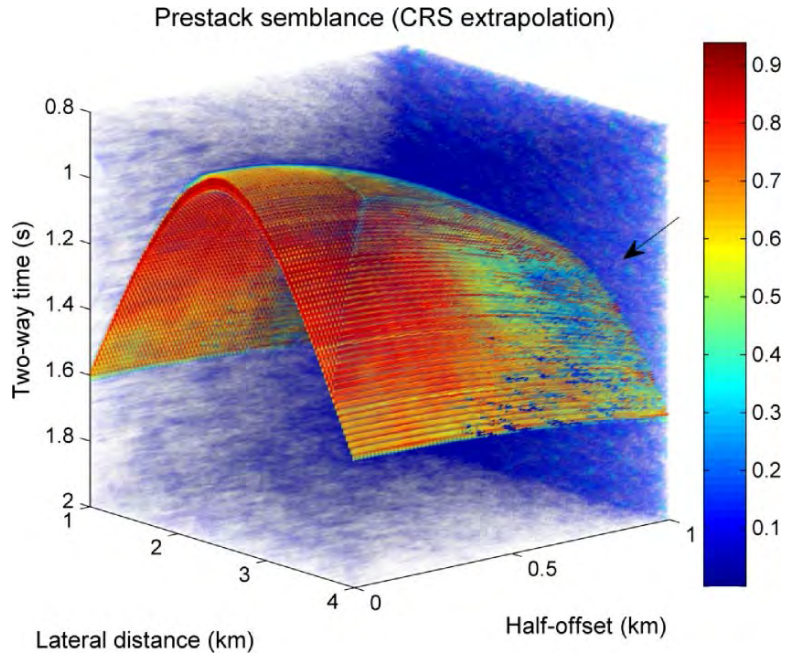

(a)

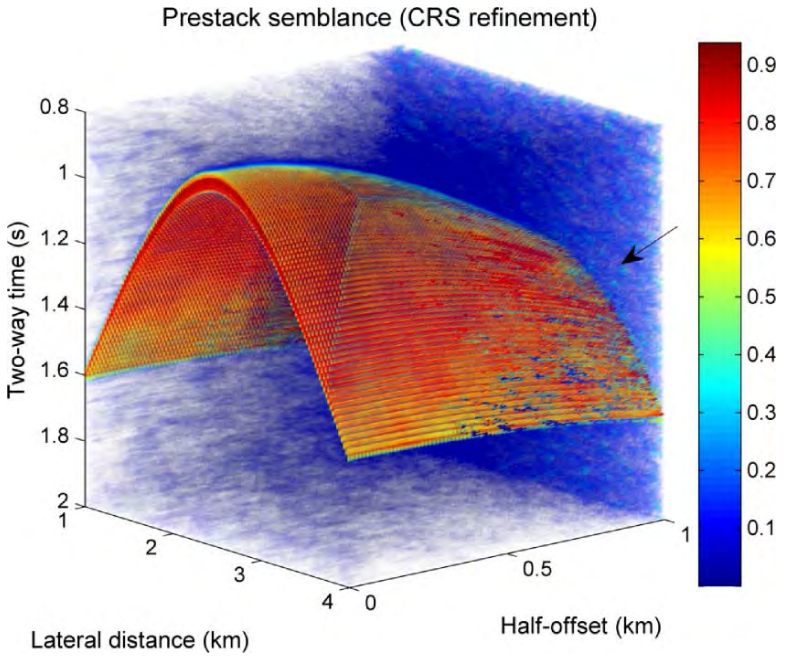

(b)

Figure 6.18.: Prestack coherence volume for the diffractor in the simple gradient background introduced in Section 6.1, resulting (a) from the application of CRS extrapolation and (b) from subsequent local slope refinement. The coherence at larger offsets is considerably higher in (b).

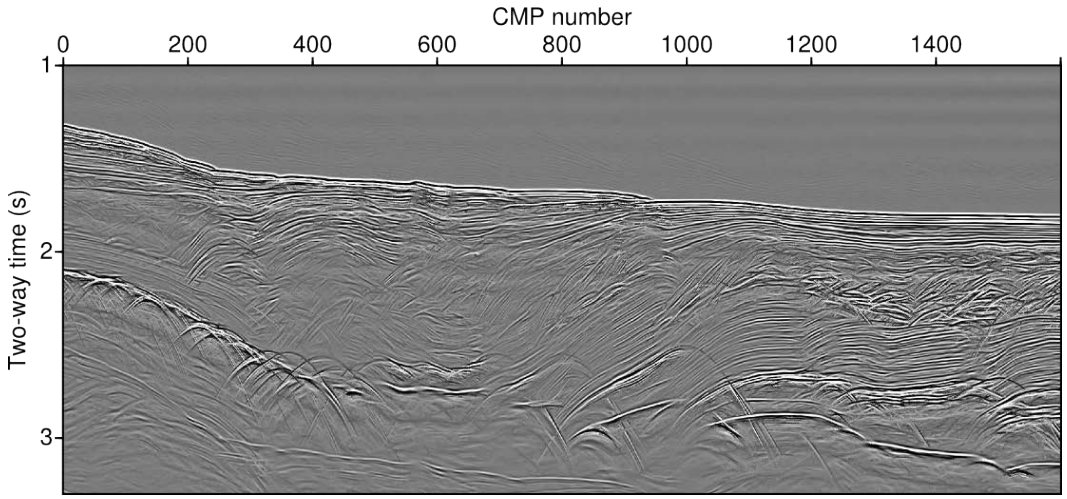

Figure 6.19.: Near-offset ($h_0 = 75$ m) stack section for an industrial field dataset from the eastern Mediterranean recorded by TGS Nopec. The underlying geology is known to be dominated by a salt-body of varying thickness, whose top is characterized by strong diffraction patterns. Please note that preprocessing was kept to a minimum and the focus is to demonstrate applicability of the suggested concepts to complex field data. More details on the dataset can be found in Appendix E.3 and, e.g., in Netzeband (2006).

edges, faults and other discontinuities in the partially migrated finite-offset sections.

Figure 6.24(a) shows the near-offset partial CRS migration coherence for a portion of the complex TGS dataset. As becomes apparent for the presented left part of Section 6.19, the partial migration coherence reveals very high values in mostly localized regions indicating that a lot of diffracted energy is contained in the dataset[7]. In fact, when used as an overlay for the respective partially time migrated section (see Figure 6.24(b)), the partial migration coherence section can serve as a diffraction map, in which high values correspond to edges and fault structures related to the underlying complicated salt geometry (Gradmann et al., 2005).

As motivated in Section 6.1, the implicit CRS diffraction operator, parametrized in apex coordinates, can be used to perform the task of partial time migration (compare Dell et al., 2012). At this point I am interested in the inverse process, i.e. the partial demigration of formerly migrated data. From the pragmatic logistical viewpoint, I argue that this can simply be achieved by applying the partial CRS stack with the implicit CRS diffraction operator parametrized in conventional local coordinates (x_0, t_0) to the partially time-migrated prestack data. Figure 6.25 shows the noise contaminated simple gradient dataset before (Figure 6.25(a)) and after subsequently applied partial CRS migration and demigration (Figure 6.25(b)). It can be concluded that the principal goal of focusing and re-spreading of diffracted energy is achieved, but that, due to waveform distortions, the original state of the data could not be fully retained. Partly, these distortions can be explained by the fact that the demigration utilizes a different set of attributes, measured at the local coordinates (x_0, t_0), whereas the migration is based on parameters estimated at the apex coordinates (x_a, t_a). In any case, I need to

[7]For details on the processing parameters, see Appendix F.

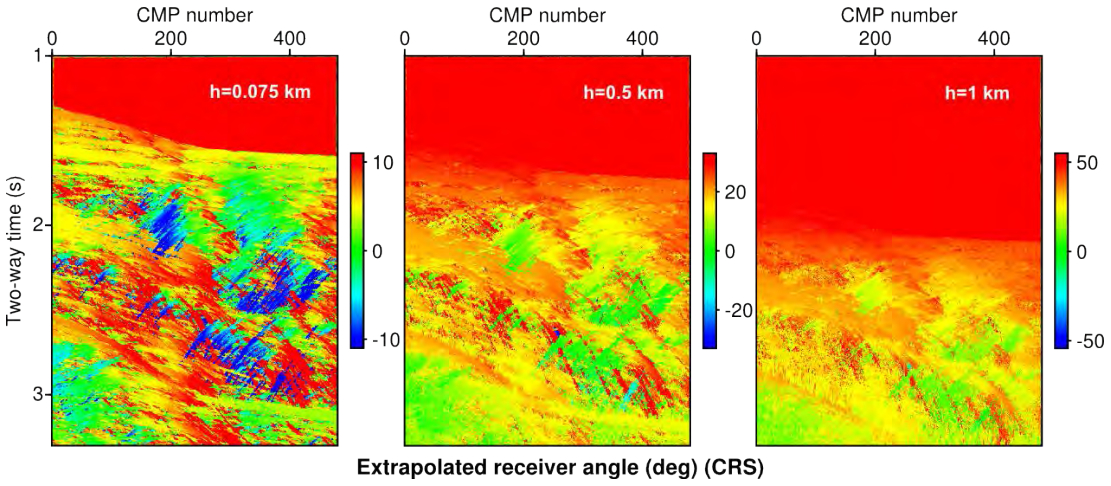

(a)

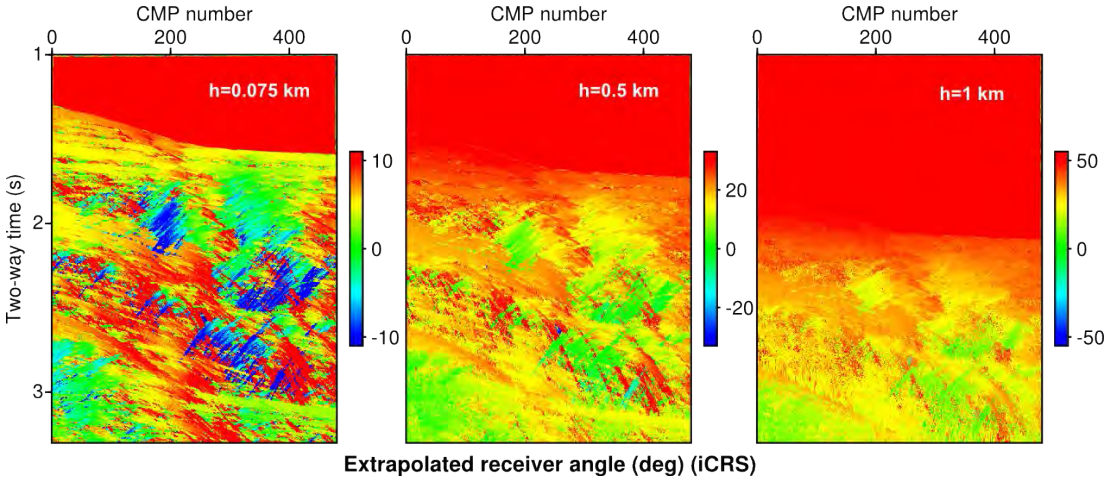

(b)

Figure 6.20.: FO receiver angle extrapolation based on (a) the conventional CRS expression and (b) on the implicit CRS (iCRS) following from geometrical considerations in Chapter 5 for the first 500 CMPs of the TGS dataset. Displayed are again the offsets $h = 0.075$ km, $h = 0.5$ km and $h = 1$ km. While the CRS extrapolation is based on a local expansion in midpoint and half-offset coordinates, the implicit CRS extrapolation is purely based on geometry (see Chapter 5).

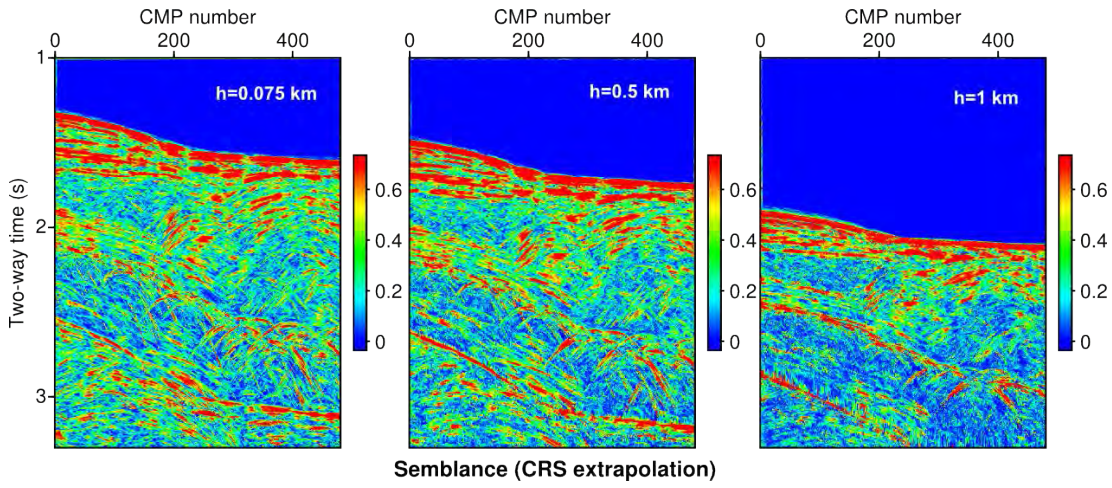

(a)

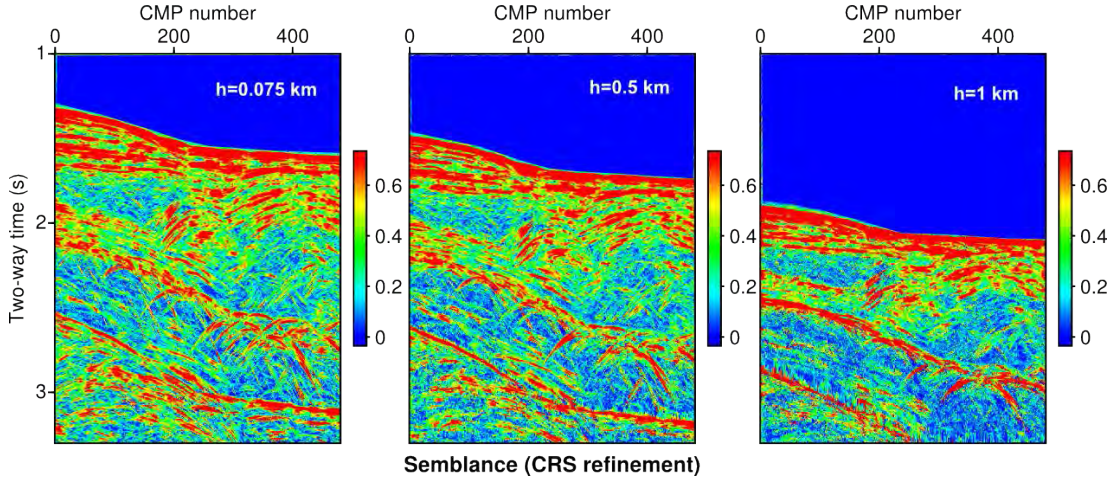

(b)

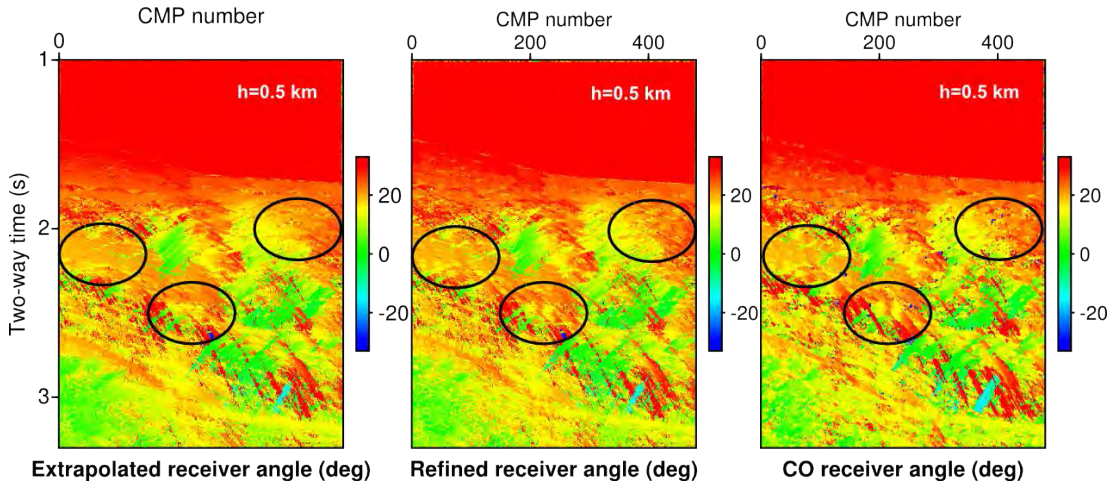

(c)

Figure 6.21.: TGS prestack coherence resulting from traveltime and slope extrapolation (a) and local FO refinement (b). The comparison of the extrapolated and refined values of the receiver angle with the generic FO CRS reference (c) demonstrates that the extrapolation is overall successful but that the subsequent FO refinement leads to improved, more fine-structured results in complex regions.

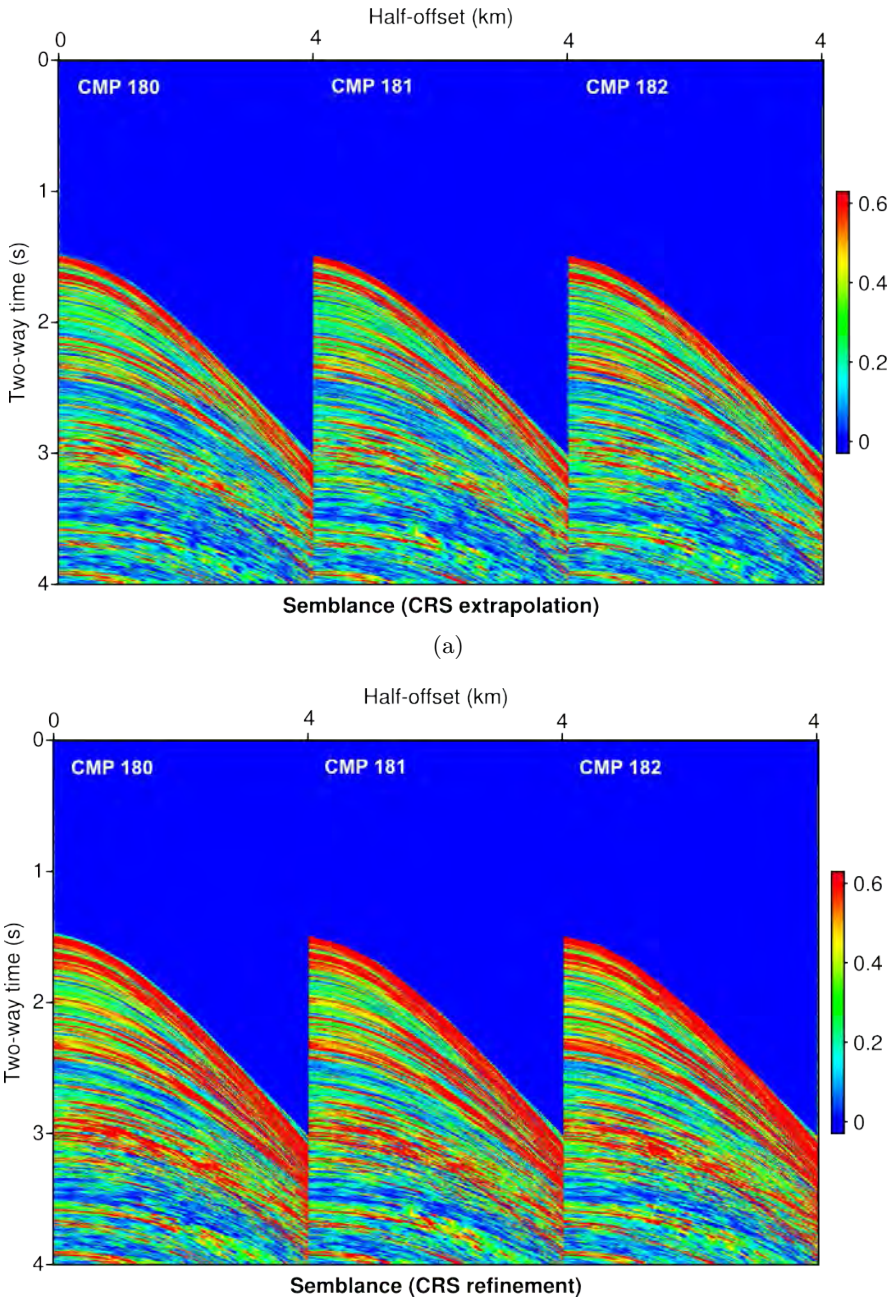

Figure 6.22.: Comparison of the prestack coherence achieved by (a) CRS extrapolation and (b) resulting from subsequent local FO refinement for three neighbouring CMP gathers of the TGS field data. Note that improvements can be observed for the full considered offset range even for higher traveltimes.

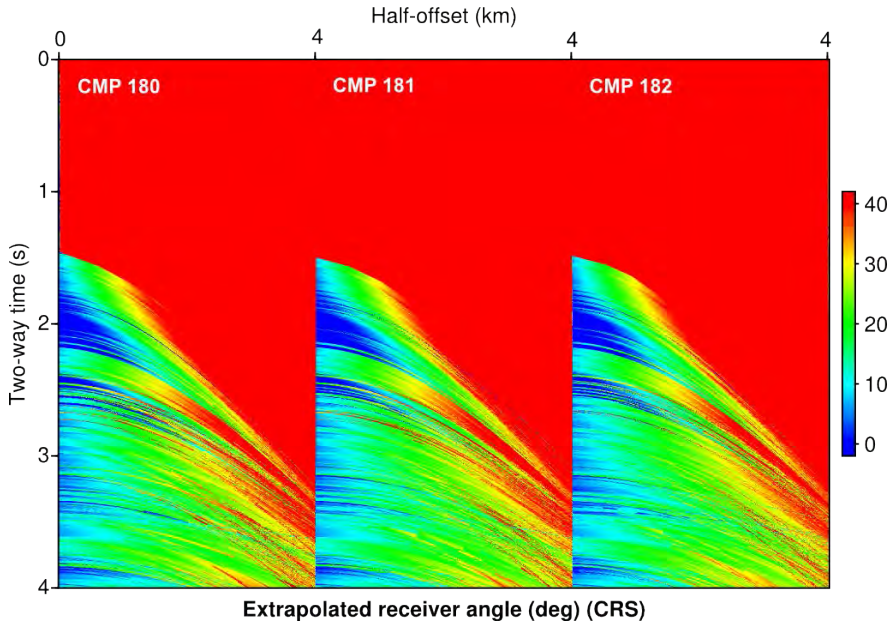

(a)

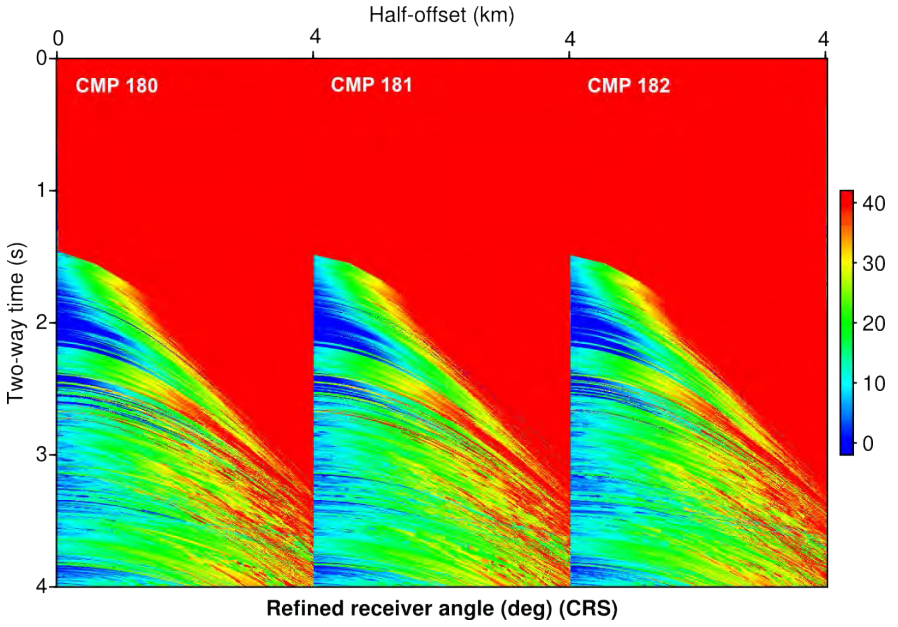

(b)

Figure 6.23.: Comparison of the FO receiver emergence angle values achieved by (a) CRS extrapolation and (b) resulting from the FO refinement for the same three neighbouring TGS CMP gathers considered in Figure 6.22. While differences are barely visible for the water bottom reflection and shallow reflections, the receiver angle values reveal finer structure (and, therefore, more local character) in the deeper parts.

stress that without appropriate amplitude and phase correction, the presented scheme cannot be considered amplitude-preserving. Note however that, due to the subsequent summation, the noise level got significantly reduced, indicating the general enhancement potential of the approach.

While, as stated above, the subsequent application of the suggested partial CRS migration and demigration did not lead to the desired full recovery of the initial state, the simple logistics underlying this approach can be utilized for efficient prestack diffraction separation. It was found in Section 6.1 that the partial migration semblance coefficient, due to the coincidence of the migration operator with a physical diffraction bears the potential to efficiently discriminate between diffractions and reflections, to which the migration operator is only tangent (e.g., Yilmaz, 2001). Consequently, I suggest to apply a threshold to the migrated coherence, leaving only focused diffracted energy in the sections. A subsequent iterative demigration of the resulting filtered coherence then leads to a prestack diffraction map, which can be used for separation[8]. Figure 6.26 reveals that this iterative migration coherence demigration leads to an accurate prestack diffraction weight for the simple gradient example. Figure 6.27 and Figure 6.28 show that the same procedure also leads to stable results for the complex BP velocity benchmark dataset and the TGS field data, indicating the general applicability of the suggested scheme.

6.5. Diffractions and tomography

In this section I will briefly demonstrate that the discussed notion of a virtual seismic source not only provides valuable insights about coupling phenomena and symmetries, but that it also directly implies the applicability of the NIP wave tomographic scheme by Duveneck (2004) to diffraction data. Figure 6.29 shows the results of NIP tomography based either on the hyperbolic CRS operator, whose accuracy was shown to deteriorate for high curvatures and the double-square-root-type implicit CRS operator. While in both cases the starting point was a background model of constant near-surface velocity $v_0 = 2$ km/s, the inverted velocity model corresponding to CRS measurements reveals a strong systematic deviation pattern that appears to be symmetric with respect to the lateral location of the diffractor (compare Figure E.1). The implicit CRS measurements of the NIP wave attributes, in turn, lead to a background velocity model that is in overall good agreement with the exact reference. In conclusion, the low degree of higher-order coupling of the hyperbolic CRS moveout, as investigated in the higher-order moveout analysis in Chapter 5, leads to biased measurements for the diffraction case and, consequently, to a systematically incorrect inverted result. Please note that in both cases only a single diffraction event was considered for the inversion.

As I argued in Chapter 2, a point diffractor can be viewed as a passive seismic source, since it ideally radiates in all directions. In the context of globality, I have shown that the finite-offset diffraction response can be decomposed into two zero-offset experiments, one carried out at the respective source position, the other at the receiver. In the context of NIP tomography I therefore conclude that, in principle, the application to diffraction data should yield higher resolution results than conventional reflection-

[8] Since the used semblance coefficient is more robust and in general of lower resolution than waveforms, the demigration can be applied iteratively to spread the migrated coherence from the apex to the prestack diffraction response (compare Figure 6.26).

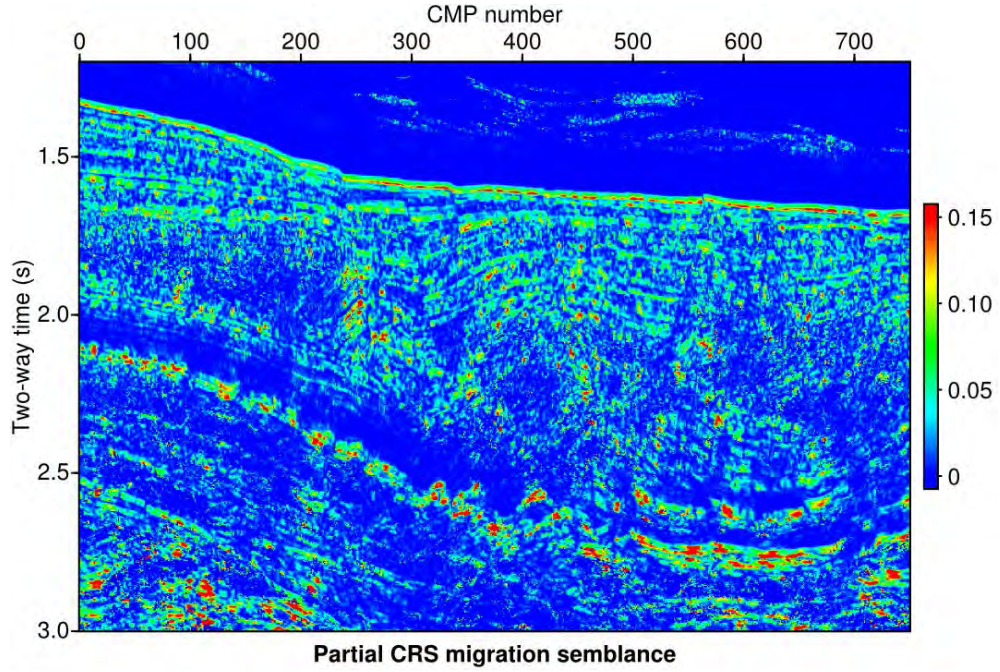

(a)

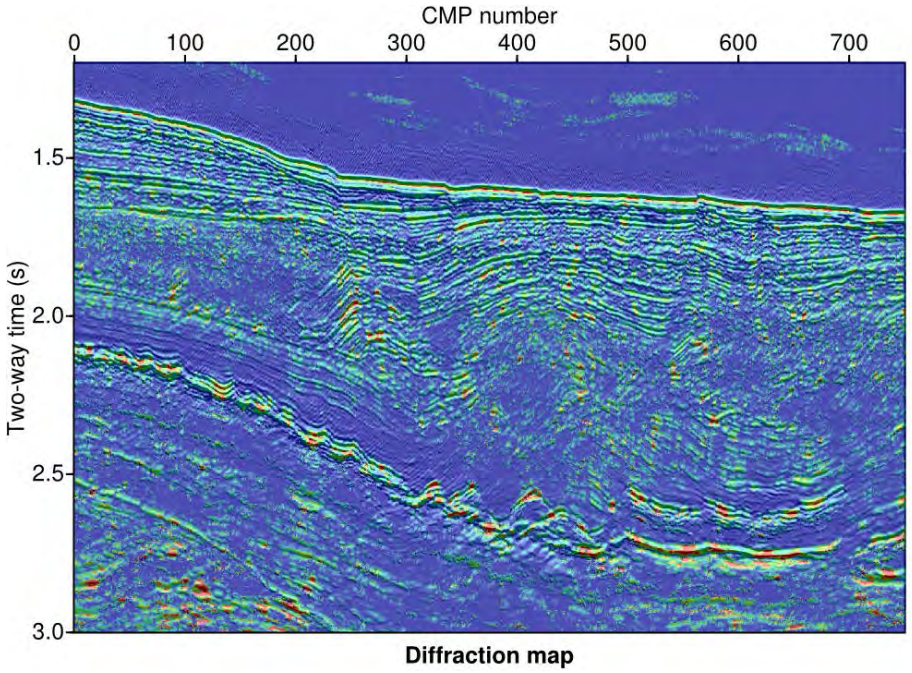

(b)

Figure 6.24.: Partial CRS migration coherence (a) and the corresponding partially CRS-migrated section with a semi-transparent overlay of the migration coherence, which can be viewed as a diffraction map (b). High partial migration coherence values turn out to accumulate near steps and faults, thereby providing a useful asset for interpretation.

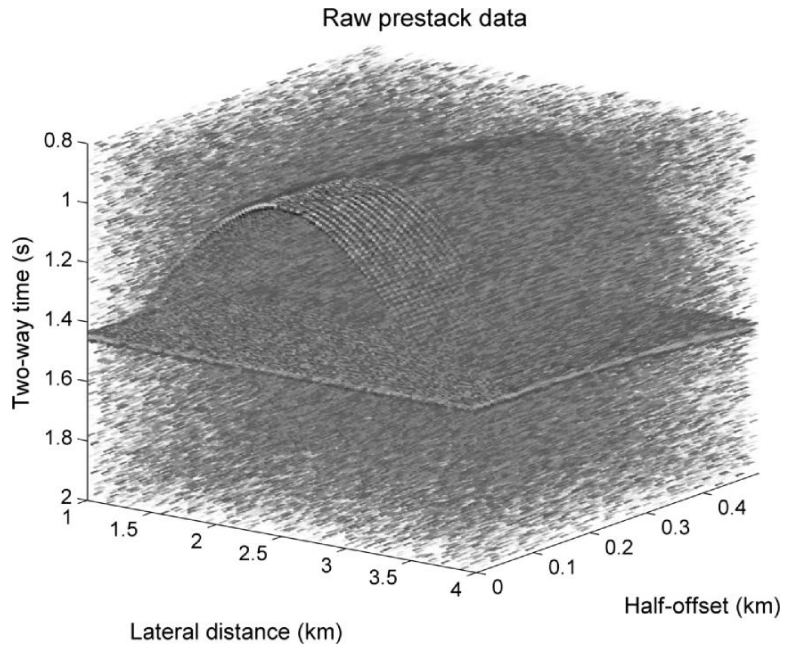

(a)

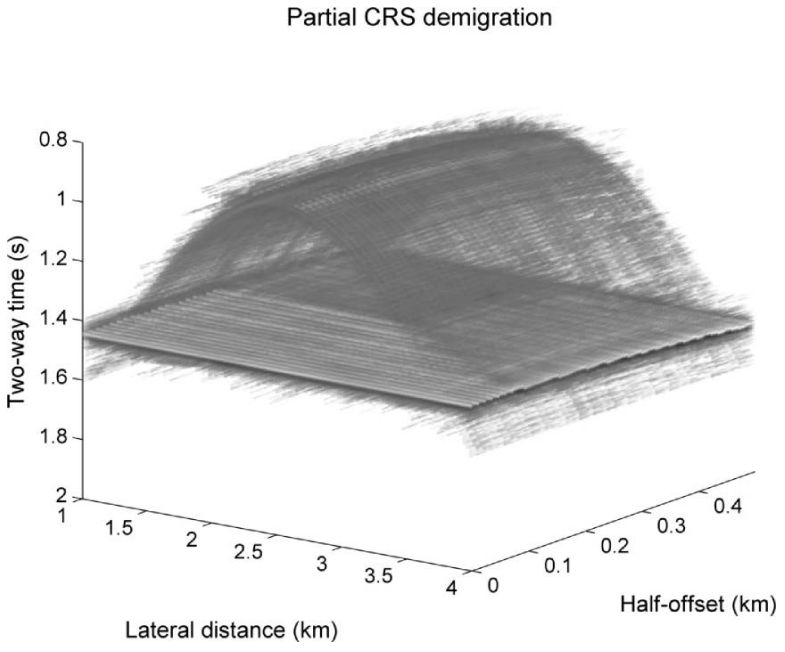

(b)

Figure 6.25.: Illustration of the partial CRS demigration capabilities for the simple gradient model introduced in Section 6.1 with a high noise level in the raw data (a). Although some demigration noise can be observed, both, the diffraction and the reflection event are nicely preserved, while the signal-to-noise ratio got significantly reduced (b).

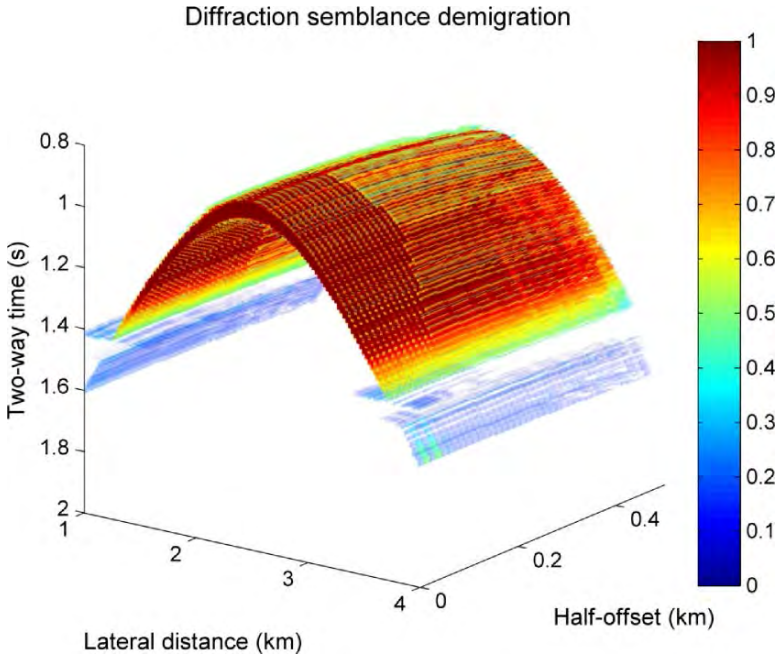

Figure 6.26.: Iterative partial CRS diffraction coherence demigration for the simple synthetic gradient model containing a planar reflector and a diffractor. Depending on the choice of a migrated semblance threshold, this approach bears the potential for efficient separation of diffractions and reflections, in which the partially demigrated coherence can be used as a diffraction weight.

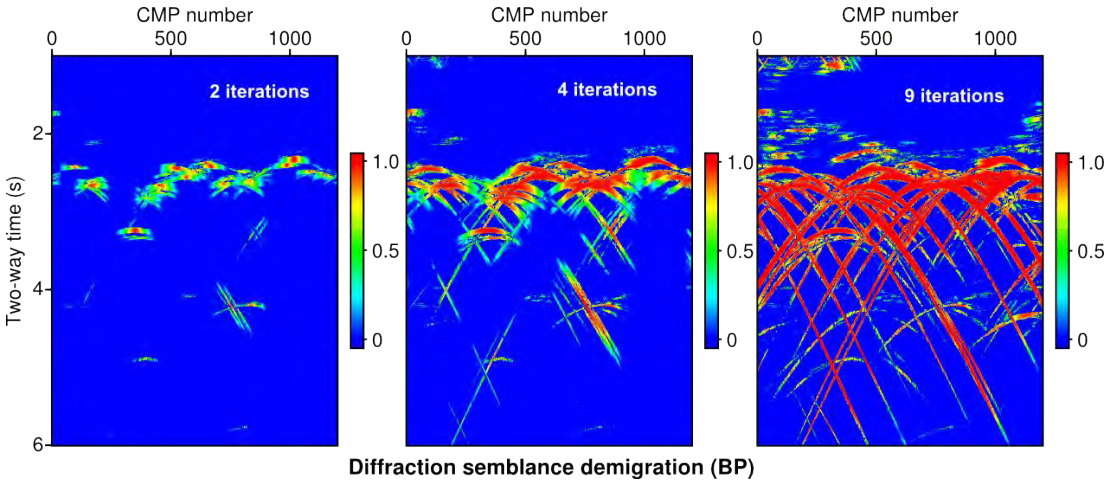

(a)

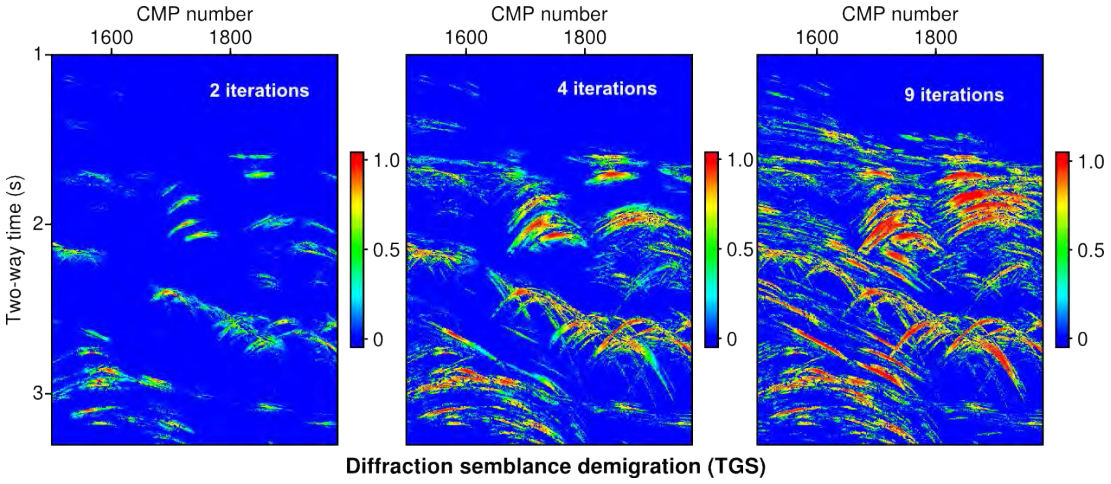

(b)

Figure 6.27.: Iterative partial CRS demigration of the migration coherence for (a) a closeup of the BP velocity benchmark and (b) applied to the first 500 CMPs of the TGS field dataset. Displayed are the respective results for 2, 4 and 9 iterations.

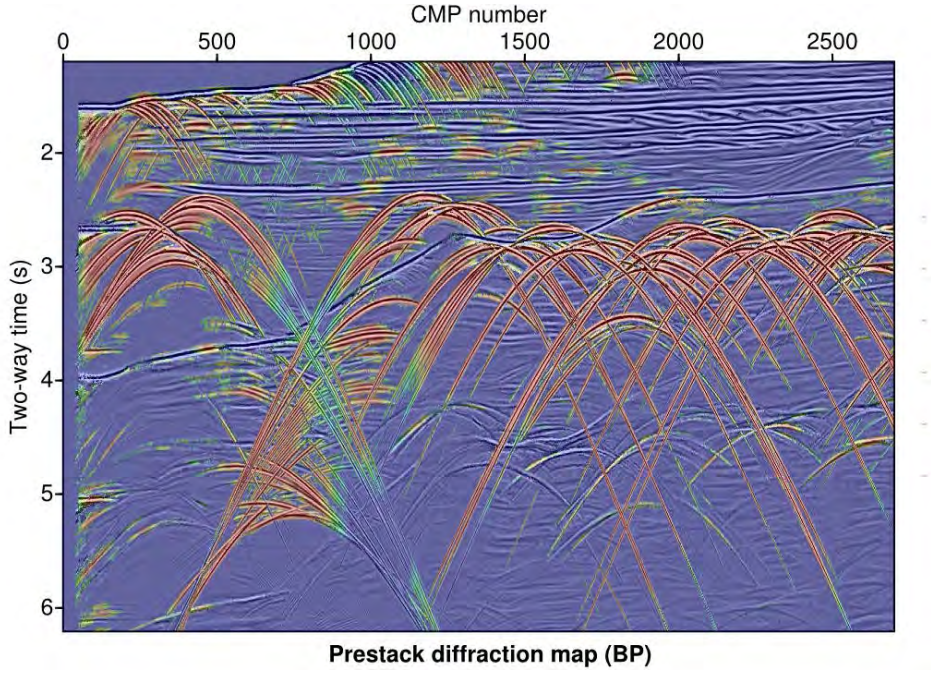

(a)

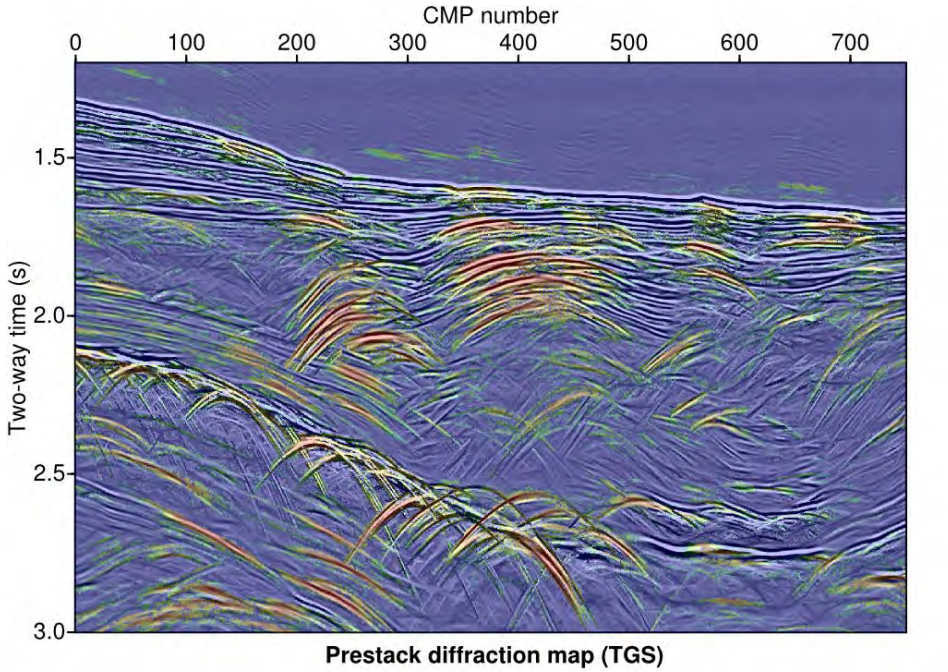

(b)

Figure 6.28.: Partial stack overlain by the corresponding iterative partial CRS diffraction semblance demigration for the BP and TGS datasets. Similar to the new diffraction weights introduced in Section 6.2, one potential application of the iterative coherence demigration could be the separation of diffractions in the prestack domain.

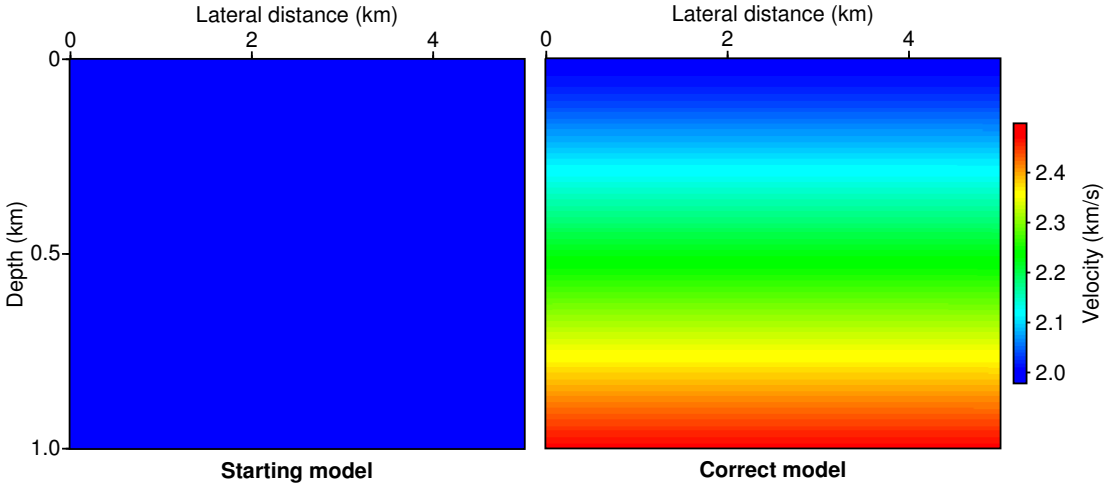

(a)

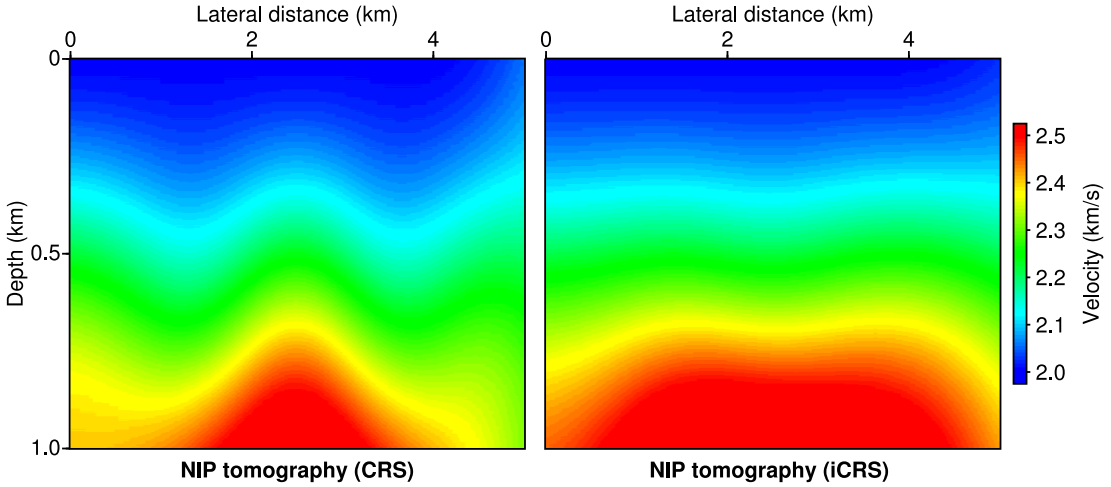

(b)

Figure 6.29.: Background velocity model inversion via NIP wave tomography based on a single diffraction event. The starting model (a) corresponds to the constant near-surface velocity $v_0 = 2$ km/s. Comparison of the inversion results (b) with the true reference background model (a) confirms the preceding findings that the double-square-root implicit CRS (iCRS) operator provides a better description for the response of highly curved subsurface features. Note the slightly different scales in (a) and (b).

based inversion[9].

6.6. A time-based passive seismic workflow

In the context of moveout traveltime correction I found that the potential effect of moveout stretch is an inherent property of the velocity-shifted representation of each operator, whereas wavelets always remain unstretched for the time-shift mechanism[10] (see Chapter 4). In this final section I seek to support the notion that both versions of each operator may not only be jointly utilized (as suggested in Section 6.2), but that the velocity-shift mechanism's characteristic dependence on the reference time t_0 may also prove to be advantageous for certain applications. In the context of passive seismic monitoring or earthquake seismology, the localization of the unknown source of a seismic event is a fundamental problem and may be approached with the data-driven method of diffraction stacking (Zhebel et al., 2011). Without loss of generality and supported by a simple synthetic test example, we present a time-based passive seismic workflow, that is data-driven and makes full use of the virtual source concept, stressed in Chapter 2 and Chapter 3 and the fundamental moveout duality presented in Chapter 4.

The concept of a virtual seismic source, utilizing raypath symmetries and reciprocity, proved to be very useful in reducing the complex two-way ray geometry of a reflection experiment to the much simpler geometry of a one-way propagating wavefront, which leads to the same description of the moveout. For a passive experiment, this one-way experiment becomes physical reality and the virtual seismic source can in this case be identified with the true source of the passive event. According to the one-way wavefront formalism introduced in Chapter 2 and, consequently, following equation (3.2), the moveout of a passive seismic event can be witten as

$$\Delta t = \frac{\sqrt{R_g^2 + 2R_g \Delta x_g \sin\alpha_g + \Delta x_g^2} - R_g}{v_g} \quad , \tag{6.10}$$

where the subscript g denotes properties observed at a receiver at the surface. Formally, this expression is exactly equivalent to the diffraction case in the zero-offset section (5.56), with the only difference that the NIP wave, per definition, travels at half the actual medium speed (see Section 2.5). Consequently, the same rules apply for the extension to the heterogeneous case and the generalized passive one-way traveltime reads

$$\begin{aligned} t &= t_{\text{source}} + t_0 + \Delta\hat{t}(\hat{t}_0, \hat{p}) \\ &= t_{\text{source}} + t_0 + \sqrt{(\hat{t}_0 + p_{0x}\Delta x_g)^2 + (\hat{p}^2 - p_{0x}^2)\Delta x_g^2} - \hat{t}_0 \quad , \end{aligned} \tag{6.11}$$

with $\hat{t}_0$ and $\hat{p}$ defined according to (4.8). The generally unknown source excitation time is denoted by t_{source} and the actual true reference time, following the convention used throughout this thesis, is t_0. In the following, I suggest a pragmatic hybrid scheme, in

[9] For more details on the attribute measurements and the tomographic inversion, I refer to Appendix D and F.

[10] Please note that moveout stretch can also be prevented for the velocity-shifted operators by accounting for the change of the shift along the wavelet. In addition, in the context of stacking, the summation can be carried out along the moveout trajectory instead of correcting the moveout before summation.

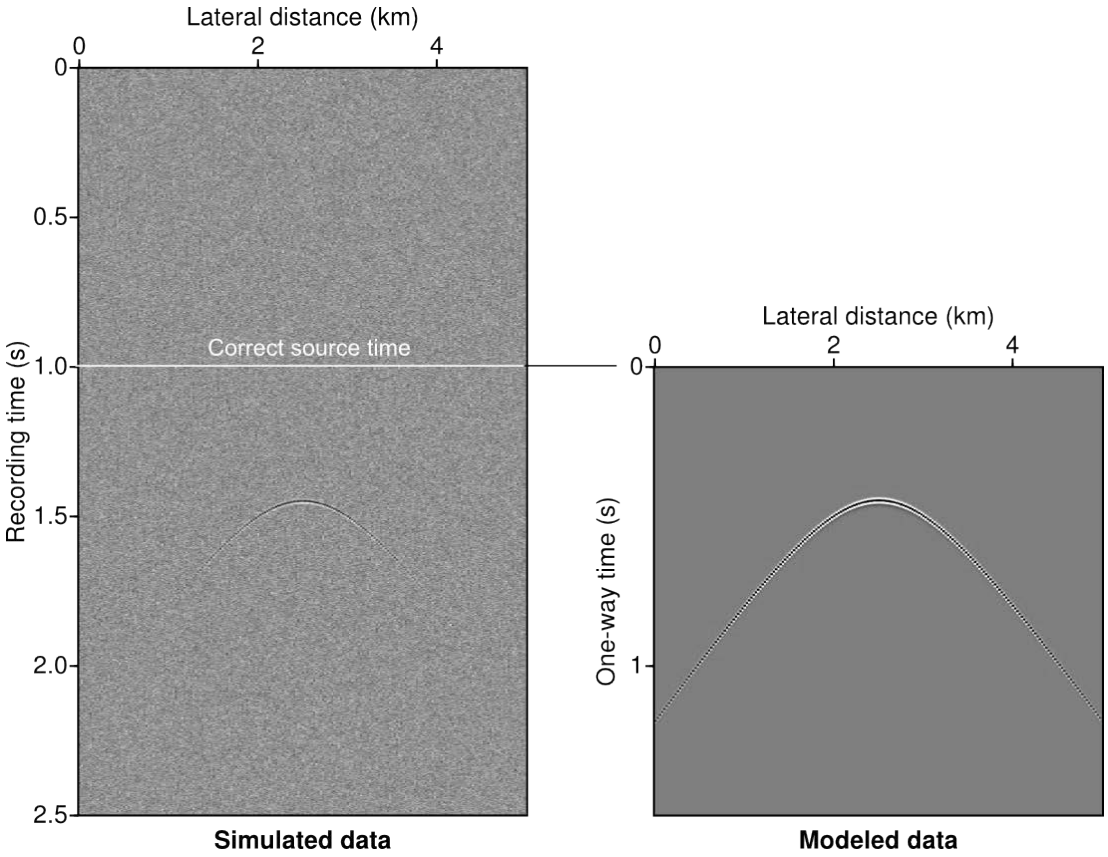

Figure 6.30.: The modeled one-way data (noise-free) on the right consists of a single source placed at 1 km depth in a constant vertical velocity gradient background (corresponding to a replacement of the diffractor in Figure E.1 by a passive seismic source). Since the main complications in passive seismic monitoring consist of missing information on the source time and a commonly low signal-to-noise ratio, a constant time delay and a sufficient amount of noise were added to the modeled data (left).

which subsets of the generalized operator (6.11) are used to sequentially measure the attributes p_{0x}, t_{shift} and t_0.

The first step is equivalent to the plane wave search suggested for the pragmatic CRS approach (e.g., Mann, 2002) and makes use of the first-order subset of the generalized passive operator (6.11)

$$\Delta t \approx \Delta t(p_{0x}) = p_{0x}\Delta x_g \quad . \tag{6.12}$$

Since I found in Chapter 4 that the slope attribute p_{0x}, i.e. the local traveltime dip, is independent of the choice of the auxiliary medium, the actual reference traveltime and the source excitation time both do not need to be known for this first measurement. The second step of the suggested pragmatic approach consists of a second-order moveout measurement for the optical projection of the problem, i.e. the time-shift mechanism. According to the findings in Chapter 4, time-shifted moveouts in general do also not depend on the actual reference time and therefore can also be accurately measured

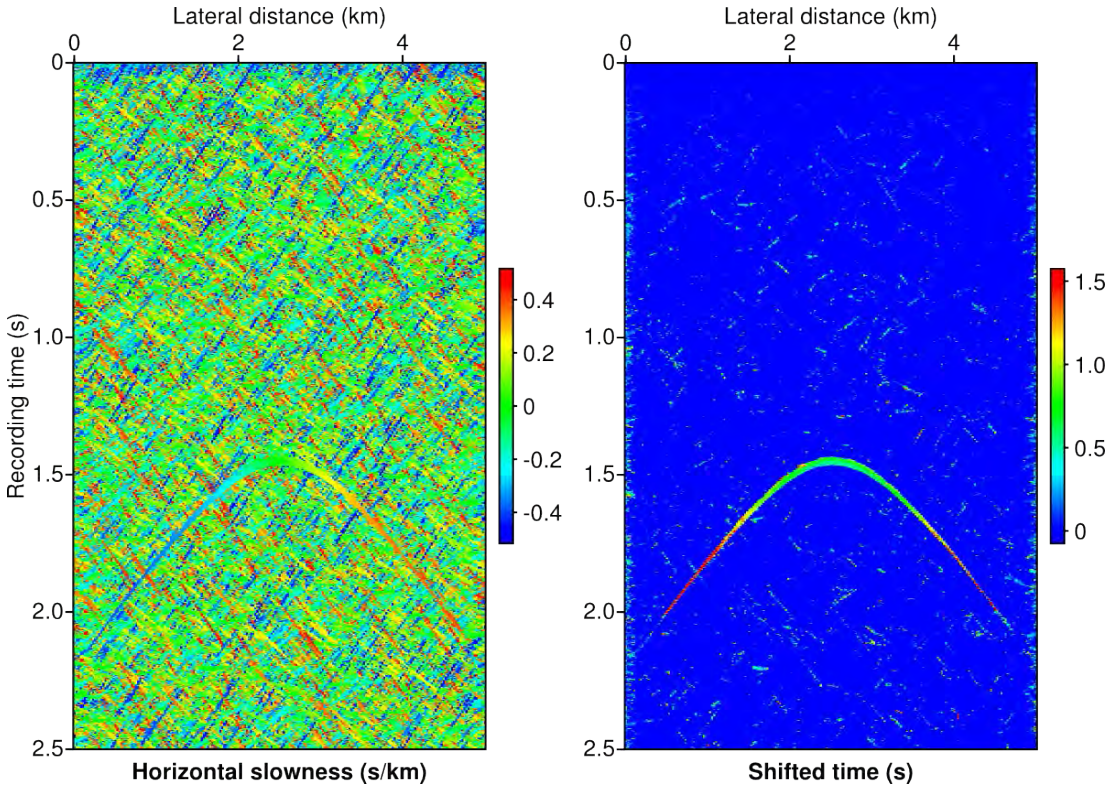

Figure 6.31.: Horizontal slowness (left) and shifted reference time (right) gained in the first and second step of the suggested time-based passive seismic workflow. Both of these attributes do not describe total traveltimes but only differences from trace to trace, i.e. traveltime moveout. Hence, they can be estimated without knowledge of the actual source time (see Chapter 4).

without the knowledge of t_0 and t_{source}

$$\Delta t = \Delta t(p_{0x}, t_{\text{shift}}) = \sqrt{(t_{\text{shift}} + p_{0x}\Delta x_g)^2 + (p_0^2 - p_{0x}^2)\Delta x_g^2} - t_{\text{shift}} \quad , \tag{6.13}$$

where $p_0 = 1/v_g$ is the inverse of the near-surface velocity, i.e. the near-surface slowness at the receiver. Since the horizontal slowness was gained in the preceding dip measurement (6.12), this second step, based on equation (6.13), consists again of a one parameter search, in this case for the shifted reference time t_{shift}.

While until now, only the time-shift mechanism was utilized, the third and final step of the suggested pragmatic scheme makes use of the second face, i.e. the velocity-shifted version of the passive moveout operator (6.11). At this point I would like to remind the reader of the general observation made in Section 4.5, according to which the velocity shift mechanism implies a dependency of the according moveout on the reference time, which in the context of moveout correction led to the undesired stretching of the seismic signal at shallow far offsets. In this frame, i.e. in the frame of a passive seismic experiment, this dependency of the velocity-shifted moveout on the actual reference time proves to be very valuable and allows for the inversion of the source excitation time. We have, again based on the preceding measurements of p_{0x}

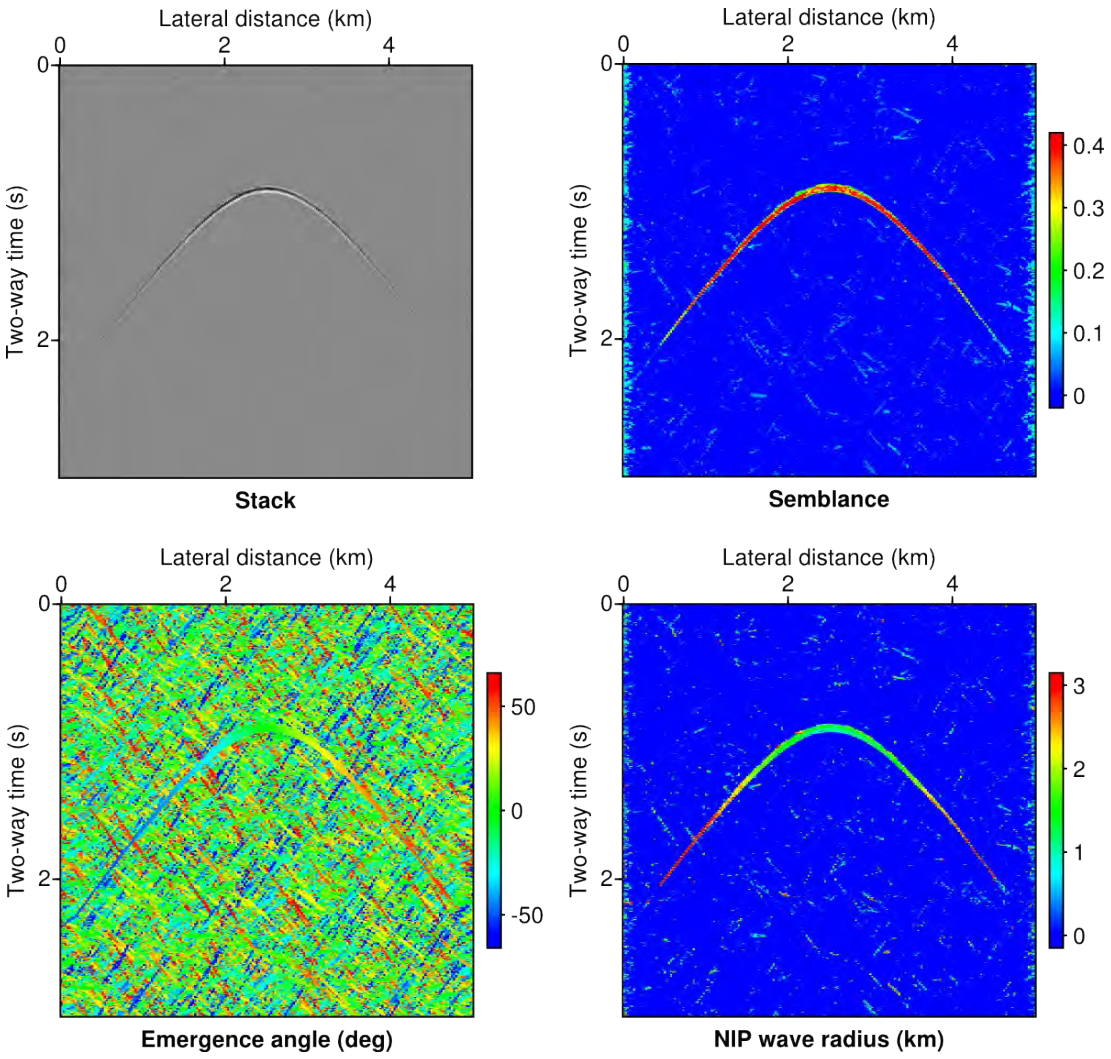

Figure 6.32.: Simulated two-way CRS attributes following from the application of the time-based passive seismic workflow proposed in this chapter. Since the source time inversion, which follows the estimation of the horizontal slownesses and the shifted reference times, relies on the complementing velocity shift mechanism, this approach to passive seismics uniquely combines the benefits of the general moveout duality formulated in Chapter 4.

and t_{shift}, a one-parameter optimization problem

$$\begin{aligned} t &= t_{\text{source}} + t_0 + \sqrt{(t_0 + p_{0x}\Delta x_g)^2 + [p^2_{\text{shift}}(t_0) - p^2_{0x}]\Delta x_g^2} - t_0 \\ &= t_{\text{source}} + \sqrt{(t_0 + p_{0x}\Delta x_g)^2 + [p^2_{\text{shift}}(t_0) - p^2_{0x}]\Delta x_g^2} \quad , \end{aligned} \tag{6.14}$$

with

$$p^2_{\text{shift}}(t_0) = p^2_{0x} + \frac{t_0}{t_{\text{shift}}}(p_0^2 - p^2_{0x}) \quad . \tag{6.15}$$

In the following, as announced in the beginning of this section, I will demonstrate the general applicabilty of the suggested passive seismic scheme for a simple synthetic data example, whose underlying model, to ensure comparability with preceding results, is the same vertical gradient as presented in the beginning of this chapter. In contrast to the configuration shown in Figure E.1, however, the diffractor is replaced by a seismic source and the acquisition is purely passive, i.e. only receivers are distributed at the surface. Figure 6.30 shows the modelling result on the right and the simulated passive experiment on the left, where an artificial time delay, which is assumed to be unknown and Gaussian noise with a signal-to-noise ratio of one were added to the data.

In Figure 6.31 the measured dip and time-shift sections are displayed. In accordance with the active seismic studies presented in the previous sections of this chapter, the attributes are reasonably smooth and coherent for the actual event, whereas for the noisy regions this smoothness cannot be observed. According to the formal correspondence of the passive seismic and the virtual NIP wave experiment, the measured dips and time shifts, according to the relations found in Section 4.2, can directly be translated to the emergence angle α and the NIP wave radius R_{NIP}. Together with the coherence and stack gained in one of the sub-searches and by correcting for the source excitation time, which, according to (6.11) follows directly from the measurement of the true reference time t_0, we arrive at attribute, stack and coherence sections, which, with the time axis multiplied by a factor of two, can directly be used as input for NIP wave tomography (see Figure 6.32). Observe in Figure 6.33 that, even though based on only a single passive event, the NIP-wave-based tomography achieves a reasonable inversion of the true velocity gradient, whose accuracy is comparable to the result gained for the two-way measurements with the hyperbolic CRS operator (compare Figure 6.29). Again, like for the active application, a constant velocity starting model with $v = v_g = 2$ km/s was chosen for the inversion.

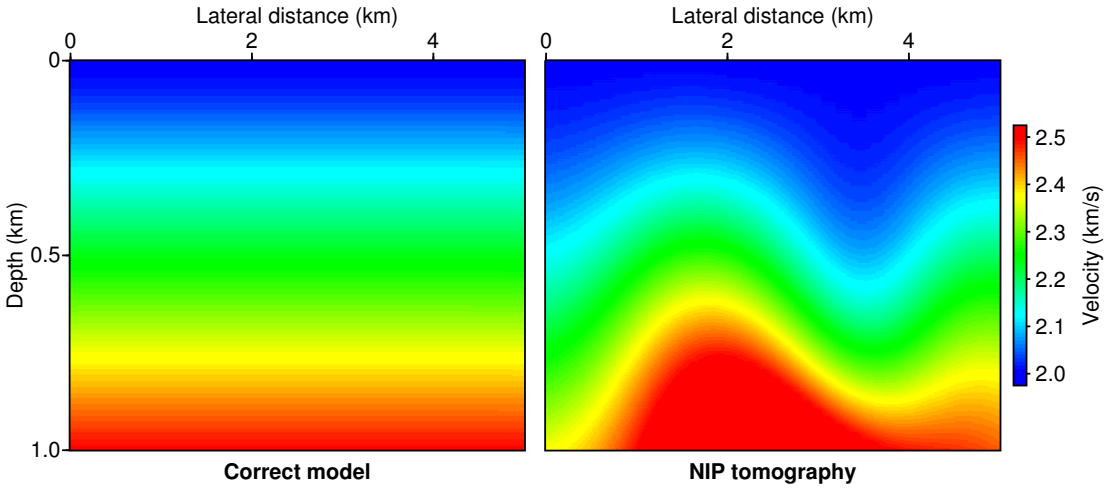

Figure 6.33.: Result of the two-way CRS-based NIP wave tomography applied to the passive seismic results. Although the correct model (left) could not be fully retrieved, the tomographic reconstruction is reasonably accurate in many parts and of similar quality as the hyperbolic CRS result in the active diffraction experiment (compare Figure 6.29(b)). Keeping in mind that this model was generated for a single event from a constant velocity starting guess (like in the active case), without knowledge of the source time and a high noise level contaminating the input data, the presented result indicates the strong potential of this fully automatic scheme.

7. Conclusions

Based on the concept of straight rays and circular wavefronts, I provided a unified view on higher-order traveltime moveout expressions. I revisited the insightful NIP and normal wave experiments, which utilize ray path symmetries to replace the two-way problem of reflection at an interface with a fictitious one-way experiment, which leads to the same moveout. In that context I argued that the general notion of a virtual seismic source can be utilized to explain moveout arising from complicated ray geometries by simple one-way wave propagation. In addition, I argue that the symmetry underlying the NIP experiment, which is based on reciprocity and Snell's reflection law, is also valid, if only finite-offset, i.e. a pure finite-offset configuration and, consequently, their CRP must be considered. Based on simple straight-ray geometry, I provided re-derivations of the hyperbolic CRS formula, multifocusing and the implicit CRS moveout. In this frame of circular wavefronts, I found that the implicit CRS, like multifocusing, can be considered a truly general approximation, since, in contrast to the hyperbolic operator, they reduce to the same exact expressions for a circular reflector in the zero-offset section, in the CRP gather and for a planar reflector. In addition, the special but important case of a diffractor and the CRE moveout, together with the CRE coordinate coupling relations, were shown to be naturally embedded in both operators, indicating the high potential for the unification of both approaches.

In the following, I showed that all traveltime operators, which provide the correct solution to a certain subsurface model, may be represented geometrically in an auxiliary medium of constant velocity. While most commonly, effects of heterogeneity are intuitively accounted for by shifting the constant velocity of the auxiliary medium, a shift in the reference time can lead to a similar adaptation of the traveltime moveout in the vicinity of a reference ray. Following from these findings and continuing the work of de Bazelaire in the late eighties, I suggested generalized expressions of the classical CMP hyperbola, conventional CRS, and the double-square-root implicit CRS and multifocusing operators, which may be shifted either in velocity or in time. As a consequence, I observed that the two different versions of each operator show systematically different behaviour in the presence of heterogeneity. This generalization revealed that the multifocusing moveout, in contrast to hyperbolic CRS and the implicit CRS, was originally formulated for the optical projection at the surface, where a time-shift accounts for heterogeneity. Comparison of double-square-root-based implicit CRS and multifocusing revealed that both operators are essentially equivalent, when the same auxiliary medium is considered. Application of both versions of an operator for simple synthetic gradient examples and the complex BP 2004 velocity benchmark dataset not only confirmed unification, but also revealed potential for diffraction or multiple identification, which lead to the design of improved diffraction filters. While time-shifted moveout corrections generally do not suffer from wavelet stretch, effective operators allow to invert for the true reference traveltime, which, in conjunction with dip and time shift measurements, lead to a purely data-driven time-based passive seismic workflow. So, in addition to the joint use, each representation turned out to have distinct advantages over the other in particular contexts of application.

Besides the moveout duality for heterogeneous media, the thorough and controlled investigation and discussion of the notion of globality formed the central ingredient of this thesis. While operators derived from paraxial ray theory generally face second-order limitations, I found that all presented straight-ray approximations, being based on the assumption of circular wavefronts, lead to higher-order accuracy for low levels of overburden heterogeneity and can even be considered exact for the specific model they can be derived from. For higher-order moveout analysis, I suggested a simple and intuitive matrix notation, which helps to distinguish mixed-order influences, responsible for coordinate coupling. I provided fourth-order finite-offset expansions of the hyperbolic CRS and the diffraction operator and found for the zero-offset diffraction case that the hyperbolic operator lacks sufficiently strong coupling, indicated by higher-order mixed terms, which are up to three times smaller than required for an accurate description. In addition, constant velocity comparison of the offset coefficients of the hyperbolic operator and the fourth-order expansion of the exact solution by Höcht et al. revealed, that the required higher-order influence of curvature, expressed by the normal wave, cannot be observed for the hyperbolic expression, which gives an intuitive explanation of its observed decreased quality of fit for diffractions. For the diffraction operator, this investigation of higher orders revealed a maximal coupling in the midpoint half-offset domain, where the cross-diagonal elements of the derivative matrix, representing elements of the same order, mixed or pure, either completely cancel or perfectly coincide, revealing a high redundancy of zero-offset and finite-offset information. This diffraction symmetry became most pronounced when source and receiver coordinates were considered, indicating a complete decoupling of the source and the receiver contributions of the moveout for all investigated orders. Based on the presented study of orders, I provide finite-offset expansion coefficients of the hyperbolic CRS, multifocusing and the implicit CRS, which can be used to extrapolate finite-offset traveltimes and attributes from zero-offset measurements. For diffractions, exploiting the complete decoupling of the source and receiver moveout contributions, I suggest a decomposition scheme, in which accurate finite-offset operators can be decomposed into two accurate zero-offset operators and vice versa.

Complementing the theoretical part of this thesis, in which simplification, unification and the understanding of error systematics of the considered moveout expressions were the central goals, I in addition suggest interesting potential applications arising from the observed symmetries and dualities. Following from the higher-order analysis of the hyperbolic CRS operator and the implicit CRS approximation, I provide a complex field data example, in which the suggested extrapolation equations led to accurate finite-offset slopes, whose quality could be confirmed by the corresponding generic finite-offset CRS results. In addition, efficient subsequent local finite-offset refinement in the full considered prestack volume led to increased quality of fit at higher offsets and fine structure in the attributes, which were shown to be in good agreement with the finite-offset reference. Following from the discussed notion of globality for the straight-ray operators and, utilizing the philosophy of the partial CRS approach, I suggested to use the zero-offset diffraction subset of the double-square-root implicit CRS moveout, expressed in its apex coordinates, for partial migration and its counterpart, expressed in conventional local coordinates, for the inverse process of partial demigration in time. Confirming the zero-offset results of Bobsin (2014) for the zero-offset migration, the application of the partial CRS migration to the complex field data example led to well-focused images for all considered offsets. The respective partial demigration could not

fully retain the initial state of the raw data. In particular for diffractions, waveforms appeared mildly distorted, which can partly be explained by the fact that, due to the use of different coordinates for migration and demigration, different attributes and, consequently, different operators were used for the two processes. However, the migration coherence, as a by-product of the partial migration, delivered high values only for diffractions, and therefore might be used as a diffraction map whose iterative demigration, in turn resulted in a prestack diffraction filter. Utilizing the virtual source concept underlying NIP wave tomography, I, in addition, presented a simple synthetic diffraction study, in which the double-square-root CRS operator, in contrast to the weakly coupled hyperbolic operator, delivered NIP wave attributes, which led to a reasonably accurate inversion of the true velocity gradient with a starting model of constant near-surface velocity. Concluding this thesis, I presented a data-driven time-based passive seismic workflow, which, being based on the virtual source concept, draws direct connections to the active seismic CRS workflow. Utilizing the formal coincidence of the fictitious NIP and the physically real passive seismic one-way experiment, subsequent inversion of the passive seismic wavefront measurements via NIP tomography resulted in a reasonable estimate for the true velocity gradient.

8. Discussion and outlook

8.1. Multiple operators

The derivations and theoretical investigations presented in the first part of this thesis mainly served two purposes,

- a formal and quantitative unification of existing approaches (where possible),
- a better understanding of the systematics of the existing differences.

While, from a theoretical viewpoint, it seems generally desirable to achieve unification and, consequently, simplification, the quantitative investigations in Chapter 6 could prove that a deeper and better understanding of existing deviations of different descriptions can in turn imply interesting and powerful applications, like, e.g., heterogeneity detection, multiple descrimination, diffraction characterization and the formulation of an efficient fully data-driven time-based passive seismic workflow.

The theoretical investigations on aspects of globality led to extrapolation or even decomposition relations (see Chapter 5), whose application in Chapter 6 resulted in a very efficient extrapolation and refinement scheme. For the presented field data example, the subsequent finite-offset refinement of extrapolated zero-offset attributes and traveltimes resulted in accurate finite-offset ray properties. Since, in that context, you start with a globally defined zero-offset operator to reach a reasonable finite-offset starting guess, I argue that it might be useful to locally refine, as suggested in Chapter 5 and Chapter 6 and in addition maintain the global connection of the finite-offset sub-operators, even during and after refinement. If those refined local finite-offset operators still *remember* to which neighbouring operators they belonged before local refinement (as a subset of the globally defined zero-offset operator used for extrapolation) one would achieve, in a data-driven manner, a global approximation with local accuracy and fine-structure (compare Figure 8.1). Consequently, the different finite-offset rays, corresponding to the respective finite-offset sub-operators would be described by one coupled multi-ray approximation.

Interestingly, diffractions, due to kinematic redundancy in their multicoverage response, are globally linked by identities like, e.g., (5.57), although the corresponding sub-operators could, in principle, be chosen arbitrarily small. First synthetic and field data applications of a decomposition stack (Bauer, 2014; Bauer et al., 2015), based on relations (5.57) revealed, although still at an early stage, that local zero-offset measurements carried out for comparably small apertures, resulted in a very high accuracy even for very large offsets. In addition to the possibility of an accurate description of finite-offset traveltimes entirely based on zero-offset measurements, the universal kinematic diffraction symmetry, in the circular wavefront picture expressed via (5.56) or (5.57), could also be used for locally accurate truly global diffraction separation, valid, in principle, for arbitrarily complex media.

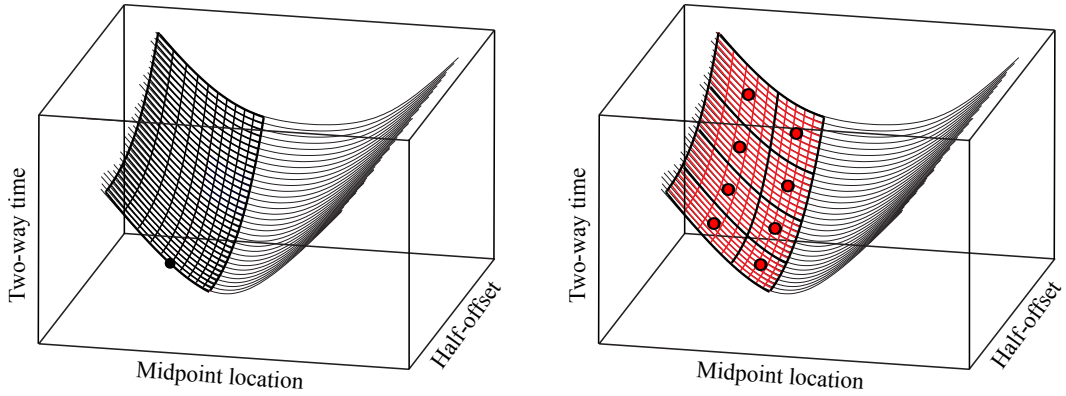

(a) One global operator (b) Many local operators

Figure 8.1.: The presented studies have shown that zero-offset moveout descriptions are reasonably accurate when lateral heterogeneity is moderate, but that local refinement of these global operators can significatly improve the fit for larger offsets.

8.2. Virtual source tomography

It can be concluded from the theoretical investigations in the first five chapters of this thesis, that there are two different views when approaching the important topic of moveout coupling. The first states that for a given set of coordinates, the traveltime moveout is influenced by generally two fictitious wavefront measurements. As was shown in Chapters 3, dealing with the straight-ray derivation of well-known operators and in Chapter 5, which is concerned with general aspects on globality, all double-square-root-type operators encounter the influence of curvature, commonly expressed by the normal wave radius, in orders higher than two (see, e.g., expressions (5.9)). This means that the virtual NIP and normal wave experiments are generally coupled with each other in the conventional midpoint half-offset and source receiver domains. The second point of view stated that, in order to describe the actual traveltime with only one wavefront measurement, the coordinates must be chosen according to Snell's law, generally implying a coupling between them.

The comparison of the parametric CRS by Höcht et al. (1999) and the implicit CRS by Schwarz et al. (2014c) (see Chapter 3 and Appendix B) clearly revealed this dual view on the phenomenon of coupling, since both description represent exactly the same moveout, i.e. the exact traveltime response for a reflector of circular shape with homogeneous overburden. While however, for the implicit CRS, the normal and the NIP wave both influence the finite-offset moveout, the parametric CRS approach describes the traveltimes with perfectly isolated NIP and normal wavefront measurements, but instead reveals coupling of the coordinates. Höcht et al. argued that for most actual applications, like the surface-based CRS stacking, their parametric expression is not well-suited, since, due to the fact that only certain coordinate combinations satisfy the CRP coupling condition, trace interpolation would be required.

For the finite-offset case, the shot and the receiver wavefront measurements are, even up to second order, generally not decoupled and therefore must be identified with two-way experiments, being excited at the source, encountering reflection at an interface

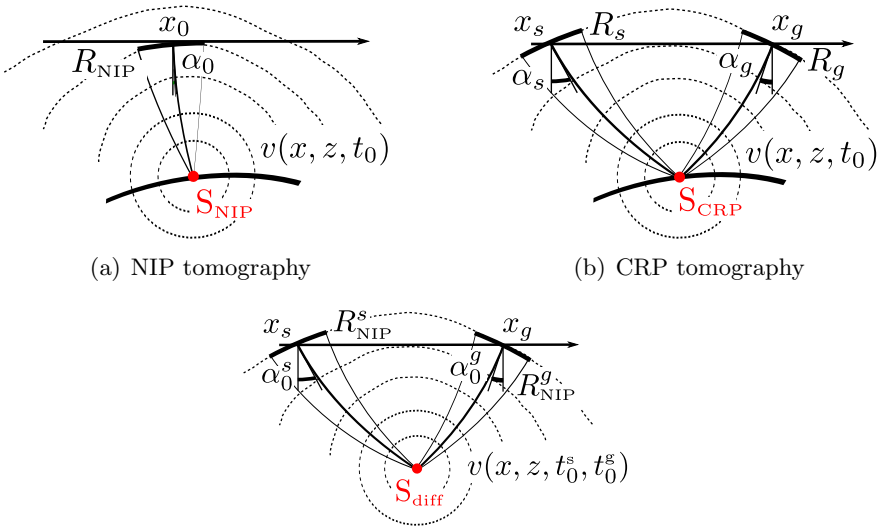

(a) NIP tomography

(b) CRP tomography

(c) Diffraction tomography

Figure 8.2.: NIP tomography aims at focusing the conceptual NIP wavefront, which is thought to originate at the virtual point source $\mathrm{S_{NIP}}$ (a). Following the same route, this concept could be extended to the more general case of a virtual source observed at the CRP in a finite-offset measurement (b). For the diffraction case (c), zero-offset and finite-offset measurements are not distinguishable, which is why standard NIP tomography applied to diffraction measurements should lead to an increased lateral resolution comparable to prestack CRP or stereotomography.

and emerging at the receiver (and vice versa). Due to the two-way character of the measured attributes and generally complex ray geometries, a straight-forward finite-offset velocity inversion scheme does not seem possible. If however, the finite-offset CRP experiment is considered (compare Figure 2.5 and Figure 3.10), the source and receiver wavefront measurements can, like in the NIP experiment for the zero-offset approximations, be related to one fictitious source in depth, coinciding with the true CRP location. The powerful implication is that, provided the finite-offset coordinate coupling is known, the focusing approach of the zero-offset based NIP tomography could be easily extended to a second-order finite-offset tomography, in which the CRP, like the NIP for the normal ray in NIP tomography, is interpreted as a virtual seismic source (compare Figure 8.2(a) and Figure 8.2(b)). The suggested concept of the finite-offset CRP tomography, in this context, could be viewed as a *marriage* of the highly illuminating prestack stereotomography approach by Billette and Lambaré (1998) and the beautifully simple and efficient focusing approach of NIP tomography.

In this context, I would like to emphasize the special yet very important subsurface configuration of a point diffractor, for which, as was shown in Chapter 5.4 and Chapter 5.5, zero-offset and finite-offset information is highly redundant (Schwarz et al., 2014b; Bauer, 2014). In the CRP interpretation, as emphasized before, the midpoint and half-offset coordinates turned out to be maximally coupled for diffractions, revealing a high degree of symmetry in this domain (see Figure 8.2(c)). The source and receiver coordinates, more importantly, were shown to be naturally decoupled, even for strongly heterogeneous media, when diffractions are considered. Following my proposal of the

extension of zero-offset NIP tomography to a finite-offset CRP tomography, I suggest that diffractions, due to their decoupling and the natural correspondence of zero-offset and finite-offset information, form the ideal (natural) virtual seismic source for focusing-based velocity inversion. The application of zero-offset NIP tomography, due to the fact that all corresponding ray segments are normal on the discontinuity, should be equivalent to finite-offset CRP tomography for the diffraction case.

8.3. Active and passive seismics

The concept of virtual seismic sources, by utilizing symmetries of the down and up-going ray segments, proved to be very useful, not only for traveltime moveout determination (see Chapter 2 and Chapter 3), but also for efficient focusing-based velocity model inversion (Duveneck, 2004). From a kinematic point of view, the main differences between the active and the passive seismic problem can be summarized as

- Two-way vs. one-way propagation,
- Known vs. unknown source (including its excitation time),
- redundancy.

Due to the fact that (for the considered case of first arrivals) only one-way propagation needs to be accounted for, the passive seismic setting is reasonably simple to describe by a single (true) wavefront measurement (e.g., Zhebel et al., 2011). As supported by this thesis, the two-way propagation of actively triggered controlled seismic sources, can in turn be described by fictitious one-way wavefronts. Therefore, I argue that the concept of a virtual seismic source, by invoking natural symmetries between the down and up-going ray paths, formally, creates a strong link between the active two-way and the passive one-way geometry.

As I tried to motivate in the final part of this thesis, which is focused on applications, the CRS stack, logistically and physically, can be viewed as essentially the most general purely data-driven time-imaging construction, covering traditional stacking and attribute extraction, interpolation, regularization and migration (see Chapter 6). With the incorporation of symmetry principles and a corresponding generalized one-way description (based on the assumption of virtual sources) I argue, backed up by the simple synthetic study in Chapter 6, that in general, CRS-related concepts, commonly deployed in active settings, can also prove to be very useful for solving passive seismic problems.

Appendices

A. Proof of the CRP/CRE equivalence

It was argued in Chapter 3 that both, implicit CRS and multifocusing, reduce to exactly the same expression in the CRP gather

$$t = \frac{\sqrt{R_{\mathrm{NIP}}^2 + 2R_{\mathrm{NIP}}(\Delta x_m - h)\sin\alpha + (\Delta x_m - h)^2}}{v} + \frac{\sqrt{R_{\mathrm{NIP}}^2 + 2R_{\mathrm{NIP}}(\Delta x_m + h)\sin\alpha + (\Delta x_m + h)^2}}{v} \quad . \tag{A.1}$$

which could be identified with the CRE moveout by Gelchinsky et al. (1999). While the equivalence of the connected coordinate coupling (3.28), formulated in terms of source and receiver displacements, follows directly from the insertion of relations (2.1), the proof of the equivalence of (A.1) and the CRP expression (3.26a) found by Höcht et al. (1999) invokes some lengthy algebra. Therefore, in this part of the appendix, I provide a sketch of the according derivations. In the first step, I take the square on both sides of (A.1) and arrive at

$$\frac{v^2t^2}{R_{\mathrm{NIP}}^2} = \left(\sqrt{\frac{(\Delta x_m - h)^2}{R_{\mathrm{NIP}}^2} + \frac{\Delta x_m - h}{r_{\mathrm{T}}} + 1} + \sqrt{\frac{(\Delta x_m + h)^2}{R_{\mathrm{NIP}}^2} + \frac{\Delta x_m + h}{r_{\mathrm{T}}} + 1}\right)^2 \quad , \tag{A.2}$$

where $2r_{\mathrm{T}} = \sin\alpha / R_{\mathrm{NIP}}$. In the following, partial insertion of the coordinate coupling (3.26b) leads to a step-wise simplification and an increased incorporation of the half-offset h. We get

$$\frac{v^2t^2}{R_{\mathrm{NIP}}^2} = \frac{4h^2}{R_{\mathrm{NIP}}^2} + \frac{4r_{\mathrm{T}}^2}{R_{\mathrm{NIP}}^2} - \frac{4r_{\mathrm{T}}\sqrt{h^2 + r_{\mathrm{T}}^2}}{R_{\mathrm{NIP}}^2} + 2\sqrt{\frac{h^2}{r_{\mathrm{T}}^2} + 1} + B \quad , \tag{A.3}$$

where

$$\begin{aligned} B &= 2\sqrt{\frac{(\Delta x_m^2 - h^2)^2}{R_{\mathrm{NIP}}^4} + \frac{\Delta x_m^2 - h^2}{r_{\mathrm{T}}^2} + 1 + \frac{2\Delta x_m(\Delta x_m^2 - h^2)}{R_{\mathrm{NIP}}^2 r_{\mathrm{T}}} + \frac{2(\Delta x_m^2 + h^2)}{R_{\mathrm{NIP}}^2} + \frac{2\Delta x_m}{r_{\mathrm{T}}}} \\ &= 2\sqrt{\frac{(\Delta x_m^2 - h^2)^2}{R_{\mathrm{NIP}}^4} + \frac{\Delta x_m^2}{r_{\mathrm{T}}^2} - \frac{h^2}{r_{\mathrm{T}}^2} + 1 + 2\sqrt{\frac{h^2}{r_{\mathrm{T}}^2} + 1}\frac{\Delta x_m^2 - h^2}{R_{\mathrm{NIP}}^2} + \frac{4h^2}{R_{\mathrm{NIP}}^2} + \frac{2\Delta x_m}{r_{\mathrm{T}}}} \\ &= 2\sqrt{\frac{(\Delta x_m^2 - h^2)^2}{R_{\mathrm{NIP}}^4} + 1 + 2\sqrt{\frac{h^2}{r_{\mathrm{T}}^2} + 1}\frac{\Delta x_m^2 - h^2}{R_{\mathrm{NIP}}^2} + \frac{4h^2}{R_{\mathrm{NIP}}^2}} \quad . \end{aligned} \tag{A.4}$$

By inserting

$$\Delta x_m^2 - h^2 = r_{\mathrm{T}}^2\left(2 - 2\sqrt{\frac{h^2}{r_{\mathrm{T}}^2} + 1}\right)$$

and

$$(\Delta x_m^2 - h^2)^2 = 4r_{\mathrm{T}}^4\left(2 - 2\sqrt{\frac{h^2}{r_{\mathrm{T}}^2} + 1} + \frac{h^2}{r_{\mathrm{T}}^2}\right) \tag{A.5}$$

into expression (A.4) we get

$$\begin{aligned}
\Rightarrow B &= 2\sqrt{\frac{4r_{\mathrm{T}}^4}{R_{\mathrm{NIP}}^4}\left(2-2\sqrt{\frac{h^2}{r_{\mathrm{T}}^2}+1}+\frac{h^2}{r_{\mathrm{T}}^2}\right)+1-\frac{2r_{\mathrm{T}}^2}{R_{\mathrm{NIP}}^2}\left(2-2\sqrt{\frac{h^2}{r_{\mathrm{T}}^2}+1}\right)} \\
&= 2\sqrt{\frac{4r_{\mathrm{T}}^4}{R_{\mathrm{NIP}}^4}\left(1-\sqrt{\frac{h^2}{r_{\mathrm{T}}^2}+1}\right)^2-\frac{4r_{\mathrm{T}}^2}{R_{\mathrm{NIP}}^2}\left(1-\sqrt{\frac{h^2}{r_{\mathrm{T}}^2}+1}\right)+1} \\
&= 2\sqrt{\left[1-\frac{2r_{\mathrm{T}}^2}{R_{\mathrm{NIP}}^2}\left(1-\sqrt{\frac{h^2}{r_{\mathrm{T}}^2}+1}\right)\right]^2} \\
&= 2-\frac{4r_{\mathrm{T}}^2}{R_{\mathrm{NIP}}^2}+\frac{4r_{\mathrm{T}}^2}{R_{\mathrm{NIP}}^2}\sqrt{\frac{h^2}{r_{\mathrm{T}}^2}+1}. \qquad \text{(A.6)}
\end{aligned}$$

Finally, the re-substitution of (A.6) into (A.3) results in the desired CRP expression found by Höcht et al. (1999)

$$\Rightarrow t^2 = \frac{4R_{\mathrm{NIP}}^2}{v^2}\frac{1}{2}\left(\sqrt{\frac{h^2}{r_{\mathrm{T}}^2}+1}+1\right)+\frac{4h^2}{v^2} \quad . \qquad \text{(A.7)}$$

Consequently, the CRE and the CRP formulae can be considered equivalent descriptions.

B. Parametric CRS vs. implicit CRS

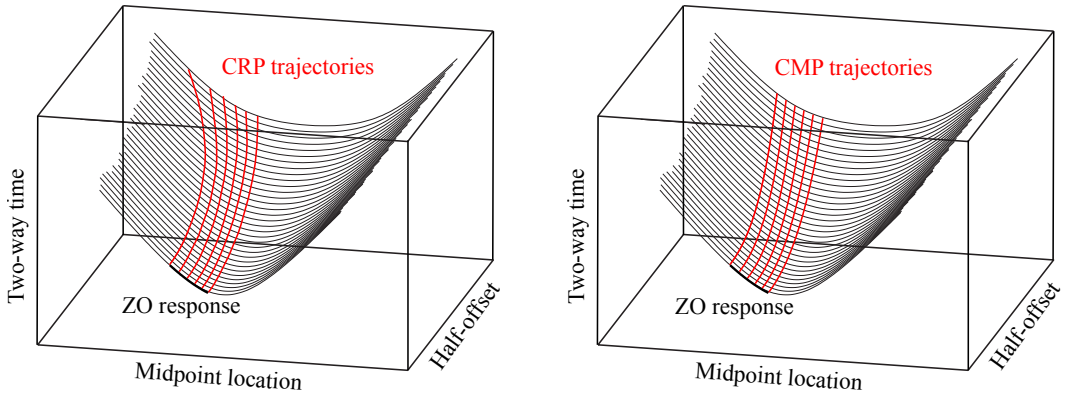

(a) Parametric CRS (b) Implicit CRS

Figure B.1.: While the parametric CRS introduced by Höcht et al. (1999) combines neighbouring CRP trajectories (a), the implicit CRS describes the moveout in adjacent CMP gathers (Vanelle et al., 2010; Schwarz, 2011). Both descriptions provide the exact solution for a circular interface and are coupled by the same relations to the same zero-offset (ZO) response.

As was found in Section 3.5, the three double-square-root operators of multifocusing, implicit CRS and parametric CRS can all be described by the same expression (3.16) in the zero-offset section and reduce to the same expressions (3.26) in the CRP gather. It was therefore concluded that the only differences between these operators constitute in the way the zero-offset and CRP experiment are linked to each other. It was found that the following set of relations can be used to link CRP gathers to a CRS-like traveltime surface

$$\Delta x_m = R_{\mathrm{N}}(\cos\alpha\tan\tilde{\alpha} - \sin\alpha) \quad , \tag{B.1a}$$

$$\tilde{R}_{\mathrm{NIP}} = R_{\mathrm{N}}\left(\frac{\cos\alpha}{\cos\tilde{\alpha}} - 1\right) \quad , \tag{B.1b}$$

where $\tilde{\alpha} = \alpha(\Delta x_m)$ and $\tilde{R}_{\mathrm{NIP}} = R_{\mathrm{NIP}}(\Delta x_m)$. It can be shown that the CRP moveout (3.26) is equivalent to the CRE expression (3.27) initially found by Gelchinsky et al. (1999) (see Appendix A). Isolating $\tilde{\alpha}$ in equations (B.1) then leads to

$$\tan\tilde{\alpha} = \tan\alpha + \frac{\Delta x_m}{R_{\mathrm{N}}\cos\alpha} \quad , \tag{B.2a}$$

$$\tilde{R}_{\mathrm{NIP}}\cos\tilde{\alpha} = R_{\mathrm{N}}\cos\alpha - (R_{\mathrm{N}} - R_{\mathrm{NIP}})\cos\tilde{\alpha}. \tag{B.2b}$$

Inserting these expressions, together with the sine definition corresponding to (B.2b)

into the CRE moveout (3.27) yields[1]

$$t = \frac{\sqrt{[\Delta x_s + R_\mathrm{N} \sin\alpha - (R_\mathrm{N} - R_\mathrm{NIP}) \sin\theta]^2 + [R_\mathrm{N} \cos\alpha - (R_\mathrm{N} - R_\mathrm{NIP}) \cos\theta]^2}}{v} + \frac{\sqrt{[\Delta x_g + R_\mathrm{N} \sin\alpha - (R_\mathrm{N} - R_\mathrm{NIP}) \sin\theta]^2 + [R_\mathrm{N} \cos\alpha - (R_\mathrm{N} - R_\mathrm{NIP}) \cos\theta]^2}}{v}, \tag{B.3}$$

which, together with (B.2a) is equivalent to the implicit CRS operator in the zero-offset section (compare the corresponding expressions in Section 3.4). Figure B.1 shows the only conceptual difference between the implicit CRS by Schwarz (2011) and the parametric CRS by Höcht et al. (1999). While the description in the zero-offset section and the link to the finite offsets is absolutely equivalent, the parametric CRS links descriptions of many neighbouring CRP gathers, whereas the implicit CRS combines many neighbouring CMPs.

[1] In this cause, the angle $\tilde{\alpha}$ is identified with the reflection point angle θ.

C. Taylor expansion coefficients

In this chapter of the appendix I provide detailed derivations of the Taylor series expansion coefficients presented and utilized in Chapter 5 and Chapter 6. Since some of the derivations invoke relatively simple but cumbersome algebra, I give more detail to these parts and introduce abbreviations or substitutions where necessary. In general, it is important to note that the different geometrically derived operators considered throughout this thesis show distinct and different behaviour in the shot receiver (x_s, x_g) and the midpoint half-offset domain (x_m, h). Since the important arguments about globality and coupling (see Chapter 5) and in particular the presented diffraction symmetries (Section 5.5) can rely on the specific differences of these domains, I start with a quick reminder of how the two sets of coordinates and their respective derivatives are connected. For the coordinates themselves, equations (2.1) apply, whereas the first-order derivatives of a traveltime operator t are connected via

$$\frac{\partial t}{\partial x_m} = \frac{\partial t}{\partial x_s}\frac{\partial x_s}{\partial x_m} + \frac{\partial t}{\partial x_g}\frac{\partial x_g}{\partial x_m} = \frac{\partial t}{\partial x_s} + \frac{\partial t}{\partial x_g} \quad , \tag{C.1a}$$

$$\frac{\partial t}{\partial h} = \frac{\partial t}{\partial x_s}\frac{\partial x_s}{\partial h} + \frac{\partial t}{\partial x_g}\frac{\partial x_g}{\partial h} = \frac{\partial t}{\partial x_g} - \frac{\partial t}{\partial x_s} \quad , \tag{C.1b}$$

$$\frac{\partial t}{\partial x_s} = \frac{\partial t}{\partial x_m}\frac{\partial x_m}{\partial x_s} + \frac{\partial t}{\partial h}\frac{\partial h}{\partial x_s} = \frac{1}{2}\left(\frac{\partial t}{\partial x_m} - \frac{\partial t}{\partial h}\right) \quad , \tag{C.1c}$$

$$\frac{\partial t}{\partial x_g} = \frac{\partial t}{\partial x_m}\frac{\partial x_m}{\partial x_g} + \frac{\partial t}{\partial h}\frac{\partial h}{\partial x_g} = \frac{1}{2}\left(\frac{\partial t}{\partial x_m} + \frac{\partial t}{\partial h}\right) \quad . \tag{C.1d}$$

By sequential application of the chain rule, we arrive at similar relations for the pure and mixed second-order derivatives,

$$\frac{\partial^2 t}{\partial x_m^2} = \frac{\partial^2 t}{\partial x_s^2} + \frac{\partial^2 t}{\partial x_g^2} + 2\frac{\partial^2 t}{\partial x_s \partial x_g}, \tag{C.2a}$$

$$\frac{\partial^2 t}{\partial h^2} = \frac{\partial^2 t}{\partial x_s^2} + \frac{\partial^2 t}{\partial x_g^2} - 2\frac{\partial^2 t}{\partial x_s \partial x_g}, \tag{C.2b}$$

$$\frac{\partial^2 t}{\partial x_m \partial h} = \frac{\partial^2 t}{x_g^2} - \frac{\partial^2 t}{x_s^2} \quad , \tag{C.2c}$$

$$\frac{\partial^2 t}{\partial x_s^2} = \frac{1}{4}\left[\frac{\partial^2 t}{\partial x_m^2} + \frac{\partial^2 t}{\partial h^2} - 2\frac{\partial^2 t}{\partial x_m \partial h}\right] \quad , \tag{C.2d}$$

$$\frac{\partial^2 t}{\partial x_g^2} = \frac{1}{4}\left[\frac{\partial^2 t}{\partial x_m^2} + \frac{\partial^2 t}{\partial h^2} + 2\frac{\partial^2 t}{\partial x_m \partial h}\right] \quad , \tag{C.2e}$$

$$\frac{\partial^2 t}{\partial x_s \partial x_g} = \frac{1}{4}\left[\frac{\partial^2 t}{x_m^2} - \frac{\partial^2 t}{h^2}\right] \quad . \tag{C.2f}$$

One of the main interests in expanding the different geometrical moveout expressions, in particular multifocusing (Gelchinsky et al., 1999) and the implicit common reflection surface (Vanelle et al., 2010; Schwarz, 2011) was to establish extrapolation equations for the second-order finite-offset CRS coefficients (Zhang et al., 2001). Although I also present expansions up to fourth order for the diffraction moveout and the hyperbolic CRS expression, I restrict myself to the above transformation relations.

C.1. Diffraction moveout (up to fourth order)

Midpoint half-offset coordinates

The zero-offset diffraction moveout is a special case, in which the traveltime differences are sufficiently described by the attributes of the NIP wave α and R_{NIP}. Both, the multifocusing moveout and implicit CRS, reduce to this expression when $R_{\mathrm{N}} = R_{\mathrm{NIP}}$. Expressed in midpoint and half-offset coordinates and following the convenient derivative matrix notation introduced in Section 5.1, the diffraction operator for a homogeneous medium with constant velocity v reads

$$t_{00} = \frac{S_{00} + G_{00}}{v} \tag{C.3}$$

with

$$S_{00} = \sqrt{(\Delta x_m - h + R_{\mathrm{NIP}} \sin\alpha)^2 + R_{\mathrm{NIP}}^2 \cos^2\alpha} \quad , \tag{C.4a}$$

$$G_{00} = \sqrt{(\Delta x_m + h + R_{\mathrm{NIP}} \sin\alpha)^2 + R_{\mathrm{NIP}}^2 \cos^2\alpha} \quad . \tag{C.4b}$$

The first derivative of the traveltime operator can, due to the double-square-root shape of the diffraction operator (C.3), be separated into two contributions,

$$t_{10} = \frac{\partial t_{00}}{\partial x_m} = \frac{1}{v}\left[S_{00} + G_{00}\right]_{10} = \frac{S_{10} + G_{10}}{v} \quad , \tag{C.5a}$$

$$t_{01} = \frac{\partial t_{00}}{\partial x_m} = \frac{1}{v}\left[S_{00} + G_{00}\right]_{01} = \frac{S_{01} + G_{01}}{v} \quad , \tag{C.5b}$$

where

$$S_{10} = \frac{\Delta x_m - h + R_{\mathrm{NIP}} \sin\alpha}{S_{00}} \quad , \tag{C.6a}$$

$$G_{10} = \frac{\Delta x_m + h + R_{\mathrm{NIP}} \sin\alpha}{G_{00}} \quad , \tag{C.6b}$$

$$S_{01} = \frac{-(\Delta x_m - h + R_{\mathrm{NIP}} \sin\alpha)}{S_{00}} \quad , \tag{C.6c}$$

$$G_{01} = \frac{\Delta x_m + h + R_{\mathrm{NIP}} \sin\alpha}{G_{00}} \quad . \tag{C.6d}$$

The higher-order derivatives of the diffraction traveltime can, accordingly, also be separated into two different contributions (see also Section 5.1). Thus, the components of the midpoint half-offset derivative matrix $\underline{\mathbf{T}}_{mh}$ can be written

$$t_{ij} = \frac{1}{v(i+j)!}\left(S_{ij} + G_{ij}\right) \quad . \tag{C.7}$$

For the second-order midpoint derivatives we get

$$S_{20} = \left[S_{10}\right]_{10} = \frac{1 - S_{10}^2}{S_{00}} \quad , \tag{C.8a}$$

$$G_{20} = \left[G_{10}\right]_{10} = \frac{1 - G_{10}^2}{G_{00}} \quad , \tag{C.8b}$$

while the half-offset derivatives can be written as

$$S_{02} = \left[S_{01}\right]_{01} = \frac{1 - S_{01}^2}{S_{00}} \quad , \tag{C.9a}$$

$$G_{02} = \left[G_{10}\right]_{10} = \frac{1 - G_{01}^2}{G_{00}} \quad . \tag{C.9b}$$

The mixed second-order terms, as motivated in Chapter 5, describe the second-order coupling between the two coordinates, as described by the considered traveltime operator,

$$S_{11} = [S_{01}]_{10} = -\frac{1 + S_{10}S_{01}}{S_{00}} \quad , \tag{C.10a}$$

$$G_{11} = [G_{01}]_{10} = \frac{1 - G_{10}G_{01}}{G_{00}} \quad . \tag{C.10b}$$

According to the NIP wave theorem (Hubral, 1983), these mixed terms vanish for the zero-offset case. Nevertheless, diffractions are still highly coupled in the midpoint half-offset domain, which reflects in the higher-order derivatives (presented up to order four),

$$S_{30} = [S_{20}]_{10} = -\frac{3S_{10}S_{20}}{S_{00}} \quad , \tag{C.11a}$$

$$G_{30} = [G_{20}]_{10} = -\frac{3G_{10}G_{20}}{G_{00}} \quad , \tag{C.11b}$$

$$S_{03} = [S_{02}]_{01} = -\frac{3S_{01}S_{02}}{S_{00}} \quad , \tag{C.11c}$$

$$G_{03} = [G_{02}]_{01} = -\frac{3G_{01}G_{02}}{G_{00}} \quad , \tag{C.11d}$$

$$S_{21} = [S_{20}]_{01} = [S_{11}]_{10} = -\frac{2S_{10}S_{11} + S_{01}S_{20}}{S_{00}} \quad , \tag{C.11e}$$

$$G_{21} = [G_{20}]_{01} = [G_{11}]_{10} = -\frac{2G_{10}G_{11} + G_{01}G_{20}}{G_{00}} \quad , \tag{C.11f}$$

$$S_{12} = [S_{02}]_{10} = [S_{11}]_{01} = -\frac{2S_{01}S_{11} + S_{10}S_{02}}{S_{00}} \quad , \tag{C.11g}$$

$$G_{12} = [G_{02}]_{10} = [G_{11}]_{01} = -\frac{2G_{01}G_{11} + G_{10}G_{02}}{G_{00}} \quad , \tag{C.11h}$$

$$S_{40} = [S_{30}]_{10} = -\frac{3S_{20}^2 + 4S_{10}S_{30}}{S_{00}} \quad , \tag{C.11i}$$

$$G_{40} = [G_{30}]_{10} = -\frac{3G_{20}^2 + 4G_{10}G_{30}}{G_{00}} \quad , \tag{C.11j}$$

$$S_{04} = [S_{03}]_{01} = -\frac{3S_{02}^2 + 4S_{01}S_{03}}{S_{00}} \quad , \tag{C.11k}$$

$$G_{04} = [G_{03}]_{01} = -\frac{3G_{02}^2 + 4G_{01}G_{03}}{G_{00}} \quad , \tag{C.11l}$$

$$S_{31} = [S_{30}]_{01} = [S_{21}]_{10} = -\frac{3S_{11}S_{20} + 3S_{10}S_{21} + S_{01}S_{30}}{S_{00}} \quad , \tag{C.11m}$$

$$G_{31} = [G_{30}]_{01} = [G_{21}]_{10} = -\frac{3G_{11}G_{20} + 3G_{10}G_{21} + G_{01}G_{30}}{G_{00}} \quad , \tag{C.11n}$$

$$S_{13} = [S_{03}]_{10} = [S_{12}]_{01} = -\frac{3S_{11}S_{02} + 3S_{01}S_{12} + S_{10}S_{03}}{S_{00}} \quad , \tag{C.11o}$$

$$G_{13} = [G_{03}]_{10} = [G_{12}]_{01} = -\frac{3G_{11}G_{02} + 3G_{01}G_{12} + G_{10}G_{03}}{G_{00}} \quad , \tag{C.11p}$$

$$S_{22} = [S_{21}]_{01} = [S_{12}]_{10} = -\frac{2S_{11}^2 + 2S_{10}S_{12} + 2S_{01}S_{21} + S_{20}S_{02}}{S_{00}} \quad , \tag{C.11q}$$

$$G_{22} = [G_{21}]_{01} = [G_{12}]_{10} = -\frac{2G_{11}^2 + 2G_{10}G_{12} + 2G_{01}G_{21} + G_{20}G_{02}}{G_{00}} \quad . \tag{C.11r}$$

Source receiver coordinates

Shot and receiver coordinates are the more natural choice, when asymmetric source receiver ray paths are considered (Schwarz, 2011). While the derivative matrices in the midpoint half-offset domain reveal a generally non-vanishing coupling for finite-offset and zero-offset (check equations C.11), the mixed terms, responsible for the coupling, vanish when shot and receiver coordinates are chosen. Again, as introduced in Chapter 5.1 and like in the midpoint half-offset case, the components of the source receiver diffraction traveltime derivative matrix $\underline{\mathbf{T}}_{sg}$ can be expressed by the respective source and receiver branches via

$$\mathcal{T}_{ij} = \frac{1}{v(i+j)!}\left(\mathcal{S}_{ij} + \mathcal{G}_{ij}\right) \quad , \tag{C.12a}$$

with the pure derivatives

$$\mathcal{S}_{10} = [\mathcal{S}_{00}]_{10} = \frac{\Delta x_s + R_{\mathrm{NIP}} \sin\alpha}{\mathcal{S}_{00}} \quad , \tag{C.13a}$$
$$\mathcal{G}_{10} = [\mathcal{G}_{00}]_{10} = 0 \quad , \tag{C.13b}$$
$$\mathcal{S}_{01} = [\mathcal{S}_{00}]_{01} = 0 \quad , \tag{C.13c}$$
$$\mathcal{G}_{01} = [\mathcal{G}_{00}]_{01} = \frac{\Delta x_g + R_{\mathrm{NIP}} \sin\alpha}{\mathcal{G}_{00}} \quad , \tag{C.13d}$$
$$\mathcal{S}_{20} = [\mathcal{S}_{10}]_{10} = \frac{1 - \mathcal{S}_{10}^2}{\mathcal{S}_{00}} \quad , \tag{C.13e}$$
$$\mathcal{G}_{20} = [\mathcal{G}_{10}]_{10} = 0 \quad , \tag{C.13f}$$
$$\mathcal{S}_{02} = [\mathcal{S}_{01}]_{01} = 0 \quad , \tag{C.13g}$$
$$\mathcal{G}_{02} = [\mathcal{G}_{01}]_{01} = \frac{1 - \mathcal{G}_{01}^2}{\mathcal{G}_{00}} \quad , \tag{C.13h}$$
$$\mathcal{S}_{30} = [\mathcal{S}_{20}]_{10} = -\frac{3\mathcal{S}_{10}\mathcal{S}_{20}}{\mathcal{S}_{00}} \quad , \tag{C.13i}$$
$$\mathcal{G}_{30} = [\mathcal{G}_{20}]_{10} = 0 \quad , \tag{C.13j}$$
$$\mathcal{S}_{03} = [\mathcal{S}_{02}]_{01} = 0 \quad , \tag{C.13k}$$
$$\mathcal{G}_{03} = [\mathcal{G}_{02}]_{01} = -\frac{3\mathcal{G}_{01}\mathcal{G}_{02}}{\mathcal{G}_{00}} \quad , \tag{C.13l}$$
$$\mathcal{S}_{40} = [\mathcal{S}_{30}]_{10} = -\frac{3\mathcal{S}_{20}^2 + 4\mathcal{S}_{10}\mathcal{S}_{30}}{\mathcal{S}_{00}} \quad , \tag{C.13m}$$
$$\mathcal{G}_{40} = [\mathcal{G}_{30}]_{10} = 0 \quad , \tag{C.13n}$$
$$\mathcal{S}_{04} = [\mathcal{S}_{03}]_{01} = 0 \quad , \tag{C.13o}$$
$$\mathcal{G}_{04} = [\mathcal{G}_{03}]_{01} = -\frac{3\mathcal{G}_{02}^2 + 4\mathcal{G}_{01}\mathcal{G}_{03}}{\mathcal{G}_{00}} \tag{C.13p}$$

and the coupling terms

$$\mathcal{S}_{11} = [\mathcal{S}_{10}]_{01} = [\mathcal{S}_{01}]_{10} = 0 \quad , \tag{C.14a}$$
$$\mathcal{G}_{11} = [\mathcal{G}_{10}]_{01} = [\mathcal{G}_{01}]_{10} = 0 \quad , \tag{C.14b}$$
$$\mathcal{S}_{21} = [\mathcal{S}_{20}]_{01} = [\mathcal{S}_{11}]_{10} = 0 \quad , \tag{C.14c}$$
$$\mathcal{G}_{21} = [\mathcal{G}_{20}]_{01} = [\mathcal{G}_{11}]_{10} = 0 \quad , \tag{C.14d}$$
$$\mathcal{S}_{12} = [\mathcal{S}_{11}]_{01} = [\mathcal{S}_{02}]_{10} = 0 \quad , \tag{C.14e}$$
$$\mathcal{G}_{12} = [\mathcal{G}_{11}]_{01} = [\mathcal{G}_{02}]_{10} = 0 \quad , \tag{C.14f}$$
$$\mathcal{S}_{31} = [\mathcal{S}_{30}]_{01} = [\mathcal{S}_{21}]_{10} = 0 \quad , \tag{C.14g}$$
$$\mathcal{G}_{31} = [\mathcal{G}_{30}]_{01} = [\mathcal{G}_{21}]_{10} = 0 \quad , \tag{C.14h}$$
$$\mathcal{S}_{13} = [\mathcal{S}_{12}]_{01} = [\mathcal{S}_{03}]_{10} = 0 \quad , \tag{C.14i}$$
$$\mathcal{G}_{13} = [\mathcal{G}_{12}]_{01} = [\mathcal{G}_{03}]_{10} = 0 \quad , \tag{C.14j}$$
$$\mathcal{S}_{22} = [\mathcal{S}_{21}]_{01} = [\mathcal{S}_{12}]_{10} = 0 \quad , \tag{C.14k}$$
$$\mathcal{G}_{22} = [\mathcal{G}_{21}]_{01} = [\mathcal{G}_{12}]_{10} = 0 \quad . \tag{C.14l}$$

Equations (C.14) show that up to fourth order there is no coupling between source and receiver coordinates for a diffraction described by (C.3). Even the generic finite-offset formula, described by two independent circular wavefronts at source and receiver,

$$S_{00} = \sqrt{(\Delta x_s + R_s \sin\alpha_s)^2 + R_s^2 \cos^2\alpha_s} \quad , \tag{C.15a}$$
$$G_{00} = \sqrt{(\Delta x_g + R_g \sin\alpha_g)^2 + R_g^2 \cos^2\alpha_g} \quad , \tag{C.15b}$$

shows no coupling of coordinates up to at least forth order, following from (C.14).

C.2. Hyperbolic CRS (up to fourth order)

In this section we provide the components of the midpoint half-offset derivative matrix $\underline{\mathbf{T}}_{mh}$ for the hyperbolic CRS traveltime operator

$$\tau_{00} = \sqrt{(t_0 + a\Delta x_m)^2 + b\Delta x_m^2 + ch^2} \quad , \tag{C.16}$$

where

$$t_0 = \frac{2R_{\mathrm{NIP}}}{v} \quad , \tag{C.17a}$$
$$a = \frac{2\sin\alpha}{v} \quad , \tag{C.17b}$$
$$b = \frac{4\cos^2\alpha}{v^2}\frac{R_{\mathrm{NIP}}}{R_{\mathrm{N}}} \quad , \tag{C.17c}$$
$$c = \frac{4\cos^2\alpha}{v^2} \quad . \tag{C.17d}$$

The coefficients are presented up to fourth order to ensure comparability with the diffraction results in the previous section of this appendix. The hyperbolic CRS move-out defined by the above formula (C.16) is known to lack accuracy for large offsets and strongly curved reflectors (e.g., Landa et al., 2010; Schwarz, 2011), which can be explained by low coupling in the higher ranks of the midpoint half-offset derivative

matrix. Up to second order the derivatives read

$$\tau_{10} = [\tau_{00}]_{10} = \frac{at_0 + (a^2 + b)\Delta x_m}{\tau_{00}} \quad , \tag{C.18a}$$

$$\tau_{01} = [\tau_{00}]_{01} = \frac{ch}{\tau_{00}} \quad , \tag{C.18b}$$

$$\tau_{20} = [\tau_{10}]_{10} = \frac{a^2 + b - \tau_{10}^2}{\tau_{00}} \quad , \tag{C.18c}$$

$$\tau_{02} = [\tau_{01}]_{01} = \frac{c - \tau_{01}^2}{\tau_{00}} \quad , \tag{C.18d}$$

$$\tau_{11} = [\tau_{10}]_{01} = [\tau_{01}]_{10} = -\frac{\tau_{10}\tau_{01}}{\tau_{00}} \quad . \tag{C.18e}$$

$$\tag{C.18f}$$

Please note that the actual Taylor expansion coefficients are defined as $t_{ij} = \tau_{ij}/(i+j)!$. For zero-offset, we have $\tau_{01} = 0$ and the mixed coefficient τ_{11} vanishes. The radius of the normal wave R_{N} only affects the midpoint derivatives, whereas it does not show in the corresponding half-offset terms for this case. As could be observed for the diffraction traveltime (C.3), the coupling between midpoint and half-offset coordinates shows in the higher-order terms for the zero-offset case. The hyperbolic counterparts to the higher-order diffraction coefficients (equations (C.11)) are

$$\tau_{30} = [\tau_{20}]_{10} = -\frac{3\tau_{10}\tau_{20}}{\tau_{00}} \quad , \tag{C.19a}$$

$$\tau_{03} = [\tau_{02}]_{01} = -\frac{3\tau_{01}\tau_{02}}{\tau_{00}} \quad , \tag{C.19b}$$

$$\tau_{21} = [\tau_{11}]_{10} = [\tau_{20}]_{01} = -\frac{2\tau_{10}\tau_{11} + \tau_{01}\tau_{20}}{\tau_{00}} \quad , \tag{C.19c}$$

$$\tau_{12} = [\tau_{11}]_{01} = [\tau_{02}]_{10} = -\frac{2\tau_{01}\tau_{11} + \tau_{10}\tau_{02}}{\tau_{00}} \quad , \tag{C.19d}$$

$$\tau_{40} = [\tau_{30}]_{10} = -\frac{3\tau_{20}^2 + 4\tau_{10}\tau_{30}}{\tau_{00}} \quad . \tag{C.19e}$$

$$\tau_{04} = [\tau_{03}]_{01} = -\frac{3\tau_{02}^2 + 4\tau_{01}\tau_{03}}{\tau_{00}} \quad , \tag{C.19f}$$

$$\tau_{31} = [\tau_{30}]_{01} = [\tau_{21}]_{10} = -\frac{3\tau_{20}\tau_{11} + 3\tau_{10}\tau_{21} + \tau_{01}\tau_{30}}{\tau_{00}} \quad , \tag{C.19g}$$

$$\tau_{13} = [\tau_{03}]_{10} = [\tau_{12}]_{01} = -\frac{3\tau_{02}\tau_{11} + 3\tau_{01}\tau_{12} + \tau_{10}\tau_{03}}{\tau_{00}} \quad , \tag{C.19h}$$

$$\tau_{22} = [\tau_{21}]_{01} = [\tau_{12}]_{10} = -\frac{2\tau_{11}^2 + 2\tau_{10}\tau_{12} + 2\tau_{01}\tau_{21} + \tau_{20}\tau_{02}}{\tau_{00}} \quad . \tag{C.19i}$$

As mentioned above, for zero-offset we have $\tau_{01} = 0$, which in turn leads to

$$\tau_{11} = \tau_{21} = \tau_{03} = \tau_{31} = \tau_{13} = 0 \quad . \tag{C.20}$$

By making use of substitutions (C.17) and by either choosing the velocity or the time shift mechanism to account for heterogeneity (see Chapter 4), the pure half-offset terms

t_{0i} (i =0,2,4) correspond exactly to the ones found by Thore et al. (1994),

$$t \approx t_0 + \frac{x^2}{2v_{\mathrm{NMO}}^2 t_0} - \frac{x^4}{8v_{\mathrm{NMO}}^4 t_0^3} \quad , \tag{C.21a}$$

$$t \approx t_0 + \frac{x^2}{2v_0^2 t_p} - \frac{x^4}{8v_0^4 t_p^3} \quad , \tag{C.21b}$$

where v_{NMO} is the normal moveout velocity and t_p corresponds to the shifted reference time (see also Chapter 4), formally introduced by de Bazelaire (1988) and $x = 2h$ is the full source receiver offset.

C.3. Multifocusing (up to second order)

The multifocusing moveout (Gelchinsky et al., 1999), similar to the diffraction moveout (C.3), consists of two main contributions

$$t_{00} = t_0 + \frac{S_{00} - s_{00}}{v} + \frac{G_{00} - g_{00}}{v} \quad . \tag{C.22}$$

Both of these contributions can be explained by a wave that is thought to originate and focus at the point, were the zero-offset reference ray and the considered finite-offset ray intersect. At the finite-offset source and receiver positions the focusing wave has the respective curvatures (see also Chapters 3.3 and Chapter 5.5)

$$S_{00} = \sqrt{(\Delta x_s + s_{00}\sin\alpha)^2 + s_{00}^2\cos^2\alpha} \quad , \tag{C.23a}$$

$$G_{00} = \sqrt{(\Delta x_g + g_{00}\sin\alpha)^2 + g_{00}^2\cos^2\alpha} \tag{C.23b}$$

where $\Delta x_s = \Delta x_m - h$ and $\Delta x_g = \Delta x_m + h$. The focusing wavefront curvatures, as they are observed at the central midpoint location, are defined as

$$s_{00} = \frac{1 - \phi_{00}}{K_{\mathrm{N}} - \phi_{00} K_{\mathrm{NIP}}} \quad , \tag{C.24a}$$

$$g_{00} = \frac{1 + \phi_{00}}{K_{\mathrm{N}} + \phi_{00} K_{\mathrm{NIP}}} \quad . \tag{C.24b}$$

In contrast to the diffraction moveout, discussed in Chapter 5.2 and in the first section of this chapter of the appendix, these two contributions are generally coupled with each other, no matter whether midpoint half-offset or shot-receiver coordinates are chosen (e.g., Landa et al., 2010). The coupling between the source and receiver contributions of the focusing wavefront is established via the focusing parameter (Gelchinsky et al., 1999) given by

$$\phi_{00} = \frac{\Delta x_s - \Delta x_g}{\Delta x_s + \Delta x_g + 2K_{\mathrm{NIP}}\sin\alpha\Delta x_s\Delta x_g} \quad . \tag{C.25}$$

For extrapolation purposes (see Chapter 5.5), I present the corresponding elements of the midpoint half-offset derivative matrix $\underline{\mathbf{T}}_{mh}$ up to second order. They read

$$t_{10} = \frac{1}{v}\left(S_{10} - s_{10} + G_{10} - g_{10}\right) \quad , \tag{C.26a}$$

$$t_{01} = \frac{1}{v}\left(S_{01} - s_{01} + G_{01} - g_{01}\right) \quad , \tag{C.26b}$$

$$t_{20} = \frac{1}{2v}\left(S_{20} - s_{20} + G_{20} - g_{20}\right) \quad , \tag{C.26c}$$

$$t_{02} = \frac{1}{2v}\left(S_{02} - s_{02} + G_{02} - g_{02}\right) \quad , \tag{C.26d}$$

$$t_{11} = \frac{1}{2v}\left(S_{11} - s_{11} + G_{11} - g_{11}\right) \quad . \tag{C.26e}$$

The corresponding focusing wavefront derivatives for the source position are

$$S_{10} = \frac{(\Delta x_s + s_{00}\sin\alpha)(1 + s_{10}\sin\alpha) + s_{00}s_{10}\cos^2\alpha}{S_{00}} \quad , \tag{C.27a}$$

$$S_{01} = \frac{(\Delta x_s + s_{00}\sin\alpha)(s_{01}\sin\alpha - 1) + s_{00}s_{01}\cos^2\alpha}{S_{00}} \quad , \tag{C.27b}$$

$$S_{20} = \frac{(1 + s_{10}\sin\alpha)^2 + s_{20}\sin\alpha(\Delta x_s + s_{00}\sin\alpha) + (s_{10}^2 + s_{00}s_{20})\cos^2\alpha - S_{10}^2}{S_{00}} \quad , \tag{C.27c}$$

$$S_{02} = \frac{(s_{01}\sin\alpha - 1)^2 + s_{02}\sin\alpha(\Delta x_s + s_{00}\sin\alpha) + (s_{01}^2 + s_{00}s_{02})\cos^2\alpha - S_{01}^2}{S_{00}} \quad , \tag{C.27d}$$

$$S_{11} = \frac{-(1 - s_{01}\sin\alpha)(1 + s_{10}\sin\alpha) + s_{11}\sin\alpha(\Delta x_s + s_{00}\sin\alpha)}{S_{00}} + \frac{(s_{01}s_{10} + s_{00}s_{11})\cos^2\alpha - S_{10}S_{01}}{S_{00}} \quad . \tag{C.27e}$$

For the receiver position, we get

$$G_{10} = \frac{(\Delta x_g + g_{00}\sin\alpha)(1 + g_{10}\sin\alpha) + g_{00}g_{10}\cos^2\alpha}{G_{00}} \quad , \tag{C.28a}$$

$$G_{01} = \frac{(\Delta x_g + g_{00}\sin\alpha)(1 + g_{01}\sin\alpha) + g_{00}g_{01}\cos^2\alpha}{G_{00}} \quad , \tag{C.28b}$$

$$G_{20} = \frac{(1 + g_{10}\sin\alpha)^2 + g_{20}\sin\alpha(\Delta x_g + g_{00}\sin\alpha) + (g_{10}^2 + g_{00}g_{20})\cos^2\alpha - G_{10}^2}{G_{00}} \quad , \tag{C.28c}$$

$$G_{02} = \frac{(1 + g_{01}\sin\alpha)^2 + g_{02}\sin\alpha(\Delta x_g + g_{00}\sin\alpha) + (g_{01}^2 + g_{00}g_{02})\cos^2\alpha - G_{01}^2}{G_{00}} \quad , \tag{C.28d}$$

$$G_{11} = \frac{(1 + g_{01}\sin\alpha)(1 + g_{10}\sin\alpha) + g_{11}\sin\alpha(\Delta x_g + g_{00}\sin\alpha)}{G_{00}} + \frac{(g_{01}g_{10} + g_{00}g_{11})\cos^2\alpha - G_{10}G_{01}}{G_{00}} \quad . \tag{C.28e}$$

The derivatives of the source wavefront observed from the zero-offset position are

$$s_{10} = \frac{\phi_{10}(K_{\mathrm{NIP}} - K_{\mathrm{N}})}{(K_{\mathrm{N}} - \phi_{00}K_{\mathrm{NIP}})^2} \quad , \tag{C.29a}$$

$$s_{01} = \frac{\phi_{01}(K_{\mathrm{NIP}} - K_{\mathrm{N}})}{(K_{\mathrm{N}} - \phi_{00}K_{\mathrm{NIP}})^2} \quad , \tag{C.29b}$$

$$s_{20} = \frac{(K_{\mathrm{NIP}} - K_{\mathrm{N}})[\phi_{20}(K_{\mathrm{N}} - \phi_{00}K_{\mathrm{NIP}}) + 2K_{\mathrm{NIP}}\phi_{10}^2]}{(K_{\mathrm{N}} - \phi_{00}K_{\mathrm{NIP}})^3} \quad , \tag{C.29c}$$

$$s_{02} = \frac{(K_{\mathrm{NIP}} - K_{\mathrm{N}})[\phi_{02}(K_{\mathrm{N}} - \phi_{00}K_{\mathrm{NIP}}) + 2K_{\mathrm{NIP}}\phi_{01}^2]}{(K_{\mathrm{N}} - \phi_{00}K_{\mathrm{NIP}})^3} \quad , \tag{C.29d}$$

$$s_{11} = \frac{(K_{\mathrm{NIP}} - K_{\mathrm{N}})[\phi_{11}(K_{\mathrm{N}} - \phi_{00}K_{\mathrm{NIP}}) + 2K_{\mathrm{NIP}}\phi_{10}\phi_{01}]}{(K_{\mathrm{N}} - \phi_{00}K_{\mathrm{NIP}})^3} \quad . \tag{C.29e}$$

In accordance, the respective derivatives for the zero-offset receiver wavefront measurement read

$$g_{10} = \frac{\phi_{10}(K_{\mathrm{N}} - K_{\mathrm{NIP}})}{(K_{\mathrm{N}} + \phi_{00}K_{\mathrm{NIP}})^2} \quad , \tag{C.30a}$$

$$g_{01} = \frac{\phi_{01}(K_{\mathrm{N}} - K_{\mathrm{NIP}})}{(K_{\mathrm{N}} + \phi_{00}K_{\mathrm{NIP}})^2} \quad , \tag{C.30b}$$

$$g_{20} = \frac{(K_{\mathrm{N}} - K_{\mathrm{NIP}})[\phi_{20}(K_{\mathrm{N}} + \phi_{00}K_{\mathrm{NIP}}) - 2K_{\mathrm{NIP}}\phi_{10}^2]}{(K_{\mathrm{N}} + \phi_{00}K_{\mathrm{NIP}})^3} \quad , \tag{C.30c}$$

$$g_{02} = \frac{(K_{\mathrm{N}} - K_{\mathrm{NIP}})[\phi_{02}(K_{\mathrm{N}} + \phi_{00}K_{\mathrm{NIP}}) - 2K_{\mathrm{NIP}}\phi_{01}^2]}{(K_{\mathrm{N}} + \phi_{00}K_{\mathrm{NIP}})^3} \quad , \tag{C.30d}$$

$$g_{11} = \frac{(K_{\mathrm{N}} - K_{\mathrm{NIP}})[\phi_{11}(K_{\mathrm{N}} + \phi_{00}K_{\mathrm{NIP}}) - 2K_{\mathrm{NIP}}\phi_{10}\phi_{01}]}{(K_{\mathrm{N}} + \phi_{00}K_{\mathrm{NIP}})^3} \quad . \tag{C.30e}$$

The focusing parameter derivatives, linking the source and receiver contributions can be written as

$$\phi_{10} = -\frac{2\phi_{00}^2[1 + K_{\mathrm{NIP}}\sin\alpha(\Delta x_s + \Delta x_g)]}{\Delta x_s - \Delta x_g} \quad , \tag{C.31a}$$

$$\phi_{01} = -\frac{2\phi_{00}[1 + K_{\mathrm{NIP}}\sin\alpha\phi_{00}(\Delta x_s - \Delta x_g)]}{\Delta x_s - \Delta x_g} \quad , \tag{C.31b}$$

$$\phi_{20} = -\frac{4\phi_{00}\phi_{10}[1 + K_{\mathrm{NIP}}\sin\alpha(\Delta x_s + \Delta x_g)] + 4\phi_{00}^2 K_{\mathrm{NIP}}\sin\alpha}{\Delta x_s - \Delta x_g} \quad , \tag{C.31c}$$

$$\phi_{02} = -\frac{4\phi_{01}\phi_{00}K_{\mathrm{NIP}}\sin\alpha(\Delta x_s - \Delta x_g) - 4\phi_{00}^2 K_{\mathrm{NIP}}\sin\alpha}{\Delta x_s - \Delta x_g} \quad , \tag{C.31d}$$

$$\phi_{11} = \frac{2\phi_{01}\phi_{10}(\Delta x_s - \Delta x_g) + 2\phi_{10}\phi_{00}}{\phi_{00}(\Delta x_s - \Delta x_g)} \quad . \tag{C.31e}$$

With help of the multifocusing derivative matrix elements C.26, similar to hyperbolic CRS and the implicit CRS, the finite-offset traveltime coefficients used i.e. in the finite-offset CRS stack (Zhang et al., 2001) can be extrapolated.

C.4. Implicit CRS (up to second order)

The implicit CRS moveout (Vanelle et al., 2010; Schwarz, 2011) and multifocusing are essentially very related approaches (Schwarz et al., 2014a). In both cases, similar like

for the generic diffraction case, the traveltime response is described by the observation of two wavefronts, one emerging at the source, the other at the receiver position. While the focus of the multifocusing wavefronts lies at the intersection point of the zero-offset and the finite-offset ray, the implicit CRS wavefronts are thought to be initiated at the finite-offset reflection point.

Again, the moveout formula can be formulated in terms of a source and a receiver contribution, representing the finite-offset reflection point (RP) wave's curvature observed at source and receiver (compare Chapter 3 and Chapter 5),

$$t_{00} = \frac{S_{00} + G_{00}}{v} \quad . \tag{C.32}$$

The finite-offset reflection point wavefront radii S_{00} and G_{00} can be parametrized by the corresponding reflection point coordinates x_{00} and z_{00}, which generally depend on the source receiver or midpoint half-offset coordinates. In terms of the reflection point coordinates they read

$$S_{00} = \sqrt{(\Delta x_s - x_{00})^2 + z_{00}^2} \quad , \tag{C.33a}$$

$$G_{00} = \sqrt{(\Delta x_g - x_{00})^2 + z_{00}^2} \quad , \tag{C.33b}$$

with $\Delta x_s = \Delta x_m - h$ and $\Delta x_g = \Delta x_m + h$. The derivatives of the traveltime can thus be expressed via (C.7). Like for the multifocusing moveout, the source and receiver wavefront measurements of the finite-offset reflection point wave are generally coupled via the reflection point coordinates, which, consequently, are also expressed in derivative matrix notation introduced in Chapter 5.1,

$$x_{00} = x_0 - R_{\mathrm{N}} \sin\alpha + (R_{\mathrm{N}} - R_{\mathrm{NIP}})\sigma_{00} \quad , \tag{C.34a}$$

$$z_{00} = R_{\mathrm{N}} \cos\alpha - (R_{\mathrm{N}} - R_{\mathrm{NIP}})\gamma_{00} \quad , \tag{C.34b}$$

where the sine (denoted by σ_{00}), the cosine (abbreviated with γ_{00}) and the tangent (λ_{00}) of the reflection point angle are also defined in derivative matrix notation,

$$\sigma_{00} = [\sin\theta]_{00} = \lambda_{00}\gamma_{00} \quad , \tag{C.35a}$$

$$\gamma_{00} = [\cos\theta]_{00} = (1 + \lambda_{00}^2)^{-\frac{1}{2}} \quad , \tag{C.35b}$$

$$\lambda_{00} = [\tan\theta]_{00} = \frac{\Delta x_m + R_{\mathrm{N}} \sin\alpha}{R_{\mathrm{N}} \cos\alpha} + \frac{h}{R_{\mathrm{N}} \cos\alpha} \frac{S_{00} - G_{00}}{S_{00} + G_{00}} \quad . \tag{C.35c}$$

With $\Delta x_{00} = x_{00} - x_0$, the source wavefront derivative matrix components read

$$S_{10} = \frac{(\Delta x_s - \Delta x_{00})(1 - x_{10}) + z_{00} z_{10}}{S_{00}} \quad , \tag{C.36a}$$

$$S_{01} = \frac{(\Delta x_s - \Delta x_{00})(-1 - x_{01}) + z_{00} z_{01}}{S_{00}} \quad , \tag{C.36b}$$

$$S_{20} = \frac{(1 - x_{10})^2 - x_{20}(\Delta x_s - \Delta x_{00}) + z_{10}^2 + z_{00} z_{20} - S_{10}^2}{S_{00}} \quad , \tag{C.36c}$$

$$S_{02} = \frac{(-1 - x_{01})^2 - x_{02}(\Delta x_s - \Delta x_{00}) + z_{01}^2 + z_{00} z_{02} - S_{01}^2}{S_{00}} \quad , \tag{C.36d}$$

$$S_{11} = \frac{-(1 + x_{01})(1 - x_{10}) - x_{11}(\Delta x_s - \Delta x_{00}) + z_{10} z_{01} + z_{00} z_{11} - S_{10} S_{01}}{S_{00}} \quad . \tag{C.36e}$$

The corresponding reflection point wave curvature, as it is observed at the receiver position, has the following first and second-order derivatives

$$G_{10} = \frac{(\Delta x_g - \Delta x_{00})(1 - x_{10}) + z_{00} z_{10}}{G_{00}} \quad , \tag{C.37a}$$

$$G_{01} = \frac{(\Delta x_g - \Delta x_{00})(1 - x_{01}) + z_{00} z_{01}}{G_{00}} \quad , \tag{C.37b}$$

$$G_{20} = \frac{(1 - x_{10})^2 - x_{20}(\Delta x_g - \Delta x_{00}) + z_{10}^2 + z_{00} z_{20} - G_{10}^2}{G_{00}} \quad , \tag{C.37c}$$

$$G_{02} = \frac{(1 - x_{01})^2 - x_{02}(\Delta x_g - \Delta x_{00}) + z_{01}^2 + z_{00} z_{02} - G_{01}^2}{G_{00}} \quad , \tag{C.37d}$$

$$G_{11} = \frac{(1 - x_{01})(1 - x_{10}) - x_{11}(\Delta x_g - \Delta x_{00}) + z_{10} z_{01} + z_{00} z_{11} - G_{10} G_{01}}{G_{00}} \quad . \tag{C.37e}$$

The reflection point derivatives are directly proportional to the derivatives of the sine and the cosine of the reflection point angle, i.e. σ_{ij} and γ_{ij}, via

$$x_{ij} = (R_{\mathrm{N}} - R_{\mathrm{NIP}}) \sigma_{ij} \quad , \tag{C.38a}$$

$$z_{ij} = -(R_{\mathrm{N}} - R_{\mathrm{NIP}}) \gamma_{ij} \quad . \tag{C.38b}$$

The respective elements of the derivative matrix $\underline{\sigma}_{mh}$ are

$$\sigma_{10} = \lambda_{10} \gamma_{00} + \lambda_{00} \gamma_{10} \quad , \tag{C.39a}$$

$$\sigma_{01} = \lambda_{01} \gamma_{00} + \lambda_{00} \gamma_{01} \quad , \tag{C.39b}$$

$$\sigma_{20} = \lambda_{20} \gamma_{00} + 2\lambda_{10} \gamma_{10} + \lambda_{00} \gamma_{20} \quad , \tag{C.39c}$$

$$\sigma_{02} = \lambda_{02} \gamma_{00} + 2\lambda_{01} \gamma_{01} + \lambda_{00} \gamma_{02} \quad , \tag{C.39d}$$

$$\sigma_{11} = \lambda_{11} \gamma_{00} + \lambda_{10} \gamma_{01} + \lambda_{01} \gamma_{10} + \lambda_{00} \gamma_{11}, \tag{C.39e}$$

and

$$\gamma_{10} = -\lambda_{00} \lambda_{10} \gamma_{00}^3 \quad , \tag{C.40a}$$

$$\gamma_{01} = -\lambda_{00} \lambda_{01} \gamma_{00}^3 \quad , \tag{C.40b}$$

$$\gamma_{20} = -(\lambda_{10}^2 + \lambda_{00} \lambda_{20}) \gamma_{00}^3 - 3\lambda_{00} \lambda_{10} \gamma_{00}^2 \gamma_{10} \quad , \tag{C.40c}$$

$$\gamma_{02} = -(\lambda_{01}^2 + \lambda_{00} \lambda_{02}) \gamma_{00}^3 - 3\lambda_{00} \lambda_{01} \gamma_{00}^2 \gamma_{01} \quad , \tag{C.40d}$$

$$\gamma_{11} = -(\lambda_{10} \lambda_{01} + \lambda_{00} \lambda_{11}) \gamma_{00}^3 - 3\lambda_{00} \lambda_{01} \gamma_{00}^2 \gamma_{10} \quad . \tag{C.40e}$$

The tangent of the reflection point angle is an implicit expression and serves for the evaluation of the finite-offset reflection point location (Vanelle et al., 2010). Therefore, the corresponding derivatives turn out to have a rather complex mathematical

structure:

$$\lambda_{10} = \frac{1}{R_\mathrm{N}\cos\alpha}\left[1 + 2h\frac{S_{10}G_{00} - S_{00}G_{10}}{(S_{00}+G_{00})^2}\right] \quad , \tag{C.41a}$$

$$\lambda_{01} = \frac{1}{R_\mathrm{N}\cos\alpha}\left[\frac{S_{00}-G_{00}}{S_{00}+G_{00}} + 2h\frac{S_{01}G_{00} - S_{00}G_{01}}{(S_{00}+G_{00})^2}\right] \quad , \tag{C.41b}$$

$$\lambda_{20} = \frac{2h}{R_\mathrm{N}\cos\alpha}\frac{(S_{20}G_{00} - S_{00}G_{20})(S_{00}+G_{00}) - 2(S_{10}G_{00} - S_{00}G_{10})(S_{10}+G_{10})}{(S_{00}+G_{00})^3} \quad , \tag{C.41c}$$

$$\lambda_{02} = \frac{2h}{R_\mathrm{N}\cos\alpha}\frac{(S_{02}G_{00} - S_{00}G_{02})(S_{00}+G_{00}) - 2(S_{01}G_{00} - S_{00}G_{01})(S_{01}+G_{01})}{(S_{00}+G_{00})^3} + \frac{4}{R_\mathrm{N}\cos\alpha}\frac{S_{01}G_{00} - S_{00}G_{01}}{(S_{00}+G_{00})^2} \quad , \tag{C.41d}$$

$$\lambda_{11} = \frac{2h}{R_\mathrm{N}\cos\alpha}\frac{S_{11}G_{00} + S_{10}G_{01} - S_{01}G_{10} - S_{00}G_{11}}{(S_{00}+G_{00})^2} \tag{C.41e}$$

$$- \frac{4h}{R_\mathrm{N}\cos\alpha}\frac{(S_{10}G_{00} - S_{00}G_{10})(S_{01}+G_{01})}{(S_{00}+G_{00})^3} + \frac{2}{R_\mathrm{N}\cos\alpha}\frac{S_{10}G_{00} - S_{00}G_{10}}{(S_{00}+G_{00})^2} \quad . \tag{C.41f}$$

D. Basics of NIP tomography

This chapter of the appendix briefly recapitulates the basic ideas and concepts underlying NIP tomography. Most formulations are taken from Duveneck (2004), whose implementation was used in the frame of this thesis. Although the concept of the NIP wave is fictitious, its properties α and R_{NIP}, measured at the registration surface, contain information about the medium traversed by the reference ray and rays in its paraxial vicinity (Hubral, 1983). One can look at NIP tomography as a scheme, in which the NIP wave, characterized by its curvature and emergence angle at the surface, gets back-propagated into the medium until it focuses (Hubral et al., 1980). Since, as emphasized in Chapter 4, the inequality

$$t_0 \neq \frac{2R_{\mathrm{NIP}}}{v_0} \tag{D.1}$$

is generally valid for heterogeneous media, the auxiliary medium of constant near-surface velocity v_0 needs to be perturbed, so that the focusing of the NIP wave is achieved after half of the true traveltime of the NIP ray t_0. In practice however, it turned out to be a more stable and logistically less demanding approach to start with potential NIPs as starting points and to forward-propagate the NIP wave and compare the resulting properties after half the reference time t_0 with the true values of α and R_{NIP}, which were measured in the data (Duveneck, 2004).

Duveneck's implementation of NIP tomography, as it was used for the synthetic examples presented in this work, can be divided into two essential steps:

1. Automatic picking,
2. Tomographic inversion.

The automatic picking can, in principle, be fully automized and demands the automatically generated CRS stack, CRS semblance and the NIP wave attribute sections as input. Picking is performed in the CRS stacked section based on a user-defined semblance threshold, which serves as an objective measure of trust to ensure pick quality. The second step, i.e. the tomographic inversion itself, needs the picked attributes and their lateral location and reference time as input.

The inversion scheme tries to minimize the misfit between the measured NIP properties, represented by the data vector $\mathbf{d}$ and the modelled NIP properties, represented by the model vector $\mathbf{m}$ in the least-squares sense (Tarantola, 1984; Paige and Saunders, 1982),

$$\min_{\mathbf{m}} \frac{1}{2} \left\| \mathbf{d} - \mathbf{f}(\mathbf{m}) \right\|^2 = \min_{\mathbf{m}} \frac{1}{2} \Delta\mathbf{d}^{\mathrm{T}}(\mathbf{m}) \underline{\mathbf{C}}_{\mathrm{D}}^{-1} \Delta\mathbf{d}(\mathbf{m}) \quad , \tag{D.2}$$

where $\Delta\mathbf{d}(\mathbf{m}) = \mathbf{d} - \mathbf{f}(\mathbf{m})$. The symmetric matrix $\underline{\mathbf{C}}_{\mathrm{D}}$ is positive definite and weights the different data components in the minimization procedure. The relationship between the data and the model components is established via the generally nonlinear operator $\mathbf{f}(\mathbf{m})$. For computational reasons, Duveneck's implementation utilizes a local optimization scheme, in which $\mathbf{f}(\mathbf{m})$ is approximated locally around the respective

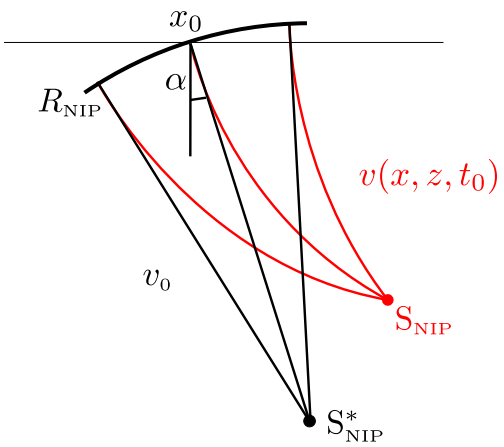

Figure D.1.: The central concept of NIP tomography is a virtual point source $\mathrm{S}_{\mathrm{NIP}}$ thought to be located at the true normal incidence point (NIP). The apparent position as it is observed in the surface measurement ($\mathrm{S}^*_{\mathrm{NIP}}$) only coincides with the true position, if the overburden is homogeneous. Only for a kinemeatically feasible velocity model, the back-propagated NIP wave focuses at the true reference time t_0.

model vector (Duveneck, 2004). To regularize the inversion, Duveneck also included the second order derivatives of the velocity model in an additional term in the cost function, which relates to the integral

$$\int_x \int_z \left[\epsilon_{xx} \left(\frac{\partial^2 v}{x^2} \right)^2 + \epsilon_{zz} \left(\frac{\partial^2 v}{z^2} \right)^2 + \epsilon v^2 \right] \mathrm{d}x \, \mathrm{d}z \quad . \tag{D.3}$$

The third term in the integral is proportional to the velocity itself which is included to ensure that the matrix describing the second-order term in the cost function is positive definite (Duveneck, 2004). While the quantities ϵ_{xx} and ϵ_{zz} represent directional weights, ϵ weighs the minimization of the velocity to ensure stability. All three weights need to be chosen by the user (my personal choices can be found in Tabular F.5). For more detailed information on the considered implementation, I refer to Duveneck (2004).

E. Datasets

The choice of the considered datasets was mostly driven by the motivation to provide an intuitive and quantitative impression of the potential of the suggested theoretical concepts. For this purpose, I designed rather generic but clear and controlled test datasets based on the assumption of simple geometrical targets in a constant vertical velocity gradient background. To prove applicability of the proposed techniques and the introduced operator duality in a more complex environment, I in addition considered the well-known 2004 BP velocity benchmark dataset (Billette and Brandsberg-Dahl, 2005) and an industrial large-offset field dataset from the eastern Mediterranean for the tests in the second part of the thesis.

E.1. Constant vertical velocity gradient

The simple synthetic test datasets were generated with the *susynlv* routine of Seismic Unix. They serve the purpose of evaluating under very controlled conditions, whether the presented theoretical concepts actually allow for implementable wavefield discrimination and imaging schemes. All of the datasets considered in Chapter 6 have in common that they contain the response of a horizontally centralized point diffractor (or source for the passive seismic example), which lies in the depth of 1 km. If not emphasized differently, the vertical gradient is 0.5 s^{-1}.

Since many of the applications suggested rely on a sufficiently accurate description of both, reflections and diffractions, the corresponding models also contain a horizontal planar interface in a depth of 1.8 km. In sections, where the imaging of one event is sufficient to illustrate the proposed technique, the model only contains the previously mentioned point diffractor. Table E.1 lists the most important dataset parameters for both, the active and the passive seismic experiment considered in Chapter 6. The modelling is utilizing analytical raytracing and therefore the data acquisition can be driven by the choice of a desired midpoint-offset geometry. As a result, the fold is constant along the full considered profile.

E.2. The 2004 BP velocity benchmark

The 2004 BP velocity benchmark dataset was introduced by Billette and Brandsberg-Dahl (2005). The underlying model (see Figure E.2) consists of a complex salt body regime and can be divided into three distinct parts, each focusing on different challenges for velocity estimation methods (Billette and Brandsberg-Dahl, 2005). The left part is dominated by a complex salt structure with rugged topography and steep flanks, while the respective macro-velocity gradient is relatively moderate. Thus, this part is mostly characterized by a complex target geometry and strong curvatures at the top-of-salt. The middle and right part of the BP model in turn are dominated by an increasing macro-velocity gradient, which becomes most pronounced at the mud volcano structure, which can be found in the very right of the model. According to Billette and Brandsberg-Dahl (2005), the three respective parts of the BP model accurately mimic typical settings in regions of interest to hydrocarbon exploration, like i.e. in the Gulf

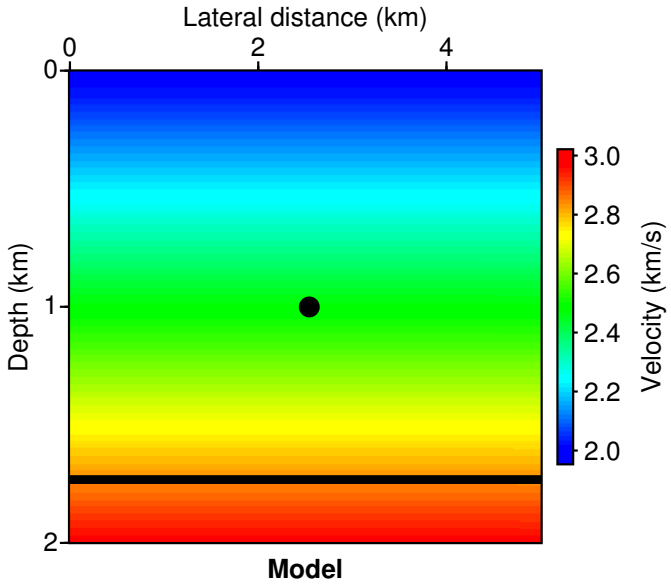

Figure E.1.: Simple synthetic model consisting of a point diffractor and a planar reflector in a constant vertical velocity gradient background. For the sake of simplicity, the acquisition line is symmetric with respect to the horizontal diffractor position. Table E.1 lists the most important parameters of the corresponding multi-coverage dataset.

Acquisition geometry (active)	
Number of CMP bins	201
Maximum CMP fold	81
CMP bin interval	25 m
Minimum offset	0 m
Maximum offset	2000 m
Acquisition geometry (passive)	
Number of receivers	201
Receiver interval	25 m
Recording parameters (active)	
Recording time	4 s
Sampling interval	4 ms
Recording parameters (passive)	
Recording time	3 s
Sampling interval	2 ms
Frequency content	
Peak frequency	30 Hz

Table E.1.: Acquisition and recording parameters of the simple constant vertical velocity gradient test datasets processed in Chapter 6. Both, an active seismic acquisition, consisting of multiple shots and a single source (passive), were performed in the same vertical velocity gradient background.

of Mexico, in the Caspian Sea or offshore Trinidad.

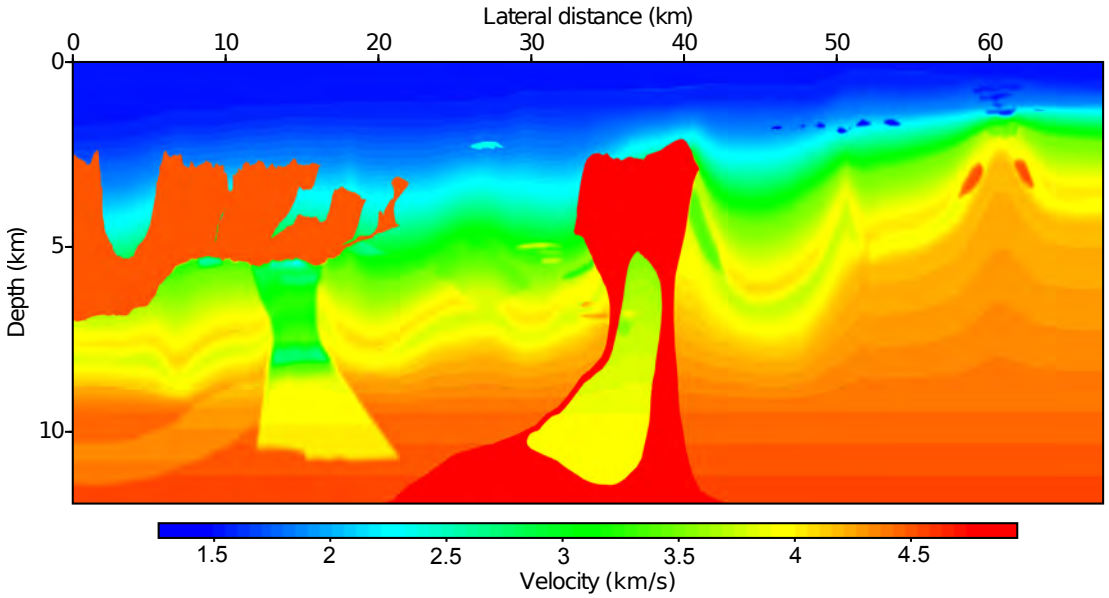

Figure E.2.: The 2004 BP velocity benchmark model. Being designed to challenge velocity inversion algorithms, the BP benchmark is also well-suited to test data-driven imaging techniques like the considered CRS methodology. While the left part of the model is dominated by complex salt structures with relatively low velocity variations above the salt, the right part shows strong velocity gradients and a shallow water bottom.

Acquisition geometry	
Number of shots	1340
Shot interval	50 m
Number of receivers	1201
Receiver interval	12.5 m
Minimum offset	0 m
Maximum offset	15000 m
Recording parameters	
Recording time	12 s
Sampling interval	6 ms
Frequency content	
Peak frequency	27 Hz

Table E.2.: Acquisition and recording parameters of the complex synthetic 2004 BP velocity benchmark dataset.

The data was generated using a time-domain acoustic finite-difference algorithm assuming a modern streamer acquisition with offsets ranging up to 15 km (Billette and Brandsberg-Dahl, 2005). The dataset is dominated by strong diffractions in the mildly heterogeneous left part and increasingly pronounced multiple reflections on the right,

Acquisition geometry	
Number of shots	1077
Shot interval	25 m
Number of receivers	1201
Receiver interval	12.5 m
Minimum offset	150 m
Maximum offset	7338 m
Recording parameters	
Recording time	5 s
Sampling interval	2 ms
Frequency content	
Peak frequency	25 Hz

Table E.3.: Acquisition and recording parameters of the industrial field dataset recorded by TGS in the eastern Mediterranean.

resulting from free-surface recording and shallow water depths. A list of important dataset parameters can be found in Table E.2. For more information on the 2004 BP velocity benchmarks, I refer to Billette and Brandsberg-Dahl (2005).

E.3. TGS field data

The industrial field dataset considered in my thesis was recorded by TGS Nopec in the eastern Mediterranean sea offshore Israel (Netzeband, 2006). Similar to the complex BP dataset, the underlying geology of this profile is known to be strongly influenced by salt tectonics connected to the formation of large salt bodies during the Messinian salinity crisis (Netzeband, 2006). Consequently the presence of a pronounced salt-roller geometry and a connected slumping complex resulted in a fair amount of diffracted energy in the recorded multi-coverage seismic data.

The data were recorded with an industry-scale streamer, leading to reasonably high offsets of up to 7 km (and above). Table E.3 contains the most important acquisition and recording parameters of the TGS dataset. Due to the salt-related regime, the presence of surface-related multiples and similar dimensions of the acquisition, both, the BP velocity benchmark and the TGS dataset are similarly demanding and, therefore, nicely complement each other.

F. Processing parameters

In this part of the appendix I provide tables containing the parameters, which were used to process the simple synthetic test datasets with a constant vertical velocity background, the complex synthetic 2004 BP velocity benchmark data, the TGS field dataset from the eastern Mediterranean sea and the passive seismic experiment. All of the CRS-based processing schemes, ranging from zero-offset stacking, partial stacking and local common-offset refinement to partial migration and demigration are based on the extended CRS implementation by Mann (2002), which was logistically expanded to the prestack domain by Baykulov and Gajewski (2009).

For the passive seismic example presented at the end of the thesis, processing was based on a self-written Matlab implementation, in which the data interaction relies on SegyMAT, an open source Matlab and Octave toolbox for reading and writing common seismic data formats. The NIP tomography code, developed by Duveneck (2004), was used to generate the tomography examples for the simple synthetics and the passive seismic data. Most aperture values were defined according to preliminary experience with the respective dataset and do not necessary reflect the ideal but rather a conservative choice. The main purpose of the presented studies was to test the general feasibility of the suggested geometry-based discrimination, imaging and inversion schemes.

General parameters	
Dominant frequency	30 Hz
Coherence measure	Semblance
Coherence time window	24 ms
Velocity and constraints	
Near-surface velocity	2000 m/s
Tested stacking velocities	1500 ... 6000 m/s
ZO stack target zone	
Simulated ZO traveltimes	0 ... 4 s
Simulated temporal sampling interval	4 ms
Number of simulated ZO traces	201
Spacing of simulated ZO traces	25 m
ZO stack apertures and taper	
Minimum midpoint aperture	500 m at 0 s
Maximum midpoint aperture	500 m at 4 s
Minimum offset aperture	2000 m at 0 s
Maximum offset aperture	2000 m at 4 s
Relative taper size	30 %
Linear ZO stack	
Tested emergence angles	$-70°$ ... $70°$
Initial emergence angle increment	$1°$
ZO stack optimization	
Coherence threshold for smallest traveltime	0.01
Coherence threshold for largest traveltime	0.01
Maximum number of iterations	100
Maximum relative deviation to stop	10^{-4}
Initial variation of emergence angles	$6°$
Initial variation of R_{NIP}	5 %
Initial variation of transformed R_N	$6°$
Partial stack and refinement	
Regularized receiver interval	25 m
Local midpoint aperture	100 m
Local offset aperture	100 m
Lower refinement coherence threshold	0.01
Upper refinement coherence threshold	0.8
Number of tested midpoint slope perturbations	20
Number of tested offset slope perturbations	20
Maximum slope angle deviation	$10°$
Partial migration and demigration	
Minimum local migration aperture	500 m
Maximum local migration aperture	1000 m
Minimum local demigration aperture	500 m
Maximum local demigration aperture	1000 m
Iterative diffraction demigration aperture	200 m

Table F.1.: Stacking and migration parameters used for the simple synthetic test datasets generated for a constant vertical velocity gradient background.

General parameters	
Dominant frequency	30 Hz
Coherence measure	Semblance
Coherence time window	24 ms
Velocity and constraints	
Near-surface velocity	1500 m/s
Tested stacking velocities	1400 ... 6500 m/s
ZO stack target zone	
Simulated ZO traveltimes	0 ... 10 s
Simulated temporal sampling interval	6 ms
Number of simulated ZO traces	11417
Spacing of simulated ZO traces	5.85 m
ZO stack apertures and taper	
Minimum midpoint aperture	300 m at 0 s
Maximum midpoint aperture	1000 m at 10 s
Minimum offset aperture	2000 m at 0 s
Maximum offset aperture	6000 m at 10 s
Relative taper size	30 %
Linear ZO stack	
Tested emergence angles	$-60°$ ... $60°$
Initial emergence angle increment	$1°$
ZO stack optimization	
Coherence threshold for smallest traveltime	0.01
Coherence threshold for largest traveltime	0.01
Maximum number of iterations	100
Maximum relative deviation to stop	10^{-4}
Initial variation of emergence angles	$6°$
Initial variation of R_{NIP}	5 %
Initial variation of transformed R_N	$6°$
Partial stack and refinement	
Regularized receiver interval	25 m
Local midpoint aperture	100 m
Local offset aperture	100 m
Lower refinement coherence threshold	0.01
Upper refinement coherence threshold	0.6
Number of tested midpoint slope perturbations	20
Number of tested offset slope perturbations	20
Maximum slope angle deviation	$10°$
Partial migration and demigration	
Minimum local migration aperture	300 m
Maximum local migration aperture	1000 m
Minimum local demigration aperture	300 m
Maximum local demigration aperture	1000 m
Iterative diffraction demigration aperture	200 m

Table F.2.: Stacking and migration parameters used for processing of the complex synthetic 2004 BP velocity benchmark dataset.

General parameters	
Dominant frequency	25 Hz
Coherence measure	Semblance
Coherence time window	20 ms
Velocity and constraints	
Near-surface velocity	1500 m/s
Tested stacking velocities	1400 ... 6500 m/s
ZO stack target zone	
Simulated ZO traveltimes	0 ... 5 s
Simulated temporal sampling interval	2 ms
Number of simulated ZO traces	2443
Spacing of simulated ZO traces	10.25 m
ZO stack apertures and taper	
Minimum midpoint aperture	300 m at 0 s
Maximum midpoint aperture	800 m at 5 s
Minimum offset aperture	2000 m at 0 s
Maximum offset aperture	5000 m at 5 s
Relative taper size	30 %
Linear ZO stack	
Tested emergence angles	$-60°$ ... $60°$
Initial emergence angle increment	$1°$
ZO stack optimization	
Coherence threshold for smallest traveltime	0.01
Coherence threshold for largest traveltime	0.01
Maximum number of iterations	100
Maximum relative deviation to stop	10^{-4}
Initial variation of emergence angles	$6°$
Initial variation of R_{NIP}	5 %
Initial variation of transformed R_N	$6°$
Partial stack and refinement	
Regularized receiver interval	25 m
Local midpoint aperture	100 m
Local offset aperture	100 m
Lower refinement coherence threshold	0.01
Upper refinement coherence threshold	0.6
Number of tested midpoint slope perturbations	20
Number of tested offset slope perturbations	20
Maximum slope angle deviation	$10°$
Partial migration and demigration	
Minimum local migration aperture	300 m
Maximum local migration aperture	800 m
Minimum local demigration aperture	300 m
Maximum local demigration aperture	800 m
Iterative diffraction demigration aperture	200 m

Table F.3.: Stacking and migration parameters used for the processing of the complex industrial field dataset recorded by TGS Nopec in the eastern Mediterranean.

General parameters	
Coherence measure	Semblance
Coherence time window	20 ms
Velocity constraints	
Near-surface velocity	2000 m/s
Dip search	
Tested emergence angles	$-70°$ ... $70°$
Emergence angle increment	$1°$
Search aperture	300 m
Shifted reference time search	
Tested reference times	0 s ... $t_{\max}$
Reference time increment	2 ms
Search aperture	1000 m
Coherence threshold	0.3
Lateral localization	
Focusing aperture	1000 m
Coherence threshold	0.3
Source time inversion	
Coherence threshold for smallest traveltime	0 s ... $t_{\max}$
Source time increment	2 ms
Search aperture	5000 m
Coherence threshold	0.3

Table F.4.: Parameters used for the processing of the simulated passive seismic example. The respective coherence thresholds are defined with respect to the preceding coherence measurement, i.e. the threshold defined in the shifted reference time search is related to the coherence output of the preceding dip search.

Velocity constraints	
Near-surface velocity	2000 m/s
Automatic attribute picking	
Picking radius	11 m
Amplitude time width	0.01 s
Coherence threshold	0.1
Maximum number of picks per trace	10
Least-squares inversion	
Initial velocity gradient	$0\ s^{-1}$
Maximum number of iterations	30
Maximum condition number	5000
Runge-Kutta step size	0.3
Regularization weight (z-direction)	10^{-4}
Regularization weight (x-direction)	10^{-4}
Velocity minimization weight	10^{-15}

Table F.5.: Parameters used for the tomographic inversion of the simple synthetic vertical gradient examples and the passive seismic experiment. In both, the active and passive example, the starting velocity model was chosen constant and equal to the near-surface velocity. The knot spacing was 500 m in horizontal and 200 m in vertical direction.

Bibliography

Bauer, A. (2014). *From zero-offset to common-offset with diffractions*. Masters thesis, University of Hamburg.

Bauer, A., Schwarz, B., and Gajewski, D. (2015). Zero-offset Based Prediction of Common-offset Diffraction Traveltimes. In *77th EAGE Conference and Exhibition-Workshops*. European Association of Geoscientists and Engineers.

Baykulov, M., Dümmong, S., and Gajewski, D. (2011). From time to depth with CRS attributes. *Geophysics*, 76(4):S151–S155.

Baykulov, M. and Gajewski, D. (2009). Prestack seismic data enhancement with partial common-reflection-surface (CRS) stack. *Geophysics*, 74:V49–V58.

Bergler, S., Duveneck, E., Höcht, G., Zhang, Y., and Hubral, P. (2002). Common-Reflection-Surface stack for converted waves. *Studia Geophysica et Geodaetica*, 46(2):165–175.

Billette, F. and Brandsberg-Dahl, S. (2005). The 2004 BP Velocity Benchmark. In *67th EAGE Conference & Exhibition*. European Association of Geoscientists and Engineers.

Billette, F. and Lambaré, G. (1998). Velocity macro-model estimation from seismic reflection data by stereotomography. *Geophysical Journal International*, 135(2):671–690.

Biondi, B. and Almomin, A. (2013). Tomographic full waveform inversion (TFWI) by extending the velocity model along the time-lag axis. In *75th EAGE Conference & Exhibition-Workshops*. European Association of Geoscientists and Engineers.

Bobsin, M. (2014). *Prestack time migration applying the iCRS operator*. Masters thesis, University of Hamburg.

Bortfeld, R. (1989). Geometrical ray theory: Rays and traveltimes in seismic systems (second-order approximations of the traveltimes). *Geophysics*, 54(3):342–349.

Burdick, S., Li, C., Martynov, V., Cox, T., Eakins, J., Mulder, T., Astiz, L., Vernon, F. L., Pavlis, G. L., and van der Hilst, R. D. (2008). Upper mantle heterogeneity beneath North America from travel time tomography with global and USArray transportable array data. *Seismological Research Letters*, 79(3):384–392.

Cruz, J., Hubral, P., Tygel, M., Schleicher, J., and Höcht, G. (2000). The common reflecting element (CRE) method revisited. *Geophysics*, 65(3):979–993.

de Bazelaire, E. (1988). Normal moveout revisited – inhomogeneous media and curved interfaces. *Geophysics*, 53:143–157.

Dell, S. and Gajewski, D. (2011). Common-reflection-surface-based workflow for diffraction imaging. *Geophysics*, 76(5):S187–S195.

Dell, S., Gajewski, D., and Vanelle, C. (2012). Prestack time migration by common-migrated-reflector-element stacking. *Geophysics*, 77(3):S73–S82.

Deregowski, S. (1986). What is DMO? *First Break*, 4(7).

Dümmong, S. and Gajewski, D. (2008). A multiple suppression method via CRS attributes. In *SEG Expanded Abstracts*. Society of Exploration Geophysicists.

Duveneck, E. (2004). Velocity model estimation with data-derived wavefront attributes. *Geophysics*, 69(1):265–274.

Eaton, D. W., Milkereit, B., and Salisbury, M. H. (2003). *Hardrock seismic exploration*, volume 10. Society of Exploration Geophysicists.

Eisenberg-Klein, G., Pruessmann, J., Gierse, G., and Trappe, H. (2008). Noise reduction in 2D and 3D seismic imaging by the CRS method. *The Leading Edge*, 27(2):258–265.

Fichtner, A., Kennett, B. L., Igel, H., and Bunge, H.-P. (2009). Full seismic waveform tomography for upper-mantle structure in the Australasian region using adjoint methods. *Geophysical Journal International*, 179(3):1703–1725.

Fomel, S. and Grechka, V. (2001). Nonhyperbolic reflection moveout of P waves. An overview and comparison of reasons. *CWP-372: Colorado School of Mines*.

Fomel, S. and Kazinnik, R. (2013). Non-hyperbolic common reflection surface. *Geophysical Prospecting*, 61(1):21–27.

Fomel, S. and Stovas, A. (2010). Generalized nonhyperbolic moveout approximation. *Geophysics*, 75(2):U9–U18.

Gelchinsky, B., Berkovitch, A., and Keydar, S. (1999). Multifocusing homeomorphic imaging – part 1. Basic concepts and formulae. *Journal of Applied Geophysics*, 42:229–242.

Gradmann, S., Hübscher, C., Ben-Avraham, Z., Gajewski, D., and Netzeband, G. (2005). Salt tectonics off northern Israel. *Marine and Petroleum Geology*, 22(5):597–611.

Hertweck, T., Mann, J., and Kluver, T. (2005). Event-consistent smoothing in the context of the CRS stack method. *Journal of Seismic Exploration*, 14(2/3):197.

Hertweck, T., Schleicher, J., and Mann, J. (2007). Data stacking beyond CMP. *The Leading Edge*, 26(7):818–827.

Höcht, G., de Bazelaire, E., Majer, P., and Hubral, P. (1999). Seismics and optics: hyperbolae and curvatures. *Journal of Applied Geophysics*, 42:261–281.

Höcht, G., Ricarte, P., Bergler, S., and Landa, E. (2009). Operator-oriented CRS interpolation. *Geophysical Prospecting*, 57(6):957–979.

Hubral, P. (1983). Computing true amplitude reflections in a laterally inhomogeneous earth. *Geophysics*, 48:1051–1062.

Hubral, P., Krey, T., and Larner, K. L. (1980). *Interval velocities from seismic reflection time measurements*. Society of Exploration Geophysicists.

Jäger, R. (1999). *The Common-Reflection-Surface Stack – Theory and Application*. Diploma thesis, University of Karlsruhe.

Jäger, R., Mann, J., Höcht, G., and Hubral, P. (2001). Common-reflection-surface stack: Image and attributes. *Geophysics*, 66:97–109.

Keydar, S., Gelchinsky, B., Shtivelman, V., and Berkovitch, A. (1990). The Common Evolute Element (CEE) stack method (zero-offset stack). In *SEG Expanded Abstracts*. Society of Exploration Geophysicists.

Khaidukov, V., Landa, E., and Moser, T. J. (2004). Diffraction imaging by focusing-defocusing: An outlook on seismic superresolution. *Geophysics*, 69(6):1478–1490.

Lambaré, G. (2008). Stereotomography. *Geophysics*, 73(5):VE25–VE34.

Landa, E. (2007). *Beyond conventional seismic imaging*. European Association of Geoscientists and Engineers.

Landa, E., Gurevich, B., Keydar, S., and Trachtman, P. (1999). Application of multifocusing method for subsurface imaging. *Journal of Applied Geophysics*, 42(3):283–300.

Landa, E., Keydar, S., and Moser, T. J. (2010). Multifocusing revisited – inhomogeneous media and curved interfaces. *Geophysical Prospecting*, 58:925–938.

Landa, E., Rauch-Davies, M., Deev, K., and Berkovitch, A. (2014). Prestack Signal Enhancement by Multi-parameter Common Offset MultiFocusing. In *76th EAGE Conference and Exhibition-Workshops*. European Association of Geoscientists and Engineers.

Lavaud, B., Baina, R., and Landa, E. (2004). Poststack Stereotomography–A Robust Strategy for Velocity Model Estimation. In *SEG Expanded Abstracts*. Society of Exploration Geophysicists.

Levin, F. K. (1971). Apparent velocity from dipping interface reflections. *Geophysics*, 36(3):510–516.

Mann, J. (2002). *Extensions and Applications of the Common-Reflection-Surface Stack Method*. PhD thesis, University of Karlsruhe.

Mayne, W. H. (1962). Common reflection point horizontal data stacking techniques. *Geophysics*, 27:927–938.

Müller, T. (1999). *The Common Reflection Surface stack method - Seismic imaging without explicit knowledge of the velocity model*. PhD thesis, University of Karlsruhe.

Netzeband, G. L. (2006). *The Levantine Basin: a seismic investigation of the crustal structure and the evolution of the Messinian evaporites*. PhD thesis, University of Hamburg.

Paige, C. C. and Saunders, M. A. (1982). LSQR: An algorithm for sparse linear equations and sparse least squares. *ACM Transactions on Mathematical Software (TOMS)*, 8(1):43–71.

Perroud, H., Hubral, P., and Höcht, G. (1999). Common-reflection-point stacking in laterally inhomogeneous media. *Geophysical Prospecting*, 47(1):1–24.

Perroud, H. and Tygel, M. (2004). Nonstretch NMO. *Geophysics*, 69(2):599–607.

Prieux, V., Lambaré, G., Operto, S., and Virieux, J. (2013). Building starting models for full waveform inversion from wide-aperture data by stereotomography. *Geophysical Prospecting*, 61(S1):109–137.

Schleicher, J., Tygel, M., and Hubral, P. (1993). Parabolic and hyperbolic paraxial two-point traveltimes in 3D media. *Geophysical Prospecting*, 41(4):495–513.

Schwarz, B. (2011). *A new nonhyperbolic multi-parameter stacking operator*. Diploma thesis, University of Hamburg.

Schwarz, B., Vanelle, C., and Gajewski, D. (2014a). Auxiliary Media - A Generalized View on Stacking. In *76th EAGE Conference and Exhibition*. European Association of Geoscientists and Engineers.

Schwarz, B., Vanelle, C., and Gajewski, D. (2014b). From Zero-offset to Common-offset with Diffractions. In *76th EAGE Conference and Exhibition-Workshops*. European Association of Geoscientists and Engineers.

Schwarz, B., Vanelle, C., and Gajewski, D. (2015a). Moveout and Geometry. In *Active and passive seismics in laterally inhomogeneous media (APSLIM) Workshop*.

Schwarz, B., Vanelle, C., and Gajewski, D. (2015b). Shifted Hyperbola Revisited - The Two Faces of NMO. In *77th EAGE Conference and Exhibition*. European Association of Geoscientists and Engineers.

Schwarz, B., Vanelle, C., Gajewski, D., and Kashtan, B. (2014c). Curvatures and inhomogeneities: An improved common-reflection-surface approach. *Geophysics*, 79(5):S231–S240.

Shah, P. M. (1973). Use of wavefront curvature to relate seismic data with subsurface parameters. *Geophysics*, 38(5):812–825.

Sheriff, R. E. and Geldart, L. P. (1995). *Exploration seismology*. Cambridge university press.

Spinner, M. (2006). 3D CRS-based limited aperture Kirchhoff time migration. In *SEG Expanded Abstracts*. Society of Exploration Geophysicists.

Spinner, M., Tomas, C., Marchetti, P., Gallo, C., and Arfeen, S. (2012). Common-Offset CRS for advanced imaging in complex geological settings. In *SEG Expanded Abstracts*. Society of Exploration Geophysicists.

Taner, M. T. and Koehler, F. (1969). Velocity spectra - digital computer derivation applications of velocity functions. *Geophysics*, 34(6):859–881.

Tarantola, A. (1984). Inversion of seismic reflection data in the acoustic approximation. *Geophysics*, 49(8):1259–1266.

Thore, P. D., de Bazelaire, E., and Rays, M. P. (1994). The three-parameter equation: an efficient tool to enhance the stack. *Geophysics*, 59(2):297–308.

Tygel, M., Santos, L. T., and Schleicher, J. (1999). Multifocus moveout revisited: derivations and alternative expressions. *Journal of Applied Geophysics*, 42(3):319–331.

Ursin, B. (1982). Quadratic wavefront and traveltime approximations in inhomogeneous layered media with curved interfaces. *Geophysics*, 47(7):1012–1021.

Vanelle, C. (2002). *Traveltime-based true-amplitude migration*. PhD thesis, University of Hamburg.

Vanelle, C. (2012). *Stacking and migration in an/isotropic media*. Habilitation.

Vanelle, C., Bobsin, M., Schemmert, P., Schwarz, B., Gajewski, D., and Kashtan, B. (2012). i-CRS: A New Multiparameter Stacking Operator for an/Isotropic Media. In *SEG Expanded Abstracts*. Society of Exploration Geophysicists.

Vanelle, C., Kashtan, B., Dell, S., and Gajewski, D. (2010). A new stacking operator for curved subsurface structures. In *SEG Expanded Abstracts*. Society of Exploration Geophysicists.

Vanelle, C., Wißmath, S., and Gajewski, D. (2014). Finite-offset CRS: Parameterisation and attribute prediction. In *Annual WIT Report*. Wave Inversion Technology.

Červený, V. (2001). *Seismic ray theory*. Cambridge University Press.

Versteeg, R. (1994). The Marmousi experience: Velocity model determination on a synthetic complex data set. *The Leading Edge*, 13(9):927–936.

Virieux, J. and Operto, S. (2009). An overview of full-waveform inversion in exploration geophysics. *Geophysics*, 74(6):WCC1–WCC26.

Wapenaar, K. and Fokkema, J. (2006). Greens function representations for seismic interferometry. *Geophysics*, 71(4):SI33–SI46.

Warner, M. and Guasch, L. (2014). Adaptive Waveform Inversion - FWI Without Cycle Skipping - Theory. In *76th EAGE Conference and Exhibition*. European Association of Geoscientists and Engineers.

Yilmaz, Ö. (2001). *Seismic data analysis*, volume 1. Society of Exploration Geophysicists, Tulsa.

Zhang, Y., Bergler, S., and Hubral, P. (2001). Common-reflection-surface (CRS) stack for common offset. *Geophysical Prospecting*, 49:709–718.

Zhebel, O., Gajewski, D., and Vanelle, C. (2011). Localization of seismic events in 3D media by diffraction stacking. In *73rd EAGE Conference & Exhibition*. European Association of Geoscientists and Engineers.

Danksagung / Acknowledgements

Die vorliegende Arbeit ist in ihrer jetzigen Form über mehrere Jahre entstanden. Ich hatte das grosse Glück, in dieser Zeit viele verschiedene Menschen, Hintergründe, Schicksale und Charaktere kennenzulernen, die meinen Blick auf die Dinge mitunter nachhaltig verändert haben. Ohne den Anspruch auf Vollständigkeit liegen mir dabei einige Namen besonders am Herzen.

Mein Dank geht an...
I am grateful to...

- **Dirk Gajewski** für das wirklich unerschütterliche Vertrauen und viele tolle fachliche, aber auch zwischenmenschliche Gespräche, die mich nachhaltig beeindruckt haben. Die Betreuung, nicht nur während meiner Zeit als Doktorant, sondern auch schon davor, als Diplomant und studentische Hilfskraft war immer vorbildlich und ich konnte in brenzligen Situationen immer mit Rückendeckung rechnen. Für die Chance, regelmässig an internationalen Konferenzen teilnehmen zu dürfen (selbst wenn mal kein eigener Vortrag vorgesehen war) bin ich wirklich unendlich dankbar. Ich kann mir keinen besseren Mentor vorstellen.
- **Claudia Vanelle** für die tolle und bedingungslose Unterstützung während der gesamten Zeit, die wir uns kennen. Neben vielen guten Gesprächen bleibt mir insbesondere die Gastfreundschaft und die Liebe zum Detail in Erinnerung. Ich glaube wir denken ähnlich über viele Dinge und ich habe viel dazugelernt. Insbesondere möchte ich hervorheben, dass diese Arbeit in ihrer jetzigen Form ohne deine Wiederentdeckung und Plausibel-machung von Shah's geometrischer Herleitung der parabolischen Formel wahrscheinlich nicht möglich gewesen wäre. Da habe ich begonnen, die ersten grösseren Zusammenhänge zu erkennen.
- **Christian Hübscher** für die Unterstützung und die Chance und das Vertrauen, zweimal gross in See stechen zu dürfen. Die gemeinsamen Erfahrungen an Bord, während des Grundpraktikums und in meiner Zeit als studentische Hilfskraft haben mir neue Blickwinkel auf die Geophysik ermöglicht und mich, so hoffe und glaube ich, zu einem besseren Wissenschaftler gemacht.
- **Thomas Hertweck** für die Chance eines spannenden Praktikums in England, das Teilen Deiner immensen Erfahrung und die tollen Gespräche und die vielen kleinen und grossen Hilfestellungen, wenn ich Hilfe brauchte und brauche.
- **Martin Tygel** for the great support and the inspiring discussions at the consortium meetings.
- **Alexander Bauer** für die gute Zusamenarbeit und das Teilen vieler Ansichten und die gemeinsame Leidenschaft Fussball. ;-) Die ersten praktischen Schritte zur *diffraction decomposition* sind allein Dir zu verdanken.
- **Korbinian Sager** für die wirklich immer tollen Gespräche. Ich bin froh, dass wir uns immernoch regelmässig sprechen und sehen. Ich kann behaupten, in Dir einen guten Freund gewonnen zu haben.

- **Martina Bobsin** für die super Zusammenarbeit und die erfrischende Ehrlichkeit. Wichtige Untersuchungen zur Migration sind Dir und Deiner Arbeit zu verdanken.

- **Khawar-Ashfaq Ahmed** for sharing the office and refreshing jokes. I truly could always count on you and, together with your loveley wife, we had an awesome time in Amsterdam. Really hope we stay in touch!

- **Philipp Witte** für den spannenden gemeinsamen Road Trip durch die Südstaaten - True Detective zum Anfassen...

- **das BMWi (insbesondere das Projekt 0325363C 'Imaging steep structures with diffractions') und das Wave Inversion Technology Konsortium (insbesondere das Projekt 'Multiparameter processing with finite offsets')** für die finanzielle Unterstützung während meiner Zeit als Doktorant.

- **TGS Nopec** für den Zugang zu den Felddaten und die Erlaubnis, die Ergebnisse zeigen zu dürfen.

Wer mich kennt, weiss: Für mich kommt die Familie wirklich (fast ;-)) immer zuerst. Der Anteil meiner Eltern an dieser Arbeit, durch die Ermöglichung des Studiums, die immer uneingeschränkte seelische Unterstützung und das Vertrauen in meine Fähigkeiten, als Student und als Mensch, sind wirklich schwer in Worte zu fassen - ich hoffe immer und jeden Tag, dass ich euch das irgendwie zurückgeben kann. Maja, danke für die tolle Hilfe beim Korrekturlesen und dass Du immer für mich da warst und bist. Ohne Dich wäre ich nicht da wo ich jetzt bin. Ausserdem gebührt mein Dank insbesondere meinem Grossvater und meiner Grossmutter, die ich (dank Dirk) regelmässig in der Woche besuchen durfte - die gemeinsame Zeit war und ist etwas ganz besonderes und ich geniesse jeden Tag.